# NEW METHODS IN 2D IR SPECTROSCOPY AND IMAGING: APPLICATION TO BIOLOGICAL AND MATERIALS SYSTEMS

By

Joshua S. Ostrander

A dissertation submitted in partial fulfillment of
the requirements for the degree of

Doctor of Philosophy
(Chemistry)

at the
UNIVERSITY OF WISCONSIN–MADISON
2019

Date of final oral examination: 05/16/2019

This dissertation is approved by the following members of the Final Oral Committee:
Martin T. Zanni, Professor, Chemistry
Randall H. Goldsmith, Associate Professor, Chemistry
Etienne Garand, Associate Professor, Chemistry
John C. Wright, Professor, Chemistry

# New Methods in 2D IR Spectroscopy and Imaging: Application to Biological and Materials Systems

Joshua S. Ostrander

Under the supervision of Professor Martin T. Zanni
at the University of Wisconsin–Madison

Two-dimensional infrared spectroscopy (2D IR) is a nonlinear spectroscopic technique with applications in fields ranging from biophysics to materials science.In this dissertation, I report several new technical advances in 2D IR spectroscopy and provide examples of some applications in biophysics and materials science. The advances presented will lead to wider adoption in both the complexity of scientific questions that 2D IR can address and reduce the barrier for non-experts to enter the field.

In the first study, I report the development of pulse shaping based Fourier transform infrared (FTIR) spectroscopic imaging. We show that the microscope can distinguish between chemical species with diffraction limited resolution. Second, I present the design and construction of the first wide-field microscope to spatially resolve 2D IR spectra. The differences in image formation between FTIR and 2D IR images are also presented. Next, I present an application of 2D IR spectroscopy to the study of energy transfer in the secondary explosive pentaerythritol tetranitrate (PETN). The FTIR and time-dependent 2D IR spectra are presented and energy transfer is identified. Additionally, we use transition dipole strength measurements to conclude that the excitations are delocalized over 15-30 nitrate ester groups. I also present methods for measuring the 2D IR spectra of monolayers by capitalizing on the signal enhancement from plasmonic gold films. Additionally, we show that a reflection geometry can further enhance signal strengths. We study the structure of cysteine terminated ovispirin on a gold surface in $D_2O$ and $H_2O$. In the seventh chapter, I present a 2D IR immuno-sensor to measure the structure of proteins extracted from solution. The experiment utilizes surface-enhanced 2D IR spectroscopy to measure a monolayer of sequence specific antibodies chemically linked to a thin film of gold. We also show that that we can resolve single isotope labels on the antibody. Finally, I present the design and construction of a 50 kHz 2D IR spectrometer with a KGW doped Ytterbium amplifier. I present the design of our home-built optical parametric amplifier and evaluate the performance of the system in high repetition rate 2D IR measurements.

# Acknowledgments

As a child, I never dreamed that I would be a scientist. Although the journey hasn't always been easy, it has been a pleasure to pursue this degree the past five years. Of course, I did not do it alone and without the support, encouragement, and guidance of those listed herein (and many who are not), this dissertation would not have been possible.

My graduate advisor, Marty Zanni, deserves the most thanks in making this work possible. In my opinion, you provided me with the ideal amount of guidance and independence. I knew that I wanted to work for you from the moment I first heard you give a talk at APS my junior year of college. It's been an honor to work with you, and I can't wait to see the amazing science the group puts out in the coming years. Thank you for helping me navigate this time of my life.

I'd also like to thank my dissertation committee for providing me guidance throughout my tenure here in Madison. Randy Goldsmith has been a constant on my mentoring committee and always provided sound scientific advice and tough hockey competition. Thanks to Etienne and John for joining my committee for the final call. I wish you both the best in your future scientific pursuits. I would also like to acknowledge Fleming Crim for sitting on my committee up until he left to go back to the NSF. Thank you for encouraging me to be the best scientist I can be.

I owe my first positive experiences in science to Mr. Steve Hamilton. I cannot imagine pursuing science without the enthusiasm you showed teaching us in fifth grade. For that, I thank you. I also would like to thank the many team members and coaches of the Northridge High School Science Olympiad team. Specifically, Jeremy Gerber and Jerry Glass who were especially formative in molding me to become a scientist. I would also like to thank Brad Zook and Bryce Cone, my high school band directors, for instilling in me the value of practice and excellence. The lessons you taught in the classroom and on the marching field have helped me to persevere in graduate school's toughest moments.

My time at Indiana Wesleyan were some of the best years of my life. I think the Chem Crew deserves special thanks, as I can not imagine going to graduate school without all of you in my life. Lisa, Nick, Toby, Kaley, Amanda, Ellen, and Connor: it was a pleasure to study and work with you all. Heath Rose deserves a special shout out. We've navigated this whole process concurrently. Thanks for helping me get to where I am today. Grant Yoder has been a friend for many years. I'm thankful that you've kept in touch and encouraged me throughout this process.

My undergraduate advisor, Steve Tripp, deserves thanks for taking me under his wing and showing me what doing science was all about. I appreciate the advice, guidance, and encouragement that you provided me then, and still do to this day. I also owe thanks to David Duecker for sparking the physical chemistry bug in me. I also would like to acknowledge Kevin Kubarych and the rest of the Kubarych group for taking me on in the summer of 2013 and giving me my first taste of ultrafast spectroscopy. You all made my summer in Ann Arbor one to remember. I would also like to thank Joe Thomaz, who I met in Ann Arbor that summer. Joe: we were two hoosiers who became fast friends. I have appreciated your friendship and scientific advice over the years.

During graduate school I have had the pleasure to work with amazing and kind scientists, both in the Zanni group and at UW-Madison. Ayan Ghosh and Arnaldo Serrano were influential in my early development as a graduate student. They taught me everything I know about the practical side of spectroscopy and I will always remember their enthusiastic scientific arguments in lab. I know you both are great professors and I look forward to reading your papers in the future. Thank you for investing in a naive and eager first year student.

Randy Mehlenbacher and Huong Kratochvil were the ranking graduate students when I joined. Randy: your desire to help others is admirable and the advice you give always sound. I know that you will succeed wherever you end up in life. I don't think I will never meet someone with more positive energy than Huong. I always appreciated that your company in the early mornings. Your intellect and hard work will surely propel you to success.

Tianqi Zhang is a biochem wizard and she always brought laughs and joy to the offices. I miss you in the group and hope we can meet again. The only positive side of Tracey Reitz's absence in the group is a significant decrease in my candy consumption... Tracey, you are a fantastic scientist, teacher and mentor. I wish you all the best in your future.

Tom McDonough was/is an enigma that can not be embodied with my words alone. Tom: you are a true legend in your field and have brightened my mood on countless occasions. I will always treasure my memories of our time at Five Guys together. Thank you for teaching me that you don't have to do something everyday. #freethepicosecond I've had the wonderful pleasure of sharing a laser source with Jia-Jung Ho for most of my graduate school career. I appreciated your scientific insight and attention to detail. I enjoyed every moment of our time together and I miss your encouragement and advice tremendously. I have no doubts that you will accomplish whatever you put your mind to.

I have been fortunate to share my time in the Zanni Group with Nick Kearns and Kacie Rich. Kacie's attention to detail and ability to trouble-shoot wet lab problems have been instrumental to group success. I'll miss the energy that you brought to the office each morning. Nick: I've gotten so much good advice from you about technical problems. I can't imagine I would have ever graduated without your careful problem solving advice. I wish you all the best in Seattle.

I was lucky to join the Zanni group with Ariel Alperstein. I have thoroughly enjoyed our 5 years in the same office and I hope that I've provided at least half of the scientific advice that you have given me. You have an amazing attention to detail and a knack for designing impeccable experiments. I know that you will do great things in life.

Jessi "Jessica" Flach has been such an asset to the group for more reasons than one. My only regret during my PhD is that we missed out on a full year of your presence while you were in Switzerland. Thanks for staying positive even when working with the most rebellious lasers in the group.

This brings me to the “The Post Doc Boom of 2016.” Andy Jones was the first to make an appearance. Andy brought an incredible amount of optics knowledge and experience to our group. I can safely say that the 100 kHz 2D IR spectrometer would not be where it is today without his advice and assistance during the preliminary stages. I’ve also enjoyed our political discussions and many lunches together. Thank you for you encouragement and guidance the past three years. I hope that we meet again soon.

Michal Maj joined shortly after Andy. Michal is one of the hardest working people I know and brought a wealth of knowledge about 2D IR spectroscopy. I know you will make a great professor and I can’t wait to read your many papers over the next few years. Justin Lomont joined at the beginning of May. I enjoyed our many collaborations and I hope that I’ve taught you at least a fraction of everything that you’ve taught me. Your wit and intellect have made my time in this group most enjoyable. Thank you.

Megan Petti joined the Zanni group at the beginning of my third year and I had the privilege of working with her on many projects during the latter half of my PhD. Megan, you are a talented spectroscopist and can do anything that you set you mind to. This dissertation would not be possible without your advice, intellect, and hard work.

The group expanded dramatically during my fourth year. I had the pleasure of building the first generation 100 kHz OPA with Cat’s assistance during her first year. Cat’s ability to quickly learn the ins and outs of OPA design while simultaneously learning about protein synthesis is truly astounding. I am confident that I will be reading many great papers about ancestors of hIAPP in the coming years. I’ve also had the great pleasure of working with Erin on the Kickapoo laser table. I have never seen Erin pessimistic about a future experiment. Don’t ever lose your optimism and desire to help others. It embodies the true Zanni group spirit. Miriam Bohlmann Kunz, although not working directly with me, has provided reams of good advice about general spectroscopy. It's been great to watch you turn in to one of the best resources on ultrafast lasers in the group.

The first years represent what might be the greatest Zanni recruiting class of all time (in height). Sid, your enthusiasm and intellect make you a great asset to our group. I promise you I'll give you a high five sometime before I leave. Zach is everything I want to be as a person. Smart, sassy, and full of life. Thanks to you, I'll never hear another NPR politics podcast without crippling anxiety. Ryan "Tallen" Allen has been a great desk mate. It's been great to see you lose your mind over coherent oscillations. Don't let my skepticism get you down! Be sure to remember me every time you hit the Ginge for some Sesame Chicken.

Finally, I have spent the last few months training Kieran "KMan,KSqueeze, 3Q, Simulation code, Kwiz" Farrell. You have learned more in 6 months than I learned in three years. I can't wait to see what you produce in this group. It's an honor to call you a colleague.

Many other Zanni group members have been influential during my PhD. Jack O'Connor was fantastic coworker with unbridled enthusiasm. I'm also grateful for Kaarin's time in the group. Tarasankar Das was always friendly and down for anything. The undergraduates that have overlapped with me have been fantastic. Elliot Eklund and Alex Blair were great collaborators on the anisotropy measurements. Dan Mark did some great leg work on the antibody experiments, learning how to tether proteins to substrates. Ben Feingold has been a hero on the most recent antibody experiments. Thanks for dealing with me as I've been writing my dissertation, building a new laser system, and trying to mentor you all at the same time.

I'm indebted to Darcie Farrow from Sandia National Lab for initiating the collaboration on the PETN samples. Thank you for taking the time to teach me about energetic materials. I'd also like to thank Mike Arnold and his group for many fruitful collaborations. Specifically, for loaning Nate Safron for initial plasmon experiments. This brings me to the legendary Vivek Saraswat. Vivek has been a fantastic collaborator and revolutionized the surface-side of the Zanni group. I'd also like to thank Ryan Young and Stephen Miller from the Wasielewski group for their invaluable advice on the 100 kHz spectrometer. Chris Middleton and Baichhabi Yakami from PhaseTech have provide great advice and loaner equipment for the pulse shaper.

Thanks to the P chem class of 2014 for getting me through my coursework. Special thanks to Alex Foote for being a great friend and co-TA in Chemistry 115. I've also appreciated Darien Morrow for advice and optics loans on more than one occasion.

Outside of chemistry (kind of...), Erik and Kayla Horak have become two of my closest friends. Thank you for many movie nights, game nights, and concert companionship. Wes, Rachel and Frankie DeRish have been excellent friends/D&D compatriots (also Bryan Campbell). Thank you for helping me keep my focus on what really matters in life. Best of luck as you move to the UK. Jon Dahl has been a friend and mentor throughout graduate school. Thanks for many breakfasts at Mickies Dairy Bar.

This brings me to those who have been in my life the longest. Thank you to my family, both immediate and extended, for encouraging and supporting me on this path. Specifically, I would like to thank my parents, Steve and Lisa, for their constant love. Thanks for teaching me to work hard and fostering my talents. Thanks to Andrew, Caleb, and Jessica for listening to me yak about chemistry on countless occasions.

To my wife, Katie: thank you for your companionship and love during this journey. I'm honored to share a life with you and am proud of your many accomplishments. I dedicate this dissertation to you.

# Contents

# List of Figures

# List of Tables

# Chapter 1

# Introduction

## Contents

---

The section on vibrational coupling was adapted from a review article I co-authored: *Chemical Reviews* **2017**, *116*, 10726-10759. It was prepared in collaboration with A. Ghosh, and M.T. Zanni.[1]

Understanding molecular structures and how these structures change is foundational to many processes in chemistry. Such events include chemical reactions, protein folding, and charge transfer.[1–3] The ideal technique would capture all relevant motions that occur in a system. A specific example is protein folding[1] where solvent motions occur on the picosecond timescale, side chains rotate in a few nanoseconds, and global conformations can exchange over the course of milliseconds to hours. There are few techniques that have both the necessary time and structural resolution to sufficiently address these challenges. Optical analogs of multidimensional spectroscopy are one approach to bridging the gap between time resolution and structural sensitivity. This dissertation is devoted to advancing the technology of 2D IR spectroscopy. I present technical advances that enable 2D IR spectroscopic imaging and outline how this new method will impact biophysics and materials science. I also studied thin-films of energetic materials in the solid state to identify extended vibrational excitons. Additionally, I report the first 2D IR measurements of protein monolayers and show how the measurements enable the development of a 2D IR immuno-biosensor. Finally, I present preliminary data from a 50-100 kHz 2D IR spectrometer, which I think represents the next generation of 2D IR measurements. These experiments make use of technical advances to impact new scientific fields.

## 1.1 Vibrational Spectroscopy

The experiments in this dissertation utilize infrared spectroscopy, which probes the chemical bond. To understand how the molecule responds to light, we solve for the nuclear motion. Two atoms come together to form a bond when there is an attractive force between them. Figure 1.1 shows a calculated potential energy that describes a Morse interatomic potential, that is one model for the potential of interaction between two atoms. Although, this crude model captures the fundamental form of diatomics, the complexity of its solution can obscure important physical insights into vibrational spectroscopy. To solve for the equation of motion quantum mechanically, we often approximate this potential as harmonic. That is, the restoring force is proportional to the displacement from the equilibrium distance.

$$V(x) = \frac{1}{2}kx^2 \tag{1.1}$$

Where *V(x)* is the potential energy, $k$ is the so-called force constant, and $x$ is the distance between the two atoms. Solving the Schrodinger Equation for this potential, we find that the allowed energies are given by equation 1.2:

$$E = \hbar\sqrt{\frac{k}{\mu}}(\nu + \frac{1}{2}) \tag{1.2}$$

Where $\hbar$ is Planck's constant divided by $2\pi$, $\mu$ is the reduced mass of the oscillator, and $\nu$ is the vibrational quantum number that can be any integer greater than or equal to 0. We can see that spacing between the allowed energy levels depends on the force constant and reduced mass. Often times we group $k$ and $\mu$ together and write it down as $\omega$, called the fundamental vibrational frequency.

In the dipole approximation, a molecule absorbs light only if the energy of the photon matches exactly the energy spacing between two transitions. Consequently, we observe characteristic peaks in an absorption spectrum. For fundamental vibrational frequencies, the features appear between 400-4000 $\text{cm}^{-1}$. Such energies correspond to oscillationg periods on the order of $10*10^{-15}$ seconds, or 10 fs. The fast vibrational periods are responsible for the inherent time resolution of vibrational spectroscopy. An often overlooked consequence of the frequency of vibration is that infrared and Raman spectra are easy to simulate with Molecular Dynamics (MD) simulations.[4]

If we only observe absorption when our incident light is resonant with the transition of interest, why do we observe broad spectral features in solution? There are two possible answers. 1. The peak is broadened due to fast fluctuations, called homogenous broadening. 2. There could be a distribution of fundamental frequencies arising from environmental distortions of the potential surface. The origin of spectral broadening is an inherent ambiguity in linear optical spectroscopy and often both mechanisms contribute to the line width. To distinguish between these two limiting scenarios, we need a nonlinear technique like a transient absorption, three-pulse photon echo experiments, or 2D spectroscopy.

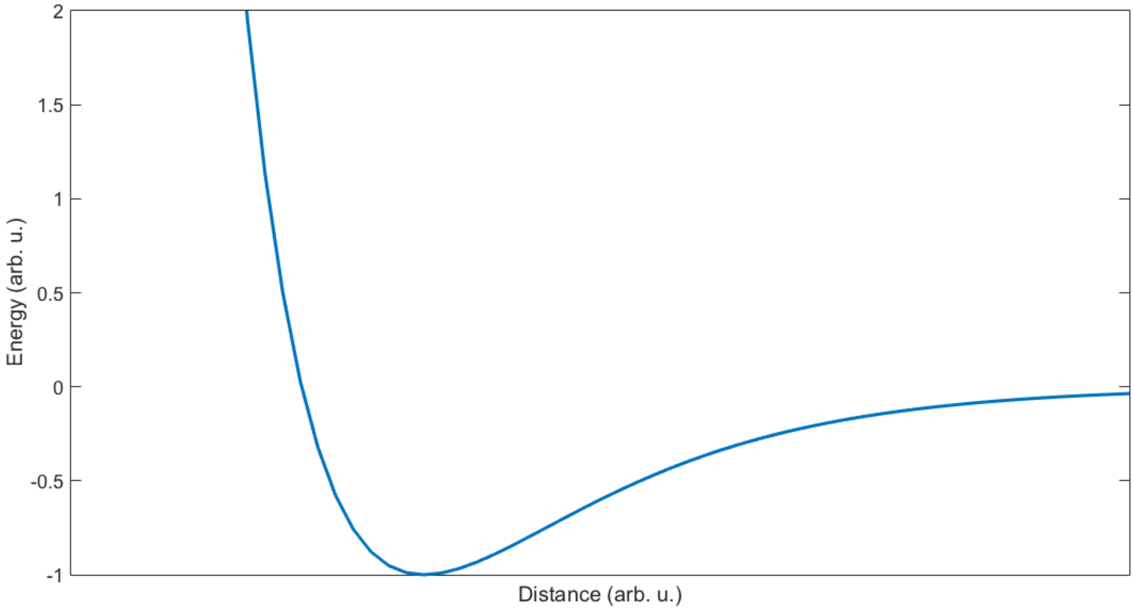

Figure 1.1: Calculated Morse potential used to describe the interaction between two atoms. At short distances, the interaction is repulsive because of the overlap of the electron clouds. At intermediate distances, the interaction is attractive leading to the formation of a chemical bond. At long distances, there is no interaction between the molecules.

## 1.2 Vibrational Coupling

### 1.2.1 Coupled Oscillators

In practice, one often wants to use an infrared spectrum of a collection of oscillators to say something about the structure. Consider two carbonyl amide-I vibrations that are placed in close proximity to one another. Because of coupling, stretching one mode affects the potential energy felt by another. If the molecules are physically connected, there can be through-bond interactions, in addition to electrostatic and electrodynamic effects.[5] We can then reasonably assume that our description of the eigenstates of an isolated vibrational mode is too simple. A crude model for this coupling is to assume that the two oscillators interact *via* a through-space dipole-dipole potential. The coupling magnitude depends on the orientation and distance of the two oscillators. In this dissertation, we will refer to the coupling interaction between an oscillator i and j as $\beta_{ij}$. Here, $\beta_{ij}$ is a function of the coordinates of the separate vibrational modes.

In an experiment, we do not observe the local mode energies, but the "normal", or "excitonic" modes. To calculate how this affects the vibrational spectrum, we need to calculate the Hamiltonian of the system. For linear spectroscopy, you only need to include the fundamental 0→ 1 excitations. However, a description of 2D IR spectroscopy must use the two-exciton Hamiltonian which will also require including anharmonicity. Assuming bilinear coupling, the Hamiltonian can be expressed as:[5,6]

$$H_{ij} = \sum_{i}^{N} \hbar\omega_i b_i b_i^{\dagger} + \sum_{j}^{N}\sum_{i\neq j}^{N} \beta_{ij} b_j^{\dagger} b_i - \sum_{i}^{N}\sum_{j}^{N} \hbar\Delta_i b_i^{\dagger} b_j^{\dagger} b_i b_j + H_{SB} \tag{1.3}$$

In equation 1.3, $b$ and $b^{\dagger}$ are the raising and lowering operators used in solving the harmonic oscillator, and $\Delta_i$ is the anharmonicity in units of $\hbar\omega$. $\hbar\omega_i$ is the fundamental frequency for oscillator *i*. These are often referred to as the "site energies" or "local mode energies" and describe the local mode frequency in the absence of coupling. $H_{SB}$ is the system-bath Hamiltonian. This term describes the interaction between the molecule and the environment. For most chemical applications in the condensed phase, this is the electric field environment of the solvent. The system-bath Hamiltonian is a function of time and will cause the site energies and the coupling between local modes to fluctuate in accordance with the environment. For the following discussion as it relates to structure, we neglect the effect of the $H_{SB}$. The coupling to the bath is extremely important to simulate and model intramolecular vibrational energy transfer and coherence transfer.[7]

To get the energies in the exciton basis, we must diagonalize the local mode Hamiltonian. To illustrate this point concretely, the local mode Hamiltonian is written out as:

$$H_{Local} = \begin{pmatrix} 0 & 0 & 0 & 0 & 0 & 0 \\ 0 & \hbar\omega_i & \beta_{ij} & 0 & 0 & 0 \\ 0 & \beta_{ij} & \hbar\omega_j & 0 & 0 & 0 \\ 0 & 0 & 0 & 2\hbar\omega_i - \Delta_i & 0 & \sqrt{2}\beta_{ij} \\ 0 & 0 & 0 & 0 & 2\hbar\omega_j - \Delta_j & \sqrt{2}\beta_{ij} \\ 0 & 0 & 0 & \sqrt{2}\beta_{ij} & \sqrt{2}\beta_{ij} & \hbar\omega_i + \hbar\omega_j \end{pmatrix} \tag{1.4}$$

This equation is diagonalized with a unitary transformation to give the eigenstates and their corresponding energies. To conceptually illustrate the results, we assume that both coupled oscillators are identical, $\omega_i$=$\omega_j$, and diagonalize equation 1.4. When doing so, we obtain:

$$H_{Exciton} = \begin{pmatrix} 0 & 0 & 0 & 0 & 0 & 0 \\ 0 & \hbar\omega - \beta & 0 & 0 & 0 & 0 \\ 0 & 0 & \hbar\omega + \beta & 0 & 0 & 0 \\ 0 & 0 & 0 & 2\hbar\omega - \frac{1}{2}\Delta - \frac{1}{2}\sqrt{\Delta^2 + 16\beta^2} & 0 & 0 \\ 0 & 0 & 0 & 0 & 2\hbar\omega - \frac{1}{2}\Delta + \frac{1}{2}\sqrt{\Delta^2 + 16\beta^2} & 0 \\ 0 & 0 & 0 & 0 & 0 & 2\hbar\omega - \Delta \end{pmatrix} \tag{1.5}$$

The diagonal elements of equation 1.5 give us the frequencies we observe in an experiment. As we will see soon, a linear experiment will allow us to observed the one-exciton Hamiltonian, while 2D IR will reveal the higher lying states in the two-exciton Hamiltonian.

To illustrate the effect of coupling on a linear FTIR spectrum, consider two transition dipoles as in Figure 1.2. The two coupled dipoles have a local mode frequency of 1700 $\text{cm}^{-1}$. As we change the angle between the two modes and calculate a spectrum, we observe peak splitting because the magnitude of the coupling depends on the relative angle. Additionally, the relative intensity of the two peaks changes as the angle is varied. This figure illustrates how one can determine structure by determining the coupling from an FTIR experiment. In practice, this is difficult to do using FTIR because it is not certain whether two peaks observed in a spectrum are from two different environments, molecules, or coupling. In a 2D IR spectrum, we will observe a cross peak between the two modes if they share a common ground state.

### 1.2.2 Transition Dipole Matrix

For a vibrational mode to absorb infrared light, there must be a change in dipole moment upon excitation from the ground to the excited state. The magnitude of this change determines the probability of absorption and, therefore, the intensity of a spectroscopic transition

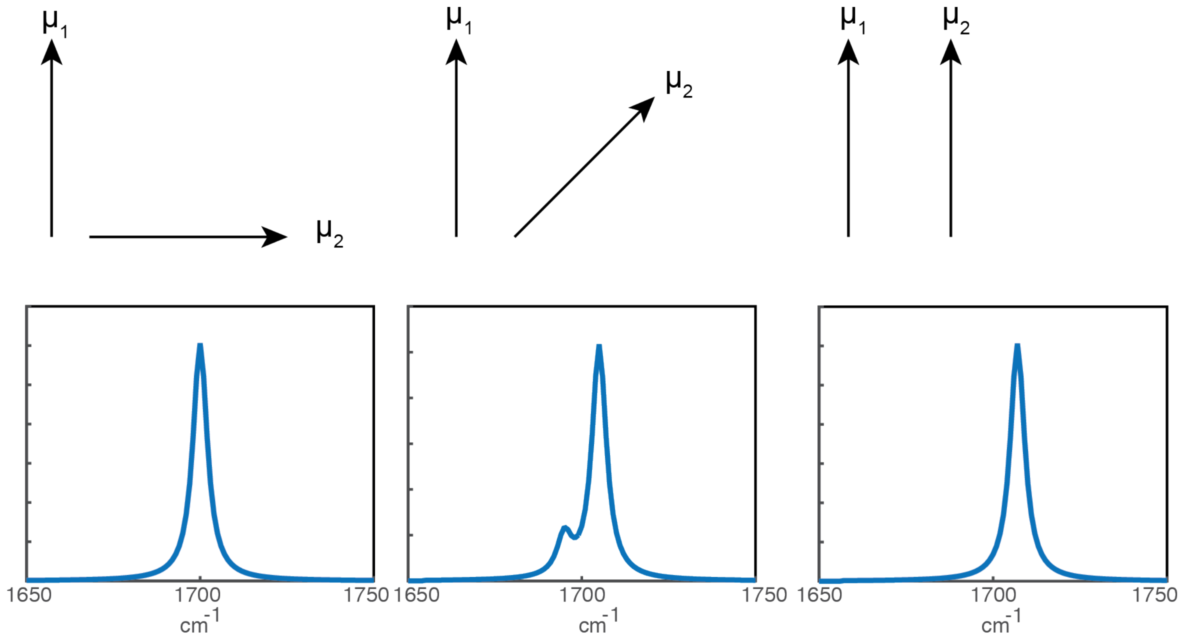

Figure 1.2: FTIR spectrum for two coupled oscillators calculated based on a transition dipole coupling model for a distance of 0.5 nm. The relative angle of each calculated is 90,45, and 0 as illustrated schematically.

observed in an experiment. In this dissertation, I extensively make use of measurements of transition dipole moments to help determine the structure,[8] signal enhancement,[9] and unassigned peaks.[10]

The transition dipole is calculated with the the transition dipole operator. For a transition from the $\nu$=0 → $\nu$=1 excited state, the expectation of the transition dipole is calculated according to equation 1.6:

$$\big\langle \mu \big\rangle = \langle 1|\hat{\mu}|0\rangle \tag{1.6}$$

With the transition dipole operator defined classically, this can be written as:

$$\big\langle \mu \big\rangle = \frac{\partial \mu}{\partial x}\langle 1|\hat{x}|0\rangle \tag{1.7}$$

The fact that the dipole operator is essentially a position operator gives rise to the dipole selection rule in vibrational spectroscopy. That is, the change in the vibrational quantum number can only be ± 1. A more detailed derivation can be found in Schatz and Ratner.[11] The magnitude of absorption is proportional to the transition dipole squared, $\mu^2$, called the transition dipole moment.

In a system of coupled oscillators, the transition dipole strength is transformed with same unitary transformation as the Hamiltonian. In a matrix representation, the matrix of $\vec{\mu}$ is transformed with the same unitary transformation we used to diagonalize the local mode Hamiltonian. This transformation has the effect of generating transition dipoles for the excitonic states that are linear combinations of the local mode transition dipoles. Mathematically, this equation is written as:

$$\vec{\mu}_{Ex} = \sum_{i}^{N} c_i \vec{\mu}_i \tag{1.8}$$

Here, the coefficients, $c_i$ are determined from the eigenvectors of the Hamiltonian. For a system with $N$ local modes, there will be the same number of excitonic modes. Additionally, we know that each excitonic mode must be normalized. That is, the sum of the ${c_i}^2$ must equal to 1. If we assume that an excitonic mode is equally distributed over all coupled local modes (all oscillators are vibrating in phase, true for the strongest mode) and that each local mode is identical, all of the coefficients will be equal to $\frac{\sqrt{N}}{N}$. Additionally, if we assume that the local modes have the same direction as the normal modes, we find that:

$$|\vec{\mu}_{Ex}| = \frac{\sqrt{N}}{N} \sum_{i}^{N} \vec{\mu}_{Loc} = \sqrt{N} \vec{\mu}_{Loc} \tag{1.9}$$

We can divide out the local mode transition dipole accordingly:

$$\frac{|\vec{\mu}_{Ex}|}{|\vec{\mu}_{Loc}|} = \sqrt{N} \tag{1.10}$$

We know from the preceding discussion that the intensity of an absorption feature is proportional to $\mu^2$. Therefore, in units proportional to the linear absorption coefficient we find that:

$$\frac{|\vec{\mu}_{Ex}|^2}{|\vec{\mu}_{Loc}|^2} = N \tag{1.11}$$

Consequently, the ratio of the absorption cross section of a coupled mode and its uncoupled one give a lower bound for the number of coupled oscillators contributing to the transition.[12] We take this to be a lower bound because disorder of frequencies and deviations of the local mode vectors from the over excitonic one will lead us to underestimate the number of modes contributing to an observed transition. Measuring this directly with linear absorption spectroscopy (FTIR) can be challenging for molecules in which the concentration is not precisely known. 2D IR spectroscopy can provide more information to precisely determine the ratio of the excitonic and local transition dipole moments.

Transition dipole strength measurements allow us to estimate the number of molecules contributing to a vibrational mode, which is known as the inverse participation ratio (IPR).[13] The IPR is defined as:

$$IPR = \frac{1}{\sum c_i^4} \tag{1.12}$$

The IPR is used in many fields, especially in the photosynthetic community,[3] to define exciton delocalization. Accurate knowledge of the IPR is often limited to theory. This discussion shows that we can estimate the IPR from experiment within the approximations outlined above.

### 1.2.3 Coupling Models

The key to relating the observed excitonic frequencies, anharmonicities, and peak intensities to molecular structure is measuring the coupling, $\beta_{ij}$. In a protein, the amide I backbone vibrations couple differently on the basis of the structure.[14,15] To relate the measured coupling to a molecular structure, we need to have some model that relates the three-dimensional position of the atoms to the measured excitonic frequencies and transition dipoles.[16–21] In principle, one can use use a fully *ab initio* calculation to account for dipole, electrostatic, electrodynamic and mechanical coupling.[22] Most biologically relevant proteins are too large for such a calculation to be feasible. In lieu of a fully quantum mechanical calculation, some models must be used to interpret the typical infrared spectrum of a protein. Typically, these models are parametrized with fully quantum mechanical calculations. The simplest of these models is transition dipole coupling.[5,6,23] In this picture, the local mode transition dipoles interact with one another via through-space dipole–dipole interactions. The coupling $\beta_{ij}$ between chromophores is expressed as:

$$\beta_{ij} = \frac{1}{4\pi\epsilon_0}\Big[\frac{\vec{\mu_i}\cdot\vec{\mu_j}}{r_{ij}^3} - 3\frac{(\vec{\mu_i}\cdot\vec{r_{ij}})\times(\vec{\mu_j}\cdot\vec{r_{ij}})}{r_{ij}^5}\Big] \tag{1.13}$$

This model is the most intuitive picture of vibrational coupling, although it neglects the effects of through-bond coupling and also breaks down at short distances.[5] Another coupling model is the transition charge density, which takes into account the electrostatic interaction energy between two coupled local modes.[5] A similar approach is the transition point charge model, which replaces the integration in the transition charge density model with a summation, which is more computationally feasible.[5] Recently, Lee et al. published a comparison of coupling models for a $\beta$-sheet.[13] Jansen and Knoester have developed coupling maps based on the effects of local electrostatics on the vibrational frequency.[19] All of these models are necessary to provide simple and intuitive interpretations of the vibrational spectra of proteins.

### 1.2.4 Transition Dipole Coupling in Model Systems

Before discussing the general features of vibrational spectra associated with proteins, we briefly discuss the infrared spectra of an infinite chain of coupled oscillators. Generally, the mathematics to determine the eigenstates and their corresponding energies are formally the same as the calculation of band structures in solid-state physics. Borrowing terminology from this field, we consider the so-called ”tight binding” model and only consider nearest-neighbor couplings. We consider degenerate site energies (i.e., the local modes are chemically identical oscillators) and we assume that the structure is periodic so all of the nearest-neighbor couplings are identical. The Bloch theorem states that the eigenstates of the system can be expressed as linear combinations of Bloch functions. The Bloch functions are the local mode wave functions modulated by a phase factor. Therefore, the wave function for state k is given by:

$$\Psi_k = \frac{1}{\sqrt{N}} \sum_j e^{i2\pi jk/N} |j\rangle \tag{1.14}$$

Here $N$ is the number of oscillators and the summation of $j$ is performed over all oscillators in the chain. The dispersion relation for an infinite chain is given by:

$$E_k = \hbar\omega_0 + 2\beta \cos\left(\frac{2\pi k}{N}\right) \tag{1.15}$$

For a truly infinite chain, the $k = 0$ state is the only one that is optically allowed. Whether this is the highest energy state or the lowest depends on the sign of the coupling and, therefore, the orientations of the transition dipoles.[5]

The $\alpha$-helix is a common secondary structure in proteins and is especially prominent in membrane-bound proteins.[24] Since an $\alpha$-helix is a three-dimensional structure, with about 3.6 amino acid residues per turn, couplings beyond nearest neighbors cannot be neglected.[5] There are three major excitonic modes in an $\alpha$-helix. The first is along the z-axis of the protein, parallel to the helical axis, called the A mode. There are two other excitonic states, the E modes, that are degenerate and lie perpendicular to the helical axis. It should be noted that the transition dipole strength and frequencies of the transitions depend on a competition between the negative and positive couplings. These couplings cause an $\alpha$-helix transition to show up at about the same frequency as a random coil. However, if we recall our discussion of the coupled dimer, we will notice that the observed anharmonic shift, that is, the difference between the fundamental and excited-state absorption in a 2D IR spectrum, is significantly smaller than the local mode anharmonicity for strongly coupled oscillators.[5] The ability to distinguish between the strong and weak coupling limit makes 2D IR spectroscopy a useful tool for distinguishing between a random coil and an $\alpha$-helix.[25]

$\beta$-Sheets of amino acids effectively form a 2D system of coupled oscillators, with interstrand and intrastrand couplings. There has been significant effort in calculating the couplings in $\beta$-sheets and relating them to observables in a 2D IR spectrum.[13,26] The linear FTIR spectrum is dominated by two excitonic modes, referred to as the $a^+$ and $a^-$ modes. The intersheet couplings dominate and lead to the intense, low-frequency mode at about 1620 $cm^{-1}$. The large frequency shift and increase in transition dipole strength allow 2D IR to better discriminate between random coils and $\beta$-sheets.[26] In combination with isotope labeling, this makes 2D IR and FTIR spectroscopies powerful tools to monitor changes in protein secondary structure on the time scale of picoseconds to hours.

## 1.3 Multidimensional Infrared Spectroscopy

Another way to describe absorption is to use Maxwell's equations to determine the polarization induced by the incident electric fields. We can expand the polarization in powers of the electric field.[5] The polarization is a product of the frequency-domain susceptibility and the incident electric field(s).

$$P(\omega) = P^{(1)} + P^{(2)} + P^{(3)} + ... \tag{1.16}$$

$$P(\omega) = \chi(\omega)^{(1)}E + \chi(\omega)^{(2)}E^2 + \chi(\omega)^{(3)}E^3 + ... \tag{1.17}$$

Most light-matter interactions occur when the light is low intensity and so only the first term in the Taylor expansion is needed to describe the physics. However, when the intensity is large, we start to see nonlinear effects. These are described by the higher order susceptibilities. As such $\chi^{(1)}$ describes linear light matter interactions, $\chi^{(2)}$ second order effects, and so on. There are two approaches to accessing these nonlinear susceptibilities. One could in principle, generate an intense light source and measure the nonlinearity of the material polarization with the intensity of the incident field. Another approach is to generate multiple light fields with distinct wavevectors $k_n$. In this approach, the number of light matter interactions determines what term is probed experimentally.

The primary experiments described in this dissertation are linear infrared spectroscopy (FTIR) and 2D IR spectroscopy. 2D IR spectroscopy is a third-order experiment and as such probes the third-order susceptibility $\chi^{(3)}(\omega)$. Experimentally, this means there must be three light-matter interactions before the signal is emitted. To measure the phase of the electric field of the signal, we also use a fourth light pulse called the local oscillator.[5] Figure 1.3 shows the generic fields needed to generate a 2D IR spectrum.

In equation 1.17, we use the frequency domain susceptibility. For time-domain measurements, like most implementations of 2D IR, the time-domain response function *R(t)* is more convenient when calculating signals. In the time-domain, the envelope of the pulses is convoluted with the molecular response function. The third-order polarization induced by the pulse sequence in Figure 1.3 is given by:

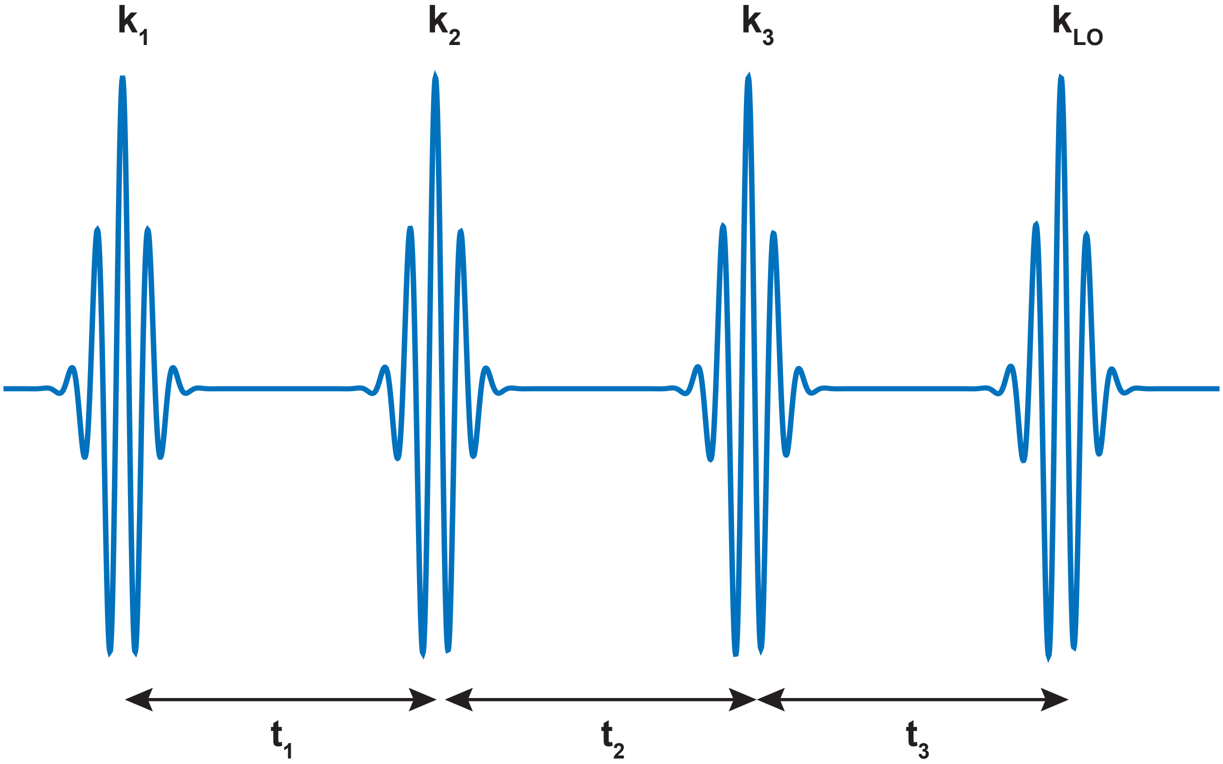

Figure 1.3: Generic pulse sequence of two pump pulses of time-delayed pulses. The first three interactions generate the signal and the fourth local oscillator is used to measure the amplitude and phase of the emitted field.

$$P^{(3)}(t_3,t_2,t_1) = \int_0^\infty dt_3 \int_0^\infty dt_2 \int_0^\infty dt_1 E_3(t-t_3)E_2(t-t_3-t_2)E_1(t-t_3-t_2-t_1)R^{(3)}(t_3,t_2,t_1) \tag{1.18}$$

Here $E_n$ is the time domain electric field and $R^{(3)}$ is the third-order molecular response function. The emitted third-order signal, which contains the information needed to generate an absorptive 2D IR spectrum is proportional to the polarization, but phase shifted by 90°:

$$E_{sig}^{(3)}(t_3,t_2,t_1) \propto iP^{(3)}(t_3,t_2,t_1) \tag{1.19}$$

An important observation here is that the emitted electric field will always be convoluted with the excitation pulses. Consequently, our 2D IR spectrum will carry information about our molecule of interest *and* our excitation pulses. The intensity of the pulses and their frequency spectrum have the most straight forward and obvious effect, but the temporal envelope and pulse chirp can also affect the measured spectrum. In the semi-impulsive limit, we assume we have infinitely broadband pulses in frequency and, therefore, delta functions in time. We the time scale of the molecular response is longer than the temporal envelope of the excitation pulses, we can discard the convolution in equation 1.18 and say the signal reflects the molecular response exactly. The signal field cannot be measured directly with mid-IR detectors, so we must interfere it with another electric field with a known phase. We call this pulse the local oscillator, $E_{Lo}$. The response function contains the information we want to learn about the molecule of interest. The mathematical description of the response functions have been described previously.[5]

To measure a 2D IR spectrum, we usually scan $t_1$ and $t_3$ to generate our pump and probe frequency axes, respectively. If waiting time dynamics are of interest, we can collect the spectra that depend parametrically on $t_2$. We can utilize a variety of different experimental approaches to collect the data. The first femtosecond 2D IR measurements used time-domain interferometry.[27] In this method, a single-pixel photodiode is used to measured the signal, $S$, as a function of the time delays between the three excitation pulses and local oscillator.

Scanning the coherence and detection times is quite laborious and time consuming. Consequently, most researchers use a mixed time-frequency method where the signal is dispersed on a spectrograph to generate the probe frequency axis ($\omega_3$) experimentally.[28] The spectrum is collected as a function of $t_1$ and the Fourier transform is computed after data collection.

### 1.3.1 2D Infrared Spectra

2D IR spectra are most intuitively interpreted in the frequency domain. In analogy to a frequency-resolved pump-probe experiment, we plot $\omega_1$ as the pump frequency on the ordinate axis and $\omega_3$ is labeled the probe frequency on abscissa. I choose to plot spectra accordingly in my dissertation because of the analogy to a pump-probe experiment. Some research groups plot the pump frequency axis on the abscissa and probe on the ordinate because of the convention in multidimensional NMR spectroscopy. Additionally, one can plot the data on a transmission or logarithmic scale. I choose to plot on the log scale, so that the spectra can be interpreted analogously to FTIR measurements. However, instead of plotting a change in optical density ($\Delta OD$), I choose to plot -$\Delta OD$. Again, this is for ease of comparing fundamental transitions to peaks in an FTIR experiment as a matter of preference. Other plotting conventions contain the same fundamental information.

Figure 1.4a shows a simulated 2D IR spectrum of an uncoupled oscillator.[1] Peaks associated with ground state bleaching and stimulated emission are associated with the $\nu$=0→1 transition show up on the diagonal with $\omega_1$=$\omega_3$ as shown in Figure 1.4a. Associated with every fundamental feature, is the associated excited state absorption peak that opposite and sign and centered off the diagonal such that $\omega_3$<$\omega_1$. This is associated with the $\nu$=1→2 transition. Colloquially, this peak is referred to as “the overtone” although, strictly speaking it is a sequence band.[5] The 2D line shape carries information on the relative homogenous and inhomogenous contributions to the spectral line width. The evolution of peak shape with waiting time provides information on spectral diffusion and the frequency-frequency correlation function. Experimentally, this is usually characterized with the center line slope (CLS),[29] although several other measures of the time scale of the FFCF have been developed.[30]

Figure 1.4b shows a simulated 2D IR spectrum for two coupled oscillators. We observed splitting of the two peaks as expected from vibrational coupling. Additionally, we observe cross peaks appear because of the coupling between the two modes. The cross peaks occur when one mode is excited during $t_1$ and, because both modes share a common ground state (i.e. they are coupled) we observe emission of a signal associated with the second mode during $t_3$. The intensity of the cross peaks changes as a function of $t_2$ because of vibrational energy transfer. In 2D IR where the energy spacing is much less than $kT$, we see cross peaks from both uphill and downhill energy transfer. In 2D electronic spectroscopy, where the energy spacing is much greater than the thermal energy, usually only downhill cross peaks are observed. The separation of the positive and negative cross peaks is the off-diagonal or mixed-mode anharmonicity and can be used to directly measure the coupling between two coupled modes.[5] The off-diagonal anharmonicity can be used to directly measure the relative orientation and distance between the two normal modes and thus provides a spectroscopic observable that can be directly related to the structure.

Additionally, we can observe the homogenous and inhomogeneous contributions to the line shape. Figure 1.5 present some simulated 2D IR spectra with different degrees of inhomogeneity and homogenous dephasing times. In each panel, the diagonal disorder and homogenous contributions to the line width are adjusted to keep the Full width at half maximum (FWHM) of the linear absorption spectrum about the same. The 2D IR spectra can be vastly different when the linear FTIR spectra would be otherwise indistinguishable. 2D IR spectroscopy can also characterize the rate at which the different molecules in an ensem-

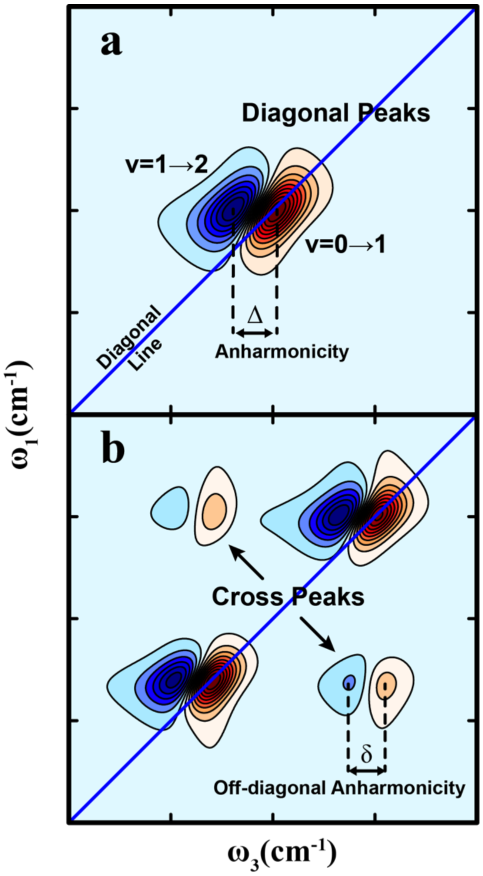

Figure 1.4: (a) Diagonal Peaks and (b) Cross Peaks. The spectra shown were calculated from third-order response functions described in Hamm and Zanni.

ble sample the possible frequencies. This is called spectral diffusion and is often measured using the center line slope.[30] The CLS quantity is directly proportional to the Frequency-frequency correlations function and characterizes how long a system carries memory of the initial excitations.

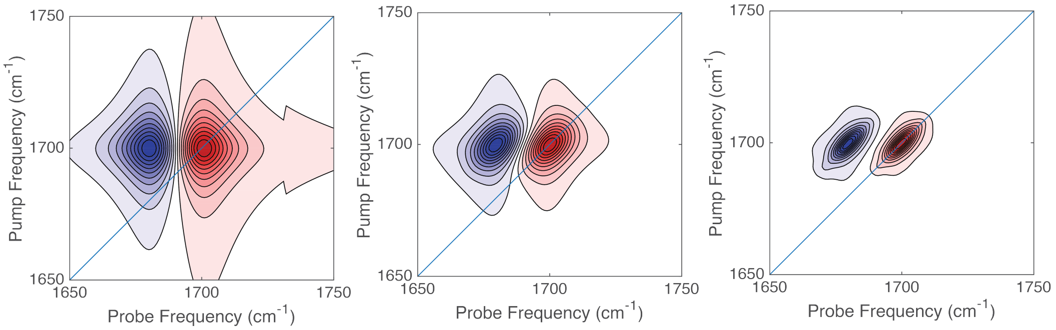

Figure 1.5: Simulated 2D IR spectrum for a completely homogenous sample (left), a partially inhomogeneous sample (center) and a completely inhomogeneous distribution of oscillators. The inhomogeneity is added by adding diagonal disorder to the Hamiltonian while the homogenous contributions is incorporated in the simulated response functions. In each spectrum, the relative homogenous dephasing and diagonal disorder is varied to keep the full-width at half maximum of the FTIR spectrum the same.

## 1.4 Surface Enhanced and Reflection 2D IR Spectroscopy

Spectroscopic characterization of monolayers and surfaces is experimentally challenging because of the small number of molecules probed in an experiment and the overwhelming bulk response. To address these problems, researchers have often turned to vibrational Sum-Frequency Generation (SFG) spectroscopy, a $\chi^{(2)}$ measurement for which signal is only allowed for non-centrosymmetric media in the dipole approximation.[31,32] SFG spectroscopy has been successfully applied to a wide range of systems, including those of fundamental interest,,[33,34] biological interfaces,,[35,36] and materials characterization.[37] Vibrational SFG provides a spectrum that is analogous to a linear vibrational FTIR spectrum with additional information on the absolute orientation in the laboratory frame. Measuring the 2D spectra of interfaces provides similar advantages that 2D IR spectroscopy has in the bulk,[38] and thus there have been efforts to improve the sensitivity of 2D IR spectroscopy to measure interfaces, and combine 2D IR with SFG to obtain surface specificity in 2D SFG measurements.[39] 2D SFG[40] provides a surface-specific 2D vibrational spectrum, but probes the $\chi^{(4)}$ nonlinear susceptibility. Thus, when compared to 2D IR spectroscopy, the experiment will have smaller signals and is experimentally complex. For molecular systems in which the vibrational mode of interest is confined to an interface, it is desirable to develop 2D IR measurements with the sensitivity to probe a single layer of molecules. The Fayer group has numerous published experiments that probe the surface response of transition metal carbonyls.[41,42] However, to probe the backbone amide-I response, which has a much smaller transition dipole strength, 2D IR experiments on protein monolayers requires methods to enhance the 2D IR signal. For example, even a well-ordered self-assembled monolayer (SAM) with high surface coverage will have an optical density(OD) that is a factor of 10 smaller than the OD in a bulk experiment. This means that, all things being equal, the 2D IR signal will be a factor of 100 smaller than the bulk response. The first 2D IR measurements of transition metal carbonyls in the Zanni group (unpublished) took about 5 hours of averaging before obtaining reasonable signal-to-noise.

### 1.4.1 Surface Enhancement of 2D IR Signals

Metallic surfaces and nanostructures contain an intrinsic optical resonance that originates from the oscillation of the conduction electrons.[43] These optical resonances are called surface plasmon resonances (SPR) and their study and applications has led the field of plasmonics. The SPR of metal surfaces is called a surface plasmon polariton. These SPRs have been used in Attenuated Total Reflection (ATR) spectroscopy to evanescently probe surfaces. The work presented in this dissertation utilizes the localized surface plasmon of metallic nanostructures. An optically excited localized surface plasmon leads to tight confinement of the electric field. This effectively increases the energy density and allows for ultra-sensitive spectroscopic measurements like surface-enhanced Raman (SERS)[44] and surface-enhanced infrared absorption (SEIRA).[45]

The past 5 years has seen a surge of interest in utilizing the plasmonic resonance of metal nanostructures to enhance 2D IR signals from the multidimensional spectroscopy community. Selig et al. have used gold nano-antennas with a plasmonic mode that is resonant with their molecule of interest to observe signals that are orders of magnitude larger than that of the bulk measurments.[46] However, when the plasmonic resonance is slightly off resonance from the molecular transition, Fano line shapes are observed that come from the interference of the broad plasmonic background with the relatively narrow molecular mode.[47,48] The Hamm group has shown that enhanced 2D IR measurements can be measured with nanostructures that have a resonance in the visible and near-IR region of the electromagnetic spectrum.[49–51] Kraack et al. have demonstrated that these off-resonant enhancement mechanisms do not substantially affect vibrational energy transfer rates.[52] Thus, one can reasonably assume that the measured line shapes and frequencies reflect the underlying molecular structure and dynamics. We take the latter approach for this reason. Additionally, the continuous gold films are advantageous when mimicking biological systems. Taken together, the use of metallic substrates increases the effective pump power and leads to a corresponding increase in the size of the signal field, $E_{sig}$.

### 1.4.2 Reflection 2D IR Measurements

The Fayer group has also pointed out that a reflection geometry can also lead to enhanced signals for monolayers and thin films.[53] This experiment capitalizes on the practical experimental implementations in the pump-probe geometry. The following derivation if presented in our group's paper on 2D IR of monolayers.[9] In a 2D IR experiment, the data is processed as:

$$\Delta OD = -\log \frac{I_{PumpOn}}{I_{PumpOff}} \propto \frac{2E_{Lo}E_{sig}^{(3)}}{|E_{Lo}|^2} \tag{1.20}$$

We can see from equation 1.20 that the measured change in optical density is inversely proportional to the field amplitude of the local oscillator. In other words, the effective signal strength can be improved by simply turning down the intensity of the local oscillator. In a fully non-collinear geometry, this is trivial. A pump-probe geometry requires a different approach because the probe serves as the local oscillator and thus cannot be tuned without affecting the signal strength. However, in a reflection geometry of monolayers and thin films, the amount of probe light reflected is determined by the Fresnel equations. The small number of molecules means that the signal is emitted equally in all directions. Thus, a reflection geometry allows us tune the intensity of the probe by changing the angle of incidence such that the experiment is done near Brewster's angle to minimize the probe light reflected. Figure 1.6 compares the transmission and reflection spectrum of a thin film of carbon monoxide releasing molecule number 3 (CORM-3). From inspection, it is clear that the signal strength is improved by a factor of 40 just by changing the experimental geometry.

### 1.4.3 SEAR 2D IR Spectroscopy

My dissertation built upon the two reported methods to enable the study of peptide monolayers in solution. By making use of the surface enhancement by thermally evaporating thin films of gold and measuring in a reflection geometry, we have measured that the 2D IR signals are enhanced by a factor of 6000. Figure 1.7 shows a schematic of the experimental geometry used in this dissertation. The optical set up is similar to an ATR mode in FTIR experiments, except without a prism to achieve an angle of incidence greater than the critical angle to achieve total internal reflection. Avoiding the use of prism is advantageous in 2D IR measurements because the thick material in the prism introduces dispersion and can be

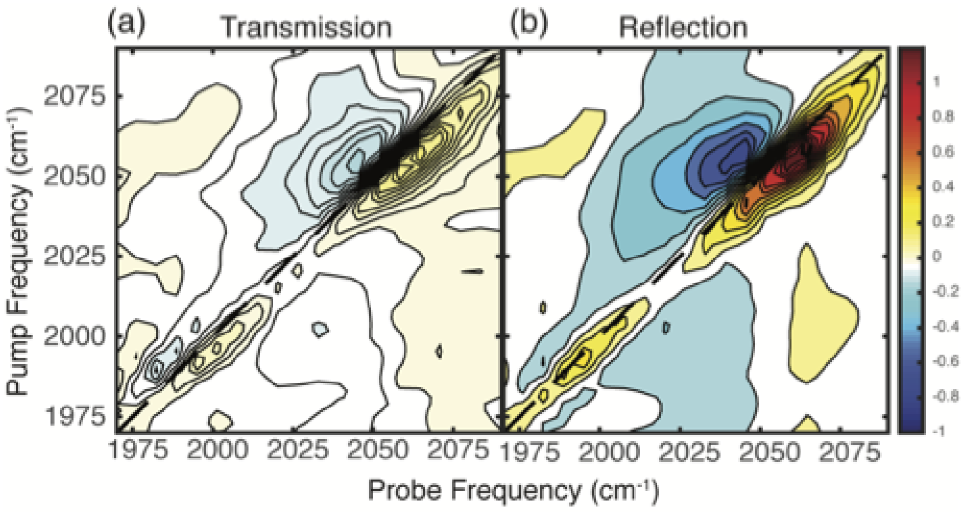

Figure 1.6: CORM-3 thin film spectra collected in (a) transmission and (b) inverted reflection geometries. The pump and probe beams are p-polarized and the spectra are plotted on the same normalized color map. Figure is from Petti et al. and used with permission.[9]

challenging to align.

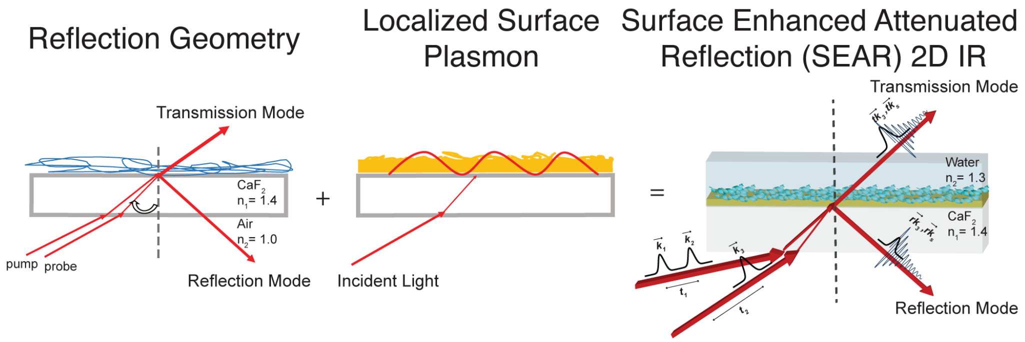

Figure 1.7: Schematic representation of how surface enhanced attenuated reflection (SEAR) 2D IR spectroscopy combines enhancement mechanisms to create a surface sensitive technique. Figure is from Petti et al. and used with permission.[9]

## 1.5 Polarization Dependence of 2D IR Signals

The cross peaks provide information on the coupling, and therefore, the angles and distances between coupled states. In 2D spectra of bulk samples, the polarization dependence of the cross peak intensity can be used to determine the relative orientations of the two modes.8

Indeed, the polarization of all four density matrix interactions can be controlled to experimentally eliminate the diagonal peaks and enhance cross peaks in isotropic samples.9 In principle, the 2D spectra of anisotropic samples carries information about orientation, but the dependence on the geometry is much more nuanced as observed in theoretical calculations on the 2D SFG spectra of interfaces.[54] Orientation is encoded in the 2D spectrum because each light matter interaction is a dot product between the vector of the interacting pulse and the average orientation of the perturbed dipoles.

To calculate the 2D IR spectrum of a two coupled modes we need to calculate the dependence of many different Feynman pathways. As Fayer and co-workers have shown, the spherical harmonic approach is the most useful when describing the waiting time dependence to extract rotational and energy transfer dynamics.[53] In this work, since we are concerned with the structural properties and not in the waiting time dependence, we use Euler angles to calculate the dependence of the signal on orientation. This approach is often used in SFG spectroscopy and amenable for matrix calculations.

To rotate the signal from the molecular frame, we use the Euler angles method as depicted in Figure 1.8. Two transition dipoles, one oriented along the $z$ axis and the other at some angle $\theta_{ab}$ relative to the first, are rotated $\phi$ for an azimuthally isotropic sample. If there is polar and uniaxial order in the lab frame, this is the only angle we average. For example, the iiii pathway of a dipole aligned along the $z$ axis in the molecular frame will interact with four different electric fields. The magnitude of each light-matter interaction is proportional to a dot product between the interacting field and the transition dipole vector, $\mu$, of the resonant transition. In this work, we take the convention of the SFG community and refer to the polarization of the light according to $\langle 1234 \rangle$ where the number refers to the time ordering of the light-matter interactions. For example, PPSS would mean $k_1$ and $k_2$ are $p$ polarizaed while $k_3$ and $k_{sig}$ are $s$ polarized.

We define two transition dipoles in the molecular frame, $\mu_i$ that is oriented along the $z$

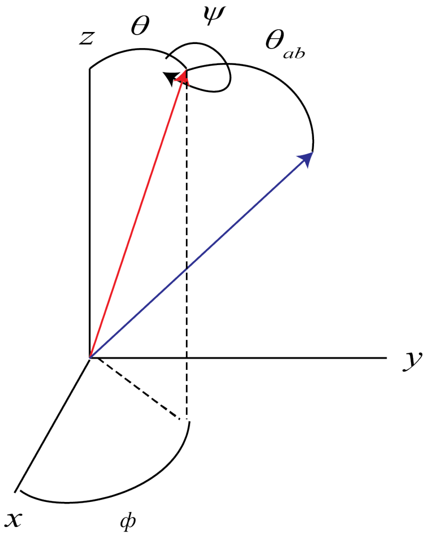

Figure 1.8: Illustration of two coupled transition dipoles in the laboratory frame. $\theta$ is the tilt angle relative to the $z$ axis, $\phi$ is the azimuthal angle, and $\psi$ the twist angle between the two dipoles. $\theta_{ab}$ is the relative angle between dipoles $a$ and $b$.

axis and $\mu_j$ at some angle $\theta_{ij}$ relative to dipole $i$.

$$i = (0, 0, 1) \tag{1.21}$$

$$i = (\sin\theta_{ij}, 0, \cos\theta_{ij}) \tag{1.22}$$

to rotate these vectors in to the lab frame, we rotate them in to the lab frame about 3 angles, $\theta$, $\psi$, and $\phi$

$$R(\theta,\psi,\phi) = \begin{pmatrix} \cos\psi & \sin\psi & 0 \\ -\sin\psi & \cos\psi & 0 \\ 0 & 0 & 1 \end{pmatrix} \begin{pmatrix} 1 & 0 & 0 \\ 0 & \cos\theta & \sin\theta \\ 0 & -\sin\theta & \cos\theta \end{pmatrix} \begin{pmatrix} 1 & 0 & 0 \\ 0 & \cos\phi & \sin\phi \\ 0 & -\sin\phi & \cos\phi \end{pmatrix} \tag{1.23}$$

Rotated in to the lab frame, these dipole vectors become:

$$i = (\sin\phi\sin\theta, \cos\phi\sin\theta, \cos\theta) \tag{1.24}$$

$$j = (\sin\theta_{ij}(\cos\phi\cos\psi - \cos\theta\sin\phi\sin\psi) + \cos\theta_{ij}\sin\phi\sin\theta, \cos\theta_{ij}) \tag{1.25}$$

To properly calculate the signal, this value must be averaged for all possible orientations of $\mu$. For example, the ZZZZ pathway for an isotropic distribution of $\mu_i$ is given by:

$$\chi^{iiii}_{ZZZZ} = \frac{1}{8\pi^2}\int_0^{2\pi} d\phi \int_0^{2\pi} d\psi \int_0^{\pi} \sin\theta d\theta \cos^4\theta = \frac{1}{5} \tag{1.26}$$

The cross peaks are calculated in a similar fashion. For example, the iijj pathway is given by:

$$\chi^{iijj}_{ZZZZ} = \frac{1}{8\pi^2}\int_0^{2\pi} d\phi \int_0^{2\pi} d\psi \int_0^{\pi} \sin\theta d\theta \cos^2\theta (\cos\theta_{ij}\cos\theta + \sin\psi\sin\theta_{ij}\sin\theta)^6 = \frac{2\cos^2\theta_{ij}+1}{15} \tag{1.27}$$

This implies that the cross peak intensity depends on the relative orientation of the coupled transition dipoles. Hochstrasser has calculated all possible elements of the polarization tensor for an isotropic distribution of dipoles.[55]

When there is macroscopic anisotropy, for example, at an interface, the limits of integration in equation 1.26 and 1.27 are determined by the allowed angles of the transition dipole vector. For isotropic samples, this integrates to a constant of 1/5. If for example, there is polar order, then the limits of integration are set by that distribution of tilt angles. In this case, this integral becomes dependent on the orientation of the molecule in the laboratory frame. For simplicity, we only consider delta function distributions of tilt and twist angles.

### 1.5.1 Polarization Signals for Surfaces

The last chapters of this dissertation utilize surface sensitive 2D IR to measure monolayers of molecules. Calculating signals for these surface measurements is more complicated because of the anisotropy. For a true interfacial measurement, we must consider multiple elements of the susceptibility tensor because the polarization of light is defined relative to the surface normal, which we set to be the z axis. *p* polarized light has both x and z components in this frame while *s* polarized light has only $y$ components. Figure xx shows an illustration of the coordinated system used in this section. Consequently, XXZZ and XZZX elements of the susceptibility will, in general, contribute to the measured signal for a *pppp* measurement. Since the $y$ component is nonzero, we can see that the cross-polarized detection is allowed for this particular pathway. More specifically, this vector is proportional to the ${E_{sig}}^{ppp}$. By placing a polarizer after the sample, we project the signal field on to a specific detection axis.

The angle of incidence and polarization of the pump, probe and signal fields will all act on this third-order susceptibility to generate the third-order signal. The x,y, and z components of the third order polarization can be described by equations 1.28-1.30.[53]

$$P_x^{(3)} = \sum_{a,b,c} \epsilon_0 \chi_{xcba} (L_{cc}^{k_3} E_c^{k_3})(L_{bb}^{k_2} E_b^{k_2})(L_{aa}^{k_1} E_a^{k_1}) \tag{1.28}$$

$$P_y^{(3)} = \sum_{a,b,c} \epsilon_0 \chi_{ycba} (L_{cc}^{k_3} E_c^{k_3})(L_{bb}^{k_2} E_b^{k_2})(L_{aa}^{k_1} E_a^{k_1}) \tag{1.29}$$

$$P_z^{(3)} = \sum_{a,b,c} \epsilon_0 \chi_{zcba} (L_{cc}^{k_3} E_c^{k_3})(L_{bb}^{k_2} E_b^{k_2})(L_{aa}^{k_1} E_a^{k_1}) \tag{1.30}$$

Where $L_{aa}$ is the ath component Fresnel coefficient, for the given electric field with electric field with wavevector $k_a$, $\epsilon_0$ is the permittivity of the vacuum, and $\chi_{dcba}$ is the dcba element of the molecular susceptibility tensor that is calculated as described in the previous section. The summation in in equation 1.28 is summed over all possible combinations of x,y, and z coordinates. The macroscopic third-order polarization of the matter leads to emission of the signal, which is given by:

$$E^{sig}_{refl,p} = \frac{i\omega}{2c\epsilon_0 \cos\theta_i}(-L^{Pr}_{xx}P^{(3)}_x \cos\theta_i + L^{Pr}_{zz}P^{(3)}_z \sin\theta_i) \tag{1.31}$$

$$E^{sig}_{trans,p} = \frac{i\omega}{2c\epsilon_0 \cos\theta_i}(\frac{\cos\theta_i}{\cos\theta_t}L^{Pr}_{xx}P^{(3)}_x \cos\theta_i + \frac{n_1}{n_2}L^{Pr}_{zz}P^{(3)}_z \sin\theta_i) \tag{1.32}$$

$$E^{sig}_{trans,refl,s} = \frac{i\omega}{2c\epsilon_0 \cos\theta_i}L^{Pr}_{yy}P^{(3)}_y \tag{1.33}$$

Here $\theta_i$ is the angle of incidence relative to the surface normal, $\theta_t$ is the angle of the transmitted beam relative to the surface normal, $n_1$ is the refractive index of on the first interface, $n_2$ is the refractive index of the second interface, $c$ is the speed of light in vacuum, and $\omega$ is the frequency of the emitted signal. For the experiments in this dissertation, we present only single color 2D IR experiments and so assume that the frequency dependence of the signal intensity is negligible. These equations show how one can use the angle of incidence, polarization, or both to obtain the $\chi$ tensor elements, which contain information about the relative and absolute orientation of the transition dipoles probed in an experiment.

## 1.6 Wide-field Microscopy with Coherent and Incoherent Sources

In this dissertation, I present advances in combining 2D IR spectroscopy with imaging to obtain spatially resolved information on molecular structure and dynamics. There are two approaches to spectroscopic imaging. One could focus the IR light tightly and raster scan across the sample to collect FTIR or 2D IR spectra at many different points on the sample. Usually a spectrogram would be used to spectrally disperse the light and measure its spectrum as shown in Figure 1.9. This is analogous to confocal fluorescence microscopy. In this implementation of spectroscopic imaging, the spatial dimension of the detector is used to measure the spectrum.

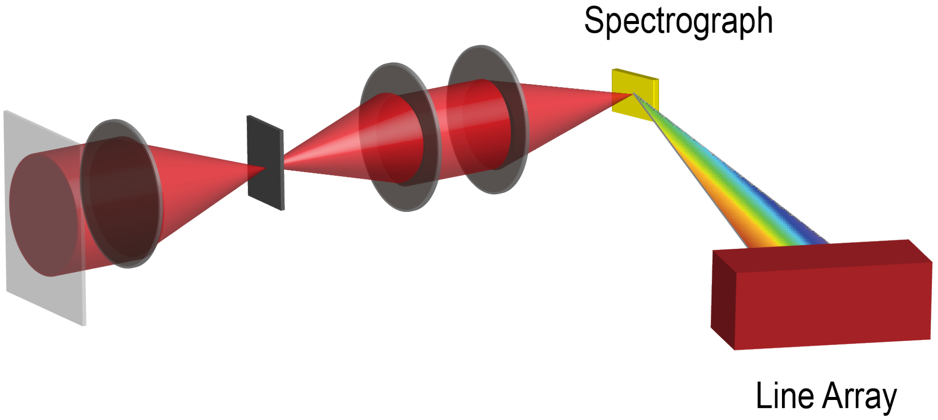

Figure 1.9: Illustration of point mapping imaging where a monochromator is used to measure the spectrum.

Alternatively, the spatial dimensions of the detector can measure an image. Traditional implementations of white-light microscopy use such an optical configuration, where a multidimensional detector, like a CCD camera. This measurement is depicted schematically in Figure 1.10. With the detector used to measure the image, there must be some other approach to obtain the spectroscopic observables. One way to do this is to build an interferometer that allows recording images at different interferometer positions. Each pixel then records an interferogram which can be used to reconstruct the spectrum. In our work, we have chosen the later approach with our 1 kHz repetition rate sources because wide-field imaging provides the fastest image acquisition with high spatial resolution.

The lasers used in our experiments have a high degree of spatial coherence. This means that the fundamental physics of image formation is different that that of traditional microscopies because of the coherence of the light source. These differences arise from the

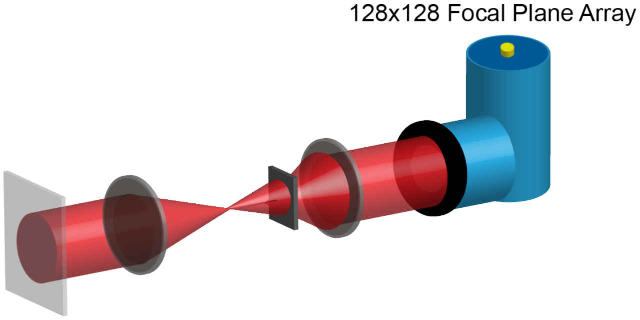

Figure 1.10: Illustration of wide-field imaging where the spatial dimensions of the detector are used to measure an image.

functional form of the point spread function (PSF) of the optical system. For both incoherent and coherent sources, the PSF is essentially a Fourier transform of the objective aperture. The key is to take care to correctly recover the units to describe the resolution. For a coherent source, the PSF, *h(x,y)*, is given by:[56]

$$h(x_1, y)1) = \frac{A}{\lambda z} \int_{-\infty}^{\infty} P(x_2, y_2) \exp\left( -i \frac{2\pi}{\lambda z} (x_1 x_2 + y_1 y_2) \right) dx_2 dy_2 \tag{1.34}$$

Here, x and y are the two-dimensional coordinates with the 1 subscript indicating the scaled coordinates at the detector and the 2 subscripts used for the dimensions of the objective aperture, which is given by $P$. $z$ is the distance of the detector from the objective and $\lambda$ is the wavelength of light. From inspection of equation 1.34, we recognize that it has the functional form of a Fourier transform.The image obtained in an optical system is determined by the convolution of the PSF with object being imaged. In coherent imaging, it is this PSF that is directly convoluted with the image, while incoherent measurements will only utilize the absolute magnitude square of $h$. Figure 1.11 shows two simulated PSFs for a microscope objective used in the Zanni group's wide field imaging experiments. The widths are slightly different and the oscillations lead to well-known interference fringes observed in coherent wide-field microscopes.[56]

Although we have chosen to initially pursue the wide-field implementation because of

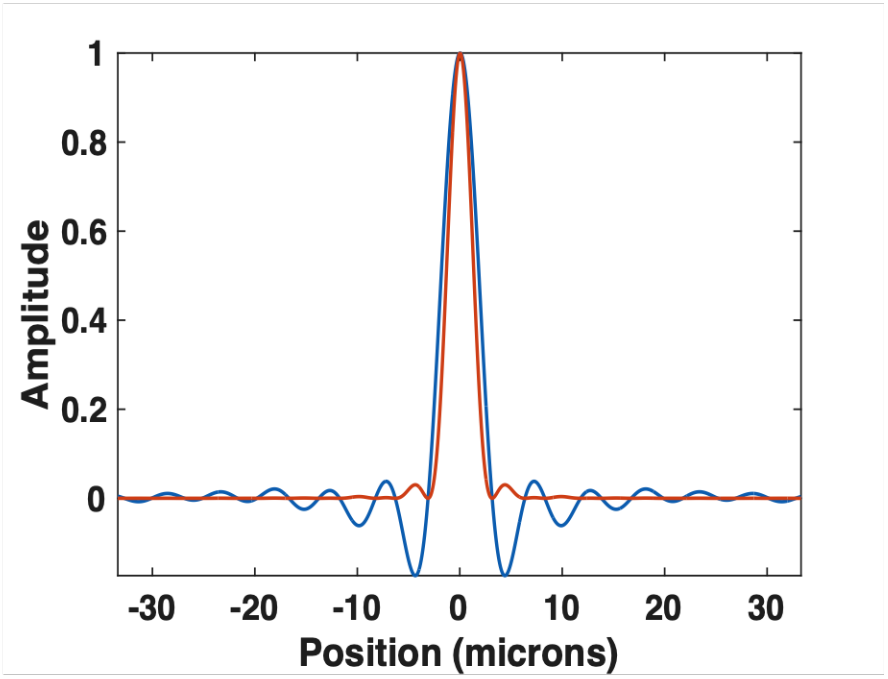

Figure 1.11: Simulated coherent and incoherent point spread functions.

the possibility of rapid-acquisition, the migration to higher repetition rate sources will limit the application of wide-field imaging in the mid-IR. The Focal Plane Array used in our microscope can currently read out at 1.8 kHz. If the source approaches repetition rates at or above 100 kHz, the integration time could be increased and time delays modulated at the read out rate of the detector. Unfortunately, the MCT detectors saturate at integration times of greater than 30 $\mu$s due to thermal background, limiting the transferability to higher repetition rate sources. It is possible that cold filters could improve these characteristics. It is important to note that visible detectors, like CCD's and CMOS detectors do not suffer from the thermal background. Thus, the wide-field approach will likely compete with point-mapping approaches in nonlinear visible spectroscopic experiments regardless of repetition rate.

## 1.7 Summary

In summary, we have explored the fundamentals of 2D IR spectroscopy and discovered how the observables in a 2D spectrum can be related to molecular structure. Provided these relationships, we have also developed the theoretical framework for imaging and interpreting spectra. The foundations developed in this chapter serve as a basis for the design of the experiments presented. Of the following chapters, two are devoted to measuring 2D IR spectra in a wide-field microscope, one to studying energy transfer in energetic materials, and two others to studying monolayer surfaces. The last chapter also presents preliminary data on the design of a 100 kHz spectrometer. All of these chapters utilize technical advances in 2D IR spectroscopy to study important scientific problems. The advances are general, and show promise in many other scientific communities beyond those presented here.

# Chapter 2

# Experimental Methods

## Contents

The two-dimensional infrared experiments in this dissertation make use of a variety of different laser technologies. In this chapter, I will describe some of the theory, practice, and other advancements that I have contributed to during my time in the Zanni group.

## 2.1 Regenerative Amplifiers

### 2.1.1 Titanium:Sapphire Regenerative Amplifier

Most of the experiments in this dissertation used a Titanium:Sapphire regenerative amplifier as initial source of femtosecond pulses. The regenerative amplifier is seeded by a femtosecond Ti:Sapph oscillator (Vitesse, Coherent). The seed is stretched with a grating stretcher before being amplified. Stretching the seed before amplification prevents damage to the optics and crystals in the amplification cavity due to extremely high peak powers of the femtosecond source. The amplifier cavity is pumped by the doubled output of an Nd:YLF laser (Evolution, Coherent). The seed is let in to the cavity by Pockel cells which are effectively electro-optic waveplates. After many round trips, the seed is amplified from 3 nJ to 4 mJ. The amplified pulse is then compressed in time to ~50 fs. The output repetition rate is 1 kHz with a center wavelength of 800 nm.

### 2.1.2 Ytterbium:KGW Amplifiers

My dissertation work also involved initial experiments with Ytterbium:KGW (Yb:KGW) amplifiers. These are effectively the same technologies as the Ti:Sapph amplifiers except the rod in the amplifier is Yb doped with KGW. This material has a longer fluorescence lifetime which leads to more correlated noise: advantageous for nonlinear spectroscopy experiments. Additionally, they offer tunable repetition rates from 50 kHz – 1MHz. Our model (Pharos, Light Conversion) outputs 20 W from 50-200 kHz. The pulse durations are a bit longer than the Ti:Sapph with 290 fs. The output wavelength is 1030 nm.

## 2.2 Optical Parametric Amplification and Difference Frequency Generation

### 2.2.1 Background

The spectrometers used in this dissertation make use of Optical Parametric Amplification (OPA) and Difference Frequency Generation (DFG) to generate the mid-infrared light needed for 2D IR experiments. Optical parametric amplification takes advantage of the large second-order nonlinear susceptibility, $\chi^{(2)}$, of nonlinear optical crystals. These crystals lack a center of inversion, which leads to large nonlinear light matter interactions. In an OPA, a weak seed and strong pump field, with frequencies $\omega_{signal}$ and $\omega_{pump}$, are overlapped spatially and temporally in a crystal. When the phase matching condition is satisfied (i.e. the crystal is appropriately oriented relative to the incoming beams) light at $\omega_{idler}$=$\omega_{pump}$-$\omega_{signal}$ is generated, in addition to the intensity of the $\omega_{signal}$ increasing substantially. The frequency of $\omega_{signal}$ and $\omega_{idler}$ can be tuned by changing the $\omega_{signal}$ and appropriately changing the angle of the nonlinear crystal. This dissertation makes use of collinear OPAs such that the pump and seed fields are fully collinear. For other applications, non-collinear OPAs (NOPA) are used to generate more bandwidth of the signal and idler fields.

Difference frequency generation is a similar process, except the pump and signal fields are of comparable intensities. This leads to a large gain in the intensity of the idler field and moderate increase in the signal fields. In our applications, DFG is used on the output of the signal and idler fields of an OPA to generate a femtosecond pulse in the mid-IR. Because of the difference in the fundamental output of the Ti:Sapph and Yb:KGW sources, I have used two different designs during the course of my PhD.

### 2.2.2 OPA 1: 800 nm Pump

The Ti:Sapph lasers in this dissertation utilize a commercially available OPA (TOPAS, Light Conversion) and a homebuilt DFG. The OPA is pumped with about 3.2 W of 800 nm light. White-light continuum in a sapphire crystal is used to seed a pre-amplification stage with a small portion of the 800 nm pump in $\beta$–Barium Borate (BBO). The signal and idler beams from the first stage is then directed to a power amplification stage where a majority of the 800 nm pump is mixed with the seed in another crystal BBO to generate around 1 W of combined signal and idler fields. The wavelength is tunable, but for our experiments we use wavelengths of about 1.4 $\mu$m and 1.8 $\mu$m. The OPA is very sensitive to the compression of the 800 nm pump pulse and conveniently acts as a diagnostic for proper pump pulse compression.

This system uses a home-built DFG set up to generate the mid-IR. We utilize a silver gallium sulfide crystal ($AgGaS_2$). A dichroic beam splitter is used to separate and recombine the signal and idler. This allows for precise control of the relative timing and spatial overlap. The cut of the $AgGaS_2$ is 42°. A germanium filter is used to separate the signal and idler from the generated mid-IR. For most experiments the mid-IR is set to be 5-6 $\mu$m and we produce mid-IR pulses of about 100 fs in duration as characterized by Frequency-resolved optical gating (FROG) measurements.

### 2.2.3 OPA 2: 1030 nm Pump

The Yb:KGW laser source that has enabled us to run high repetition rate experiments has a different fundamental output wavelength than the Ti:Sapph systems. As such, the usual BBO-based OPA's require modification to work with these laser sources. For these experiments, we have built an OPA in house that is based on a two stage design with BBO and KTP. Additionally, we use GaSe as the DFG crystal. We present the design and analysis in more detail later in this dissertation.

Despite differences in the OPA and DFG design, the general design fo the 2D IR spectrometers is about the same. The germanium filter used to filter out the signal and idler is conveniently used to overlap a 630 nm laser diode tracer beam (colloquially referred to as ”the HeNe” because previous spectrometers used a proper Helium Neon laser as the tracer). The diode tracer and mid-IR are overlapped over a long path length to ensure they are propagating collinearly. This allows the visible HeNe to be used for alignment rather than and infrared detector.

## 2.3 Mid-IR Pulse Shaping

### 2.3.1 Germanium-AOM Pulse Shaper

All of the 2D IR spectrometers in the Zanni group make use of a pump-probe geometry. The mid-IR is split in to pump and probe lines using a $CaF_2$ wedged-beamsplitter. About 95% is sent to the pump line and the rest is used as the mi-IR probe. Alignment of the probe is straightforward. The probe is aligned on to a translation stage to precisely control the timing of pump and probe pulses.

To generate a 2D IR spectrum, the pump line must utilize some method to generate a pump-pulse pair with the ability to experimentally control the timing between the first two pulses. In a pump-probe geometry, many researchers utilize a Mach-Zender interferometer,[57] or wedge pair.[58] This cost-effective option is useful but suffers from inherent ambiguities in the $t_1$=0 which can lead to phase ambiguities in the resulting 2D spectrum. To get around this, the Zanni group is known for using Germanium Acousto-optic modulator (AOM) as the foundation of a pulse shaper to generate a pump-pulse pair. The AOM based pulse shaper has numerous advantages over the other methods of generating a replica pulse, albeit at the sacrifice of pump power because of the poor efficiency of the pulse shaper. The AOM allows shot-to-shot modulation of the pump pulse. Additionally, there are no uncertainties in the phase of the 2D spectrum. Not only that, but the AOM allows phase control, which allows for the subtraction of lower order signals and scatter. The time delay and phase are controlled with an arbitrary waveform generator (AWG) which can be controlled with a computer. This means that the acquisition time for the experiment is limited by the repetition rate of the laser source.

### 2.3.2 Pulse Shaper Theory

The Ge-AOM pulse shapers used in this dissertation are based on a $4f$ zero dispersion compressor. It is comprised of a diffraction grating that disperses the pulse in wavelength. A 1D parabolic mirror is placed one focal length away from the grating. Two focal lengths away from this mirror, a second parabolic mirror is placed which recombines the dispersed pulse on to a second grating. The optics effectively take the pulse from the time-domain to the frequency-domain, and back again. The Germanium-AOM is placed in the Fourier plane exactly between the two parabolic mirrors. An RF-amplifier is used to amplify the output of an AWG card to send a computer-programmable acoustic-wave across the aperture of the AOM

The basic ideas behind the $4f$ pulse shaper capitalize on the mathematical properties of the Fourier transform. The mathematics of shaping follows the experiment.[59] The grating takes the Fourier transform of the input electric field, $E_{in}t$.

$$E(\omega) = \frac{1}{\sqrt{2\pi}} \int_{-\infty}^{\infty} E(t) e^{i\omega t} dt \tag{2.1}$$

The RF acoustic wave, referred to as a "mask," allows control of the amplitude and spectral phase at each frequency. Mathematically, we describe this as:

$$E(\omega)_{out} = M(\omega) E(\omega)_{in} \tag{2.2}$$

Our goal is then to find the mask, $M$ that transforms our input electric field to the desired output field in equation 2.2.

From the properties of the Fourier transform, we can qualitatively examine the effect of our applied mask, $M$, on the output electric field. For example, we know that a frequency dependent phase shift leads to a change in time. This operation is extremely important for our application as we want to control the relative timing of two pulses. We can also add a constant phase factor to change the phase of the field beneath the pulse envelope.

One advantage of pulse shaping is that measurements of the 2D IR signal can be completed in the rotating frame. From the previous chapter, we know that that the 2D IR signal oscillates as:

$$S(t_1, \omega_3) \propto \cos(\omega t_1 + \Delta\phi_{12}) \tag{2.3}$$

With the shaper, we can change the phase of the moving pulse as a function of the time delay between the two pump pulses. The imposed time-dependent phase effectively changes the observed frequency. We choose a rotating frame such that:

$$\phi_{rot} = i\omega_{rot}t \tag{2.4}$$

By shifting the oscillation period from about 5-10 fs to around 80-100 fs, the measured free induction decays oscillate at around 50-200 cm$^{-1}$. Under-sampling as such allows us to collect fewer data points and thus collect a 2D spectrum significantly faster. Figure 2.1 shows the measured pulse spectrum in different rotating frames.

For most of our applications, we fix one of the pulses in time at $t_1$=0 and we want the same relative amplitude between the two pulses. With these considerations in mind, the mask we apply to input field becomes:

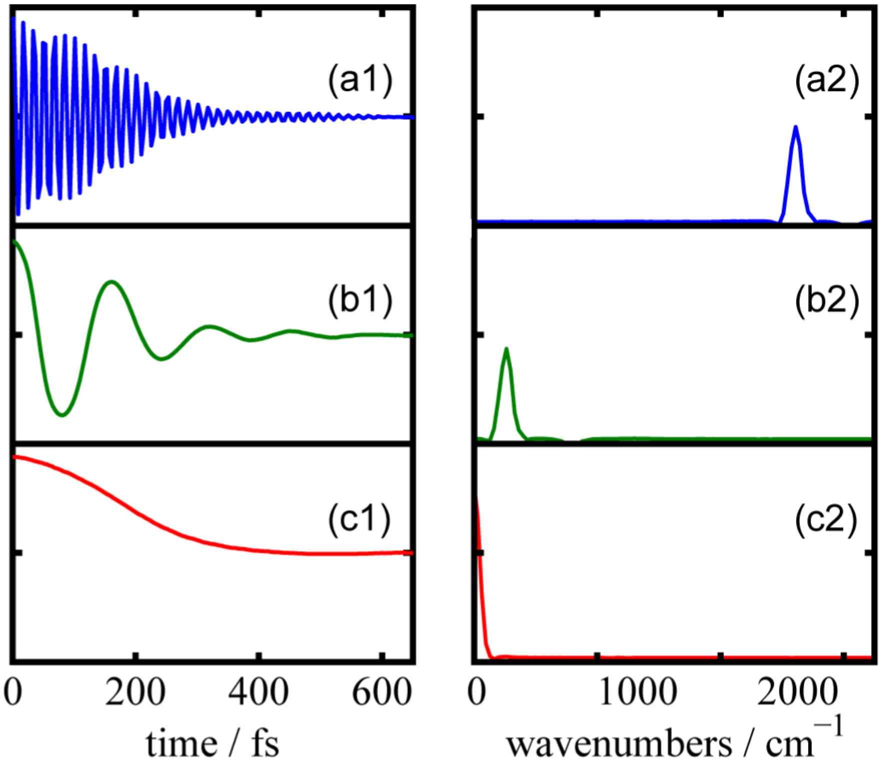

Figure 2.1: Measured one-sided interferograms, generated using rotating frame frequencies of (a) 0 (b) 1800 and (c) 2000 cm$^{-1}$, along with their respective Fourier transforms (a2-c2). Phase cycling shifts the apparent carrier frequency so that fewer data points are needed to sample the interferogram.

.

$$M(\omega) = \frac{1}{2}(e^{i\phi_1} + e^{2\pi i(\omega-\omega_{rot})t+\phi_2}) \tag{2.5}$$

After apply the mask to transform the pulse in the frequency domain with the AOM, we recombine all the frequencies on the second diffraction grating, again experimentally taking the Fourier transform back to the time domain.

### 2.3.3 Chirp Compensation

Propagation of the mid-IR pulse through the AOM and other dispersive components in the optical path introduces chirp to the pulse. That is, the frequencies travel at different speeds. We can mathematically describe this chirp through a Taylor expansion. The terms important for compression of mid-IR pulses are the group velocity dispersion (GVD) and the third-order dispersion (TOD).[60] A chirped pulse can lead to artifacts in the experimental spectrum in addition to degrading the inherent time resolution in the waiting time.[39] Mid-IR detectors do not operate fast enough to directly measure the electric field of optical pulses. Therefore, we require some nonlinear process to measure, or gate, the pulse measurement. The most common and best measurement is a Frequency resolved optical gating (FROG) measurement. However, to a first approximation, we can measure the efficiency of a nonlinear process like second harmonic generation (SHG) or two-photon absorption and optimize the efficiency by applying a frequency dependent phase across our mask. In my first years in the Zanni group, we optimized the doubling efficiency in $AgGaS_2$. Later in the group, we used fast photodiodes with band gaps that are insensitive to one-photon absorption of the mid-IR, but a two-photon process can promote carriers. Thus, we can empirically chirp the pulse to produce the most intense signal on the photodiode. In the shaper, we can do this by translating the second grating in the pulse shaper. This does introduce spatial chirp to the beam profile. Once this grating is set, we can fine tune the pulse compression by applying a frequency dependent phase according to:

$$\phi_{chirp}(\omega) = \frac{1}{2}\beta_{GVD}(2\pi)^2(\omega - \omega_0^2) + \frac{1}{6}\beta_{TOD}(2\pi)^3(\omega - \omega_0)^3 \tag{2.6}$$

Where $\omega_0$ is the center frequency of the pulse around which we perform the Taylor expansion to describe the pulse chirp. $\beta_{GVD}$ is the GVD in units of $s^2$ and $\beta_{TOD}$ is the TOD in units of $s^3$. From my measurement, the compressed pulse is usually around 200 fs after the pulse shaper.

### 2.3.4 Frequency Calibration

As can be seen from equation 2.6, accurate generation of time delays is predicated on knowledge about what frequencies your mask is shaping. In practice, we can do this by applying a frequency comb mask (specific frequencies of the pulse at regular intervals) and experimentally measuring the AOM pixels and their corresponding optical frequencies. Additionally, two separate measurements to let through a single frequency, one of the combs in the previous mask, is needed to uniquely determine the spatial mapping of frequency to mask element. This is then fit to a second-order polynomial.

$$\omega = p_2 x^2 + p_1 x + p_0 \tag{2.7}$$

Where $x$ in this equation is the effective pixel in the generated mask from the AWG card. Although the $p_2$ term is quite small, it can have a large effect on the amount of temporal and spatial chirp induced in the AOM.

### 2.3.5 Other Practical Considerations for the Pulse Shaper

There are other practical considerations related to pulse shaping that must be considered. To maximize the deflection efficiency to the first order beam, the angle of the incident light going in to the AOM must be controlled and set to maximize the transmitted beam in the shaper pulse. This can be controlled in two ways: 1. the AOM can be mounted so that it can pivot about its center or 2. the parabolic mirrors can be rotated iteratively to maximize the intensity of the first order beam.

One important aspect of the AOM is ensuring that the amplified RF mask reflects the applied waveform and that the shaper is in the linear regime. To do this, we measure the deflection efficiency with a mid-IR detector (pyroelectric detector or MCT) and systematically increase the mask amplitude until we no longer observe an increase in deflection efficiency with an increase in amplitude.

One important point learned from experience, is ensuring a uniform amplitude of the mask for high repetition rate experiments. The older models of the RF amplifier used to amplify the generated waveform cannot be run at 100% duty cycle, and therefore must be gated. That is, we have an electronic pulse that effectively turns on the amplifier when the AWG sends the desired waveform to be amplified. For the Yb:KGW experiments described in the last chapter, the maximum duty cycle is close to the desired operational rep rate. We found that if the RF amplifier gate pulse was too close to the mask in time, the amplification of the waveform was not uniform in time. Figure 2.3 shows a 2D spectrum acquired under conditions that led to nonuniform amplification of the RF mask. Multiple pulses generated lead to extremely incorrect line shapes and spurious peaks in the spectrum.

## 2.4 2D IR Spectrometer

### 2.4.1 Spatial Overlap

The probe pulse, $E_3$, is sent on to a translation stage to control the waiting time, $t_2$. The second pump pulse, $E_2$ is kept static in time with the shaper and $E_1$ is scanned. The pump and probe beams are overlapped spatially at the sample and focused with a 90° off-axis parabolic. Initial overlap is achieved by replacing the parabolic with a mirror so that the

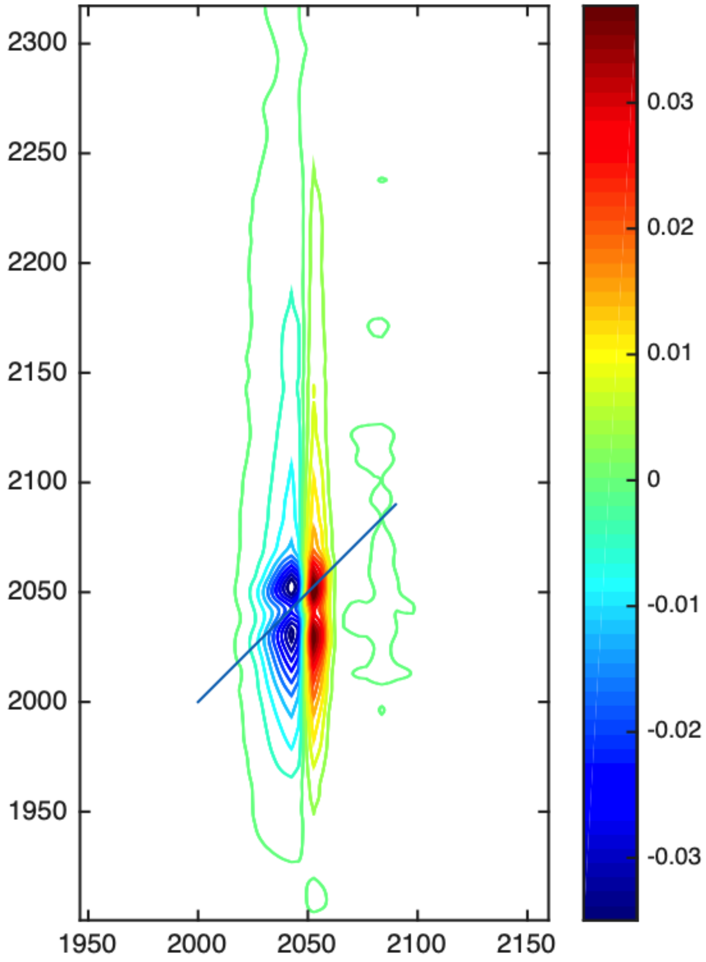

Figure 2.2: 2D IR Spectrum with RF gate arriving just before the desired mask to be amplified.

.

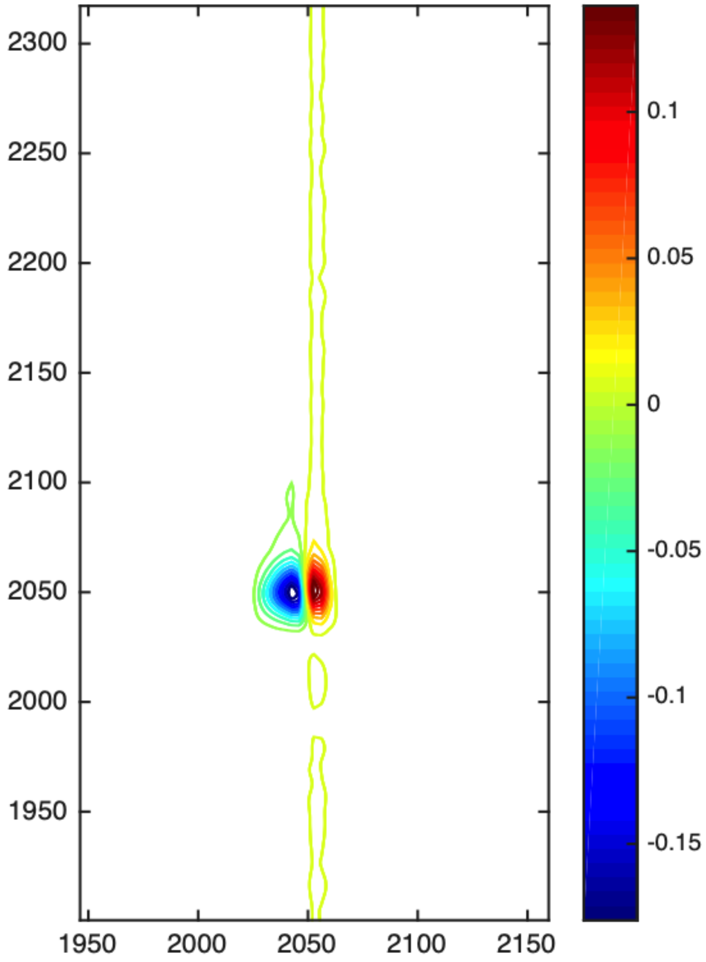

Figure 2.3: 2D IR Spectrum with RF gate several microseconds before the desired mask to be amplified. The correct 2D spectrum is observed.

.

incoming beams are reflected back on their incoming path. Irises on both lines are then used to make sure that reflected beams travel the exact incoming path. This alignment procedure, in my experience, makes it so overlap can be found by simply translating the sample relative to the focus of the mid-IR laser.

### 2.4.2 Phase Cycling

From the previous chapter, we know that the 2D IR signal is dependent on the incident phase of all four pulses.

$$S_{2DIR} \propto \cos(\mp\phi_1 \pm \phi_2 + \phi_3 - \phi_{Lo}) \tag{2.8}$$

For the pump-probe geometry, the signal is self-heterodyned and $k_3$=$k_{Lo}$ and so $\phi_3$=$\phi_{Lo}$. This means that the 2D IR signal becomes only dependent on the relative phase between the two pump pulses.

$$S_{2DIR} \propto \cos(\Delta\phi_{12}) \tag{2.9}$$

From equation 2.6, we know that we can simply change the phase of $k_1$ relative to $k_2$. This is useful because although a 2D IR signal will change sign, any DC components will be unaffected by the phase. This is useful to suppress background signals. In the next section, we will examine how we can use phase cycling to subtract spurious signals in collinear and pump-probe geometry measurements.

### 2.4.3 Signal Detection and Data Processing in the Pump-Probe Geometry

The fundamental challenge in 2D IR spectroscopy is measuring the electric field of the signal emitted by the sample, $E_{sig}$. In the pump-probe geometry, the two pump pulses, $k_1$ and

$k_2$ are collinear. The probe, with wave vector $k_3$ comes in at a small angle (usually about 5-10 degrees). The signal field is then emitted in the $k_{sig}$ direction. Because the first two interaction wave vectors are the same, the signal field is emitted in the same direction as the probe pulse. Our probe pulse then can be conveniently used as a heterodyning field, called the local oscillator. To resolve our probe frequency axis, we disperse the signal and probe pulse in a spectrograph on to a 64 element MCT array detector. Mid-IR detectors are square law detectors and measure intensity. Mathematically, we detect the signal as follows:

$$S = |E_{Lo}|^2 + |E_{Sig}|^2 + 2Re(E_{Lo}E_{Sig}^*) \tag{2.10}$$

Here the first two terms represent the intensity of the local oscillator and the signal, respectively, and the last term is the interference between the fields. If phase-resolved measurements are not necessary, one can, in principle, simply measure the intensity of the signal $E_{sig}{}^2$. This is referred to as a homodyne spectrum. If a phase resolved spectrum is desired, known as a heterodyned spectrum, then it is the interference term that we are interested in. In practice, even if one is collecting a homodyne spectrum, the interference term is used to extract the absolute value of the signal because the intensity of the third-order signal is so small. In fact, we neglect this term because it is so much smaller than the local oscillator. Equation 2.10 then becomes:

$$S = |E_{Lo}|^2 + 2Re(E_{Lo}E_{Sig}^*) \tag{2.11}$$

The most basic 2D IR experiment in a pump-probe geometry can be thought of as a transient absorption experiment with the two pump pulses generated for a series of coherence time, $t_1$, delays. Such an experiment requires amplitude modulating the pump pulse and measuring the change in absorption in the probe when the pump is on and when it is off. To measure this the data is processed in the following way:

$$\Delta OD(t_1, \omega_3; t_2) = -\log \frac{I_{On}^{Probe}}{I_{Off}^{Probe}} \tag{2.12}$$

The measured change in optical density, $\Delta OD$, is measured at a series of $t_1$ time delays at each frequency in the dispersed probe pulse. The signal also depends parametrically on the delay between pump and probe, $t_2$. Figure 2.4 shows a typical raw data set collected as function of the pump pulse time delay. However, for non-ideal samples like protein aggregates and solid samples, the pump pulse can scatter in the same direction as the signal. Since the moving pulse can interfere with the probe, we can see spurious oscillations from scatter. Therefore, in practice, we usually use a four-frame phase cycling sequence that allows us to subtract scatter terms and the transient absorption background. This is done by collecting the signal at each coherence time with different relative phases of the two pump pulses:

$$S_1(\phi_1 = 0, \phi_2 = 0) \tag{2.13}$$

$$S_2(\phi_1 = \pi, \phi_2 = 0) \tag{2.14}$$

$$S_3(\phi_1 = 0, \phi_2 = \pi) \tag{2.15}$$

$$S_4(\phi_1 = \pi, \phi_2 = \pi) \tag{2.16}$$

We then process the data according to equation 2.17.

$$S(t_1, \omega_3) = \log \frac{S_1 + S_4}{S_2 + S_3} \tag{2.17}$$

This processing scheme allows us to subtract off the interference between the pump pulses that can obscure the signal. However, it does not subtract off the $k_1$ $k_2$ scatter. To do this, the probe must also be amplitude modulated (i.e. chopped) or phase cycled. This is necessary for collinear measurements, where pump, probe and signal all travel in the same direction.

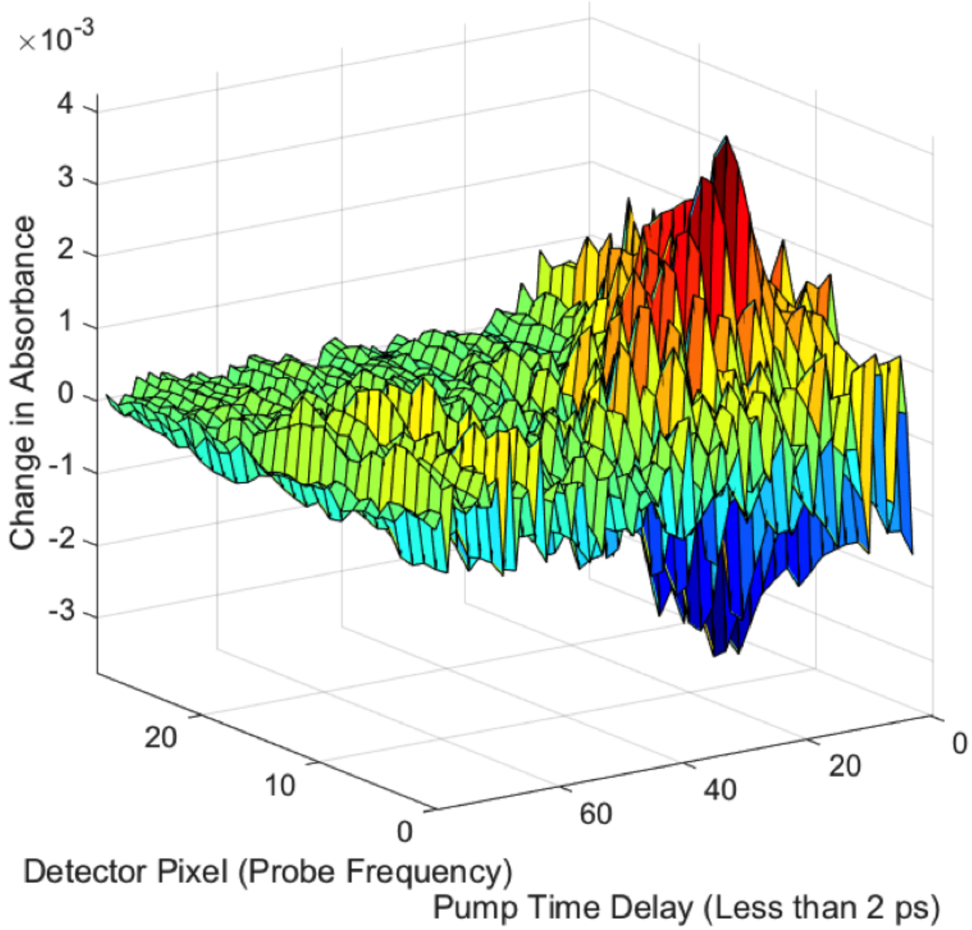

Figure 2.4: Representative free induction decay (FID) after the processing of the phase cycling sequence.

.

To run an experiment, we upload to the AWG card a series of $N$ masks, where $N$ is on the order of 400 different combinations of time delays and phases. The AWG card cycles through each mask every laser shot. This means that for a 1 kHz repetition rate, a 2D spectrum is collected about every 400 ms. The AWG card also sends a marker to the mid-IR integrator when it is on the first mask in the sequence. This allows us to automate the sorting of the data so that each coherence time is at the beginning of the data set. To average, the 2D spectra are collected, averaged and saved. The processing of the phase cycling and Fourier transforms are then completed on a computer after the experiment is completed.

### 2.4.4 Experimental Considerations for the Collinear Geometry

For the microscopy experiments described in Chapter 3, we use a fully collinear experiment for the microscope. For imaging, a fully collinear experiment is desired for two reasons. In a point scanning microscope, the size of the focus will be minimized when the objective aperture is filled completely. Wide-field experiments benefit from a collinear experiment because it makes corrections for the spatial dependence of the pump intensity straightforward. However, the dynamic range of MCT detectors is limited. Therefore, the signals are too small to be observed over the intense pump spectrum. For example, most of the MCT detectors have a 16 bit analog-to-digital resolution. This means that the nominal $\Delta OD$ measurable is $\sim 1 \mu OD$. To mitigate this, collinear experiments can be measured with the pump and probe beams orthogonally polarized. With a polarizer placed before the detector, the pump intensity is effectively eliminated. However, because the extinction ratios of polarizers are not infinite, there is still a small amount of residual pump intensity measured by the detector. Making the comparison to equation 2.10, a collinear experiment measures:

$$
\begin{aligned}
S = |E_1|^2 + |E_2|^2 + |E_3|^2 + |E_{Lo}|^2 + |E_{Sig}|^2 \\
+2Re(E_1 E_2^*) + 2Re(E_1 E_3^*) + 2Re(E_1 E_{Lo}^*) + 2Re(E_1 E_{Sig}^*) \\
+2Re(E_2 E_3) + 2Re(E_2 E_{Lo}^*) + 2Re(E_2 E_{Sig}^*) \\
+2Re(E_3 E_{Lo}^*) + 2Re(E_3 E_{Sig}^*) \\
+2Re(E_{Lo} E_{Sig}^*)
\end{aligned}
\tag{2.18}
$$

By inspection, it is clear that completely isolating the interference between the local oscillator and signal is non-trivial. As such, we will require a more complicated phase cycling scheme to isolate the signals. This is described in Chapter 3. Although this is in the context of a collinear experiment, I will note that the eight-frame scheme presented is also useful in subtracting background signals in strongly scattering samples.

# Chapter 3

# Wide Field FTIR Microscopy Using Mid-IR Pulse Shaping

## Contents

This chapter was adapted from: *Optics Express* **2015**, *14*, 17815-17827. It was prepared in collaboration with A.L. Serrano, A. Ghosh, and M.T. Zanni. I contributed to the experimental data collection, sample preparation, and the simulations.

## 3.1 Introduction

The structural sensitivity of Fourier transform infrared (FTIR) vibrational spectroscopy has long made it an attractive candidate as a microscopic contrast agent. The only requirement for detection is an infrared active chemical bond, which means that molecular systems intrinsically possess the labels necessary for chemical imaging. For this reason, researchers have worked for decades to develop imaging in the mid-infrared.[61–64] Most of that work has relied on thermal sources, whose low fluxes limit the signal-to-noise that can be obtained. With a weak source, improvements in signal-to-noise can only be made at the cost of spatial resolution.[65] Synchrotron sources are about 1000 brighter and so provide better signal-to-noise while maintaining high resolution.[66,67] The ideal light source would be as widely available as a thermal source and as bright as a synchrotron.

In the last few years, large advances have been made in table top femtosecond lasers that can now generate mid-IR light with fluxes comparable to synchrotrons. The repetition rates of these sources (typically 1-5 kHz) make them compatible with the readout rates now possible with focal plane arrays (FPA) made of mercury cadmium telluride (MCT). With an FPA, it is possible to measure continuous images over a large area, as compared to spatially scanning an area using a single point detector.

To generate an IR spectral image with an FPA, one can scan the laser wavelength, as has recently been done using quantum cascade lasers,[63] or create an interferogram and scan its delay as is done in an FTIR microscope. In the FTIR approach, a Michelson or similar interferometer is used to create two overlapping infrared beams and then mechanically translate a leg of the interferometer to scan the relative delay. Mid-infrared pulse shapers now make it possible to control the time and frequency profiles of mid-IR light so that pulse sequences for creating interferograms can be computer generated.[68–70] Optical pulse-shaping has been used in CARS and two-photon imaging.[71,72] Mid-IR pulse shaping was recently used to obtain near-diffraction limited 2D IR images by point-to-point scanning.[73] A pulse shaper using a Ge acousto-optic modulator has no moving parts and so can instantaneously set the interferometric delay to any value within its resolution. In addition, the phase of the pulses that generate the interferogram can be set independent of the delay, which enables sub-Nyquist sampling and background subtraction, with a scan rate set by the repetition rate of the laser.

In this article, we combine the high power of a table top IR source with mid-IR pulse shaping and multiplexed FPA detection to measure wide-field, sub-diffraction limited, FTIR images. We explore chemical imaging using a sample of metal-carbonyl compounds absorbed in polystyrene beads and determine the resolution using a standard USAF test target. We demonstrate background subtraction and rotating frame data collection using phase cycling. We also compare the spectral images collected with coherent and diffuse radiation.

## 3.2 Methods

### 3.2.1 Instrument Layout

The layout of our instrument is shown in Figure 7.1. The methods used for pulse shaping are based on those described previously.[28] Briefly, 100 fs mid-IR pulses, centered at 5 $\mu$m and generated by difference frequency generation in $AgGaS_2$ from the outputs of an optical parametric amplifier (TOPAS, Light Conversion) pumped by a 1 kHz amplified Ti:Sapphire laser (Libra, Coherent Libra), are modulated in the frequency domain using a 4f-geometry Ge AOM based shaper to generate double pulses which are then directed into a home built transmissive microscope. The microscope consists of a 150 mm focal length $CaF_2$ spherical lens (Thor Labs) used as the condenser to focus the beam in front of the sample, which then expands over a distance of 6 mm to the size of the region of the sample to be imaged, thereby providing uniform illumination. For images presented herein, a 12.5 mm focal length, 0.7 NA, aspherical ZnSe lens (Edmund Optics) is used as an objective to map an image of the sample onto a 128 x128 MCT mid-IR FPA, which is placed either 150 or 440 mm away in order to generate either 12x or 36x images, respectively. For comparison purposes, measurements were also performed using a finite corrected 74x, 0.65 NA Schwarzschild type reflective objective (ReflX, Edmund Optics).

We also report images using a 2 mm thick $CaF_2$ diffuser made either with 240 grit sand paper, or by sandblasting with 36 grit beads (PIKE Technologies). The diffuser was placed after the shaper to degrade the coherence of the laser beam [15].[74] If the diffuser is used, the beam is recollimated by adding a 150 mm focal length $CaF_2$ lens, with a 20 mm focal

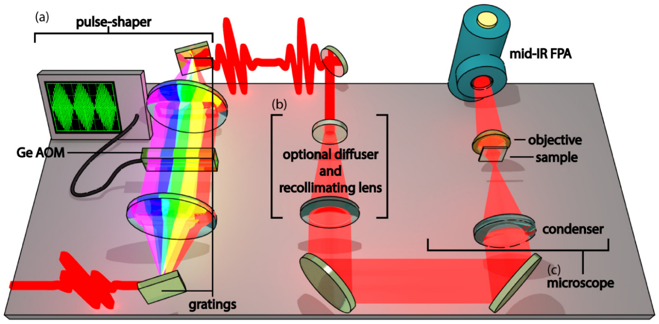

Figure 3.1: Diagram of the experimental setup showing the (a) Ge-AOM pulse shaper, (b) the optional diffuser/recollimating device used for incoherent imaging and (c) the microscope.

length, 0.3 NA, $CaF_2$ lens (Thor Labs) acting as a condenser. The diffuser was placed in a motorized rotating mount and rotated at $\sim$2 Hz.

The 128x128 mid-IR FPA was read out at the repetition rate of the laser, using a Teledyne Xcelera PCIe frame-grabber. During acquisition, the frame grabber is triggered by the pulse shaper to collect 40k frames, which are written directly to memory before being averaged and saved, after which the frame-grabber resets to read another trigger. This method results in a drop in duty cycle of about 5% during the processing of the memory buffer but allows for data acquisition over indefinitely long periods of time.

A negative chrome USAF resolution pattern, etched on $CaF_2$ (Max Levy Autograph) was used to measure the spatial resolution of the optical system.

### 3.2.2 Numerical Simulations

All numerical simulations and calculations were performed using custom MATLAB codes. Simulated images of the USAF test target were carried out in the Fresnel diffraction limit. A detailed description of the theoretical methods can be found in the Appendix.

### 3.2.3 Sample Preparation

Two samples of Polystyrene beads (106-125 $\mu$m, Polysciences Inc.) with absorbed metal-carbonyl compounds were prepared, one using $W(CO)_6$ as the absorbate and the other $Mn_2(CO)_{10}$. The beads were swelled in a saturated chloroform solution of the absorbate for 2 hours. Following this, the two samples were diluted into methanol, spun down, washed in methanol, mixed in a 1:1 ratio, and dried under nitrogen before being suspended in water and deposited between two $CaF_2$ windows (2 mm and 0.5 mm thick, Crystran Ltd.) with a 100 $\mu$m Teflon spacer. Beads saturated with $W(CO)_6$ have optical densities of about 0.8.

## 3.3 Results and Discussion

Computer control of the phase and amplitude of the acoustic wave in the Ge crystal of the shaper was used to generate a pair of pulses with a well-defined time-delay and relative phase, as shown in Figure 3.2. The pulse sequence is updated at the laser repetition rate, enabling rapid acquisition, background subtraction and unambiguous undersampling. To illustrate, consider the intensity measured from a monochromatic component of the field:

$$I(\tau) = |E_1|^2 + |E_2|^2 + 2|E_1||E_2| \cos[\phi_1 - \phi_2(\tau) + 2\pi\nu\tau] \tag{3.1}$$

where $\tau$ is the imposed delay between the two fields, with the relative phase of the first and second pulses, $\phi_1$-$\phi_2(\tau)$, controlling the phase of the cross term between the pulses. Using a 2-frame phase cycling scheme, every $\tau$ value was generated twice, once with a relative phase of 0 and then again with a phase change of $\pi$, as seen in Figure 3.2(a). The difference between adjacent data points could then be taken to give the interferogram alone:

$$I(\tau, \phi_1 = 0) - I(\tau, \phi_1 = \pi) = 4|E_1||E_2| \cos[2\pi\nu\tau - \phi_2(\tau)] \tag{3.2}$$

as illustrated in Figure 3.2(b). Thus, this 2-frame phase cycling scheme removes the background of the laser pulses themselves every other laser shot, improving signal to noise by a factor of ~2.

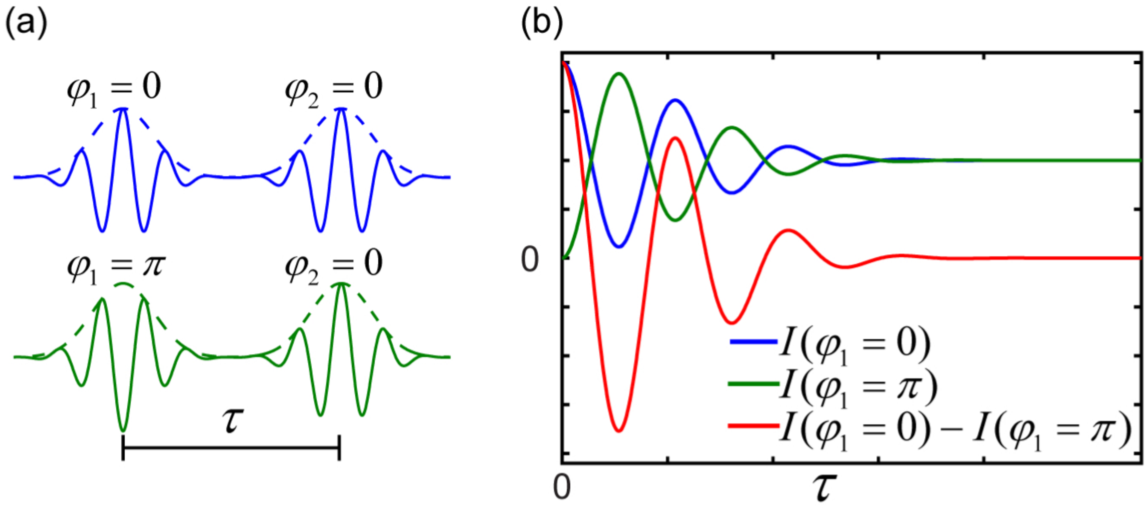

Figure 3.2: (a) Illustration of shaped pulse pairs with relative phase shifts of zero (blue) and $\pi$ (green). (b) Simulated interferograms for the two cases depicted in (a), according to color, along with their difference (red). Subtracting the phase cycled interferograms doubles the interference signal while removing the laser background.

In addition to the $\pi$ phase shifts, the phase of the moving pulse,$\phi_2(\tau)$, was also controlled to manipulate the apparent frequency of the measured interferograms. By making $\phi_2(\tau)$=$2\pi\nu_{rot}\tau$, the apparent carrier-wave frequency of the interferogram can be shifted to any desired value. To demonstrate, Figure 3.3 shows three measured interferograms using different values of the rotating frame frequency,$\nu_{rot}$, and their Fourier transforms. The carrier-wave can be shifted all the way to zero-frequency, leaving only the envelope. The envelope is the important quantity to know, because it, not the carrier frequency, contains the interferences that create the amplitudes, peak spacings, and linewidths in the final FTIR spectrum. After Fourier transformation, the frequency axis is corrected by adding back $\nu_{rot}$. By shifting the carrier frequency, fewer data points are needed to sample the interferogram so that it can be collected more quickly with no risk of aliasing, which has been shown to improve signal-to-noise in 2D IR experiments.[75]

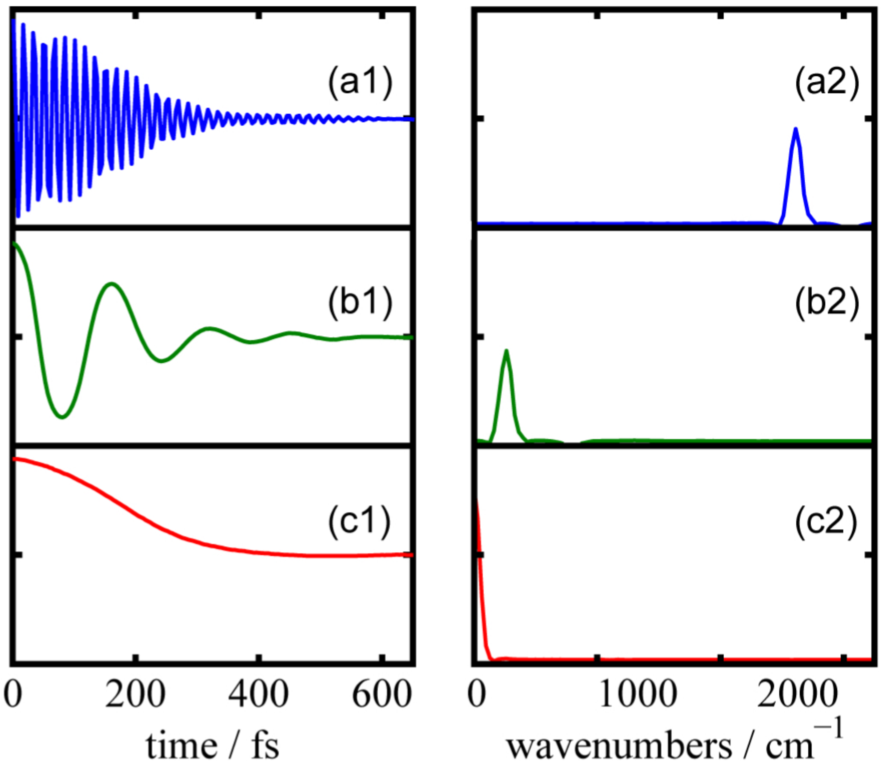

Figure 3.3: (a1-c1) Measured one-sided interferograms, generated using rotating frame frequencies of (a) 0 (b) 1800 and (c) 2000 cm$^{-1}$, along with their respective Fourier transforms (a2-c2). Phase cycling shifts the apparent carrier frequency so that fewer data points are needed to sample the interferogram.

For all the measured FTIR images in this study, a rotating frame frequency of 1800 cm$^{-1}$ was used, and one-sided interferograms were collected using 2-frame phase cycling, 50 fs steps, to a final delay of 8.5 ps, giving a spectral resolution of 0/[2.99 x 1010(cm/s) x 8.5 x 10$^{-12}$s] = 1.8 cm$^{-1}$. Averaging times for the samples and test targets presented here were ∼30 and ∼10 minutes, respectively. Thus, the interferogram was sampled with 170 delays, whereas one would need about 1200 delays to sample at the fundamental frequency if one could not collect in the rotating frame. Measuring all of the delays faster results in better signal-to-noise.[75]

Shown in Figure are images of polystyrene beads labeled with either $W(CO)_6$ or $Mn_2(CO)_{10}$

metal-carbonyls at 12x magnification. Figure 3.4(a) plots an image of the integrated transmitted IR intensity and so has no frequency resolution. The polystyrene beads are visible as concentric rings of light. The beads are visible because the optical density of the surrounding water is higher than that of the beads, but this does not present a problem in extracting absorption spectra of the metal-carbonyls because the water spectrum is broad and featureless in this frequency range. Shown in Figure 3.4(b) are absorption spectra measured at the pixels indicated, which are for beads enclosed in the cyan and red boxes. Absorbances were calculated by referencing to a region on the same image containing only water, and a third order polynomial fit was used to remove the water absorbance. One spectrum has a peak at 1971 $cm^{-1}$ while the other has peaks at 2004 and 2038 $cm^{-1}$. These spectra correspond to $W(CO)_6$ and $Mn_2(CO)_{10}$, respectively. Using these frequencies, it is straightforward to identify which beads contain $W(CO)_6$ or $Mn_2(CO)_{10}$, as shown by the false color images in Figure 3.4(c) plotted for the absorbance measured at 1971 $cm^{-1}$ (red) and 2004 $cm^{-1}$ (cyan), respectively. Notice that there is no correlation between the intensity of the beads in the integrated intensity image of Fig. 4(a) and the false color image; frequency specificity is needed to identify the chemical composition of each bead.

We note that the frequencies of $W(CO)_6$ or $Mn_2(CO)_{10}$ are slightly red shifted by 4-12 $cm^{-1}$ from previous measurements of these compounds in aprotic solvents,[28,76] which we attribute to differences in hydration. Support for this claim can be seen in the baseline. The two dips in the baseline of the $W(CO)_6$ spectrum between 1990 and 2040 $cm^{-1}$ are not due to poor signal to noise, but rather to $Mn_2(CO)_{10}$that has dissolved into the water and thus has a slight absorbance in the region used as a reference.

The concentric ring pattern visible within each bead is due to the spatial coherence of the laser source used in these measurements and represent a combination of diffraction and refraction effects coming from the transmissive and highly spherical beads.[77] We have also collected incoherent images by adding a rotating diffuser system, following Kole et al.,[78] to

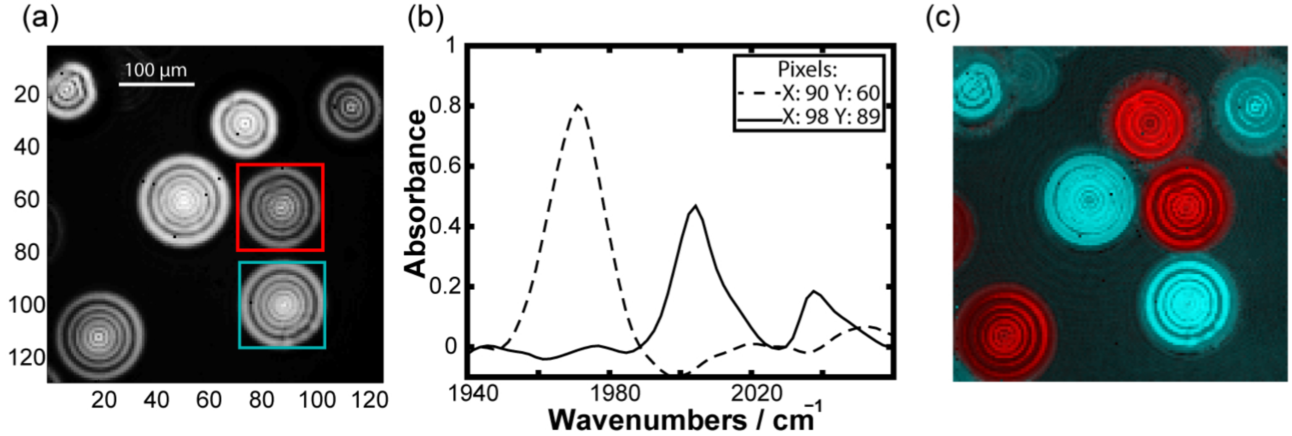

Figure 3.4: Images of a mixture of $Mn_2(CO)_{10}$ or $W(CO)_6$ soaked polystyrene beads suspended in water. (a) Transmitted IR light image of bead sample. (b) Fourier transform infrared (FTIR) absorption spectra of different beads, as indicated by pixel numbers. (c) False color FTIR absorption image. The $W(CO)_6$ (1971 cm$^{-1}$) absorption is mapped to red while the $Mn_2(CO)_{10}$ (2004 cm$^{-1}$) is colored in cyan.

lower the spatial coherence of our beam as described in Methods above. In Figure 4.5, FTIR absorption images of a W(CO)6-containing polystyrene bead collected with and without the rotating diffuser show that we can eliminate coherent fringes by rotating at 2 Hz while maintaining the same averaging time. Interestingly, the absorption signal integrated over the entire bead for the two experiments are the same within 5%. It is often assumed that coherent imaging is inferior to incoherent imaging for resolving objects near the diffraction limit,[79] although fringe features in the image might be exploitable in future experiments for holographic generation of 3 dimensional distributions of chemical species.[80] Nonetheless, these measurements show that high quality coherent or incoherent images can both be collected with our setup.

At a magnification of 12x , the images in Figure 3.4 span 422 x 422 $\mu m^2$ with each pixel covering 3.3 x 3.3 $\mu m^2$. At that magnification, each pixel is larger than the best possible spatial resolution. To quantify the spatial resolution of our microscope, we increased the magnification to sample the largest possible spatial frequency of the field, which is fixed by the numerical aperture of the objective and $\lambda$ to be $\nu = (7\ \mu m)^{-1}$. The Nyquist sampling

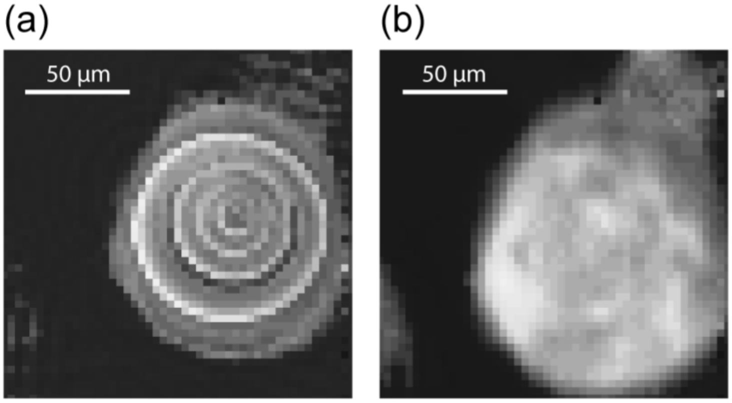

Figure 3.5: FTIR absorption images of a bead containing $W(CO)_6$ measured at 1970 $cm^{-1}$ with (a) no diffuser and (b) a rotating diffuser.

theorem demands pixels spaced at $1/(\nu \text{ x } 2)$, or 3.5 $\mu$m, though oversampling by a factor of 4 (or 8 pixels per airy disk) is a more conservative limit that accounts for pixel size and image contrast.[81] We performed numerical calculations (see Appendix) to conclude that an oversampling rate of ~6 pixels per Airy disk is sufficient to provide contrast of greater than 20% at the distance specified by the Rayleigh criterion. We therefore chose an effective pixel size of 1.1 $\mu$m, meaning a magnification of 36x , to measure our resolution. The high spatial coherence of our laser beam makes resizing of our illuminated region to the new 140 x 140 $\mu m^2$ area easily attainable, even in the case where a diffuser is used to make the beam partially incoherent (throughput of the microscope is high enough that, in all experiments, the shaper output was attenuated by more than 50% to avoid detector saturation), and absorption images of the beads are readily collected at this higher spatial resolution (data not shown).

With 36x magnification in place, transmission images of the group 7 elements of a USAF resolution pattern on $CaF_2$ are shown in Figure 3.6(a) for a rotating diffuser experiment and Figure 3.6(b) for a fully incoherent scalar-wave simulation performed using an idealized optical setup (see Appendix for details). The 1951 USAF resolution test chart is a common standard for imaging systems, where resolution is determined by the smallest element that gives better than 20% contrast between the minimum between two lines and the line intensity. From the cut through the group 7 elements, in Figure 3.6(c), for the experiment (blue points), it can be seen that our microscope achieves a resolution of 3.11 $\mu$m. Interestingly, our experiment clearly outperforms the resolution predicted by the simulation (red curve). Comparison of our resolution to the Rayleigh criterion for our experimental conditions, 0.61 x $\lambda/\mathrm{NA} = 4.3$ $\mu$m,[82] shows that we exceed the classical diffraction limit for incoherent imaging by a significant amount.

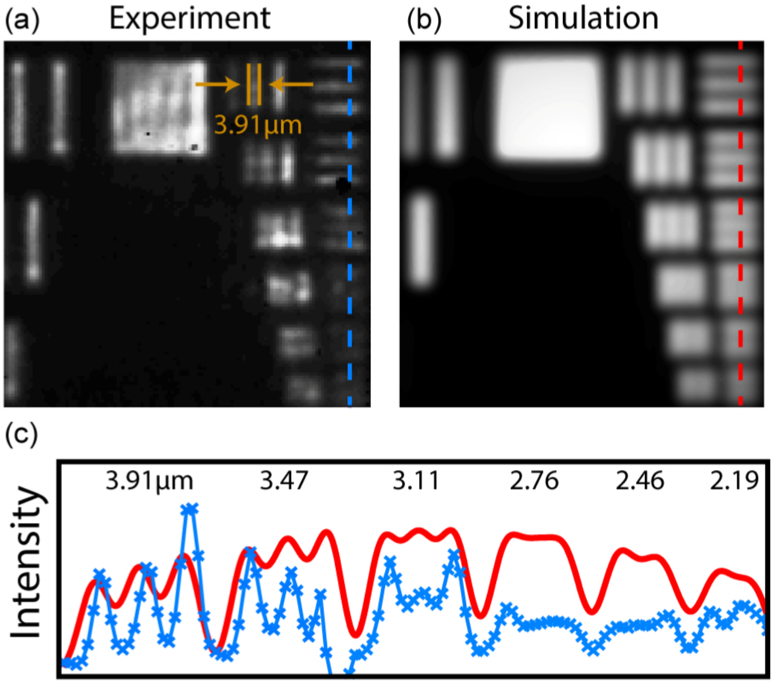

Figure 3.6: Experimental and simulated transmission images of group 7 of a USAF resolution pattern at $\lambda = 5$ $\mu$m. (a) Experimental image using a rotating diffuser and (b) a simulated image using incoherent illumination. (c) Cuts through the resolution elements in the experiment (blue) and simulation (red) labeled with element linewidths, as indicated by the dashed lines in (a) and (b).

Sub-diffraction imaging has been seen previously in synchrotron-based FTIR microscopy.[83] That work attributed sub-diffraction resolution to the mode quality created by a Schwarzschild objective, which we discuss below. Another factor that could create sub-diffraction resolution is the partial coherence of the laser beam, which has also been discussed with regard to synchrotron sources.[84,85]

To explore the effects that a reflective objective would have on our coherent imaging system, we used a 74x , 0.65 NA reflective objective to image our USAF resolution pattern. The major difference between refractive and reflective objectives like a Schwarzchild objective is that the latter uses a small convex mirror that obscures light near the center of the aperture, effectively putting a high-pass filter on the images it forms. Simulated point-spread-functions for refractive (blue) and reflective (green) objectives with the same numerical aperture are shown in Figure 3.7(a). The central (zero order) distribution of the reflective object is narrower for the reflective objective, while the diffraction wings are larger. As an illustration, Figure 3.7 (b-c) shows simulated coherent images of group 6, element 1 (7.8 $\mu$m width lines), for both the refractive and reflective case. The wings cause large amplitude modulations in the image. Experimentally, we found that these effects were too severe from the reflective objective to produce high-quality images near the diffraction limit, even when using the rotating diffuser (not shown). From these simulated and experimental results we can conclude that, for the case of a highly spatially coherent source, refractive objectives are preferable for high resolution imaging.

We have also compared our signal-to-noise to that reported by Hughes et al. who used a similar imaging setup and FPA, but with a glow-bar rather than a laser for the mid-IR source. They obtained a signal-to-noise ratio of 42 for an 8 minute acquisition. The estimated root mean squared noise level of our microscope without the diffuser, based on the 100% level line method [27],[86] referenced against a pixel in the same image, for a 40 second acquisition is 3.4%. With this noise level, we get a signal-to-noise ratio of ~100 under the same conditions. The single biggest source of noise in our data is from the shot-to-shot fluctuations of the laser, which are much larger than the glow-bar. The signal-to-noise might be further improved with a more stable laser, or more sophisticated pulse sequences such as with non-sequential delays to reduce correlated noise, or narrow band frequency scanning

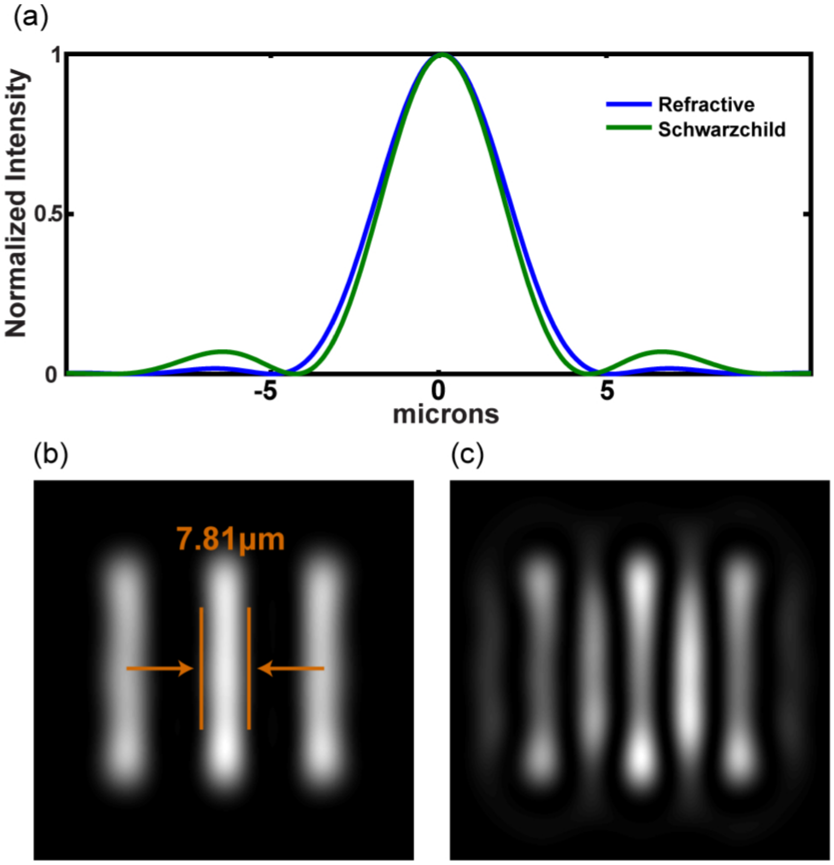

Figure 3.7: a) A cut through the simulated intensity point-spread-function for a refractive (blue) and a Schwarzchild (green) objective, the later using a central obscuration 0.2 times the size of the outer diameter. Simulated images of Group 6 element 1 for (b) a refractive and (c) Schwarzchild objective.

measurements when only a narrow spectral range is of interest.[28, 78, 87]

Perhaps the greatest disadvantage to using a fs laser based FT-IR microscope comes in regards to spectral bandwidth. Common table top mid-IR laser systems are tunable between 3 and 8 $\mu$m, but only deliver about 300 cm$^{-1}$ of spectral bandwidth at one time. That being said, great strides have been made in recent years in the development of continuum lasers, and next generation mid-IR sources will likely become competitive with thermal FTIR sources in regards to bandwidth.[88–90] If a high quality supercontinuum IR laser source became available, the factors limiting the spectral range of our instrument would become dispersion in the transmissive optics[91] and the number of spectral elements (i.e. bandwidth) of the shaper.[60]

## 3.4 Conclusion

We have presented a new technique for performing wide-field FTIR microscopy using a table top laser source, a mid-IR pulse shaper, and an MCT FPA. Our optical design takes advantage of the large energies and high spatial coherence of a femtosecond laser source to produce a microscope with high throughput, even when using a diffuser to produce partially incoherent signals similar to those measured in traditional glow-bar based FTIR microscopes. We showed that with our method we can perform shot-to-shot background elimination and unambiguous undersampling of delays to allow rapid scanning, producing chemical images with high signal-to-noise in minutes. We also demonstrated that our optical system achieves diffraction limited resolution using conventional refractive optics.

There are roughly 2000 femtosecond laser systems worldwide that could be modified into the instrument reported here. In addition, the use of femtosecond laser pulses opens the door to new directions for wide-field IR microscopy. Chemical, materials or biological events could be triggered and then monitored with sub-picosecond time-resolution. Variations analogous to step-scan FTIR spectroscopy might be performed but with improved time-resolution. Additional pulses would enable ultrafast 2D IR spectra to be collected from which vibrational couplings, energy transfer kinetics, and solvent dynamics could all be measured, as is beginning to be explored by Baiz et al. with point-to-point 2D IR imaging.[73] One of the biggest challenges with IR imaging is scatter from inhomogeneous samples, which causes phase artifacts in conventional experiments.[92] The potential for phase cycling to remove these artifacts using pulse shaping represents a new opportunity to study these systems.

## 3.5 Supporting Information

In order to choose an effective pixel size to adequately sample images at the diffraction limit, we simulated the effect of pixilation on two Airy patterns overlapping at the distance defined by the Rayleigh criterion by convoluting the pattern with a square window set to different fractions of the Airy disk diameter, as can be seen in Fig. 3.8. We found that a sampling rate of 6 pixels per Airy pattern was sufficient to give better than 20% contrast.

We employed a scalar-wave Fourier optics approach to simulate the action of the microscope and sample on the input light. The simulated microscope is pictured in Fig. 3.9, where a condenser lens of focal length $f$ focuses the laser light down at a distance $d$ before the sample, after which it illuminates the sample with a diverging wave-front, and finally the field is imaged onto the detector with the objective lens.

Following Reddy et al.,[93] we use Dirac notation to simplify the spectral decomposition of the field, where the scalar amplitude of the electric field,$E_z(r)$, in some plane perpendicular to the optical axis, z, can be described by the projection of a state vector $|E\rangle$ onto either the real-space basis vectors $|r\rangle$, $E_z(r) = \langle r|E_z\rangle$, or the plane wave basis, $|\nu\rangle$ i.e. $\widetilde{E}_z(\nu)=\langle \nu|E_z\rangle$, where $\widetilde{E}_z(\nu)$ is the Fourier transform of $E_z(r)$. For a monochromatic plane wave, $\nu$ is just the projection of the wave-vector onto the plane perpendicular to the optical axis and is called

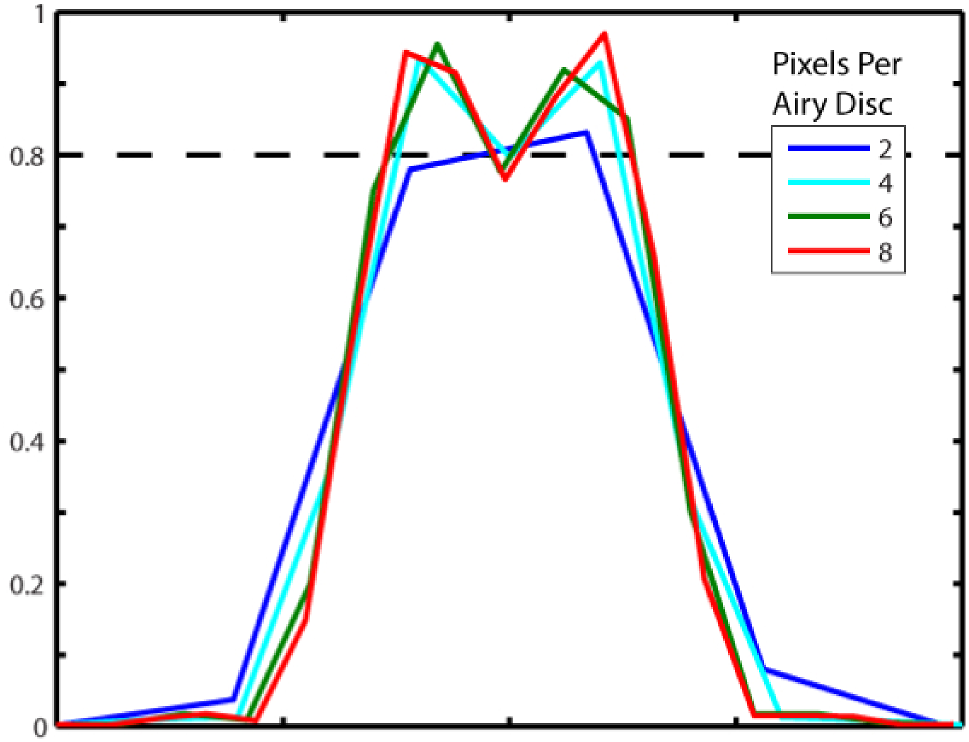

Figure 3.8: Two overlapping Airy patterns set to the distance defined by the Rayleigh criterion, convoluted with windows of different size to simulate pixilation

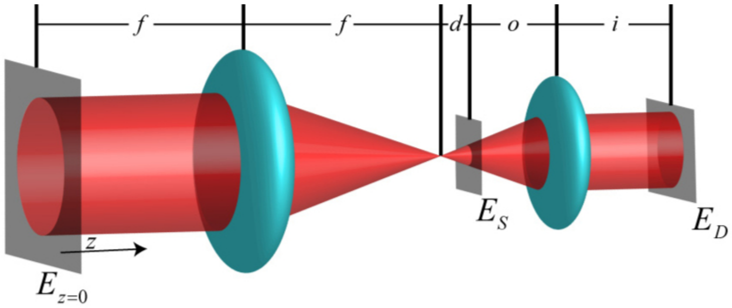

Figure 3.9: Scheme of the simulated optical system.

the spatial frequency, so that free-space propagation in the z direction can be described by:

$$|E_z\rangle = \int_{-\infty}^{\infty} d^2\nu \, |\overrightarrow{\nu}\rangle \, e^{i2\pi\nu_z(\overrightarrow{\nu})z} \, \langle\overrightarrow{\nu}|E_{z=0}\rangle \tag{3.3}$$

where $1/\nu_z(\overrightarrow{\nu})$ is the effective wavelength along z of the plane wave $|\overrightarrow{\nu}\rangle$. Making the Fresnel (small angle) approximation:

$$|E_z\rangle = \int d^2\nu \, |\overrightarrow{\nu}\rangle \, e^{-i\pi\lambda\overrightarrow{\nu}*\overrightarrow{\nu}z} \, \langle\overrightarrow{\nu}|E_{z=0}\rangle \tag{3.4}$$

where a constant phase factor and the integration limits have been dropped for clarity. From Eq. 6.4), it becomes straightforward to express propagation in real-space by use of the identity operator, $1{=}\int\langle\overrightarrow{r_1}|\overrightarrow{r_1}\rangle \mathrm{d}^2\mathrm{r}_1$

$$|E_z\rangle = \int d^2r_1 \int d^2\nu \, |\overrightarrow{r_1}\rangle \, \langle\overrightarrow{r_1}|\overrightarrow{\nu}\rangle \, e^{-i\pi\lambda\overrightarrow{\nu}*\overrightarrow{\nu}z} \, \langle\overrightarrow{\nu}|E_{z=0}\rangle \tag{3.5}$$

$$|E_z\rangle = \int d^2r_1 \, |\overrightarrow{r_1}\rangle \int d^2\nu \;\; \langle\overrightarrow{\nu}|E_{z=0}\rangle \, e^{-i\pi\lambda\overrightarrow{\nu}*\overrightarrow{\nu}z} \tag{3.6}$$

By the convolution theorem, Eq. 6.3 becomes:

$$|E_z\rangle \propto \int d^2r_1 \, |\overrightarrow{r_1}\rangle \int d^2r_0 \, \langle\overrightarrow{r_0}|E_{z=0}\rangle \, e^{\frac{i\pi(\overrightarrow{r_1}-\overrightarrow{r_0})(\overrightarrow{r_1}-\overrightarrow{r_0})}{\lambda z}} \tag{3.7}$$

By projecting onto $|\overrightarrow{r}\rangle$, Eq. 6.6 becomes the Fresnel diffraction equation. Thus, the free-space propagator ,$\widehat{U}_z$, can now be expressed in either the spatial frequency or real-space bases:

$$\overrightarrow{U}_z = \int d^2\nu \, |\overrightarrow{\nu}\rangle \, e^{-i\pi\lambda\overrightarrow{\nu}*\overrightarrow{\nu}z} \, \langle\overrightarrow{\nu}| \tag{3.8}$$

$$\overrightarrow{U}_z = \int d^2 r_1 \left|\overrightarrow{r_1}\right\rangle \int d^2 r_0 e^{\frac{i\pi(\overrightarrow{r_1}-\overrightarrow{r_0})(\overrightarrow{r_1}-\overrightarrow{r_0})}{\lambda z}} \left\langle \overrightarrow{r}_0\right| \tag{3.9}$$

The action of an ideal lens of focal length $f$ on the field front is expressed by the operator:

$$\widehat{L}_f = \int d^2 r \left|\overrightarrow{r}\right\rangle A(\overrightarrow{r}) e^{\frac{-i\pi \overrightarrow{r} * \overrightarrow{r}}{\lambda f}} \left\langle \overrightarrow{r}\right| \tag{3.10}$$

where $A(\overrightarrow{r})$ is the aperture of the lens. Using these operators, and treating the sample as a linear transmissive mask, $\widehat{S}$, the field incident on the detector can be expressed as:

$$E_D(\overrightarrow{r}) = \left\langle \overrightarrow{r}\right| \widehat{U_i}\widehat{L_{f_2}}\widehat{U_0}\widehat{S}\widehat{U_d}\widehat{U_f}\widehat{L_f}\widehat{U_f} \left|E_{z=0}\right\rangle \tag{3.11}$$

Two special cases of a lens operator sandwiched between two propagators can be used to greatly simplify Eq. 6.10, as evaluating the propagators directly for high numerical aperture systems can become computationally impractical. The first case propagates the field from one focal length before the condenser lens to one focal length after:

$$\left\langle \overrightarrow{r}\middle|E_{2f}\right\rangle = \int d^2 r_1 A(\overrightarrow{r}_1) \left\langle \overrightarrow{r_1}\right| \widehat{U_f} \left|E_{z=0}\right\rangle e^{i\pi \overrightarrow{r} * \overrightarrow{r}/\lambda f} e^{-2\pi \overrightarrow{r} * \overrightarrow{r}/\lambda f} \tag{3.12}$$

Using Eq. 6.5, and substituting back for $\nu$:

$$E_{2f}(\overrightarrow{r}) = \widetilde{A}(\overrightarrow{r}/\lambda f) * \widetilde{E_{z=0}}(\overrightarrow{r}/\lambda f) \tag{3.13}$$

Meaning that the field at the lens focus is just the convolution of the Fourier transforms of the field at z=0 with the aperture, scaled by $\lambda f$.

The second special case concerns the formation of an in-focus image of the sample onto the detector:

$$\left\langle \overrightarrow{r}\middle|E_{o+i}\right\rangle = \left\langle \overrightarrow{r}\right| \widehat{U_i}\widehat{L_f}\widehat{U_o} \left|E_{samp}\right\rangle \tag{3.14}$$

Using Eq. 6.6 expanding the quadratic terms, applying the thin lens formula ($1/f$=$1/d_o$+$1/d_i$), and rearranging the order of integration, and recognizing the functional form of the Fourier transform, the field at the detector is:

$$E_D(\overrightarrow{r}) = e^{i\pi \overrightarrow{r} * \overrightarrow{r}/\lambda d_i}\left[\left\{e^{i\pi \overrightarrow{r} * \overrightarrow{r}/\lambda d_o} E_{samp}(\overrightarrow{r}/M)\right\} * \widetilde{A}(\overrightarrow{r}/\lambda d_i)\right] \tag{3.15}$$

Where $M$ is the magnification of the image at the detector. This shows that, neglecting a quadric phase across the wave front, the field incident on the detector is a convolution of the magnified image with $\widetilde{A}(\overrightarrow{r}/\lambda\, f)$ which is often called the coherent point spread function, or PSF.

This completes the set of operations we need to be able to simulate the experimental scenario depicted in Fig. 3.9, which is expressed in the equation:

$$E_D(\overrightarrow{r}) = e^{i\pi \overrightarrow{r} * \overrightarrow{r}/\lambda d_i}\left[\left\{e^{i\pi \overrightarrow{r} * \overrightarrow{r}/M^2 \lambda d_o} S(\overrightarrow{r}/M)\,\langle \overrightarrow{r}|\,\widehat{U_d}\,|E_{2f}\rangle\right\} * \widetilde{A_2}(\overrightarrow{r}/\lambda d_i)\right] \tag{3.16}$$

Where $\widehat{U}_d$, which operates on the field at the focus of the condenser lens in order to propagate it to the sample, remains the only explicit integration of the Fresnel diffraction equation. Since the size scale at the focus, 5 $\mu$m, compares well to the region illuminated on the sample, about 200 $\mu$m, such an integration is not as computationally taxing as it would have been to explicitly propagate the field along the other distances, $f$, $o$, $i$.

For an experiment using square-law detection, the measured quantity is the magnitude of the field squared, integrated over a long time period relative to the dynamic properties of the field:

$$I(\overrightarrow{r}) = \int_{-\infty}^{\infty} |E_D(\overrightarrow{r}, t)|^2 dt \tag{3.17}$$

The loss of phase information of the field upon detection has important consequences on the effect of spatial coherence on the measurement. In the limiting case of a fully coherent wave front:

$$I(\overrightarrow{r}) \propto |\left[e^{i\pi \overrightarrow{r} * \overrightarrow{r}/M^2 \lambda d_o} E_{samp}(\overrightarrow{r}/M)\right] * \widetilde{A}(\overrightarrow{r}/\lambda d_i)|^2 \tag{3.18}$$

For the completely incoherent case, all cross terms between field components originating from different parts of the sample vanish, and the intensity simplifies to:

$$I(\overrightarrow{r}) \propto |E_{samp}(\overrightarrow{r}/M)|^2 * |\widetilde{A}(\overrightarrow{r}/\lambda d_i)|^2 \tag{3.19}$$

meaning that, in the incoherent case, the effective PSF is the square of the coherent PSF, and the signal can, in principle, be directly deconvoluted without the need for phase retrieval.

# Chapter 4

# Spatially Resolved Two-dimensional Infrared Spectroscopy via Wide-field Microscopy

## Contents

This chapter was adapted from: *ACS Photonics.* **2016**, *7*, 1315-1323. It was prepared in collaboration with A.L. Serrano, A. Ghosh, and M. T. Zanni.[94]

## 4.1 Introduction

Imaging techniques that rely on the nonlinear interaction of light with matter have been invaluable to the study of biology and materials science. Methods such as two-photon absorption,[95] second-harmonic generation,[96] transient absorption,[97–99] and coherent anti-Stokes

Raman scatttering (CARS)[72,100] have all been instrumental in developing a more complete understanding of complex systems. Additionally, there has been recent interest in combining ultrafast spectroscopic techniques with microscopy to spatially map chemical dynamics. While all of these techniques are nonlinear in their light-matter interactions, they provide essentially one-dimensional spectra. For example, CARS generates a Raman spectrum of vibrational frequencies. In contrast, nonlinear spectroscopies, such as two- dimensional infrared spectroscopy (2D IR) and two-dimensional visible spectroscopy,[3,101] provide multiple frequency axes that correlate optical transitions. Combining nonlinear microscopy with multidimensional spectroscopy would enhance the information content of images and provide new modes of contrast.

FTIR spectroscopy and imaging have long been utilized as simple, nondestructive, and label-free modes of chemical contrast.[83,93] 2D IR spectroscopy, the multidimensional analog of FTIR, is an ultrafast technique that has contributed to the study of protein folding[102] and aggregation,[103,104] liquid structure,[105–107] and the dynamics of small molecules.[108–110] 2D IR spectroscopy exhibits sensitivity to molecular structure and local environments by spreading the vibrational spectrum across a pump and a probe frequency axis. Figure 4.1 shows a typical single-pixel 2D IR spectrum of dimanganese decacarbonyl ($Mn_2(CO)_{10}$, DMDC). A 2D spectrum consists of a positive peak along the diagonal that arises from ground-state bleach and stimulated emission of the $\nu = 0$ to $\nu = 1$ transition (red contours, labeled A in Figure 4.1a) and an anharmonically shifted negative peak that comes from excited-state absorption from the $\nu = 1$ to $\nu = 2$ transition (blue contours, labeled B in Figure 4.1a). The line shapes in a 2D spectrum report on the relative contributions of the homogeneous and inhomogeneous line widths to the total line shape measured in a conventional linear spectrum. The change in the 2D line shape as a function of time delay between the pump and the probe pulses yields information on the time scale of structural dynamics and solvation.[111] Additionally, cross-peaks located off of the diagonal (labeled C in Figure 4.1a) can reveal

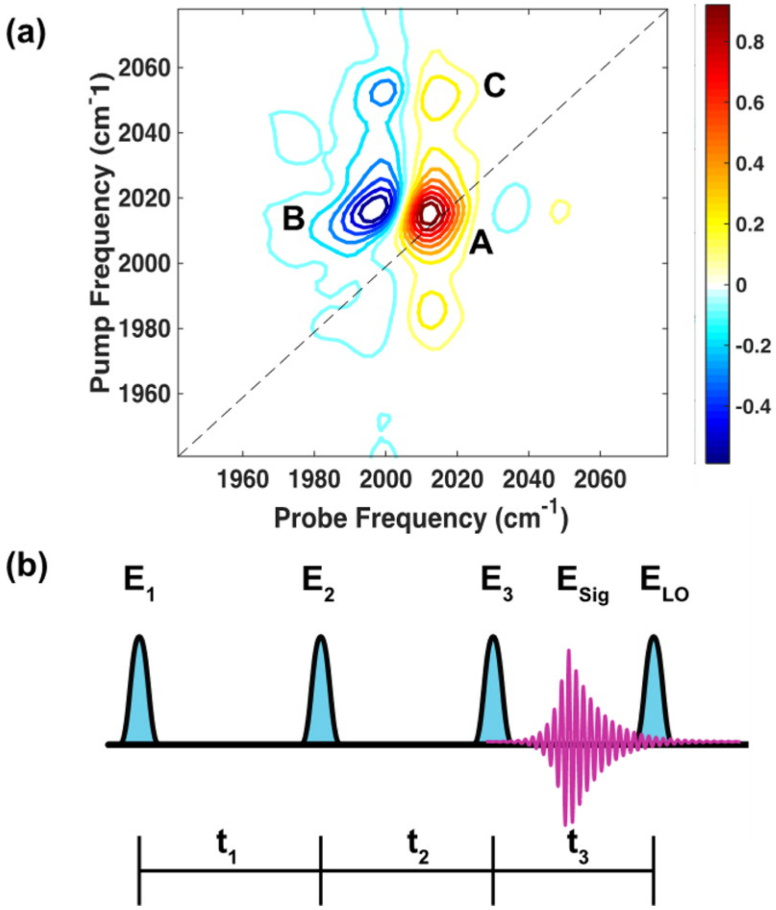

Figure 4.1: Example 2D IR spectrum and general pulse sequence to measure 2D IR spectra. (a) 2D IR spectrum of $Mn_2(CO)_{10}$ absorbed in a polystyrene sphere. Peak A is a fundamental transition at $\nu = 0$–1, peak B is its corresponding excited-state absorption transition (sometimes called the overtone or sequence band) at= 1–2, and peak C is one of a pair of cross-peaks. (b) Generic pulse sequence of two pump pulses, $E_1$ and $E_2$, a probe pulse, $E_3$, the signal-free induction decay, $E_{Sig}$, and the local oscillator, $E_{Lo}$. Time delays are given by $t_n$.

energy transfer,[112] chemical exchange,[113] or vibrational coupling, which can assist in the determination of molecular structure and dynamics.[114] With 2D wide-field IR microscopy we show below that we can now measure the spatial dependence of these properties, which opens the door to new ultrafast 2D IR experiments on complex, heterogeneous systems.

2D IR images can be generated using a standard spectrometer by carefully focusing all the laser pulses and raster scanning across the sample. In this manner, Valim et al. generated images using a mixed infrared/visible homodyne variant of 2D IR.[115] Baiz et al. used a commercial IR microscope and a pulse shaper to create images from a grid of 2D IR spectra collected one after the other.[73] These experiments serve as great examples of the new modes of contrast multidimensional spectroscopic imaging can offer.

With the exception of recent two-photon[116] and CARS experiments,[117] all nonlinear microscopy experiments to date have relied on point-mapping or confocal methods to produce spatial resolution. In contrast to point-mapping methods, we simultaneously collect thousands of 2D IR spectra (one 2D spectrum per image pixel), from which we spatially map 2D IR spectral features with diffraction-limited resolution. We call our technique two-dimensional wide-field infrared microscopy, or 2D-WIRM.

Figure 4.1b shows a generic pulse sequence for measuring 2D IR spectra. Most researchers in the field use a mixed–time–frequency method of data acquisition.[5] In this scheme, the pump frequency dimension is acquired by scanning the time delay between two pump pulses, $E_1$ and $E_2$ . A third pulse, $E_3$ , probes the sample, and the 2D IR signal field, $E_{Sig}$ , is emitted in the phase-matching direction. The spectrum of $E_{Sig}$ is then measured in the frequency domain by dispersing the signal and a reference pulse, often referred to as the local oscillator, $E_{Lo}$ , in a spectrograph (in some experimental implementations of 2D IR, $E_3$ is also used as $E_{Lo}$ ). By Fourier transforming the $E_{Sig}$ spectrum as a function of the pump pulse time delay, $t_1$, one generates the pump frequency axis of a 2D IR spectrum. Taking the approach of Baiz et al., an image can be generated by scanning the sample to generate spatial resolution.[73]

When point mapping, the detector is used to measure the spectrum of $E_{Sig}$ rather than its spatial distribution. Wide-field imaging requires a different approach for detection because the detector measures an image and so cannot be used to measure the spectrum. Instead, we recover the spectrum of $E_{Sig}$ by collecting images for a series of time delays between $E_3$ and $E_{LO}$ for each delay between $E_1$ and $E_2$ . In other words, we eliminate the need for the spectrograph by scanning both the t1 and t3 time delays and subsequently compute a double Fourier transform to generate the two axes of a 2D IR spectrum.[114] A similar procedure is used in other 2D spectroscopies that use nonoptical detection.[118,119] In this manner, a 2D IR spectrum is simultaneously generated for each pixel on the camera with a spatial resolution and field of view set by the focusing conditions of the microscope.

In this article, we report diffraction-limited 2D IR images collected using a 128 by 128 pixel mercury cadmium telluride (MCT) focal plane array (FPA). Only recently has the FPA technology progressed enough to be compatible with the kHz repetition rate of regeneratively amplified ultrafast laser systems. We use two germanium acoustic optic modulators (AOMs) to create the desired pulse sequences. The AOM pulse shapers allow the time delays and phases of each pulse to be updated shot-to-shot for rapid data acquisition and background subtraction.[120] This is, to our knowledge, the first implementation of wide-field, nonlinear microscopy in the mid-IR.

## 4.2 Results and Discussion

### 4.2.1 Microscope Design

The 2D-WIRM microscope was constructed by addition of a pump pulse pair, generated with a mid-IR pulse shaper, to our FTIR microscope, described in detail previously.[121] A schematic of the setup is given in Figure 4.2. In brief, the 1 kHz output of a regenerative amplifier (Coherent Libra) is used to pump a commercial optical parametric amplifier (OPA,

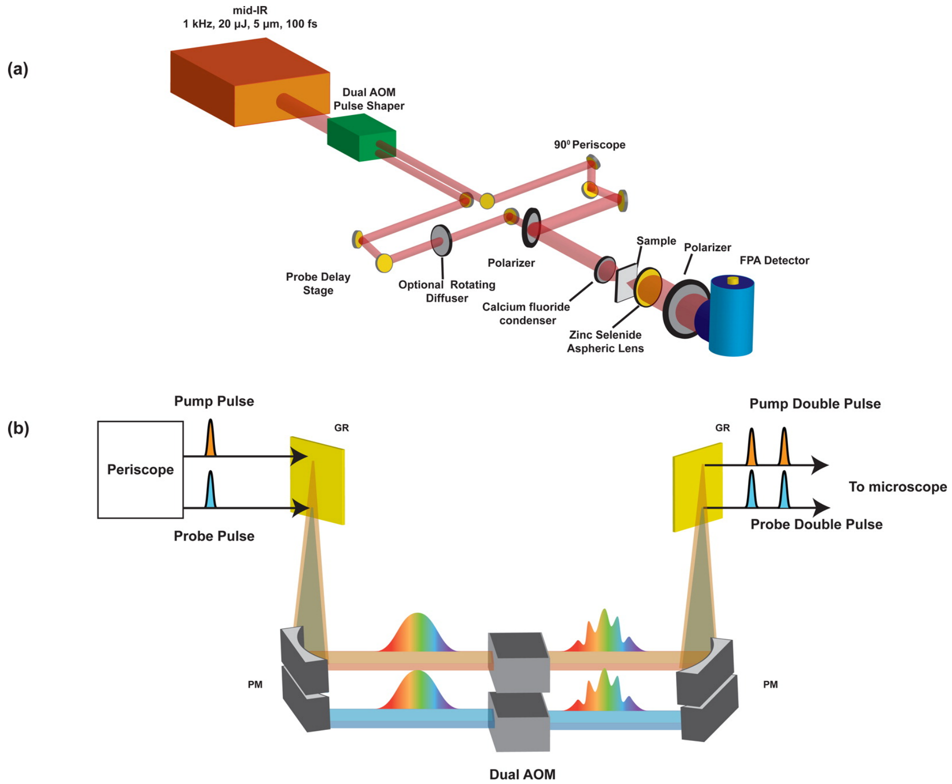

Figure 4.2: Example 2D IR spectrum and general pulse sequence to measure 2D IR spectra. (a) 2D IR spectrum of $Mn_2(CO)_{10}$ absorbed in a polystyrene sphere. Peak A is a fundamental transition at $\nu = 0–1$, peak B is its corresponding excited-state absorption transition (sometimes called the overtone or sequence band) at= 1–2, and peak C is one of a pair of cross-peaks. (b) Generic pulse sequence of two pump pulses, $E_1$ and $E_2$, a probe pulse, $E_3$, the signal-free induction decay, $E_{Sig}$, and the local oscillator, $E_{Lo}$. Time delays are given by $t_n$.

TOPAS, Light Conversion) and a home-built difference frequency generation (DFG) module. The 20 $\mu$J mid-IR pulses are approximately 100 fs in duration and centered at a wavelength of 5 $\mu$m. The output is sent through a periscope, where a 90/10 beam splitter is used to generate vertically offset beams that are sent into a pulse shaper equipped with two Ge-AOMs stacked on top of each other.[28] Although we shape using stacked AOMs, two separate pulse shapers would serve the same purpose. Pulses are modulated in the frequency domain in a 4f-geometry. After shaping to generate two pairs of double pulses, the pump polarization is rotated 90° relative to the probe before both pump and probe pulses are collinearly overlapped using a wire-grid polarizer. The light is focused with a calcium fluoride lens to illuminate a 100 $\mu$m diameter area on the sample, which can be adjusted depending on the desired field of view. A 0.7 numerical aperture ZnSe aspheric lens is used as the imaging objective to form an image at the focal plane on the FPA. A wire grid polarizer is placed before the detector to prevent pump light from saturating the MCT detector.

The magnification of the microscope is set by moving the FPA and the sample relative to the objective to satisfy the thin lens equation. For the images reported, the camera is set to generate a 36x magnification image. The physical size of the pixels is about 40 x 40 $\mu$m, which means each pixel records a 1.1 $\mu$m area under these focusing conditions. In the Supporting Information, we also report 50x magnification images that have a pixel size of about 0.8 $\mu$m. These images oversample the airy disk of the point-spread function, which we use to measure the spatial resolution of our microscope.

As described above, our approach is to measure the third-order response function, $E_{Sig}$ , at each image pixel utilizing the time–time method of acquisition.[28] More specifically, one AOM generates the pump pulse pair to set the $t_1$ delay and phases of $E_1$ and $E_2$ . The other AOM generates the probe pulse pair to set the $t_3$ time delay and the phases of $E_3$ and $E_{Lo}$ . For the data presented in this paper, $t_1$ was scanned from 0 to 3.48 ps in 60 fs increments, while $t_3$was scanned from 0 to 3.48 ps in 30 fs steps. The phase of the moving pulse was adjusted at each time delay to shift the observed frequency of the signal by 1900 $\text{cm}^{-1}$. This rotating frame allows for unambiguous undersampling of the two-dimensional interferogram and significantly decreases the number of data points needed to satisfy the Nyquist criterion.[120] The waiting time, $t_2$, was set to 1 ps using a translation stage, although scanning this time could be used to study the ultrafast evolution of the 2D spectrum and would provide even more contrast mechanisms, as recently demonstrated by Baiz et al.[73] For the experiments reported, we collect over 16 000 spectra in about 50 s. The pulse sequence is then repeated until the desired signal-to-noise ratio is achieved. All images reported required about 2 h to collect.

### 4.2.2 Phase Cycling Scheme for the Collinear Geometry

There are many types of 2D IR spectra. We are interested in generating absorptive spectra because they have the highest frequency resolution.[5] Absorptive spectra are produced by adding together the rephasing and nonrephasing components of the third-order response function. In addition to these desired signals, the collinear optical geometry of the 2D-WIRM microscope also results in lower order signals and pulse interferences that create a background, only some of which are reduced by the polarizer before the detector. To eliminate these unwanted signals, we utilize the phase dependence of the 2D IR signal, which is given by:[5, 97, 122]

$$S_{2DIR} \propto \cos(\mp\phi_1 \pm \phi_2 + \phi_3 - \phi_{Lo}) \tag{4.1}$$

where $\phi_i$ is the phase, in radians, of the $i$th laser pulse. Table 4.1 illustrates the phases used for each pulse sequence. After collecting all of these phase combinations for each $t_1$ and $t_3$ time delay, the data can be processed as in eq 2 or 3, depending on the plotting convention desired.

$$S_{2DIR}(t_1, t_2, t_3) = \log \frac{S_1 + S_4 + S_6 + S_7}{S_2 + S_3 + S_5 + S_8} \tag{4.2}$$

$$S_{2DIR}(t_1, t_2, t_3) = S_1 + S_4 + S_6 + S_7 - S_2 - S_3 - S_5 - S_8 \tag{4.3}$$

From the time-domain data the 2D IR spectra are generated by computing a two-dimensional Fourier transform.

Figure 4.3 demonstrates the reduction in background when phase cycling. 2D IR spectra shown were collected in the 2D-WIRM microscope without (a) and with (b) phase cycling. In Figure 4.3a a very large feature is observed at zero frequency that is created by the background signals. It completely obscures the 2D spectrum. In Figure 4.3b phase cycling

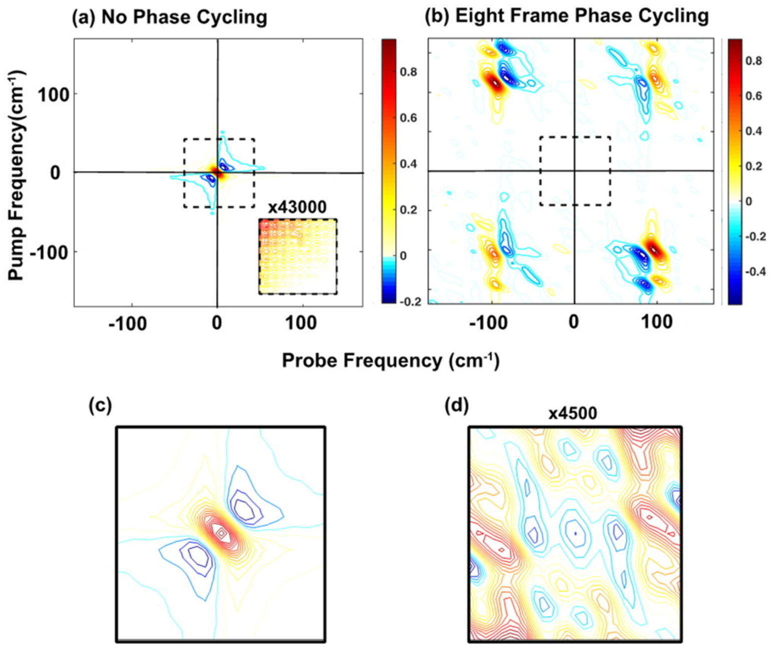

Figure 4.3: Demonstration of background reduction with an eight-frame phase cycling scheme. (a) Averaged spectrum without phase cycling that is dominated by a large zero-frequency feature. The inset shows the region where there should be signal multiplied by 43 000. (b) Averaged spectrum with phase cycling revealing the rephasing and nonrephasing spectra. The axis labels are shown before correction with the rotating frame frequency. (c) Zero-frequency feature, labeled with the black box in (a), that dominates without phase cycling. (d) The same frequency region as in (c) but with phase cycling multiplied by 4500. This region is now only noise.

Table 4.1: Phase Cycling Scheme for Isolating 2D IR Signals

| – | $\phi_1$ | $\phi_2$ | $\phi_3$ | $\phi_{Lo}$ |
|---|---|---|---|---|
| $S_1$ | 0 | 0 | 0 | 0 |
| $S_2$ | $\pi$ | 0 | 0 | 0 |
| $S_3$ | 0 | $\pi$ | 0 | 0 |
| $S_4$ | $\pi$ | $\pi$ | 0 | 0 |
| $S_5$ | 0 | 0 | $\pi$ | 0 |
| $S_6$ | $\pi$ | 0 | $\pi$ | 0 |
| $S_7$ | 0 | $\pi$ | $\pi$ | 0 |
| $S_8$ | $\pi$ | $\pi$ | $\pi$ | 0 |

reduces this background feature by a factor of43000 to reveal rephasing and nonrephasing spectra in their respective quadrants.[5,122] Figure 4.3c and d illustrate the reduction of this zero-frequency feature. Absorptive spectra are generated by adding the rephasing and nonrephasing components together (not shown). Indeed, even when plotting more contours or zooming in to the regions where we know there is 2D signal, the inset in (a), the signal is still unobservable and dominated by the wings of the zero-frequency feature. This eight-frame phase-cycling scheme is well known to be advantageous and has been used in other 2D spectroscopies.[73,122,123]

### 4.2.3 Imaging Transition Metal Carbonyls in Polystyrene Beads

To test the microscope, we measure polystyrene beads labeled with one of two different metal carbonyl solutions. The experimental details for preparing polystyrene beads are provided in the Methods section. Briefly, polystyrene beads were soaked in saturated solutions of either dimanganese decacarbonyl or tungsten hexacarbonyl ($W(CO)_6$) for about 2 h. They were then spun down and washed in methanol. Beads were deposited onto a calcium fluoride window and dried under nitrogen before imaging. At the frequency of their respective transition, the 106–120 $\mu$m beads have an optical density of about 0.6, while we estimate the 25 $\mu$m beads to have an optical density of about 0.05–0.075.

In Figure 4.4 we present images of 110 $\mu$m polystyrene beads swelled in DMDC and $W(CO)_6$. Figure 4.4a shows a 2D IR spectrum at pixel (x = 88, y = 98) on the FPA detector for a bead labeled with DMDC. The spectrum matches solution phase data, as expected. Figure 4b shows the corresponding image of the integrated fundamental peak area (peak A in Figure 4.1a). Similarly, in Figure 4.4c and d we plot a single-pixel 2D IR spectrum and corresponding image for a $W(CO)_6$-labeled polystyrene bead. Interestingly, the cross-peak off the diagonal in Figure 4.4c does not appear in solution spectra of $W(CO)_6$. We attribute this to an accidental degeneracy with a combination or overtone band whose oscillator strength is larger in the polystyrene environment, although we do not explore this observation further.[124]

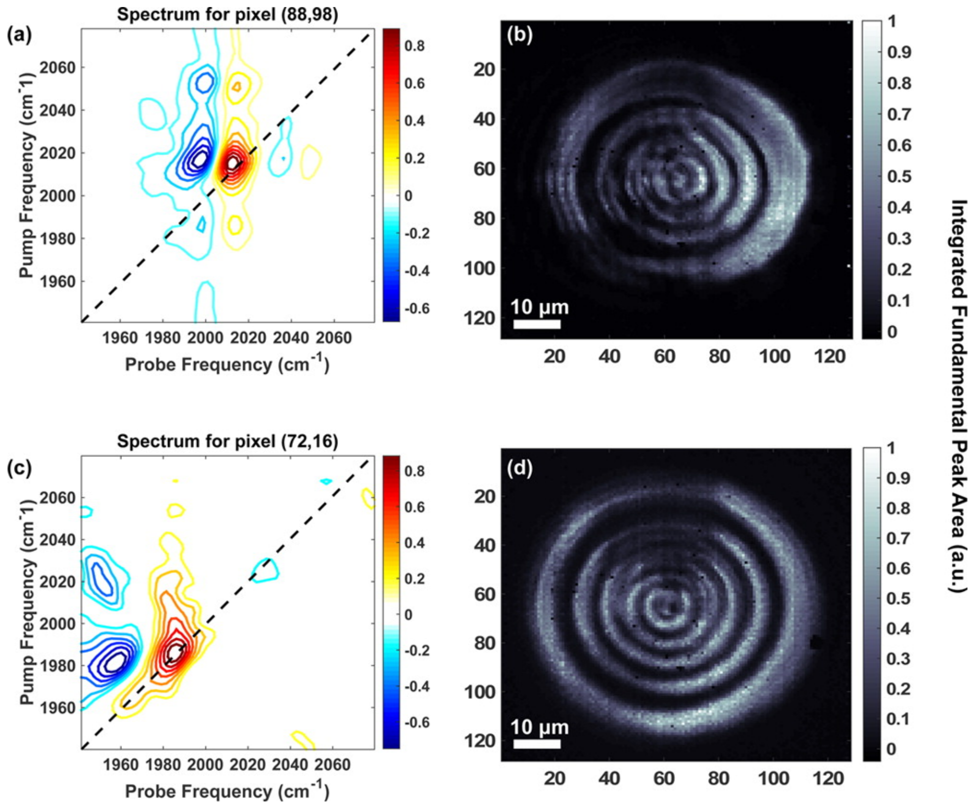

Figure 4.4: 2D-WIRM images of $\mu$ 110 $\mu$m beads. (a) Representative single-pixel 2D IR spectrum and (b) image of the fundamental integrated peak area of a bead labeled with DMDC. (c) Representative 2D IR spectrum and (d) image of the integrated fundamental peak area of a bead labeled with $W(CO)_6$

.

### 4.2.4 Imaging with Rotating Diffuser

The concentric rings in the intensity image are created by refraction and diffraction of the spatially and temporally coherent probe pulse. While the image on the detector contains interferences, illumination at the sample is uniform because the interference effects are significant only in the far field. Most wide-field microscopes use incoherent illumination or measure fluorescence and do not contain the coherent interferences in our images. The coherent images are difficult to interpret by eye because it contains extra spatial phase information not typically present in incoherent images. In principle, the interferences can be removed by measuring the point-spread function. The point-spread function could be measured by passing a local oscillator around the sample and thereby measuring the spatial phase shift introduced by the optical path of the microscope.[80, 125] If the point-spread function is not measured, it could be modeled using a maximum entropy method to obtain the most likely phase distribution at the image plane.[126] In the future, we plan to deconvolute the 2D IR images, but for now we experimentally scramble the spatial coherence using a rotating diffuser, as reported previously.[78, 121](35, 44)

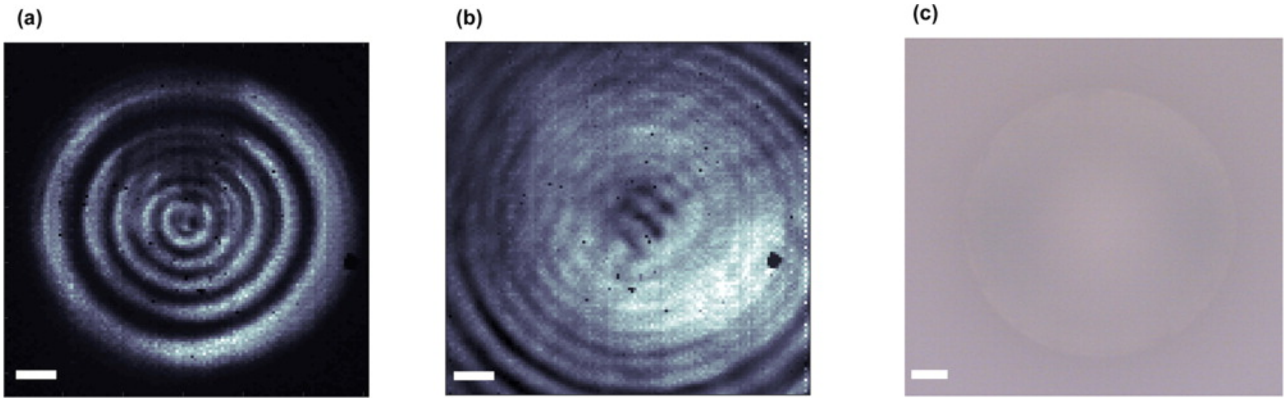

Figure 4.5: 2D-WIRM images of $\mu$ 110 $\mu$m beads. (a) Representative single-pixel 2D IR spectrum and (b) image of the fundamental integrated peak area of a bead labeled with DMDC. (c) Representative 2D IR spectrum and (d) image of the integrated fundamental peak area of a bead labeled with $W(CO)_6$

.

To implement this alternative approach in the 2D-WIRM microscope, we place the rotating diffuser on the probe line (see Figure 4.2) and rotate it at ∼2 Hz. Figure 4.5 shows a comparison between 2D-WIRM images collected with and without the rotating diffuser, in addition to a white-light image of a representative bead. The white-light image is very uniform but has low contrast. The 2D IR images have much higher contrast because they come from the molecular absorption. The diffuser helps to alleviate coherent artifacts because it decreases the spatial coherence of the probe pulse. A diffuser is not needed in the pump line because only the probe light is used to measure the spatial distribution of the 2D IR spectra. The rotating diffuser is used to scramble the spatial phase of the incoming light. To completely eliminate the interferences, the spatial phase must average to zero for each pixel on the detector. In the limit of infinite random phase distributions, a perfectly incoherent image would be recovered. The 2D IR signal depends only on the relative phases of the laser pulses,; thus this random spatial phase will introduce only a small decrease in signal-to-noise. In this image the diffuser does not completely remove the interferences. The diffuser is most effective at lower magnifications[121] because it is easier to create phase differences on the order of the pixel size. The interferences can create images that are not intuitive to interpret, but they also provide more information about the signal. For example, the interferences have been exploited to measure the 3D topography.[80,125] Thus, they can be diminished or exploited to learn more about the sample. In the image with the diffuser, the bead appears slightly larger because incorporating the diffuser requires adjustments to the microscope focus to maximize throughput and minimize coherent interferences. These adjustments can slightly move the image plane, and so a strict comparison between bead sizes in Figure 4.5 should not be made.

### 4.2.5 Imaging Vibrational Coupling

2D IR spectra contain many more observables than conventional FTIR spectra, such as off-diagonal peaks created by transitions to overtone and combination bands. In Figure

5.4, we show that 2D-WIRM images generated with constraints that include off-diagonal features dramatically improve image quality. To this end, we image mixtures of 25 $\mu$m diameter beads labeled with different metal carbonyl molecules. Figure 5.4a shows the probe spectrum with the frequency of the DMDC transition marked with the dashed line at 2015 cm$^{-1}$. The resulting image reveals six beads with about equal intensities. These beads likely have different labels, but it is impossible to tell since the linear absorption is below our microscope's signal-to-noise. We performed various background subtraction methods, in the time and frequency domain, but were unable to observe the linear spectrum.

Figure 5.4c shows a representative single-pixel 2D IR spectrum of the DMDC bead. Clearly, even though we cannot observe the linear absorption spectrum, a 2D IR spectrum is readily measured. Figure 5.4d shows the resulting image made by plotting the intensity of the diagonal peak of DMDC. The 2D-WIRM image clearly shows that the bead in the upper corner is labeled with DMDC, although there is some signal in other regions. This could come from (1) noise or (2) leakage of the metal carbonyls upon mixing. If there is leakage of the labels outside of the beads, these regions should show an off-diagonal peak characteristic of the 2D spectrum of DMDC. Shown in Figure 5.4c is a dashed red box that encompasses both the fundamental and an overtone transition of DMDC, which have opposite signs. Figure 5.4f is a 2D-WIRM image that plots the fundamental intensity, but only if there is a corresponding negative intensity at the frequency of the overtone. In other words, we are plotting only the intensity of pixels that show signal that is characteristic of a 2D spectrum. In this image, only the upper left bead shows any intensity, indicating that the residual intensity in Figure 5.4d was due to noise. Noise in a 2D IR spectra is random. Thus, the more constraints that are applied, the better the molecular discrimination. This is illustrated in Figure 5.4e by plotting the residual intensity in the dashed white box in Figure 5.4d. As more constraints are applied to the DMDC 2D IR image, the number of pixels with residual intensity in the dashed white box, the region with no DMDC beads, is dramatically

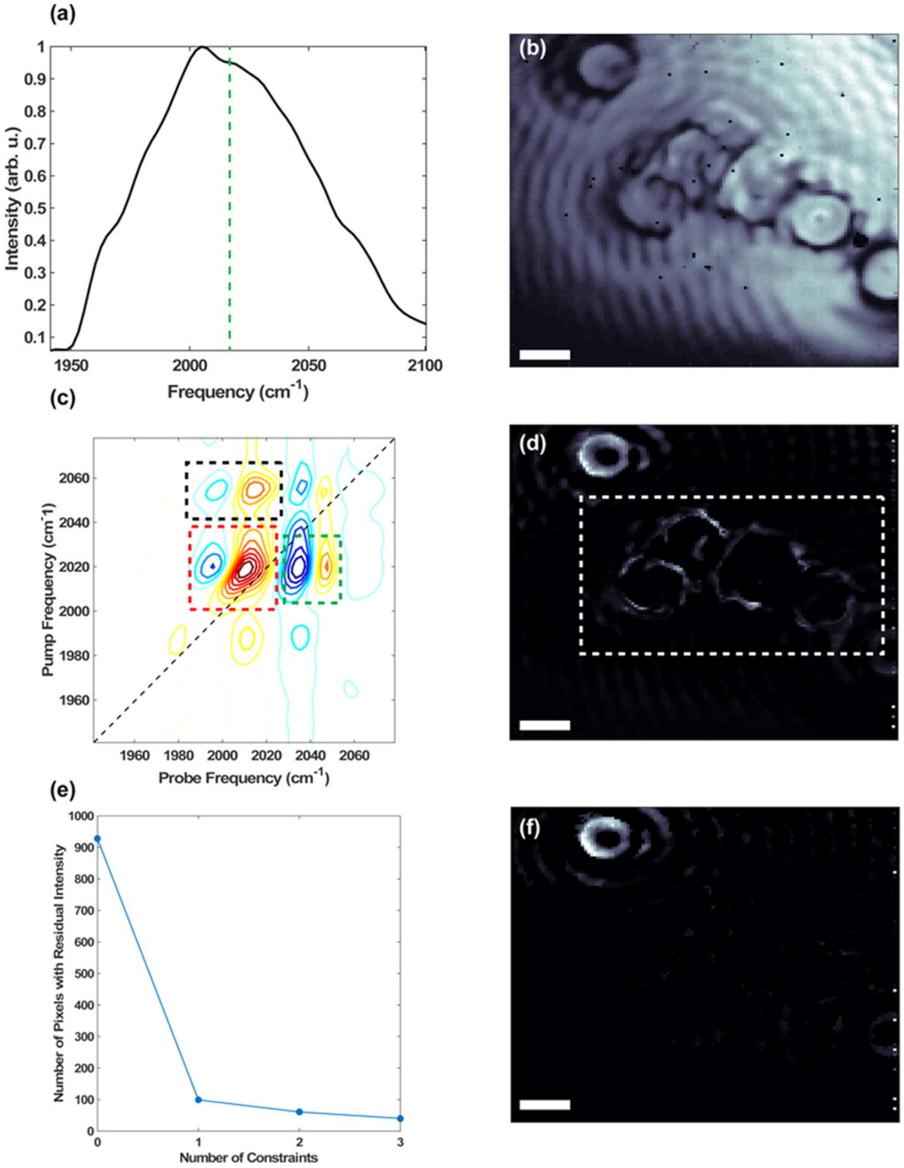

Figure 4.6: Comparison of image quality for different processing methods. (a) Spectrum of the probe pulse used to generate FTIR transmission image (b) at 2015 cm$^{-1}$. Representative DMDC (c) 2D IR spectrum and (d) 2D IR amplitude image of the DMDC peak with no constraints. (e) Graph showing pixels in the dashed white box with residual intensity with the indicated constraints in (c) labeled by the dashed boxes. (f) Amplitude image generated by including only spectra with out-of-phase peaks (i.e., one constraint) in the dashed red box in (e). All scale bars are 10 $\mu$m.

.

decreased. This demonstrates that 2D IR microscopy can improve molecular discrimination even with weakly absorbing samples.

### 4.2.6 Chemical Imaging with 2D IR

Analogous to the hyperspectral cube, as it is often called in the FTIR imaging community,[83] we have two frequency and two spatial dimensions, or a hyperspectral tesseract. This multidimensional data can be used to generate false color images with different colors mapped to distinct spectral features. Figure 4.7a shows the fundamental intensity of ($W(CO)_6$)mapped to blue and the DMDC fundamental intensity mapped to red. Representative single-pixel 2D IR spectra are shown in Figure 4.7c and d, respectively. The images require a negative intensity at the frequencies of their respective excited-state absorption frequencies. It is clear that even with linear absorption that is difficult to observe with our microscope, we can still generate high-quality, single-pixel 2D IR spectra.

Another advantage of 2D-WIRM is the multitude of spectral signatures that can be used as contrast mechanisms to generate images. Figure 4.7b shows the cross-peak amplitude of DMDC spatially mapped. In future experiments, we imagine that images like the one shown will aid in mapping vibrational coupling as a function of space, which can then be used to determine microscopic variations in molecular structure. Additionally, the waiting time dependence of cross-peaks can be used to observe energy transfer and chemical exchange in heterogeneous materials. Picosecond dynamics can improve the structural contrast in a 2D IR image to monitor hydration, for example,[59, 73, 127] which might be interesting observables in a structurally heterogeneous system like a cell.

### 4.2.7 Spatial Resolution of 2D-WIRM

We also measured the spatial resolution of 2D-WIRM for comparison to FTIR microscopy. To do so, we used a negative USAF test target (Max Levy Autograph) patterned on calcium

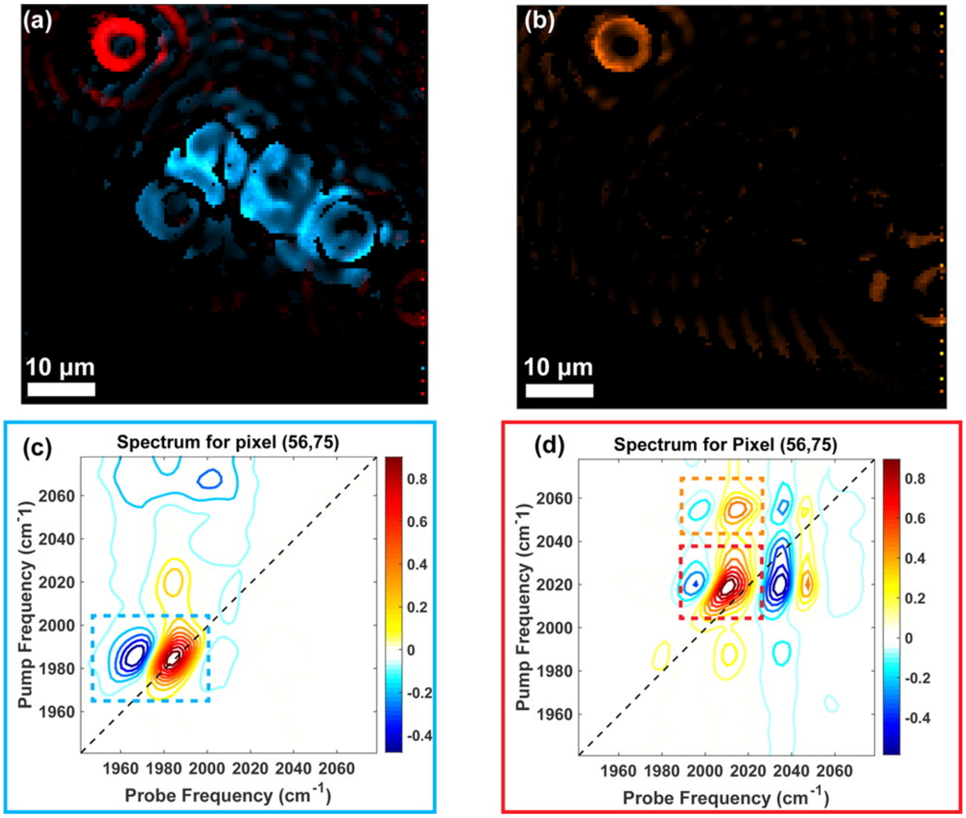

Figure 4.7: Chemical images generated with 2D-WIRM. (a) Fundamental intensity of DMDC mapped to red and ($W(CO)_6$) mapped to blue. (b) Cross-peak image of the DMDC transition indicated by the dashed orange lines in (d). (c) 2D IR spectrum of ($W(CO)_6$) at the indicated pixel. (d) 2D IR spectrum of DMDC at the indicated pixel. Dashed boxes contain features used to generate the images.

.

fluoride. A standard USAF test target consists of a series of equally spaced bars that are frequently used to test image formation in microscopes. DMDC was dissolved in methanol and placed between two calcium fluoride windows, one bare and one with the USAF test target pattern. Figure 4.8a shows a 2D IR amplitude image of elements four, five, and six of group 6, while Figure 4.8b shows the corresponding image of the test target at 2015 cm$^{-1}$, the probe frequency of the DMDC fundamental peak. The element line widths and spacings are labeled in Figure 4.8a. Diffraction through the slits can lead to ringing features, as can been seen in the small line around pixel 80 in the FTIR scan.[78,121] The interferences are less pronounced with the test target compared to the beads because it lacks the 3D topography of the large beads. To test the spatial resolution, we imaged group 7 elements, which are shown in the Supporting Information, and determined that there was no significant difference in spatial resolution between the FTIR and 2D-WIRM images.

From visually inspecting the slice, it seems that the 2D-WIRM image shows enhanced contrast as opposed to the conventional IR transmission image: the difference from peak to trough is exaggerated in 2D IR images compared to FTIR. To quantify the difference, we define a contrast ratio, $C$, as:

$$C = \frac{S_{Peak} - S_{Trough}}{S_{Peak} + S_{Trough}} \tag{4.4}$$

where $S_{Peak}$ is the signal at the peak of the elements and $S_{trough}$ is recorded at the trough. We used group 6, element 5 bar (orange box) to estimate the improvement in contrast. Using these elements, with the strongest 2D IR signal, the contrast ratio of 2D-WIRM is estimated to be about 0.96, while the FTIR is 0.77. The difference between the 2D-WIRM and FTIR contrast is even greater for the group 6, element 6 bar, separated by 4.38 $\mu$m, because these elements are even more closely spaced.[81] We rationalize this observation using the dependence of linear and 2D IR measurements on the absorption cross-section. In 2D IR measurements, the signal scales with cross-section squared, while FTIR measurements scale

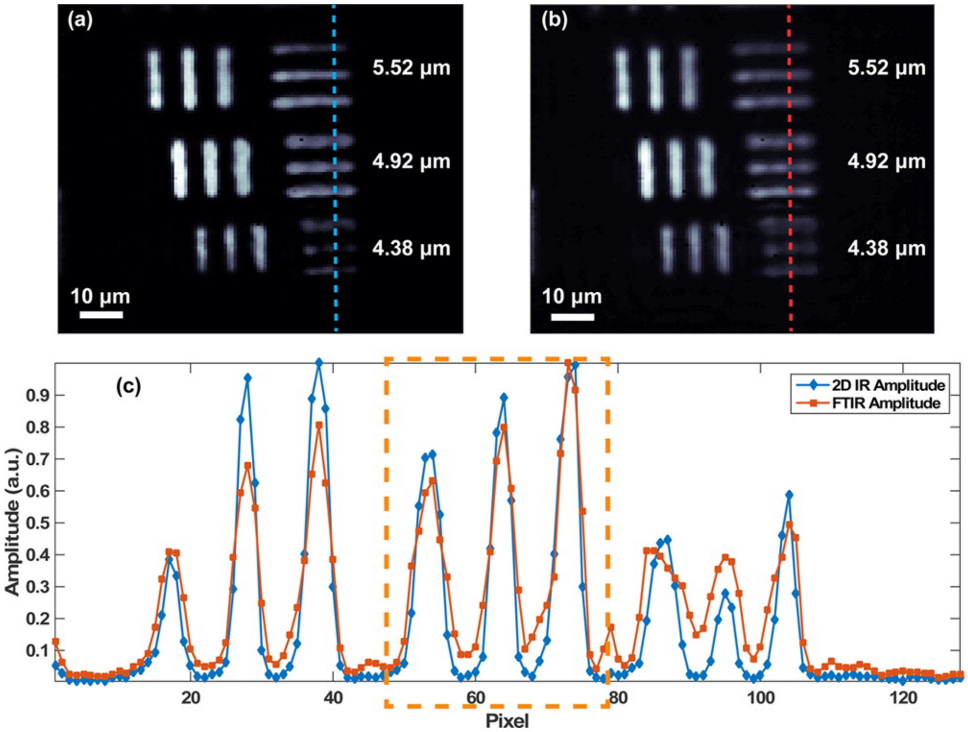

Figure 4.8: Comparison of image contrast and resolution between FTIR and 2D-WIRM imaging. (a) 2D IR amplitude image and (b) FTIR amplitude image at the probe frequency of the fundamental peak of a USAF test target with DMDC solution in the sample cell. (c). Slices through the columns indicated by the dotted lines in (a) and (b). Element line widths and spacings are labeled in (a) and (b).

.

linearly.[12] The improved image contrast adds to the list of advantages that 2D IR exhibits over FTIR. The resolution is estimated to be at least 3.48 $\mu$m. We determined this number by measuring the smallest resolvable elements of the test target at the 20% contrast level (see Figure S2). The 3.11 $\mu$m features cannot be resolved; therefore, the resolution is between 3.11 and 3.48 $\mu$m (significant figures given by the manufacturer of the test target). As we observed in our previous FTIR experiments, this is better than the Rayleigh criterion of $0.61\lambda/NA$ which yields a predicted resolution of 4.3 $\mu$m.[121]

## 4.3 Conclusion

In summary, we have used a dual-AOM mid-IR pulse shaper in conjunction with a wide-field transmissive microscope to collect 2D IR spectroscopic images. We exhibited our ability to collect diffraction-limited 2D IR images of metal carbonyl beads and a USAF resolution test target. This is the first implementation of wide-field nonlinear microscopy in the mid-IR. Although these data use a combined AOM shaper, two separate pulse shapers could be used to generate 2D-WIRM images. Our images are diffraction limited and exhibit enhanced contrast compared to linear microscopy. Optimized pulse sequences and other technological developments could decrease acquisition time.[128,129] One can also envision future experiments based on the many implementations of transient 2D IR spectroscopy.[109,130] We anticipate wide-field 2D IR imaging will be complementary to point-mapping approaches; data collection on a per pixel basis is desirable, but point mapping might be better for sparsely mapping larger sample areas. With either method, the extra dimension of 2D-WIRM opens the door for new modes of chemical sensitivity and label-free biological imaging. This technique has the potential to impact researchers in the field of 2D IR spectroscopy by allowing more complicated, heterogeneous samples to be analyzed, in addition to IR microscopists, by offering new observables that could aid in cancer diagnostics and label-free characterization of tissues.

## 4.4 Methods

The output of a 4.0 W, 50 fs regenerative amplifier (Coherent Libra) with wavelength centered at 800 nm is used to pump a commercial OPA (TOPAS, Light Conversion). Signal and idler pulses are then mixed collinearly in a $AgGaS_2$ DFG crystal to generate mid-IR with a center wavelength of 5 $\mu$m. Mid-IR pulses are about 100 fs in duration and have pulse energies around 20-22 $\mu$J. The mid-IR output is then sent through a 90/10 wedged CaF2 beam splitter. Immediately after, a periscope is used to generate vertically offset beams for separate shaping of the pump and probe pulses. Both pulses are shaped in the frequency domain using a dual, 4f Ge AOM (Isomet) based pulse shaper described previously.[131] Two separate arbitrary waveform generators (AWGs) are used to generate RF masks to independently generate pump and probe double pulses with absolute control over their phases. Masks are updated at 1 kHz, the repetition rate of the laser, so pulses are shaped every laser shot. Pump and probe pulses are scanned in opposite directions in time, such that the waiting time, $t_2$, is constant. The pump pulses' polarizations are rotated 90° relative to the probe and subsequently recombined on a wire-grid polarizer. The collinear pulses are then sent to a home-built transmissive microscope. The IR light is focused using a 150 mm focal length $CaF_2$ lens. The light is expanded over $\sim$0.5 mm before illuminating the sample. A 0.7 numerical aperture (NA) zinc selenide aspheric lens (Edmund Optics) is used to form an image of the sample at the FPA detector, located about 450 mm away. A Teledyne Xcelera PCIe frame grabber is triggered by a 5 V square pulse that is emitted when the pump and probe AWG cards are each on the first mask of their respective sequences. For $n$ pump masks, there are $n \pm 1$ probe masks, with the last probe mask in the sequence being a null mask that is removed before processing. This allows for complete sampling of all $n(n \pm 1)$

combinations of phases and time delays. For the images reported here, we scanned to a max time delay of 3.48 ps with 30 fs time steps on the probe line and 60 fs time steps for the pump line. Additionally, the rotating frame of each AOM is set to be 1900 cm$^{-1}$. With the eight-frame sequence used in this paper, that corresponds to 236 pump and 235 probe masks for a total of 55460 laser shots to generate a 2D spectrum.

Polystyrene beads were purchased from Polysciences and used as received. In this paper, we used 25 $\mu$m and 106–120 $\mu$m beads. The 106 $\mu$m beads were prepared by swelling them in chloroform solutions saturated with DMDC (Mn2(CO)10) or W(CO)6. After they had been soaked for 2 h, the chloroform solution was decanted and beads were washed in methanol. The beads were then dried on a CaF_2 window before being placed in a sample cell for imaging. The 25 $\mu$m beads were prepared in the same manner, except that a mixture of 30% chloroform and 70% methanol, by volume, was used for swelling since pure chloroform solution was observed to overswell the beads.

## 4.5 Supporting Information

The vertically offset pump and probe pulses are generated in periscope as shown in Figure 5.8. To avoid the back reflection from interfering with the pulses, a wedged beam splitter is used to so that this reflection does not travel parallel to the pump and probe pulses. From this periscope, the pump and probe pulses are directed into the dual-AOM pulse shaper.

Figure 4.10 shows the 2D-WIRM image of group 7, elements 1,2, and 3 of a standard USAF test target. The elements have line widths of 3.91, 3.48, and 3.11 $\mu$m. Figure S3 shows a close up of the smallest elements resolvable and a comparison between FTIR and 2D IR images. We estimate our resolution to be about 3.48 $\mu$m using the 20% contrast method, which we observed with our previous fully coherent pulse shaping-based FTIR microscope.

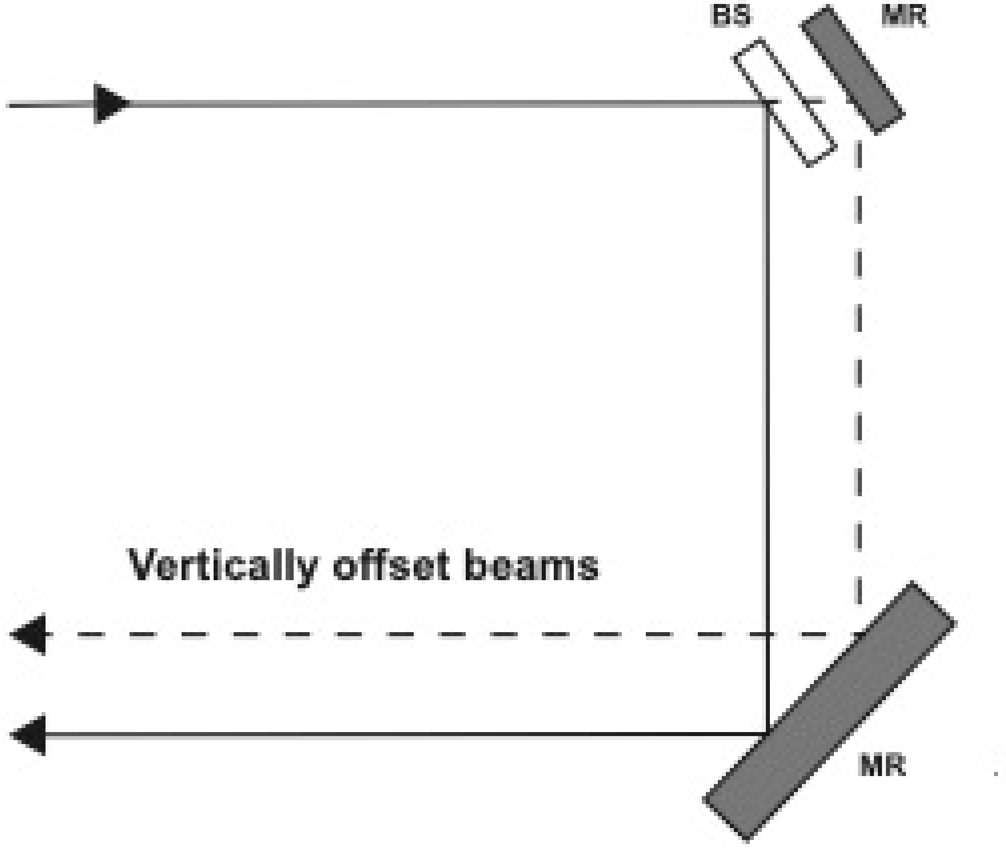

Figure 4.9: Periscope used to generate vertically offset beams. MR stands for mirror and BS represents a calcium fluoride wedged beam splitter.

.

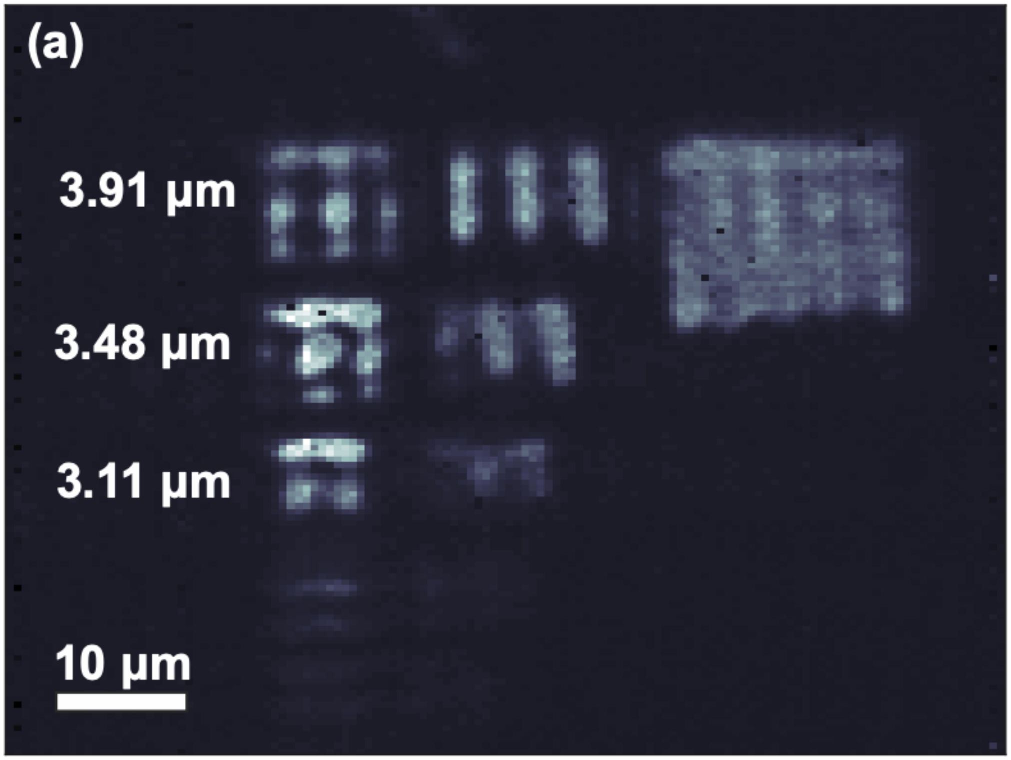

Figure 4.10: 2D-WIRM Amplitude image of the Group 7, elements 1,2, and 3 of a standard USAF test target.

.

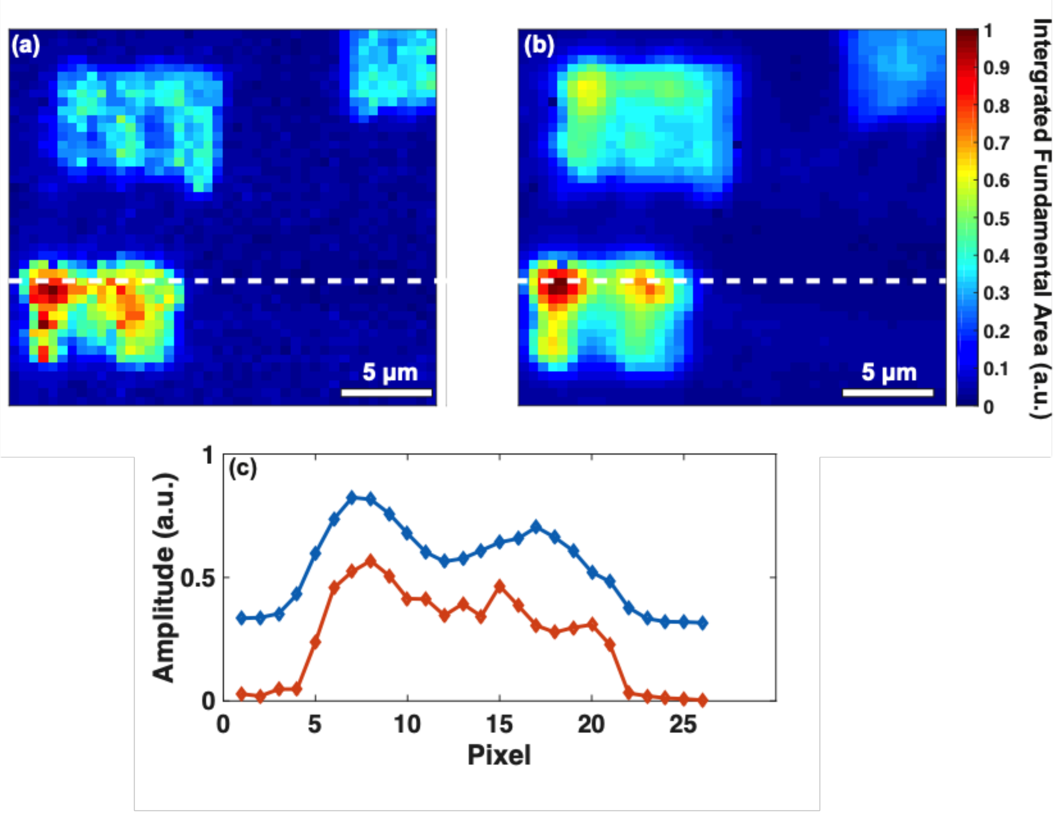

Figure 4.11: . (a) 2D-WIRM image and (b) FTIR image of elements 2 and 3 of Group 7. Slices through the dashed white lines are shown in, corresponding to elements separated by 3.11 $\mu$m (c). Blue is the FTIR slice while red is the 2D IR image slice.

.

# Chapter 5

# Energy Transfer Between Coherently Delocalized States in Thin Films of the Explosive Pentaerythritol Tetranitrate (PETN) Revealed by Two-Dimensional Infrared Spectroscopy

## Contents

---

This chapter was adapted from: *Journal of Physical Chemistry B.* **2017**, *121*, 1352-1361. It was prepared in collaboration with R. Knepper, A. S. Tappan, J. J. Kay, M. T. Zanni, and D.A. Farrow.[10]

## 5.1 Introduction

Understanding the response of explosive materials to external stimuli, such as shock and impact, requires a detailed understanding of vibrational energy transfer dynamics.[132] For example, pentaerythritol tetranitrate (PETN) and erythritol tetranitrate (ETN) are two energetic materials that are chemically similar with four NO2 groups responsible for their explosive properties. Because of different structures and packing, the two have different impact sensitivities.[133] Crystal structures of ETN reveal destabilizing intermolecular hydrogen bonds,[133] while PETN is known to show many stabilizing inter- and intramolecular interactions, including a weak hydrogen bond of $NO_2$with the $CH_2$on adjacent PETN molecules.[134] It has been suggested that the disruption of hydrogen bonding networks during shock deformation may precede initiation of other energetics with similar hydrogen bonding interactions.[135,136] Depending on the geometry, hydrogen bonding and intermolecular interactions may mechanically stabilize materials.[137] Since $NO_2$ loss is an important step in the shock initiation of PETN,[138] the rate of energy transfer in the presence and absence of these weak intermolecular bonds is of interest to the greater explosive community. For all of these reasons, it is important to understand the nature of these interactions in explosive materials.

Hydrogen bonding may shift impact sensitivity by changing the rate of mechanical energy transfer from the shock front to vibrational degrees of freedom coupled to reaction.[139] Hong et al. reported the first measurements of energy transfer in an explosive (nitromethane).[140] In one experiment, small amounts of methanol (MeOH) were added to solutions of nitromethane. An IR pump was used to excite MeOH (OH stretch) and the energy transfer into nitromethane was monitored by Anti-Stokes Raman scattering. Using isotopic substitution, measurements revealed (OH)MeOH → (C–H)MeOH → (C–H bend) MeOH → ($NO_2$ )NM to be the dominant pathway and C–H bending modes as efficient donors of vibrational energy to nitro stretching vibrations. Subsequent IR pump-probe measurements of explosives (TNAZ, RDX, HMX, and CL-20) dissolved in deuterated acetone or ethanol appear to rule out intermolecular coupling to the solvent.[141] The authors observed a sub-ps decay in parallel pump–probe experiments, but not in the magic angle measurements. The sub-ps decay of dipole orientation can only be explained by vibrational energy transfer or fast wobbling motions of the $NO_2$ groups (i.e., the orientational diffusion was much slower than experimental measurements of similar molecules). However, a weak correlation between sample temperature and decay rate was used to rule out intermolecular energy transfer to the vibrational modes of the solvent.[141] Two-dimensional infrared (2D IR) spectroscopy measurements on polycrystalline and solvated PETN can provide new information that both corroborate and clarify aspects of these early experiments.

2D IR is a nonlinear vibrational spectroscopy that is analogous to a pump-probe experiment with the frequencies of the pump pulse resolved. The theory behind 2D IR spectroscopy has been described in detail previously.[5,6,32,142] Compared to conventional linear FTIR spectroscopy, 2D IR provides more experimental observables by spreading the vibrational spectrum across two frequency axes. This provides additional insight into vibrational coupling and energy transfer that are revealed through the off-diagonal cross peaks.[5,6,143]Additionally, the two-dimensional shape of the diagonal peaks in a 2D IR spectrum report on the time scale of structural dynamics and solvation[5] and the shape of the cross peaks yields information on vibrational frequency correlations.[142,144] All of these spectroscopic observables report on molecular structure and dynamics that are of particular interest to explosives chemists.

Complementing other methods of probing vibrational energy transfer,[145,146] the cross peaks in a 2D IR spectrum provide a direct probe of vibrational coupling and energy transfer between IR active modes. Cross peaks present with temporally overlapped pump and probe pulses are indicative of vibrational coupling and their frequencies, along with the vibrational anharmonicities, can be related to the three-dimensional structure of a molecule.[114] Additionally, the time-dependence of these cross peaks has been used to observe intramolecular vibrational energy redistribution (IVR) in small molecules[147–150] and energy transfer in peptides.[111] Recently, there has been considerable effort to study intramolecular energy transfer using dual-frequency 2D IR.[112,143,151,152] Additionally, recent work by Chen et al. has used 2D IR to observe resonant and nonresonant energy transfer in crystals.[153,154] Considering the proposed importance of phonon energy transfer in energetic materials,[155,156] 2D IR is especially well-suited to bring insight into the molecular structure and vibrational dynamics that may impact explosive design.

In this article, we use, for the first time, femtosecond 2D IR spectroscopy to study couplings and energy transfer through the vibrational dynamics of vapor-deposited PETN. We probe the asymmetric stretch of the nitrate ester groups. Additionally, we measure 2D IR spectra of PETN in acetone to determine how the absence of intermolecular interactions influences the observed spectral dynamics.

## 5.2 Methods

### 5.2.1 2D IR Spectroscopy

The details for the 2D IR setup have been described previously.[131] Briefly, the 4.0 W output of a 100 fs regenerative amplifier (Spectra Physics, Solstice) is used to pump a commercial optical parametric amplifier (OPA, Light Conversion, TOPAS). Signal and idler pulses are then used to pump a home-built, collinear difference frequency generation (DFG) module. The 25 $\mu$J mid-IR pulses are centered at 1620 cm$^{-1}$ and ∼100 fs in duration. A wedged calcium fluoride beam splitter is used to split off about 5% of the light to be used as the probe pulse. The remaining 95% is used to generate the two pump pulses. Pump pulse pairs are created using a fully reflective germanium acousto-optic modulator (AOM) pulse shaper in the 4f geometry, described in detail previously.[131] The Ge-AOM uses acoustic waves to shape the light in the frequency domain to generate a pulse-pair with computer-controlled time delays and absolute phase control. The pulse shaper is also used to compress the pulses in time by optimizing the second-harmonic signal from the mid-IR output with an $AgGaS_2$crystal. A four frame phase-cycling scheme is used to subtract the background and suppress pump scatter[120] and the data are processed as in equation 5.1:

$$S_{2DIR}(t_1, t_2, t_3) = \log \frac{S_1 + S_4 + S_6 + S_7}{S_2 + S_3 + S_5 + S_8} \tag{5.1}$$

where $S_{2DIR}$ is the 2D IR signal, and $\phi_i$ indicates the phase of the $i$th laser pulse. Pump and probe beams are overlapped spatially and focused on to the sample using parabolic mirrors. Timing between the pump and probe pulses, called the waiting time ($t_2$), is controlled by a motorized stage (Newport). The probe pulse is dispersed in a spectrograph and measured with a 64 element mercury–cadmium-telluride (MCT) array (Infrared Associates).

### 5.2.2 Theoretical Modeling and Calculations

To calculate the couplings between discrete nitrate ester groups, a transition dipole coupling (TDC) model is employed that treats each chromophore as a point dipole. A similar method is employed in interpreting the spectra of peptides and proteins.[5,15,23] In this model, the coupling constant, $\beta_{ij}$ between local modes $i$ and $j$ is calculated according to equation 5.2:

$$\beta_{ij} = \frac{1}{4\pi\epsilon_0}\Big[\frac{\vec{\mu_i} \cdot \vec{\mu_j}}{r_{ij}^3} - 3\frac{(\vec{\mu_i} \cdot \vec{r_{ij}}) \times (\vec{\mu_j} \cdot \vec{r_{ij}})}{r_{ij}^5}\Big] \tag{5.2}$$

Where $\mu_i$ is the transition dipole moment for chromophore $i$ and $r_{ij}$ is the distance vector between chromophores $i$ and $j$. DFT calculations were performed on an isolated PETN molecule using the B3LYP functional and a 6-31G(d,p) basis set in Gaussian '09.[157] The local mode transition dipoles from the DFT results were used for TDC calculations.[158] The transition dipole vectors are assumed to be the same for all nitrate ester groups and have the same direction relative to the N–O bond axis as determined from the DFT calculations. The crystal structure of PETN was used to calculate the vibrational coupling constants between each nitrate ester group in the crystal. From this, the one-exciton Hamiltonian is diagonalized to generate the normal-mode frequencies and eigenvectors,[5] which were then used to simulate the linear FTIR spectrum.

### 5.2.3 Thin Film Preparation

Thin films of PETN used for both linear FTIR and 2D IR measurements were deposited by vacuum thermal evaporation in a custom deposition system.[159] PETN powder was loaded into an effusion cell deposition source and the chamber was evacuated to a base pressure of $\sim 10^{-6}$ Torr. The effusion cell deposition source was heated to a temperature of $\sim 130$ °C. PETN evaporated from the effusion cell and deposited as a thin film on $CaF_2$ substrates held in a cooled assembly. This substrate holder was rotated for uniformity. PETN thickness was measured using a surface profiler (Dektak XT) and determined to be $\sim 1$ $\mu$m thick.

## 5.3 Results

### 5.3.1 FTIR Spectrum of Solution and Thin-film PETN

The linear FTIR spectrum of PETN in the vapor-deposited film and acetone is shown in Figure 5.1. In acetone, there are two peaks; one is at 1660 cm$^{-1}$ and the other at 1685 cm$^{-1}$. The PETN film vapor-deposited on calcium fluoride exhibits a broad, red-shifted peak at 1645 cm$^{-1}$. The PETN film contains a much broader peak than in solution. This change in line shape could mean that there are more vibrational modes, the homogeneous lifetime is shorter, or that there is an inhomogeneous distribution of frequencies in the film. Additionally, changes in intermolecular coupling can alter absorption line shapes by splitting peaks and altering intensities.[3]

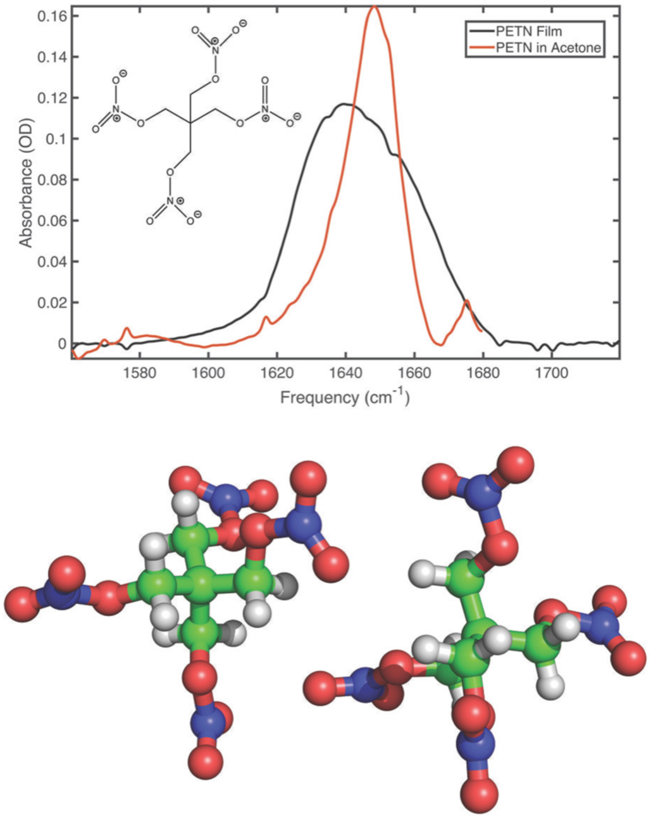

Figure 5.1: (a) FTIR of PETN in acetone (red) and a thin film of vapor-deposited PETN (black). For the acetone measurement, data above 1680 cm$^{-1}$ is omitted due to background absorption from the carbonyl absorption of acetone. The inset shows the molecular structure of PETN. (b) Structure of two PETN molecules taken from the crystal structure previously published for the film.

### 5.3.2 Comparison of Anisotropy Decay

In addition to the time delays and phases of the pump and probe pulses, the polarization of the electric fields can also be controlled to provide more information about the molecular response. The strongest signal in 2D IR spectroscopy is yielded when the pulses are polarized parallel to one another, often represented as $\langle \text{XXXX} \rangle$. Although this polarization condition returns the strongest third-order signal, its decay as a function of the waiting time contains contributions from both population and orientational relaxation. These separate relaxation mechanisms can be disentangled by measuring the 2D IR signal when the pump fields, $E_1$ and $E_2$, are polarized orthogonally to $E_3$ and $E_{Lo}$, indicated by $\langle \text{XXYY} \rangle$. Using equation 5.3:

$$r(t) = \frac{S_{XXXX} - S_{XXYY}}{S_{XXXX} + 2S_{XXYY}} \tag{5.3}$$

the anisotropy, *r(t)*, can be recorded as a function of the waiting time. This quantity is proportional to $0.4$*C(t)* where *C(t)* is the normalized orientational correlation function.[5,160,161] For a perfectly isotropic sample, the anisotropy will have an initial value of 0.4 and decay to zero at infinitely long delay times. Population relaxation can be measured by measuring the response when the pump pulses are polarized at the so-called magic angle relative to the probe pulse.[160] The decay of the anisotropy can come from two possible mechanisms: (1) The transition dipoles lose correlation due to rotation (this typically occurs on the order of 5–10 ps for small molecules[5]). (2) Energy transfer or an excitation localization that leads to a change in transition dipole orientation. The latter can occur on subpicosecond time scales, as observed in recent experiments on ions in water.[148,162]

Figure 5.2 shows the anisotropy decay for the thin film averaged over the 2D IR spectrum of PETN compared to that of PETN in acetone for the most intense nitrate ester transition. This corresponds to 1660 $\text{cm}^{-1}$ for PETN in acetone and 1645 $\text{cm}^{-1}$ for the thin film. The decay of the solution anisotropy is well fit by a single exponential decay with a time constant of 3.7 ± 0.81 ps. In contrast, the anisotropy of the thin film of PETN exhibits a much different decay. This data is better fit by an exponential with a decay of 0.41 ± 0.081 ps. Additionally, the film anisotropy decay has a significant offset at longer waiting times. That is, the anisotropy does not decay to zero in the time frame of the experiment.

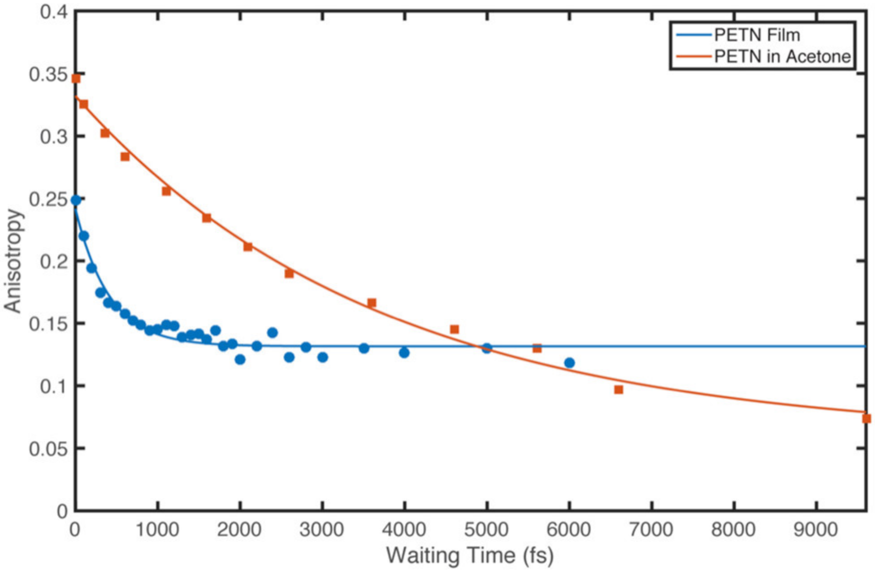

Figure 5.2: Comparison of the anisotropy decays of PETN in a thin film (blue circles) and in acetone (red squares). Solid lines are the exponential fits to the data

### 5.3.3 Comparison of Solution and Solid-State 2D IR Spectra

Figure 5.3 shows the 2D IR spectra of the asymmetric stretching modes of PETN in the thin film and in solution. Conceptually, 2D IR tags vibrational frequencies with two pump fields ($E_1$ and $E_2$) and monitors the evolution of the oscillators with a probe pulse ($E_3$). The signal is measured in a spectrograph and heterodyned with a fourth reference pulse called the local oscillator ($E_{Lo}$). In some implementations of 2D IR, including the work presented here, data are collected in the pump–probe geometry so that $E_3$ also serves as $E_{Lo}$. The evolution of a 2D IR spectrum as a function of the time delay between $E_2$ and $E_3$, called the waiting time or $t_2$ in this work, reports on the molecular dynamics of the sample. A typical 2D IR spectrum consists of a pair of peaks, a positive diagonal feature, arising from the ground state bleach and stimulated emission of the $\mu = 0$ to $\mu = 1$ transition (where $\mu$ denotes the vibrational quantum number), and a negative peak anharmonically shifted off the diagonal that arises from the excited state absorption of the $\mu = 1$ to $\mu = 2$ transition. Comparing the 2D IR spectra of PETN dissolved in acetone (Figure 5.3a,b) and vapor-deposited PETN (Figure 5.3c,d) reveals several features hidden beneath the broad and convoluted FTIR. We label the two diagonal peaks in acetone $A_1$ and $A_2$. Although only one peak is verifiable in the FTIR of the film, the 2D IR spectra reveal that there are indeed two peaks, labeled $B_1$ and $B_2$ in Figure 5.3. Additionally, the waiting time dependence of the spectra clearly reveals an off-diagonal cross peak (labeled $B_{12}$) between the $B_1$ and $B_2$ modes. This is further confirmation that there is more than one transition in the film.

### 5.3.4 Transition Dipole Measurements

We also measured the transition dipole strength, $\mu^2$, of the PETN film at 1640 $\mathrm{cm}^{-1}$ through a comparison of the 1D and 2D IR spectra following previously reported methods.[12,163] The transition dipole strength cannot be determined in the crystalline film using standard FTIR methods because the film thickness (and hence the concentration) cannot be known with enough accuracy. To measure $\mu^2$, we need the terms in the following equation:

$$|\mu|^2 = \frac{\frac{\Delta OD_{Sample}}{OD_{Sample}}}{\frac{\Delta OD_{Calibrant}}{OD_{Calibrant}}} \times |\mu_{Calibrant}|^2 \tag{5.4}$$

where $\Delta$OD is the 2D IR signal, OD is the optical density as determined from the laser spectrum, and ${\mu_{Calibrant}}^2$ is the transition dipole squared of the calibrant molecule. Each of these terms were measured, with the ${\mu_{Calibrant}}^2$ taken from the literature,[163] and the values are given in Table 5.1. Note that the data differs slightly from Figure 5.1 because the linear optical density must be measured with the laser and MCT array and, therefore, the data is from a slightly different spot on the sample. We used l-serine as a calibrant molecule because it has a maximum absorbance near the PETN peak. Using this procedure, we measured the transition dipole strength to be 3.1 $D^2$.

Table 5.1: Measured Transition Dipole Strength of PETN

| Molecule | OD | $\Delta$OD | $\mu^2$ ($D^2$) |
|---|---|---|---|
| L-serine (calibrant) | 0.64 | 0.06 | 0.2 |
| PETN | 0.09 | 0.13 | 3.1 ± 0.1 |

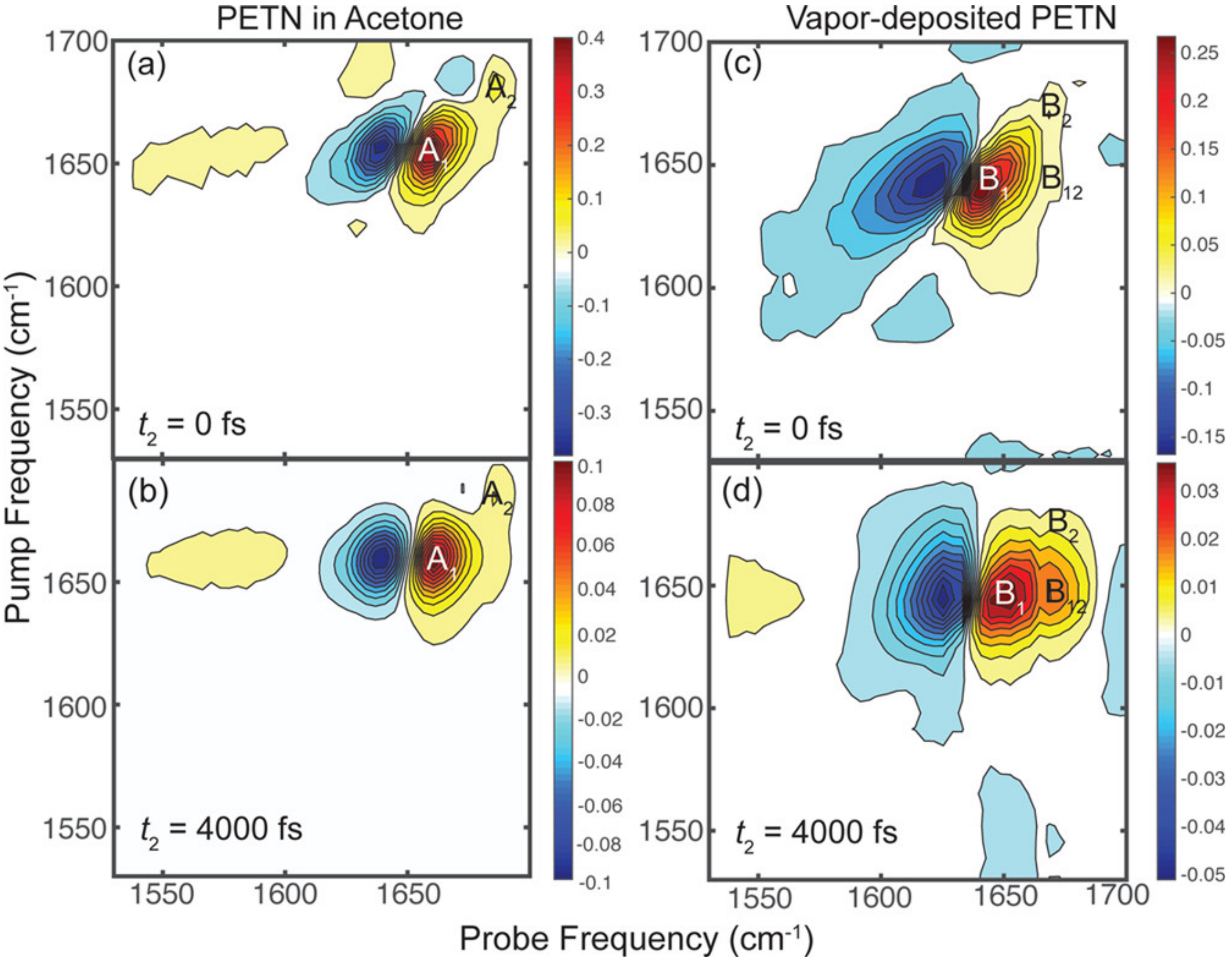

Figure 5.3: Waiting time dependence of the 2D IR spectra of PETN. (a) 2D IR spectrum of PETN in acetone at $t_2 = 0$ fs. (b) 2D IR spectrum of PETN in acetone at $t_2 = 4000$ fs. (c) 2D IR spectrum of vapor-deposited PETN at $t_2 = 0$ fs. (d) 2D IR spectrum of vapor-deposited PETN at $t_2 = 4000$ fs. Letters in the figure label the peaks described in the main text. $A_1$ and $A_2$ are the diagonal peaks of the nitrate ester asymmetric stretch in acetone. $B_1$ and $B_2$ label the diagonal peaks of the nitrate ester asymmetric stretch in vapor-deposited PETN. $B_{12}$ is the cross peak between the low and high frequency transitions observed in the thin-film.

### 5.3.5 Energy Transfer Rates

Additionally, the cross peak ($B_{12}$) grows in relative to the diagonal peaks as a function of the waiting time. This could be evidence for chemical exchange or energy transfer. Since there are no known dynamic conformational changes, the most likely candidates for chemical exchange,[164] we assign this cross peak to energy transfer between coupled modes in vapor-deposited PETN. This means that the time-dependence of this cross peak will reveal the rate of energy transfer between the two transitions. Figure 5.4 shows the cross peak growth for both the $\langle XXXX \rangle$ and $\langle XXYY \rangle$ polarization conditions. We find that the cross peak growth, and therefore the energy transfer rates, can be fit to single exponentials with time constants of 1.9 ± 0.31 ps and 2.4 ± 0.49 ps for the $\langle XXXX \rangle$ and $\langle XXYY \rangle$ polarizations, respectively. Taking the approach of Ghosh et al.,[111] we extract an energy transfer rate of about $1/2.4\ \mathrm{ps}^{-1}$.

### 5.3.6 Frequency Dependent Anisotropy Observed in the Thin Film

The polarization selective 2D IR spectra can also be used to examine the frequency dependence of the anisotropy decay. Figure 5.5a shows the 2D anisotropy plot of PETN in acetone and Figure 5.5b shows the 2D anisotropy of vapor-deposited PETN at $t_2 = 100$ fs. Since the anisotropy diverges with weak signal, pixels in frequency space are removed if they have <10% of the maximum value for a given waiting time. The sensitivity of anisotropy to noise at low signal levels causes the spurious negative features along the diagonal in the thin film. The PETN in acetone shows an essentially homogeneous anisotropy within the vibrational line shape of the ground state bleach and excited state absorption. In contrast, the vapor-deposited film exhibits a much more complex structure in the 2D anisotropy. The cross peak has a negative anisotropy of -0.18, which predicts that the two coupled transition dipoles will have a relative angle of 80° in the exciton basis. Additionally, the film shows an increasing anisotropy with decreasing frequency in the excited state absorption. This is labeled A in

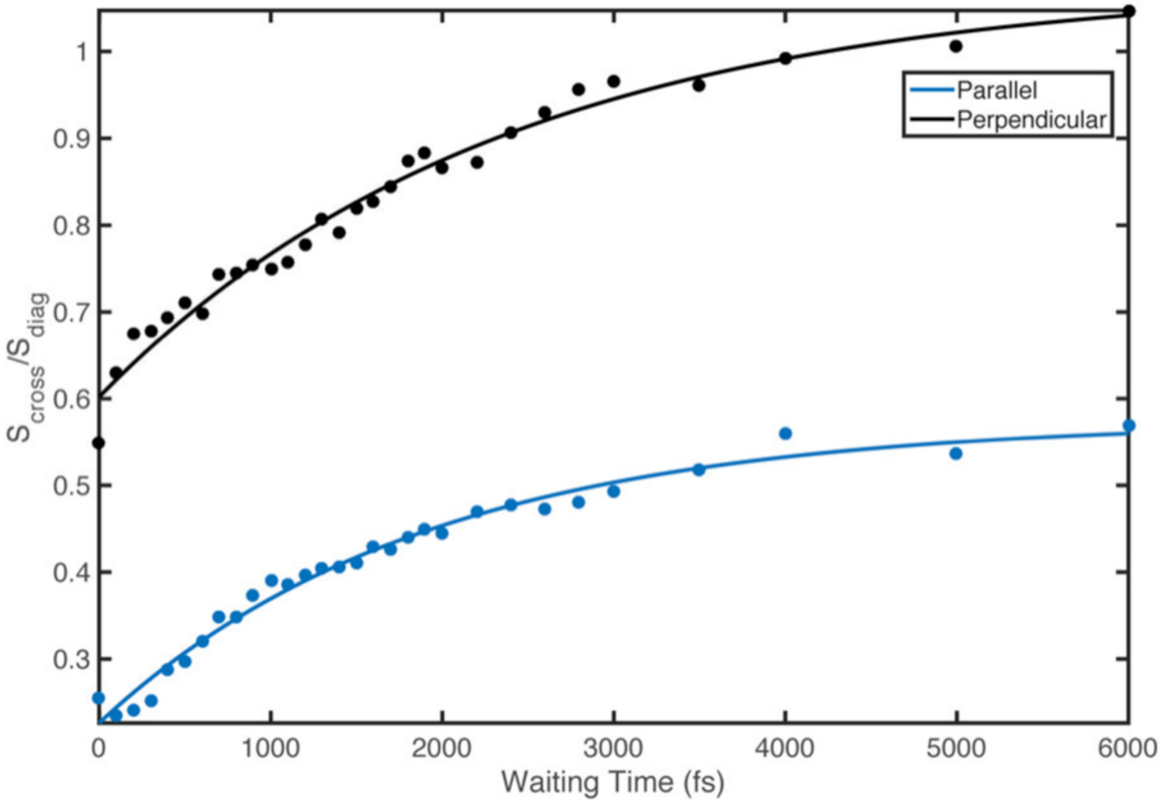

Figure 5.4: Time-dependent growth of the cross peak labeled $B_{12}$ in Figure 5.3 normalized to the intensity of the most intense diagonal peak. Black circles show data collected in the perpendicular polarization ($\langle$XXYY$\rangle$) condition and blue circles show data collected under the parallel ($\langle$XXXX$\rangle$) polarization condition. Solid lines show exponential fits to the data which yields time constants of 1.9 and 2.4 ps for the $\langle$XXXX$\rangle$ and $\langle$XXYY$\rangle$ polarizations, respectively.

Figure 5.5b. Frequency dependent anisotropy dynamics have been previously observed in 2D IR spectroscopic studies on hydrogen bond rearrangements in water.[165] In this work, the heterogeneous dynamics were revealed at later waiting times, which is qualitatively different from what we observe here. That is, the initial value of the anisotropy is drastically different across the absorption band at early waiting times.

## 5.4 Discussion and Simulations

### 5.4.1 FTIR Peak Assignments

The spectral region presented here probes the asymmetric stretch of the nitrate ester groups. DFT calculations of PETN with $S_4$ symmetry have proposed that all four vibrational modes are essentially the same frequency,[166] and so only one peak would be observed in this experiment. However, PETN is known to exhibit conformational flexibility in solution, and this is the likely origin of the second peak in acetone.

### 5.4.2 Assignment of Decays Observed in 1D Anisotropy

Previous theoretical treatments of PETN crystals have noted the relationship between explosive impact sensitivity and vibrational energy transfer.[167] The energy transfer kinetics will present themselves in the time-dependent anisotropy in an ultrafast IR experiment because, in general, an energy transfer event will lead to a randomization of the transition dipole orientation. The decay of 3.7 ps in acetone could possibly arise from either rotational relaxation or from intramolecular energy transfer. This time scale is faster than is conventionally expected for rotational relaxation. However, since the molecule has four vibrational chromophores, oriented at various angles with respect to each other, it is likely that rapid intramolecular vibrational energy transfer leads to the decay. For the thin film, the rapid anisotropy decay could come from fluctuations of the $NO_2$ groups[168–170] or rapid

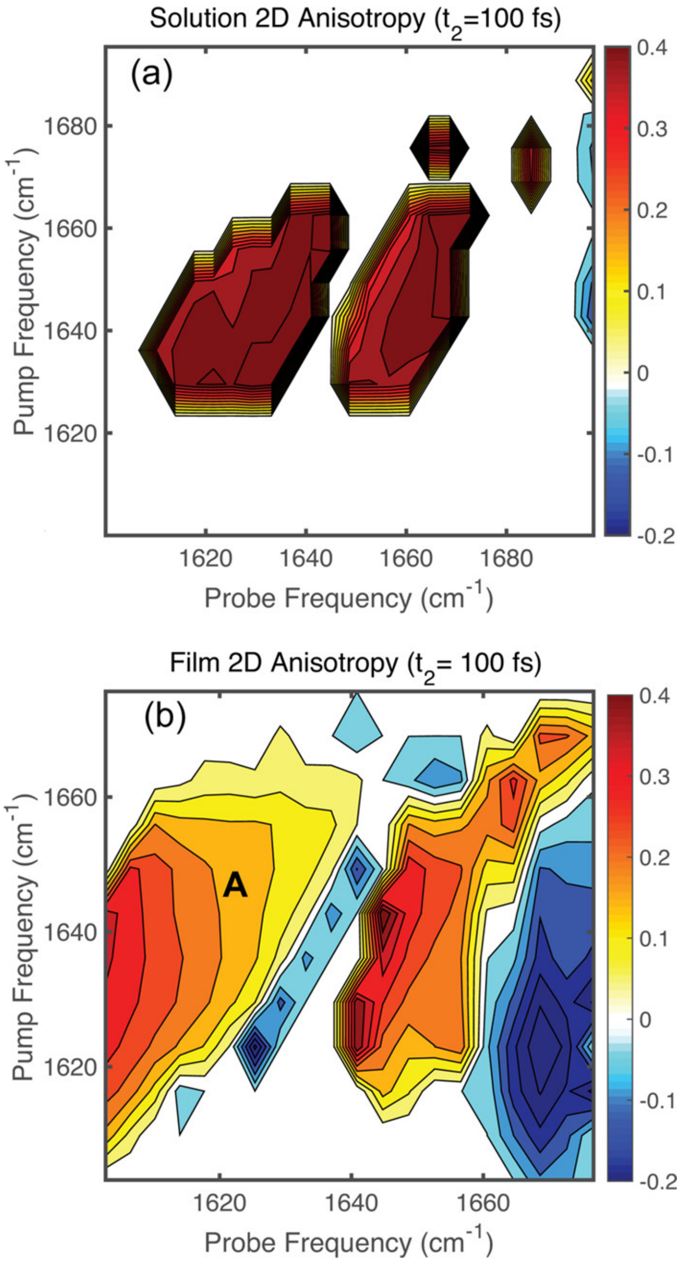

Figure 5.5: Frequency resolved two-dimensional anisotropy plots. (a) 2D anisotropy of PETN dissolved in acetone at $t_2$ = 100 fs. (b) 2D anisotropy of the vapor-deposited PETN at $t_2$ = 100 fs. Data points with less than 10% of the maximum signal for a given spectra are omitted for clarity. The negative anisotropy values in the film 2D anisotropy are from the cross peak and give a relative orientation of transition dipoles of ∼80°. The label A shows the excited state absorption feature which exhibits spectrally heterogeneous anisotropy.

energy transfer.[171,172] Because the fast component is absent in solution, we attribute the decay in the thin film to rapid energy transfer that is only made possible by intermolecular vibrational coupling in the film. One may expect the anisotropy decay to be slower in a solid compared to molecules in a solution, due to rigid local structure. We make a point that our results indicate otherwise. In the solid, new channels of energy transfer, namely between adjacent molecules, become available and can lead to faster anisotropy decay than in solution. To further elucidate the energy transfer pathways in the thin-film, we turn to frequency-resolved 2D IR measurements.

### 5.4.3 Assignment of Observed Features in the 2D Spectrum

It is also important to note that we have measured 2D IR spectra on different spots on the sample. We observe minor differences in the 2D spectrum; mainly changes in the relative peak intensities of the two diagonal modes and different cross peak intensities. Additionally, the initial anisotropy values vary significantly, sometimes above 0.4, the maximum value for an isotropically oriented sample. The only way that this value can be obtained is if the sample has some residual orientation on the order of the beam diameter at the focus (∼100 $\mu$m in this experiment). Despite the differences in the initial anisotropy values, we observe very similar anisotropy dynamics for every spot (300–500 fs) and therefore conclude that the decay of the anisotropy can be used to determine the molecular basis that leads to this ultrafast decay.

### 5.4.4 Discussion of Cross Peak Dynamics

The difference between the cross peak dynamics (∼2 ps) and anisotropy decay (∼400 fs) leads to the conclusion that there are many different energy transfer pathways in the thin film. The anisotropy decays are fast enough that any meaningful dynamics likely occurs within the time resolution of the experiment while the cross peak growth is on the order of 2 ps. By examining the frequency dependence of the anisotropy decay, we hope to gain further insight into the energy transfer pathways that occur on the 400 fs time scale. By inspection of Figure 5.5, it is clear that the film exhibits a dramatic frequency dependence for the initial value of the anisotropy in the excited state absorption. Even in other scans with the different initial values of *r(t)*, presumably because of macroscopic orientation, this structure is still reproduced in the 2D anisotropy. In this system, we interpret the frequency dependent anisotropy as additional evidence for downhill energy transfer to low frequency phonon modes. The initial anisotropy varies from ∼0.4 at low frequencies to 0.1 at higher frequencies. We take this to indicate that the rate of energy transfer is strongly dependent on the vibrational frequency. Despite the clear frequency dependence in the ESA feature, there does not appear to be any meaningful structure in ground state bleach. Since the excited state absorption feature arises from high energy vibrational excitations of the $1 \rightarrow 2$ transition, we attribute this lack of structure in the 2D anisotropy of the bleach to smaller coupling between the acceptor modes of the $0 \rightarrow 1$ transition. Since the ESA features arise from much higher energy excitations, there are many more intramolecular and phonon modes that can accept the energy deposited by the laser pulse.

### 5.4.5 DFT and Transition Dipole Calculations

To gain further insight into the molecular origin of the intermolecular interactions that lead to energy transfer, we model the vibrational modes of the crystal using DFT electronic structure calculations and a transition dipole coupling (TDC) model as outlined in the Methods Section. DFT calculations of the PETN monomer were used to determine the local mode transition dipole direction and magnitude (see Methods Section and Supporting Information). The local mode properties were then assigned to each nitrate ester group in a crystal of 128 PETN molecules replicated from the known structure of the unit cell. Using the TDC model, the dipole coupling elements between all combinations of the 512 nitrate ester groups in the crystal were calculated. These couplings generate the local mode Hamiltonian. Diagonalization of this matrix leads to the normal modes and the linear FTIR spectra in the one-exciton basis. To simulate the spectra, each normal mode is convoluted with an empirical 10 $\mathrm{cm}^{-1}$ Gaussian function to simulate the disorder and homogeneous lifetime of the film.

The local mode Hamiltonian, generated from the TDC model, contains many couplings of less than 2 $\mathrm{cm}^{-1}$. The magnitude of the couplings are about the same, whether the interactions are between nitrate esters on the same molecule (intramolecular) or between nitrate esters on neighboring molecules (intermolecular). Although the majority of the couplings are small, there are notable interactions that exhibit much larger vibrational coupling constants. The relative orientation of two PETN molecules, taken from the crystal structure, is shown in Figure 5.1. In this structure, the largest coupling constant is -4.60 $\mathrm{cm}^{-1}$ and occurs between nitrate ester groups on different molecules. Intermolecular couplings will cause the nitrate esters on different molecules to share a common eigenstate if the coupling strengths are larger than the disorder of the local mode frequencies. Shared common eigenstates will create vibrational modes that are delocalized throughout the crystal.

In Figure 5.6a, we show the simulated FTIR spectrum of the 128-molecule crystal in red and the experimental FTIR spectrum in blue. The individual normal modes, shown in Figure 5.6a as the green sticks, are binned in 1 $\mathrm{cm}^{-1}$ increments and the intensity of each eigenstate is given by $\mu^2$, where $\mu$ is the transition dipole of the mode. In Figure 5.6b we also plot the green stick spectrum with each eigenstate given by $\mu^4$ to approximate a simulated 2D IR diagonal slice (more sophisticated methods are computationally difficult for the size of the system required to reproduce the frequency splitting observed in the experiment). The resulting simulated 2D diagonal slice is shown in red and the experimental data is shown in blue. The simulated FTIR spectrum gives a broad distribution of eigenstates, which is in reasonable agreement with experiment (blue). The distribution of eigenstates for the

2D IR slice is dominated by a few intense modes because of the $\mu^4$ scaling of the 2D IR signal. In the low frequency region, the eigenstate at 1640 cm$^{-1}$ has the strongest transition dipole and creates a narrowed spectrum compared to the FTIR, which is consistent with the experiment. The eigenstate at 1661 cm$^{-1}$ has an even stronger transition dipole and leads to a distinct peak in the 2D IR spectrum. We also calculated the relative angles between the two most prominent excitonic transition dipoles, located at 1640 and 1661 cm$^{-1}$, which was 83°. Experimentally, the cross peak anisotropy was measured to be -0.18, which corresponds to a relative angle of 80 ± 10°. Thus, while the TDC model has limitations, we conclude that the computed eigenstates are representative of the features of the spectra since they give frequencies, intensities, and anisotropies that are in reasonable agreement with experiment. We note that this agreement only occurs for calculations including the full crystal; the dimer calculation alone predicts a splitting 50% smaller than is observed experimentally.

With reasonable agreement between simulation and experiment, we investigate the motion in the crystal from the corresponding eigenvectors. Figure 5.7a shows the structure of the simulated 3D crystal. From this angle, it is clear that the crystal consists of chains of nitrate esters with alternating orientations. Figure 5.7b illustrates this arrangement for one chain of nitrate esters, onto which we also plot the local mode transition dipole vector with some of the carbon skeletons omitted for clarity. The magnitude and sign of the eigenvectors of the one-exciton Hamiltonian determine the contribution of each local mode to the total vibrational motion. Mathematically, this is written as:

$$\vec{\mu_{ex}^{i}} = \sum_{k}^{N} c_k^i \vec{\mu_k} \tag{5.5}$$

where ${\mu_{ex}}^i$ is the $i$th excitonic mode transition dipole, ${\mu_k}^i$ is the transition dipole of the $k$th local mode, and ${c_k}^i$ is the eigenvector coefficient for the given normal mode. The intensity of each IR transition is given by $({\mu_{ex}}^i)^2$. Figure 5.7c,d plots the contributions of each ${c_k}^i{\mu_k}^i$ to the 1632 cm$^{-1}$ mode and the 1661 cm$^{-1}$, respectively, projected on to the x,

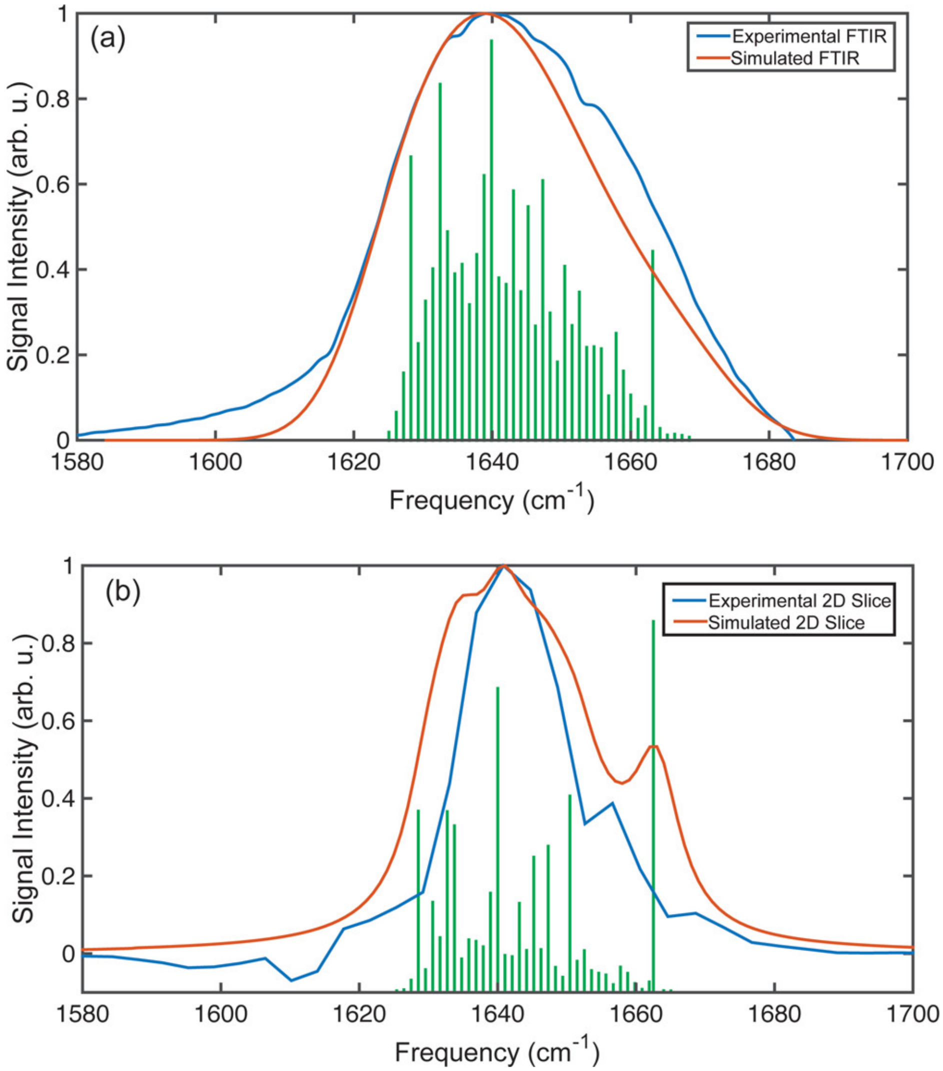

Figure 5.6: Comparison of experimental data to the simulated spectra from the TDC model. (a) Simulated FTIR spectrum of crystalline PETN (red) and experimental FTIR spectrum (blue). The green lines in (a) show the stick spectrum from the excitonic Hamiltonian. The height of each stick is proportional to the transition dipole squared. (b) Simulated 2D IR diagonal slice of vapor-deposited PETN (red) and the experimental diagonal slice of the 2D IR spectrum (blue). The green lines in (b) show the stick spectrum with the height proportional to the transition dipole to the fourth power. Each normal mode is binned together in 1 cm$^{-1}$ increments so that the height of each stick is proportional to the number of modes at that frequency and the indicated transition dipole scaling.

y, and z axes of the crystal. The x and y components of $c_k{}^i \mu_k{}^i$ for the 1632 cm$^{-1}$ mode are in phase along the chain, while the z components are out of phase. This means that there is no contribution along the z-axis to the transition dipole for this particular chain. In contrast, the 1661 cm−1 mode shows that the x and y components are out phase, while the z components are in phase. Thus, these two particular eigenstates look similar to the one-dimensional linear chain of coupled oscillators.[5,173] A similar analysis of the most intense mode at 1640 cm$^{-1}$ yields more complex motion, as expected for a mode not at either extreme in an excitonic dispersion relation.

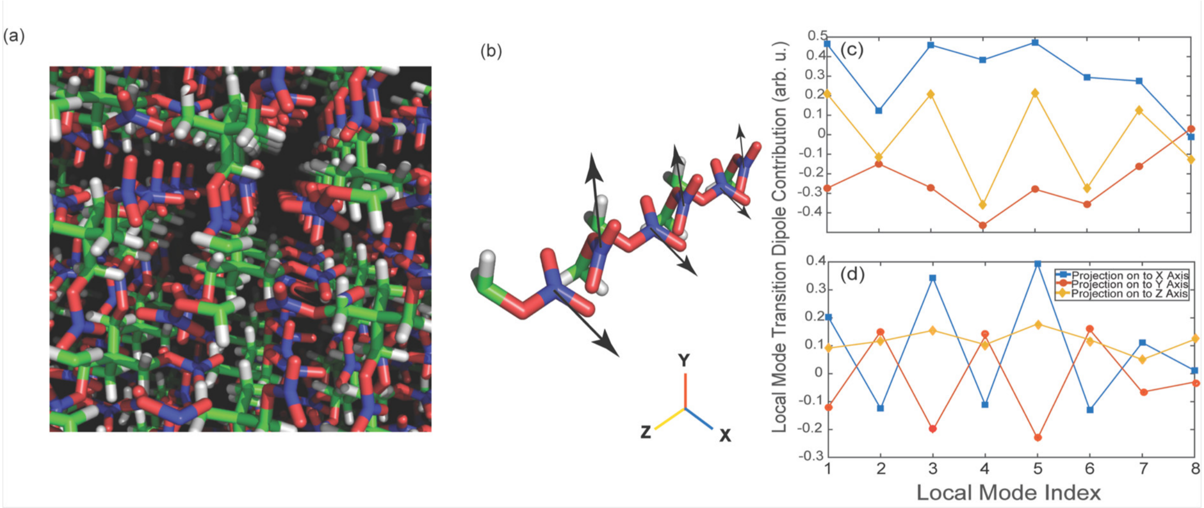

Figure 5.7: Visualization of the eigenvectors from the TDC simulation. (a) Structure of the simulated PETN crystal. Carbon: green; oxygen: red; nitrogen: blue; and hydrogen: white. (b) Select nitrate ester groups and the corresponding local mode transition dipole vectors. (c) Contributions of select local modes to a normal mode at 1632 cm$^{-1}$. Blue squares are the projection on to the x-axis, red circles are the projection on to the y-axis, and yellow diamonds are the projection on to the z-axis. The solid lines are guides to the eye. (d) Contributions of the same local modes in (c) to the normal mode at 1661 cm$^{-1}$. The same legend applies as in (b). The axes on to which projections are plotted are shown in (b).

The TDC modeling above does not include disorder of the local mode frequencies in the Hamiltonian. As a result, the excitonic modes will extend over all of the molecules in the box. Thus, the TDC simulation above provides an understanding of the origin of the coherent vibrations, but not an estimate of the inverse participation ratio (IPR), which is a measure of how many vibrational modes (i.e., molecules) are coherently coupled.[13] One can estimate the IPR by adding environmental and structural disorder to the TDC model[76] or by modeling dephasing rates,[174] each of which relies on complicated modeling procedures and assumptions (for example, adding structural disorder is usually done with fixed distributions of diagonal disorder without taking into account dynamical line narrowing effects).[175] Instead, we take an experimental approach and measure the transition dipole strength of the PETN modes by comparing 1D and 2D IR spectra. Of course, the measurement has its own uncertainties, but we have established that, to a first approximation, it gives a lower bound to the inverse participation ratio, because the measured transition dipole represents a sum of vector quantities.[12,163] This method utilizes the fact that 1D and heterodyne 2D IR spectra depend on the transition dipole strength to the $\mu^2$ and $\mu^4$ powers, respectively, but both scale linearly with concentration. Thus, for a sample like this film in which we cannot determine the concentration, we can still measure the transition dipole strength by comparing their relative intensities using a calibrant molecule.(46) We measured $\mu^2 = 3.1 \pm 0.1$ D$^2$ at 1640 cm$^{-1}$ for the thin film of PETN. We estimate from our work and the reported molar absorptivity of nitro stretches[176] that a single nitrate ester has an absorptivity of 0.1 to 0.2 D$^2$. Thus, the transition dipole strength measured in the PETN crystal is between 15 and 30 times larger than one would expect for a single nitrate ester. That means, that the vibrational modes in PETN are delocalized over at least 15–30 local modes in the crystal. The coupling strength between nitrate esters on adjacent PETN molecules is about twice as large as between nitrate esters on the same PETN molecule, indicating that those 15–30 nitrate esters mostly extend across molecules. It also includes thermal effects, since it is derived from experimental data. As a point of comparison, we note that this transition dipole method was applied to peptide amyloid fibers to discover that amide vibrations were delocalized over 12 amino acids encompassing multiple proteins, consistent with previous simulations that had calculated inverse participation ratios of 12 to 24 amino acids depending on the size of the fiber.[13,163] The peptide system will almost certainly have more disorder than a crystal and has comparable coupling strengths, so our conclusion appears to be intuitively correct.

The physical origin of the vibrational modes has implications for energy transfer in PETN and related materials. We learn that vibrational energy is delocalized over many PETN molecules, all vibrating in unison. The growth of the cross peak in the experimental 2D IR spectrum corresponds to energy transfer between these two coherent vibrational modes. The eigenvectors are collective phonon motions. We do not want to imply that these delocalized, high frequency vibrations are limited to only explosive materials. Instead, we hypothesize delocalized vibrations may be important in shock initiation and impact sensitivity, as they could provide a pathway for efficient energy propagation. Future theory and experiments can compare the nature of intermolecular coupling in other explosive materials to determine if there is a correlation between the bulk properties and the vibrational structure.

## 5.5 Conclusion

In summary, we have collected the first 2D IR spectrum of explosive molecules in the solid-state. 2D IR spectroscopy reveals mode splitting and coupling not easily revealed in the FTIR spectrum because of heterogeneity and line broadening. Additionally, the femtosecond time resolution of the 2D experiment helps to reveal intermolecular energy transfer on the sub-500 fs time scale. The 2D IR spectra reveal one important pathway through cross peak growth and this was shown to be consistent with delocalized vibrations arising from intermolecular coupling with TDC calculations. Finally, 2D anisotropy measurements have revealed frequency dependent relaxation kinetics to low frequency intramolecular and phonon modes in thin-films of PETN. This is in contrast to solution measurements, which showed homogeneous kinetics within the vibrational band. This article shows that 2D IR spectroscopy can directly probe observables that are related to explosive shock and impact sensitivity.

Recent computational studies suggest intermolecular hydrogen bonds involving nitro groups significantly contribute to the relative sensitivity of nitro energetics.[177–179] The 2D IR spectra of vapor deposited energetic materials and solvated PETN suggest nitro vibrations are delocalized throughout crystalline PETN. This could have important implications for nitro aromatic explosives, where nitro-pi and nitro-amine (TATB) are correlated to energetic sensitivity.[177](64) Future 2D IR measurements on PETN analogs (ETN, PO-PETN) could test this hypothesis. Computational studies of vibrational coupling in crystalline PETN and PETN analogs are also underway. Broadband[162,180] and dual-frequency[181] 2D IR could reveal energy transfer pathways to other vibrational modes. Additionally, 2D Sum Frequency Generation spectroscopy could probe the vibrational dynamics of PETN thin-films at an interface.[39,182–184] Furthermore, the spatial heterogeneity in the film could be examined using vibrational imaging[93] and further studies could use recently developed 2D IR microscopy[73,94] to study domain-specific vibrational dynamics and energy transfer in a thin film.

## 5.6 Supporting Information

Figure 5.8 shows the vibrational lifetimes of the most intense asymmetric stretch of the $NO_2$ groups in acetone (red squares) and in vapor-deposited PETN (blue circles). The vibrational lifetimes were determined from 2D IR spectra collected at magic angle, with the pump pulse polarized 54.74° relative to the probe pulse. Spectra collected in this geometry remove the effects of rotational relaxation and measures directly the population relaxation. The decays can be fit to single exponential decays of the form of $A*\exp(-t/\tau)$. The characteristic decay times are given by $2800 \pm 524$ fs and $4000 \pm 387$ fs for the solution and thin-film, respectively. These lifetimes are consistent with previous lifetime measurements on similar molecules in solution.

As described in the text, DFT calculations were performed with the B3LYP functional

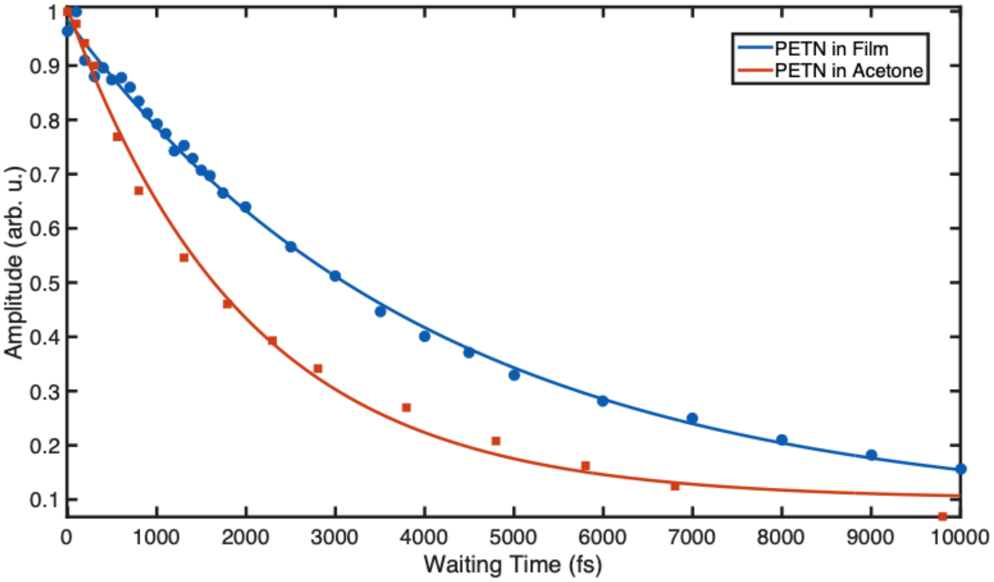

Figure 5.8: Vibrational lifetimes of the ground state bleach of the asymmetric stretch of the nitrate ester group in PETN in acetone (red squares) and a thin film of vapor-deposited PETN (blue circles).

and a 6-31G(d,p) basis set. To extract the local mode transition dipoles, DFT calculations were performed on the optimized structure of PETN. To calculate the local mode frequencies and transition dipoles, three of four nitrate ester groups were isotope labeled *in silico* by a factor of 3 to decouple them from the other nitrate esters. The median dipole derivative was used and determined to be 11.5 km/mol. From these calculations, each local mode transition dipole was assumed to have the same direction along the N–O bond axis. Additionally, the crystal structure of PETN was used to generate a super-cell with a given number of PETN molecules. To simulate the linear FTIR spectrum, the one-exciton Hamiltonian was generated from the coupling constants calculated in the crystal structure. The one-exciton Hamiltonian was then diagonalized, and each normal mode was convoluted with a line shape function to generate a realistic spectrum. To make sure that the size of the simulated crystal was large enough, the size of the simulation was systematically increased until the frequency shift observed did not change.

# Chapter 6

# Enhancing the Signal Strength of Surface Sensitive 2D IR Spectroscopy

## Contents

This chapter was adapted from: *Journal of Chemical Physics* **2019**, *150*, 024707. It was prepared in collaboration with M.K. Petti, V. Saraswat, E.R. Birdsall, K.L. Rich, J.P. Lomont, M.S. Arnold and M.T. Zanni. I contributed to the experimental data collection, sample preparation, and partially to the manuscript writing.

## 6.1 Introduction

Interfacial molecular structure and dynamics play an integral role in chemistry, materials science, and biology. From charge transfer in solar cells, to the structural dynamics of voltage-gated ion channels, elucidating the structure of molecules at an interface is central to understanding their function. However, the molecular details of surface chemistry are often lost because most techniques measure signals that are dominated by the bulk response or do not have the sensitivity to measure the small number of molecules present at the surface. For this reason, there has been significant effort to develop techniques that have sufficient signal-to-noise to measure monolayer or sub-monolayer systems.

Vibrational spectroscopy is a widely used tool for studying the molecular structure in the bulk as well as at surfaces. Such one-dimensional techniques include Infrared Reflection Absorption spectroscopy,[185–188] Attenuated Total Reflection (ATR) spectroscopy,[189,190] and Sum Frequency Generation spectroscopy.[191–195] More recently, multiple efforts have been made to extend the monolayer sensitivity of these techniques to vibrational spectroscopies of higher dimensionality.[38,196,197] Two-dimensional infrared (2D IR) and other multidimensional spectroscopies contain additional features that are not accessible to one-dimensional spectroscopy, such as cross-peaks between coupled oscillators and the ability to experimentally separate the inhomogeneous and homogenous contributions to the linewidth.[5,6,32] These spectra provide rich information on the structure and dynamics of a sample and have proven to be useful in studying bulk systems in both biology and materials science.[1,198] The application of two-dimensional vibrational spectroscopy to surfaces and interfaces is difficult due to the small number of molecules present. The optical density (OD) of a molecular monolayer is easily 1000-times smaller than the typical OD that is often used in a bulk solution sample. Thus, for 2D IR spectroscopy to measure a monolayer, a 1000-time enhancement of the signal is necessary.

The ways to achieve this enhancement are apparent in the mathematical formalism of the third order signal. In general, two-dimensional spectroscopy most often measures the third-order polarization, which in the time domain can be written as:[5,6,32]

$$E_{sig}^{(3)}(t_3,t_2,t_1) \propto P^{(3)}(t_3,t_2,t_1) \tag{6.1}$$

$$P^{(3)}(t_3,t_2,t_1) \propto \int_0^\infty dt_3 \int_0^\infty dt_2 \int_0^\infty dt_1 E_3(t-t_3)E_2(t-t_3-t_2)E_1(t-t_3-t_2-t_{t1})R^{(3)}(t_3,t_2,t_1) \tag{6.2}$$

where $E_1$,$E_2$, and $E_3$ are the electric fields of the three incident light pulses, $R^{(3)}$ is the third-order response function, $P^{(3)}$ is the third order polarization and $E_{sig}$ is the emitted third-order signal field. The variable $t_1$,$t_2$,$t_3$ are the relative times between the pulses. This emitted field is then heterodyned with a local oscillator to give the measured signal.[5,6,32]

$$S(t_{LO};t_2,t_1) \propto \int_0^\infty |E_{Lo}(t_3-t_{Lo}+E_{sig}^{(3)}(t_3,t_2,t_1)|^2 dt_3 \propto \tag{6.3}$$

$$\simeq |E_{Lo}(t_3-t_{Lo})|^2 + |E_{sig}(t_3,t_2,t_1)|^2 + 2E_{Lo}(t_3-t_{Lo})E_{sig}(t_3,t_2,t_1) \tag{6.4}$$

where $2E_{Lo}$(t$_3$-t$_{Lo}$)$E_{sig}$(t$_3$,t$_2$,t$_1$) is the heterodyned signal of interest. To isolate this term, which contains the desired phase information, we subtract off the local oscillator intensity and ignore the contribution from the emitted field intensity as it is much smaller than the former term. In practice, this is done by modulating the amplitude of the pump or by phase cycling.23 The absorptive signal (-ΔOD) is then calculated. To the first order, the absorptive signal is:[5,6,32]

$$-\Delta OD = \log\left(\frac{I_{pumpon}}{I_{pumpoff}}\right) \tag{6.5}$$

$$\simeq \frac{2E_{Lo}(t_3-t_{Lo})E_{sig}^{(3)}(t_3,t_2,t_1)}{|E_{Lo}(t_3-t_{Lo})|^2} \tag{6.6}$$

In this manuscript, we plot the signal as -$\Delta$ODsuch that the fundamental transitions are positive. From equation 6.6, it is evident that there are two ways to enhance the signal. One can are either increase ${E_{sig}}^{(3)}$ or one can decrease ${E_{Lo}}^2$, so long as the signal strength is not altered.

One approach that increases ${E_{sig}}^{(3)}$ while simultaneously creating surface sensitivity is a 2D IR spectroscopy variant of attenuated total reflection (ATR). In previous work, Hamm and co-workers use non-resonant plasmonic surface enhancement to increase the third-order signal.[49, 199, 200] Others have used gold nano-antennas to obtain even larger signals through on-resonant enhancement, albeit not in an ATR geometry.[46, 48, 201] In Hamm's surface enhanced 2D ATR IR spectroscopy, a nanostructured layer of gold coats the surface of a prism that acts as one face of the sample cell. These gold nanostructures have a maximum plasmon absorption in the visible region that extends into the mid-IR. The pump and probe beams of a 2D IR spectroscopy pulse sequence travel through the prism, coming through to the back side of the gold at an angle slightly larger than what is required for total internal reflection. The evanescent waves of the pulses are enhanced by the plasmonic resonance of the gold, which are subsequently absorbed by the molecules near the surface. Hamm has reported plasmonic enhancements that increase the signal size 10-1000 times for monolayers of metal-carbonyl molecules and small molecules with nitrile functional groups.[49, 199, 200] The enhancement is dependent on the polarization of light and the localization of the electric field around rough edges or islands on the surface.[49, 199] The electric field strength can be so large that vibrational ladder climbing occurs.[200] The ATR design can be used with a flow cell and strongly absorbing solvents, unlike transmission experiments that typically require $D_2O$ or other solvents with little mid-IR absorption.

To provide enhancement by decreasing ${E_{Lo}}^2$, one can use a four-wave mixing geometry, where the local oscillator is independent from the pump and probe beams. Alternatively, one can use a pump-probe geometry and control the polarization of the emitted signal field relative to the polarization of the probe to provide signal enhancement.[202] More recently, in a method developed by Fayer and co-workers, the reflection at an interface is used to decrease the intensity of the local oscillator in a pump-probe geometry.[42,53] In their experiments, a probe beam impinges on the surface of a sample at an angle near Brewster's angle for that air/liquid or air/solid interface so that only a small percentage of the probe is reflected. Instead of measuring the transmitted probe, as usually done in 2D IR spectroscopy, the reflected probe is collected instead. The monolayer of molecules emits a free induction decay in all directions, but because there is less probe light in the reflected direction, the ratio of the emitted signal field to the probe intensity is larger, via equation 6.4. Like the methods mentioned above, the measured reflected local oscillator intensity is independent from the incident probe field, allowing $E_{sig}$ to be maximized as described in equations 6.1 and 6.2, respectively. As a result, the $\Delta$OD is enhanced as the third-order signal strength is independent from the measured attenuated local oscillator that is reflected from the surface. This reflection enhanced 2D IR spectroscopy has been applied to interfaces where the probe beam impinges on the sample from the air so that there is a large change in the index of refraction, creating a relatively large Brewster's angle. Nishida et al. reported signal enhancement of 50-times.[53] While this enhancement is not as large as plasmon enhanced 2D IR,[46] it is applicable to solution surfaces where interesting phenomena using metal carbonyl molecules has been observed.[42]

In this article, we report a variation of 2D IR spectroscopy that combines the approaches of Fayer and Hamm Figure 6.1. We measure a reflected probe beam like Fayer and co-workers, but we invert the sample geometry so that the first interface impinges from the back of our sample cell. In the inverted geometry, the probe light travels from an interface of higher refractive index (in this case $CaF_2$), to lower refractive index (air or water). In standard ATR, the beams impinge at the critical angle. Here, the critical angle is purposely avoided to decrease the local oscillator intensity, consequently any sample window can be used, limiting dispersion introduced by ATR prisms. The inverted reflection geometry allows for the use of strongly absorbing solvents as well as flow cells. Following Hamm and co-workers, we coat the sample cell window with nanostructured gold to induce localized surface plasmons. The combination of these two sources of enhancement, localized surface plasmon and reflection geometry, create a method we call surface enhanced attenuated reflection (SEAR) 2D IR spectroscopy. These mechanisms allow the ΔOD to be enhanced by increasing the generated third-order signal, while decreasing the intensity of the local oscillator. We have measured enhancements of 190-20 000 times. We demonstrate SEAR 2D IR spectroscopy by measuring at 6 $\mu$m the amide I mode on a monolayer of peptides in both $D_2O$ and $H_2O$ solvents.

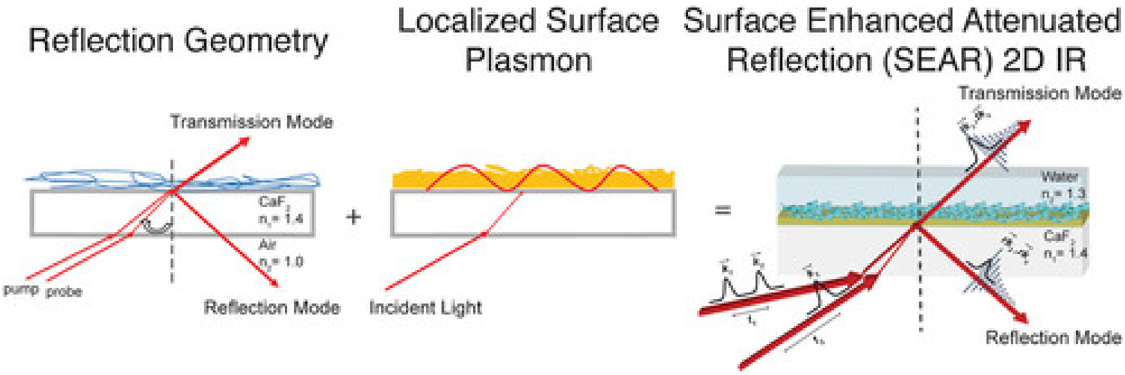

Figure 6.1: Schematic representation of how surface enhanced attenuated reflection (SEAR) 2D IR spectroscopy combines enhancement mechanisms to create a surface sensitive technique.

## 6.2 Methods

### 6.2.1 Laser System

A regenerative amplifier (Coherent Libra) with an output of 3.4 W, 50 fs, centered at 800 nm pumps a commercial optical parametric amplifier (OPA) (TOPAS, Light Conversion). The signal and idler pulses are then mixed collinearly in a $AgGaS_2$ difference frequency generation (DFG) crystal to generate mid-IR light with a center wavelength of 6 $\mu$m. The mid-IR pulses have a duration of about 100 fs with pulse energies around 18-20 $\mu$J. The mid-IR output is sent through a 90/10 $CaF_2$ beam splitter to create the pump and probe lines. The pump pulse is shaped by using a germanium acousto-optical modulator (Ge-AOM) pulse shaper as previously described.[120] Both probe and pump pulses are polarized to either s- or p-polarization by using half wave plates and polarizers.

The pump and probe pulses are spatially and temporally overlapped at the sample and are focused using 7.5 cm focal length gold parabolic mirrors. For the reflection geometry, the sample is rotated perpendicular to the table. The back-substrate interface is the first interface the mid-IR light hits. The reflected signal is collimated using a convex lens before being directed to a 32-pixel MCT array.

### 6.2.2 Sample Preparation

CORM-3 Thin film: Carbon monoxide releasing molecule 3 (CORM-3) was purchased from Sigma-Aldrich. A 2 mg/ml solution of CORM-3 was made in chloroform. Thin film samples were made by slowly drying the CORM-3 solution on a $CaF_2$ substrate in a nitrogen rich environment. From the linear FTIR spectrum, we estimate the film thickness to be 1-3 nm. Cys-terminated Ovispirin-1: Cys-terminated ovispirin-1 (cys-ovispirin-1) was synthesized using a standard fluorenylmethyloxycarbonyl (FMOC) protecting group solid-phase peptide synthesis with a CEM Liberty Blue Automated Peptide Synthesizer, cleaved with trifluoroacetic acid (TFA), and purified using reverse-phase high-performance liquid chromatography (HPLC).[103,120] The purified peptide was made into a 0.02 mM solution in 10% tris buffer (pH = 12.16) and 90% HPLC grade ethanol. Gold films (Au > 99.99%) with thicknesses of 3 nm were deposited on $CaF_2$ substrates in a thermal evaporator. The deposition rate was 0.1 A/s at a vacuum of 8 x $10^{-7}$ torr. The thickness was monitored via a quartz crystal microbalance. Determination of the plasmon frequency was found with a UV-Vis spectrometer. The Au/$CaF_2$ substrate was submerged in the cys-ovispirin-1 solution for 12 h to form a monolayer. The sample was gently rinsed with HPLC grade ethanol and dried under nitrogen for subsequent measurement. For the hydrated sample, either $D_2O$ or deionized $H_2O$ was added on top of the monolayer.

## 6.3 Results

In the following, we first quantify the enhancement of reflection enhanced 2D IR spectroscopy employed in an inverted geometry using a strongly absorbing metal carbonyl system. Second, we thermally evaporate gold onto a $CaF_2$ window and measure the resulting plasmonic enhancement in a standard transmission geometry for a monolayer of peptides. Third, we measure the additional improvement in the signal by measuring the peptide sample in a reflection, rather than transmission, geometry. Finally, we hydrate the peptides with $D_2$ O and $H_2$ O to demonstrate the utility of the method for measuring monolayers of peptides in strongly absorbing solvent.

### 6.3.1 Signal enhancements of a metal carbonyl thin film on a dielectric surface using an inverted reflection pump-probe geometry

Shown in Figure 7.2 are the 2D IR spectra of carbon monoxide releasing molecule 3 (CORM-3) drop-cast onto a 2 mm $CaF_2$ window to make a thin film. The optical density of the film is approximately 10 mOD. While CORM-3 has 3 metal carbonyl functional groups, one of the axial carbonyls becomes a carboxylic acid group in the inactive state.[203] CORM-3 has previously been used as a precursor to label proteins to study protein-water interfaces.[204] In Fig. 2(a), a 2D IR spectrum is shown of the CORM-3 film using a standard transmission pump-probe geometry in which the pump and probe beams impinge on the sample at 35° to the normal at the $CaF_2$/air interface. Figure 7.2(a) is the spectrum obtained by collecting the transmitted probe beam. The spectrum contains two sets of diagonal pairs of peaks, at $\omega_{pump} = 2060\ \text{cm}^{-1}$ and $1980\ \text{cm}^{-1}$ , which are created by the metal carbonyl modes of CORM-3 in its inactivated form.The bleaches of the ground state vibrational modes appear close to the diagonal and are plotted to have a positive intensity. The peaks are elongated along the diagonal, indicating that the vibrational modes are inhomogeneously broadened. This broadening is expected for thin films and is similar to ions previously studied in a glass[205] and other films of metal carbonyls.[41, 206, 207]

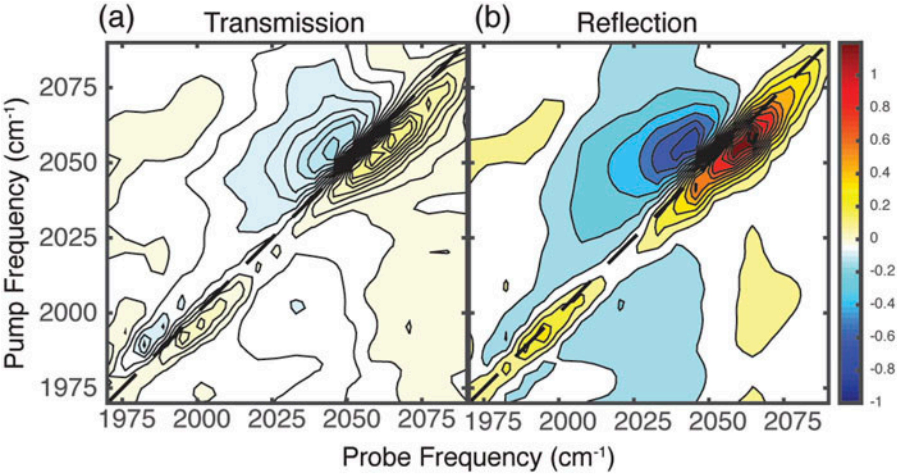

Figure 6.2: Schematic representation of how surface enhanced attenuated reflection (SEAR) 2D IR spectroscopy combines enhancement mechanisms to create a surface sensitive technique.

Shown in Fig. 7.2(b) is the CORM-3 thin film sample measured in an inverted-reflection pump-probe geometry. The same beam geometry and angle of incidence is used as before, but rather than measuring the portion of the probe that is transmitted through the thin film, the small portion of probe light reflected off the interface between the $CaF_2$ and the film of CORM-3 is measured. The amount of reflected light from the interface depends on the polarization of light used and the incident angle. Here, p-polarized pump and probe beams were used. The p-polarized probe beam travels from $CaF_2$, a higher refractive index (n = 1.4) material, to air, a lower refractive index (n = 1.0) material, at an incident angle of 35° at the $CaF_2$/air interface, causing less than 1% of the probe beam to be reflected.

The raw data is collected as a change in optical density (ΔOD). This ΔOD is normalized to the reflection experiment and depicted in Fig. 7.2. We measure a 40-times enhancement in the reflection over the transmission 2D IR spectrum, consistent with measurements of Fayer and co-workers on similar samples. Thus, an inverted-reflection pump-probe geometry, i.e., coming back from the back of the sample, provides the expected enhancement for a reflection geometry.

### 6.3.2 Surface plasmon enhancement of a peptide monolayer on a rough nanometer thin Au/$CaF_2$ substrate

Having observed signal enhancement with the inverted reflection geometry comparable to what was reported by Fayer and co-workers,[53] we now investigate the use of localized surface plasmons, like what has been used with Hamm and co-worker's 2D ATR IR method.[199,200] We apply this approach to measure the amide I mode of a polypeptide monolayer, requiring 6 $\mu$m mid-IR light. The amide I mode probes the protein backbone and the resulting peak frequencies provide information on the secondary structure of the peptide.[1] The measured peptide, ovispirin-1, is an antimicrobial amphipathic peptide consisting of 18 residues. Based on high-resolution nuclear magnetic resonance (NMR) experiments, it forms an $\alpha$-helix from residues 4–16 in helix-promoting solvents of 33% 2,2,2-trifluoroethanol/67% phosphate buffer solution at pH 6.5.[208] Due to its amphipathic nature, it also forms an $\alpha$-helix on lipid bilayers[127] as well as polystyrene surfaces[209] with a kink at residue 14 according to solid-state NMR[210] and 2D IR spectroscopy studies.[127] Here, a cysteine residue was added to the C-terminus to form a monolayer on a gold surface through a cysteine thiol-gold bond.[211,212] This functionalized 19-residue peptide will be referred to as cys-ovispirin-1. As described in Sec. II, gold was deposited onto a $CaF_2$ substrate using thermal-evaporation to a thickness of 3 nm. Gold films deposited in this way and at this thickness are rough and contain nanostructures that can support mid-IR nonresonant localized surface plasmon enhancement.

To explore the enhancement caused by localized surface plasmons, we first use transmission pump-probe 2D IR spectroscopy. Figure 7.3(a) is a transmission 2D IR spectrum of a dried monolayer of cys-ovispirin-1 on 3 nm Au/$CaF_2$. The spectrum contains a diagonal pair of peaks at $\omega_{pump} = 1653$ cm$^{-1}$ as well as a peak at $\omega_{pump} = 1634$ cm$^{-1}$. Figure 7.3(b) shows the transmission 2D IR spectrum of the same sample, except in a $D_2O$ hydrated environment. As in the dried sample, a diagonal pair of peaks at $\omega_{pump} = 1653$ cm$^{-1}$ is observed, as well as a peak at $\omega_{pump} = 1634$ cm$^{-1}$. A third peak is observed in the D2O hydrated peptide at $\omega_{pump} = 1621$ cm$^{-1}$ and a small cross-peak is observed between the two lower frequency modes.

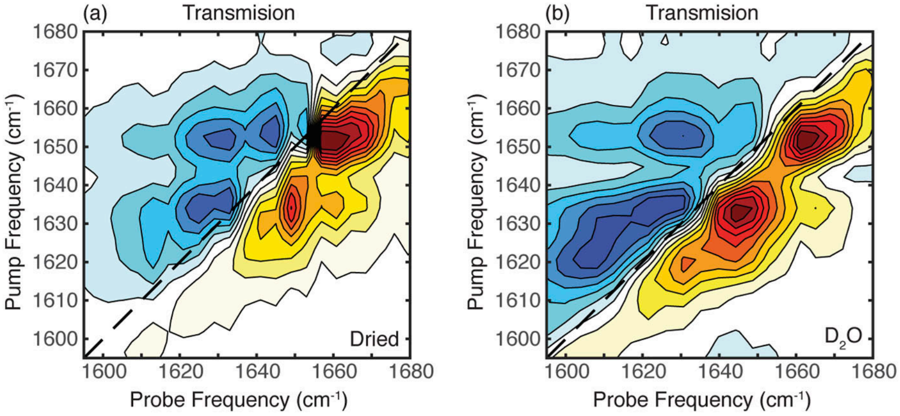

Figure 6.3: (a) Transmission spectrum of dried cys-ovispirin-1 on 3 nm Au/$CaF_2$. (b) Transmission spectrum of cys-ovispirin-1 on 3 nm Au/$CaF_2$ hydrated with $D_2O$. s-polarized pump and probe beams were used for both spectra.

Based on prior work,48 in our spectra of cys-ovispirin-1, we attribute the higher frequency peak at 1653 cm$^{-1}$ to $\alpha$-helical components, while we assign the lower frequency peak at 1634 cm$^{-1}$ to random coil contributions of cys-ovispirin-1. From the intensities of these peaks, we conclude that cys-ovispirin-1 has a partial $\alpha$-helical structure when bound to the gold surface in both dehydrated and hydrated environments, although we do not attempt to quantify the structural distribution as it is not necessary for the purposes of this manuscript. The conservation of both diagonal peaks between the dried and hydrated cys-ovispirin-1 monolayers [Figs. 7.3(a) and 7.3(b)] is evidence that the signal is from proteins only at the surface and not from the bulk . We attribute the third peak in the $D_2O$ hydrated spectrum at $\omega_{pump} = 1621$ cm$^{-1}$ to different hydrogen bonding environments of the peptide backbone, as some residues may be facing the hydrophobic Au surface, while others are fully hydrated with $D_2O$.[16,19,213,214]

To quantify the enhancement created by the localized surface plasmon, we take an approach first outlined by Grechko and Zanni[8,12,163] and then adopted for signal enhancement calculations by Donaldson and Hamm.[49] The enhancement is found by determining the relative transition dipole strength as described in Eq. 6.7. The linear absorption signal is proportional to the concentration, c, and the transition dipole strength, $\mu^2$, while the heterodyned 2D IR signal is proportional to c x $\mu^4$ Taking the ratio of the linear and nonlinear signals with respect to a calibrant allows for the transition dipole strength of the molecule of interest to be found independent of concentration and instrument parameters. In this case, N-methylacetamide (NMA) in chloroform was used as a calibrant because it absorbs at nearly the same frequency as the surface-bound peptide.[213] The calibrant is needed to account for any discrepancies in the laser fluence or spatial overlap of the pump and probe pulses for the 2D IR experiment.[215]

$$|\mu|^2_{sample} = \frac{|\mu|^2_{calibrant}(S^{2DIR}_{sample}/A^{IR}_{sample})}{S^{2DIR}_{calibrant}/A^{IR}_{calibrant}} \tag{6.7}$$

To find the enhancement factor from the surface plasmon, the ratio of the transition dipole strength of the monolayer and bulk is taken [Eq.6.7]. Bulk cys-ovispirin-1 in buffer adopts an $\alpha$-helix conformation. However, based on the spectra in Fig. 7.3, we know that the peptide monolayer does not adopt a completely $\alpha$-helical conformation, but also contains random coil structure. Thus, the bulk transition dipole strength of the peptide sample with the same conformation as that of the monolayer is not known. To account for this variable, we report a range of enhancement factors based on the two secondary structures observed in the peptide monolayer spectra. A previous study has determined the transition dipole strength of an $\alpha$-helix to be 0.24 $D^2$, while a random coil conformation has a transition dipole strength of 0.12 $D^2$.[12] We use these values when calculating the enhancement factors.

The enhancement factor squared is the effective 2D signal enhancement due to the scaling of the transition dipole strength in the nonlinear absorption signal. We again report a range based on the enhancement factors found for the two secondary structures observed in the peptide monolayer. The reported enhancement factors and 2D signal enhancement (Table 6.1) are qualitatively similar to what has been reported previously for linear infrared absorption spectroscopy[216–218] and 2D IR spectroscopy.[199]

Table 6.1: Calculated localized surface plasmon enhancement for 2D IR signals based on measurements of the effective transition dipole strength

| Molecule | Random coil $\mu^2$ ($D^2$) | $\alpha$-helix $\mu^2$ ($D^2$) | Enhancement factor | 2D Signal Enhancement |
|---|---|---|---|---|
| Cys-ovispirin-1 on 2 nm Au/$CaF_2$, dry | 0.92 | 18.8 | 7.69-78.3 | 59.1-6140 |
| Cys-ovispirin-1 on 2 nm Au/$CaF_2$, with $D_2O$ | 1.48 | 2.81 | 11.7-12.4 | 137-153 |

### 6.3.3 SEAR 2D IR Spectroscopy in a Strongly Absorbing Solvent

With the enhancements from the inverted reflection geometry and localized surface plasmon quantified, we now use SEAR 2D IR spectroscopy to measure two peptide monolayer samples. One sample is dried cys-ovispirin-1 on 3 nm Au/$CaF_2$, and the second sample is $D_2O$ hydrated cys-ovispirin-1 on 3 nm Au/$CaF_2$. The two spectra are shown in Figs. 4(b) and 4(d), respectively. These SEAR 2D IR spectra are obtained with an angle of incidence of 32° from the normal of the air/$CaF_2$ interface. This external incident angle at the air/$CaF_2$ interface corresponds to an internal incident angle of 22° at the $CaF_2$/sample interface, and it is the reflection from this internal interface that is measured. For the two samples measured, both the pump and probe beams were set to s-polarized. For comparison, the transmission 2D IR spectra of the dried and hydrated monolayer samples of cys-ovispirin-1 on 3 nm Au/$CaF_2$ from Figs. 7.3(b) and 7.3(c) are replotted in Figs. 7.4(a) and 7.4(c), respectively. The z-axis of Figs. 7.4(a) and 7.4(c) are scaled to that of Figs. 7.4(b) and 7.4(d). When comparing, the two spectra for the dried sample [Figs. 7.4(a) and 7.4(b)], the 1653 $cm^{-1}$ peak and 1634 $cm^{-1}$ peak are retained, as well as the inhomogeneous line shape. For the $D_2O$ hydrated sample [Figs. 7.4(c) and 7.4(d)], again the frequency of the three peaks are retained (1653 $cm^{-1}$, 1634 $cm^{-1}$, and 1621 $cm^{-1}$). The reflection geometry provides additional enhancements of 3.2 and 2.5 times in Figs. 7.4(b) and 7.4(d) over the transmission geometry. These enhancements, while smaller than in Fig. 7.2, still reduces the data collection time, as explained in Sec. IV.

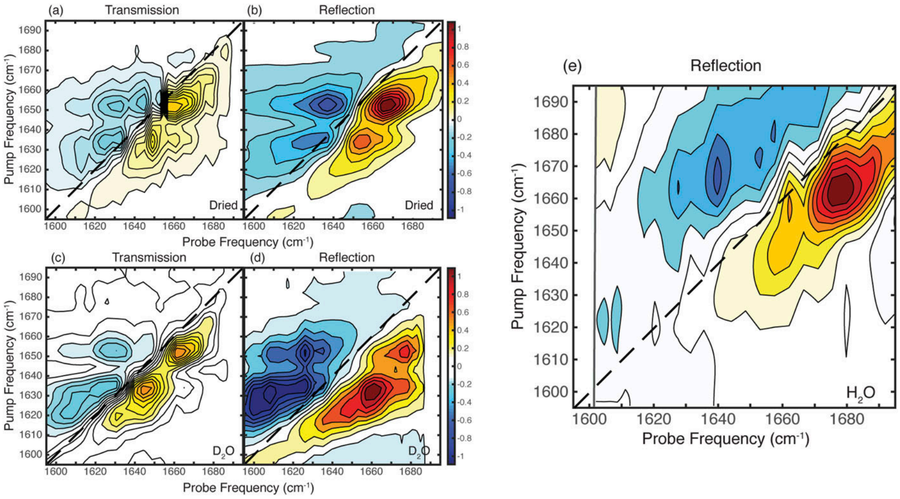

Figure 6.4: Dried monolayer of cys-ovispirin-1 on 3 nm Au/$CaF_2$ 2D IR spectra taken in a (a) transmission geometry and with (b) SEAR 2D IR spectroscopy plotted on the same normalized color map. Monolayer of cys-ovispirin-1 on 3 nm Au/$CaF_2$ hydrated with $D_2O$ 2D IR spectra taken in a (c) transmission geometry and with (d) SEAR 2D IR spectroscopy plotted on the same normalized color map. (e) Monolayer of cys-ovispirin-1 on 3 nm Au/$CaF_2$ hydrated with $H_2O$ spectrum taken with SEAR 2D IR spectroscopy. The vertical grey line indicates the last pixel of the MCT detector. Consequently, frequencies lower than 1600 $cm^{-1}$ are not detected. A s-polarized pump and probe were used for all the spectra shown here.

Figure 7.4(e) is a SEAR 2D IR spectrum of cys-ovispirin-1 on 3 nm Au/$CaF_2$ hydrated with $H_2O$. The amide I band of peptides and proteins are usually measured in $D_2O$ when using IR spectroscopy because the bending vibrational mode of $H_2O$ absorbs in this same region,[219] prohibiting samples with a reasonable path-length. With SEAR 2D IR spectroscopy, water absorption is minimized since the reflected probe beam does not penetrate deeply into the solvent and the emitted field is generated close to the surface. We note that the SEAR 2D IR spectrum of cys-ovispirin-1 on 3 nm Au/$CaF_2$ hydrated with $H_2O$ has two features like in the $D_2O$ spectra, but these peaks are blue shifted by 8 $cm^{-1}$ and the ratio of intensities are different. In $H_2O$, there is one very intense peak at $\omega_{pump} = 1661$ $cm^{-1}$ , and one less intense peak at $\omega_{pump} = 1642$ $cm^{-1}$ . We discuss these differences below.

## 6.4 Discussion

SEAR 2D IR spectroscopy builds from previous work that allows for surface sensitive 2D IR spectroscopy. Here, the combination of a reflection geometry and localized surface plasmons effectively decreases the local oscillator intensity while also increasing the third-order signal, providing enhancements of the measured $\Delta$OD of the amide I mode of a peptide monolayer. Table 6.2 outlines the signal enhancement observed from the localized surface plasmon, the inverted reflection geometry, and the total enhancement of SEAR 2D IR signals for cys-ovispirin-1 on 3 nm Au/$CaF_2$. Since we cannot measure a spectrum of peptides without plasmon enhancement, the total enhancement of SEAR 2D IR spectroscopy is calculated by multiplying together the two sources of enhancement used in the technique. Thus, the overall signal enhancement obtained using SEAR 2D IR spectroscopy is 190-20 000-times (Table 6.2), with most of the enhancement coming from the use of localized surface plasmons. Below, we discuss the mechanism of enhancement for SEAR 2D IR spectroscopy and experimental considerations for this technique. SEAR 2D IR spectroscopy also allows for the use of strongly absorbing solvents and is demonstrated here with a peptide monolayer hydrated with $H_2O$. We report on differences in the amide I mode of a peptide monolayer in $D_2O$ and $H_2O$.

Table 6.2: Enhancements of 2D IR signals from localized surface plasmons, the inverted reflection geometry, and SEAR 2D IR spectroscopy

| Molecule | Plasmon enhancement | Reflection enhancement | SEAR 2D IR enhancement |
|---|---|---|---|
| Cys-ovispirin-1 on 2 nm Au/$CaF_2$, dry | 59.1-6140 | 3.2 | 190-20 000 |
| Cys-ovispirin-1 on 2 nm Au/$CaF_2$, with $D_2O$ | 137-153 | 2.5 | 340-380 |

### 6.4.1 Enhancement Mechanisms of SEAR 2D IR

The dominate enhancement factor in SEAR 2D IR spectroscopy comes from the use of localized surface plasmons (Table 6.2). In terms of the 2D IR signal, using localized surface plasmons enhances the generated third-order signal field [Eqs. 6.2 and 6.3], leading to a larger measured $\Delta$OD [Eq. 6.4]. Previously, it was found that the enhancement from the localized surface plasmon from the rough gold nanostructures was dependent on the polarization of light. Because of the rough structure of the gold used in their study, there were gaps between nanostructures within the plane of the substrate. When using s-polarized light, the localized surface plasmon was polarized within the plane of the surface and confined more tightly in these gaps, making "hot-spots" of high intensity fields that provided 10-100-times greater (depending on the thickness of gold) enhancement then when p-polarized light was used.2 The same confinement effect was not observed for p-polarized light, as the surface plasmon is polarized perpendicular to the surface normal and "hot-spots" are not observed. It should be noted that this enhancement is based on localized surface plasmons and not surface plasmon polaritons, which have different excitation mechanisms. We used s-polarized pump and probe beams to take full advantage of the localized surface plasmon enhancement mechanism. While the non-resonant localized surface plasmon used here provides large enhancement (Table 6.2), more enhancement can be obtained by considering the plasmon frequency. As the plasmon frequency moves closer to resonance with the vibrational modes of interest, the enhancement increases drastically. Other plasmonic structures, such as nano-arrays, nano-antennas, or nano-stars may have different plasmon frequencies and polarization dependencies that can be considered to provide more enhancement. Here, the rough nanometer thin Au on $CaF_2$ substrates used have a plasmon frequency in the visible that extended into the mid-IR and provides 50-6000-times enhancement (Table 6.2).

While the use of localized surface plasmons increases the third-order signal, the inverted reflection geometry decreases the intensity of the local oscillator. The purely absorptive 2D IR signal measured here is inversely proportional to the intensity of the local oscillator, as described by Eq. 6.4. Thus, decreasing this background intensity will increase the third-order signal. In a fully non-collinear geometry, this is trivial, as the local oscillator can be independently attenuated without influencing the third-order signal. However, in a partially collinear geometry, as used here, the probe pulse acts as the local oscillator, and the generated signal is in the same phase-matched direction as the probe pulse. Fayer and co-workers used the reflection from a surface to control the intensity of the local oscillator in a pump-probe geometry. SEAR 2D IR spectroscopy uses this same principle, except in an inverted reflection geometry.

In SEAR 2D IR spectroscopy, two conditions are controlled: the incident angle of the incoming light at the sample and the polarization of light used. The amount of light reflected vs. transmitted at the interface is determined by the refractive indices of the materials that make the interface, the angle of incidence, and the polarization of light. For p-polarized light, the amount of reflected light goes to zero at Brewster's angle. Thus, by setting the incident angle close to Brewster's angle, and using p-polarized light, the amount of reflected local oscillator can be diminished. Alternatively, s-polarized light can be used, which reduces the local oscillator by 90% for most angles. Either way, the reflected signal field strength ($E^{(3)}{}_{sig}(3)$) is maintained and the local oscillator intensity $E_{Lo}{}^2$ is substantially reduced, resulting in a large signal over a small background.32,33 To determine the incident angle and the polarization of light to use, it is helpful to calculate the percentage of light reflected from different interfaces.

The Fresnel equations describe this reflectivity and are used to produce the graphs for three different interfaces in Fig. 5. These equations are as follows:

$$R_s = (\frac{n_1 \cos(\theta_1) - n_2 \cos(\theta_2)}{n_1 \cos(\theta_1) + n_2 \cos(\theta_2)})^2 \tag{6.8}$$

$$R_p = (\frac{n_1 \cos(\theta_1) + n_2 \cos(\theta_2)}{n_1 \cos(\theta_1) - n_2 \cos(\theta_2)})^2 \tag{6.9}$$

where R$_s$ and R$_p$ correspond to the reflection coefficients of s- and p-polarized light reflected. n$_1$ and n$_2$ are the refractive indices for the first and second interface, respectively. The refractive indices for the materials used are n = 1 for air, n = 1.4 for CaF$_2$, and n = 1.26 for water. $\theta_1$ is the angle of incidence, while $\theta_2$ is the angle of transmittance. Brewster's angle is where p-polarized light (green in Fig. 5) goes to zero and is defined as:

$$\theta_{Brewster's} = \tan^{-1} \frac{n_2}{n_1} \tag{6.10}$$

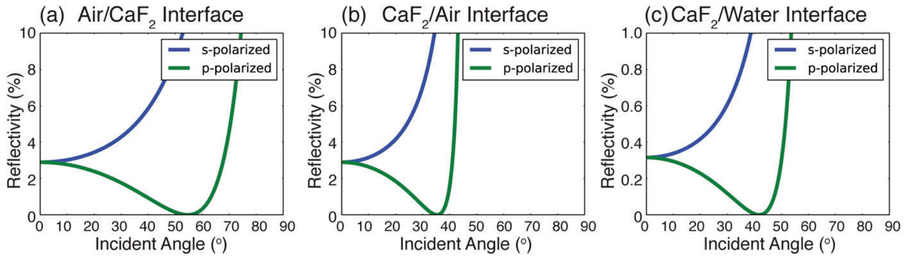

Figure 6.5: The amount of light reflected (%) as a function of incident angle at (a) air/CaF$_2$, (b) CaF$_2$/air, and (c) CaF$_2$/water interfaces as defined by the Fresnel equations for both s- and p-polarized light.

For the air/$CaF_2$ interface, Brewster's angle is 54.5°, whereas for the $CaF_2$/air interface, Brewster's angle is the complement angle at 35.5°. With the inverted reflection geometry, less than 3% of p-polarized light and less than 10% of s-polarized light is reflected for all incident angles less than Brewster's angle at the $CaF_2$/air interface. For p-polarized light, this leads to a predicted enhancement of 7–10-times at angles less than Brewster's angle, which then drastically increases as the incident angle moves closer to Brewster's angle, until ultimately diverging. For s-polarized light, a maximum enhancement of 7-times is expected for incident angles less than Brewster's angle, before going to zero at the critical angle. Thus, to get a large enhancement, the pump and probe should both be p-polarized and the incident angle should be within 2°–3° of Brewster's angle. Doing so diminishes the amount of reflected light (Fig. 6.5) by 99%–100% (theoretically) and effectively decreases the local oscillator to increase the measured $\Delta$OD as described in Eq. 6.4. The enhancement obtained when using an inverted reflection geometry is an order of magnitude less than the enhancement from the localized surface plasmons. For this reason, we capitalized on the localized surface plasmon enhancement and use s-polarized light for the SEAR 2D IR measurement of the peptide monolayer. Doing so results in an enhancement of 3.2-times for the dried monolayer [Fig. 7.4(b)] and 2.5-times for the $D_2O$ hydrated monolayer [Fig. 7.4(d)] over the transmission spectra. Compared to the inverted reflection geometry enhancement observed with CORM-3, this enhancement is an order of magnitude less. The difference between the CORM-3 and cys-ovispirin-1 spectral enhancement based on the inverted reflection geometry is that in the latter case, there is 5% more reflected light with the experimental conditions used. Because of this difference in reflection, the local oscillator is not attenuated as much in the cys-ovispirin-1 spectra as in the CORM-3 spectrum, leading to lower reflection enhancements as predicted and observed.

Additionally, we would expect that the hydrated cys-ovispirin-1 monolayer would be enhanced more than the dry cys-ovispirin-1 monolayer based on the amount of light reflected from the hydrated interface (Fig. 6.5). However, we observe similar enhancements (Table 6.2). We attribute this discrepancy to the reflectivity of the nanostructured gold on the $CaF_2$ substrate. This thin layer of gold is reflecting more light than what would be predicted for a $CaF_2$/air or $CaF_2$/water interface, leading to observed enhancements that are less than expected. While these enhancements are smaller than expected, using a reflection geometry does reduce the data collection time. For example, to obtain a transmission spectrum of the dried or $D_2O$ hydrated cys-ovispirin-1 on 3 nm Au/$CaF_2$ with the same signal-to-noise as the SEAR 2D IR measurements taken with s-polarized light, the spectrum would have to be averaged 5-10 times longer. It should also be noted that in the peptide monolayer case, the spectra are also enhanced by the localized surface plasmon. This leads to an overall SEAR 2D IR enhancement of 100-20 000-times (Table 6.2) and is much larger than what could be obtained by either enhancement technique alone.

In practice, the quality of the spectra that one can gain from SEAR 2D IR spectroscopy, or any method that attenuates the local oscillator, is limited by the noise limit of the detector. While attenuating the local oscillator improves the $\Delta$OD, one still needs sufficient local oscillator intensity to be above the dark counts of the detector. In the case here, s-polarized light was used to maximize the localized surface plasmon enhancement but was also necessary to have sufficient light hit the detector. We estimate that 40 nJ is reflected at the CaF2/water interface for our samples, which is the limit of detection for our monochromator and detector. By considering the sample interface, both the polarization of light and the incident angle can be selected for an experiment to provide sufficient signal-to-noise.

### 6.4.2 Measuring a peptide monolayer in a strongly absorbing environment

In SEAR 2D IR spectroscopy, the signal field is emitted in all directions and the heterodyned signal is measured in the reflection direction. The signal field and probe pulse in this direction do not penetrate the solvent environment. For biological experiments where amide I modes are of interest, this allows for those systems to be measured in $H_2O$. Currently, 2D IR experiments on peptides and proteins in a transmission geometry rely on deuterated solvents. Being able to use $H_2O$ or other strongly absorbing solvent increases the variety of systems that can be measured with 2D IR spectroscopy, such as biological tissues, electrochemical surfaces, and photovoltaic devices. We demonstrate this capability by measuring a peptide monolayer hydrated with $H_2O$.

The SEAR 2D IR spectrum of cys-ovispirin-1 on 3 nm Au/$CaF_2$ hydrated with $H_2O$ has two diagonal peaks associated with $\alpha$-helical and random coil secondary structure contributions [Fig. 7.4(e)]. The spectrum of cys-ovispirin-1 on 3 nm Au/$CaF_2$ hydrated with $D_2O$ also has two sets of peaks [Fig. 7.4(d)]. The main differences in these two spectra are the frequency at which the $\alpha$-helical and random coil amide I peaks absorb, and the relative intensity of these two peaks. There are two factors that contribute to these differences: the transition dipole strength and hydrogen/deuterium (H/D) exchange.

Regarding the former, the amide I mode consists of 85% C=O stretch, 10% C-N stretch, and 5% N-H in-plane bending.[23] When the N–H is changed to a N–D, the amide vibrational mode is altered. This change is validated by calculating the carbonyl vibrational frequency and intensity of N-methylacetamide (NMA) and deuterated N-methylacetamide (d-NMA). A B3LYP functional and cc-pvtz basis was used and found that for NMA, the amide I vibrational frequency is 1697.039 $\text{cm}^{-1}$, while for d-NMA, the frequency is red shifted to 1681.673 $\text{cm}^{-1}$. The transition dipole strength of the d-NMA carbonyl frequency is $\mu^2 = 0.150\ \text{D}^2$ or 1.07-times more than NMA. 2D IR signals are proportional to $\mu^4$,meaning that the d-NMA carbonyl vibrational mode will be 1.14-times more intense in the 2D IR measurement. Thus, deuterating the nitrogen of the amide I modes increases the intensity over non-deuterated amide I modes.

Regarding the latter, different peptide conformations undergo H/D exchange at different rates. For random coil structures, H/D exchange happens on the milliseconds to seconds time scale, while $\beta$-sheets and $\alpha$-helices take anywhere from a few minutes to hours to completely exchange.[220] In our experiments, spectra were collected immediately after solvation, so only the random coil regions will be fully exchanged. When hydrated with $H_2O$, the peptide monolayer spectrum resulted in a more intense $\alpha$-helix peak at $\omega_{pump} = 1661$ cm$^{-1}$ and a less intense random coil peak at $\omega_{pump} = 1642$ cm$^{-1}$. The peptide monolayer was then dried and hydrated with $D_2O$, and the resulting SEAR 2D IR spectrum has an $\alpha$-helix peak at $\omega_{pump} = 1653$ cm$^{-1}$ and a random coil peak at $\omega_{pump} = 1634$ cm$^{-1}$. Thus, both amide I peaks frequencies have redshifted as expected.[15] The random coil peak has also increased in relative intensity compared to the $\alpha$-helix and is consistent with incomplete H/D exchange of the $\alpha$-helix. Therefore, our data is consistent with full H/D exchange of the random coil peptide secondary structure and partial exchange of the $\alpha$-helix.

## 6.5 Conclusions

SEAR 2D IR spectroscopy combines two techniques that each provide different mechanisms to achieve signal enhancement and monolayer sensitivity. Previously, Fayer and co-workers have established a reflection enhanced 2D IR spectroscopy in a pump-probe geometry, while the use of localized surface plasmons for surface enhanced 2D ATR IR has been pioneered by Hamm and co-workers. A reflection geometry allows the local oscillator to be attenuated independently and maintain the maximum $E_{sig}$ strength, analogous to fully collinear geometries and polarization methods. The use of localized surface plasmons increases the $E_{sig}$ field strength of molecules on the surface. Taken together, these techniques lower the intensity of the local oscillator in a pump-probe geometry and increase the third-order signal field strength of the measurement. Mathematically, this decreases the denominator and increases the numerator that define the $\Delta$OD measured, optimizing the way that signal enhancement can be achieved. The individual enhancement of the two approaches used and the overall enhancement of SEAR 2D IR spectroscopy were demonstrated and quantified. We report an enhancement of 20 000-times. SEAR 2D IR spectroscopy was applied to the surface bound peptide ovispirin-1 in both dehydrated and hydrated environments. With SEAR 2D IR spectroscopy, the spectrum of a monolayer of peptide was obtained in $H_2O$, a strongly absorbing solvent.

These proof of principle experiments presented here establish more general criteria to increase the measured 2D IR signal by enhancing the third-order signal with plasmon enhancement and decreasing the local oscillator intensity. By using an inverted reflection geometry, the method is not limited to the strict angle requirements of ATR IR spectroscopy. In fact, using an angle that is far from total internal reflection provides enhancement to the $\Delta$OD. We also use an inverted reflection geometry on a solid/liquid interface. Specifically, a peptide monolayer is tethered to a $Au/CaF_2$ substrate and hydrated with $H_2O$, demonstrating the potential of SEAR 2D IR spectroscopy for more experiments in environments containing strongly absorbing solvents that were not previously possible. One such experiment includes developing 2D IR spectroscopy biological assays that require high sensitivity and low detection limits. The SEAR method could also be applied to the visible spectrum, creating SEAR 2D electronic spectroscopy (ES). While interfacial dynamics of charge carries in photovoltaic materials at electrodes are currently being investigated by other surface sensitive techniques, implementing SEAR 2D ES would make these measurements experimentally easier due to the enhanced signals observed. Moreover, the data collection with SEAR 2D IR spectroscopy is 5-10 times faster than our conventional transmission 2D IR experiments, making possible more difficult experiments, such as transient 2D IR spectroscopy. In general, SEAR 2D IR spectroscopy can be implemented in any 2D spectrometer, broadening the usefulness of multidimensional spectroscopy as an analytical tool as it can now be applied to monolayers and bulk systems of both gas and condensed phase samples.

## 6.6 Supporting Information

### 6.6.1 Plasmon Frequencies of Rough Nanometer thin Au/$CaF_2$ Substrates

To make the plasmonic substrates, different thicknesses (2 nm and 3 nm, respectively) of gold were thermally evaporated onto $CaF_2$ windows. In the main text, only the 3 nm Au/$CaF_2$ substrates were used to make the cys-ovispirin-1 monolayers. Here, the 2 nm Au/$CaF_2$ substrate is just used for comparison. UV-vis spectroscopy was used to determine the plasmon frequency. For the 2 nm Au/$CaF_2$, the peak is at 650 nm, while for the slightly thicker 3 nm Au/$CaF_2$ samples, the plasmon frequency is at 725 nm and is red shifted as expected. When $D_2O$ is added to the 3 nm Au/$CaF_2$ substrate, as is done in the main text, the peak is blue shifted relative to the bare 3 nm Au/$CaF_2$ plasmon frequency to 695 nm. The intensity of the peak also decreases. The peaks are broad and extends into the mid-IR, indicating that the plasmonic enhancements observed with SEAR 2D IR spectroscopy is a non-resonant effect, as previously used.

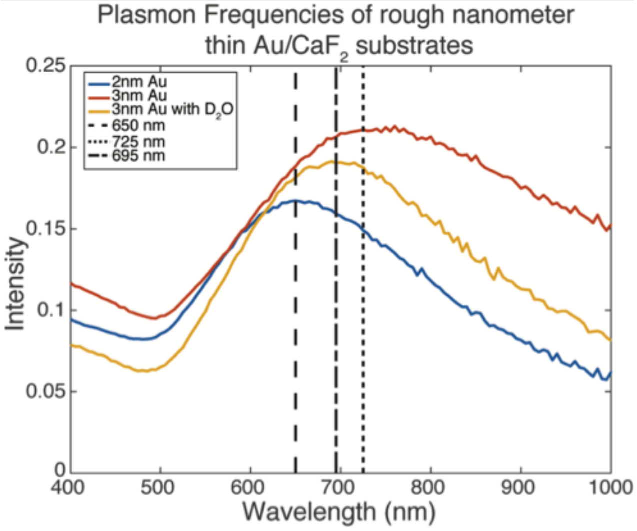

Figure 6.6: UV-vis spectra of 2 nm Au/$CaF_2$ (blue), 3 nm Au/$CaF_2$ (red), and 3 nm Au/$CaF_2$ with $D_2O$ (yellow) thermally evaporated samples. Peak maxima are shown with dotted lines.

# Chapter 7

# Monolayer Sensitivity Enables a New 2D IR Immuno-biosensor for Studying Protein Structures: Application to Amyloid Polymorphs

## Contents

This chapter was adapted from a submission to: *Journal of Physical Chemistry Letters.* **2019**, It was prepared in collaboration with J.P. Lomont, K.L. Rich, V. Saraswat, B.R. Feingold, M.K. Petti, E.R. Birdsall, M.S. Arnold, and M.T. Zanni.

## 7.1 Introduction

Immunosensors use antibodies to isolate an antigen, often a protein or other biomarker of interest, from a complex solution. These assays often rely on colorimetric,[221] fluorescence,[222] or electrochemical detection.[223] Consequently, the information obtained is typically limited to the presence and amount of antigen present. Some antibodies can be crystallized in the presence of the antigen to obtain atomic detail,[224] but often no direct structural information is relayed by an immunoassay. Antibodies are typically grown by injecting the protein of interest into an animal, such as a rabbit, and the resulting antibodies are harvested. Many antibodies bind a distribution of protein structures,[225] which Ma et al. have invoked as an explanation for why there are not more crystallography studies of amyloid proteins using such an approach.[226] Indeed, particular populations of polymorphs might be linked to the disease, and thus, a structural assay could be invaluable.[227–229]

Almost all two-dimensional infrared spectroscopy (2D IR) experiments have been carried out in bulk solutions. Through a combination of technical advances, it has recently become possible to measure the 2D IR spectrum of a monolayer of molecules using plasmonic enhancement provided by metallic nanostructures. Some plasmonic enhancements have been reported to improve the 2D IR signal strength by $10^2$-$10^3$, alleviating the need for bulk samples.[9,46,47,199] Significant enhancements can also be obtained at interfaces using a reflection detection.[53] These two methods, *viz.* plasmonic enhancement and reflection detection, can also be combined, to afford an even larger enhancement.[9] In this report, we extend these recent technological advances to antibody surfaces, inspired by the work of the Gerwert group.[228–230] The Gerwert group utilized Attenuated Total Reflection Surface-Enhanced Infrared Absorption (ATR SEIRA) to measure the infrared spectrum of an antibody-antigen complex immobilized on a surface.[228–230] They found a correlation between the maximum frequency of the IR spectrum of the amide I and amid II bands and the progression of Alzheimer's disease, presumably due to a change in the distribution of protein structures. In this manuscript, we extend the antibody assay to detection *via* plasmonically enhanced 2D IR spectroscopy. 2D IR spectroscopy has a number of advantages over ATR or other linear IR spectroscopies.[8,231]Besides frequencies, 2D IR spectroscopy measures cross peaks and diagonal anharmonicities that are sensitive to structure. It also contains 2D lineshapes that reflect the surrounding electrostatic environment and its dynamics.[1] The signal strength also scales very differently from linear IR spectroscopy. 2D IR spectroscopy scales quadratically, rather than linearly, with extinction coefficient, which enhances the signals of excitonically delocalized vibrational modes that occur in $\alpha$-helices, $\beta$-sheets, and other secondary and tertiary structures.[1]

The newfound ability to measure monolayers with 2D IR spectroscopy makes these experiments possible. To measure 2D IR spectra of an antigen bound to an antibody, an accurate background spectrum must be collected to remove unwanted signals from the antibodies and surface-passivating proteins. For this, a flow cell is needed to monitor the same spot on the sample. This enables a precise measurement of the background with and without the presence of antigen under identical conditions. Additionally, a flow cell facilitates in situ hydrogen-deuterium exchange, making it possible to use either $H_2O$ or $D_2O$ as a solvent. Monolayer sensitivity also enables the use of a flow cell with 2D IR spectroscopy, analogous to the popular method of ATR-FTIR spectroscopy.

In this article, we present an immuno-multidimensional-infrared biosensor to measure the 2D IR spectrum of human islet amyloid polypeptide (hIAPP).[232] As with the proteins for many amyloid diseases,[225] the oligomeric intermediates of hIAPP, prior to forming amyloid fibrils, are the cytotoxic species.[233–236] Little structural information is known about the oligomers of hIAPP, but we have previously identified a transient oligomeric species with a unique ordered structure by using isotope labeling and 2D IR spectroscopy.[103,237] Transient oligomers are difficult to study because they exist at low concentrations, are in equilibrium with monomers, and are kinetically evolving towards fibrils.[238] By creating an immunosensor using antibodies that are selective for the hIAPP sequence, we extract a subset of the protein populations and record their 2D IR spectrum. We establish a new approach for studying protein structures with 2D IR spectroscopy and discover, through measurements of proteins with a single amino acid isotopically labeled, that these particular antibodies trap amyloid polymorphs.

## 7.2 Results and Discussion

The details of the spectroscopic methods and sample preparation are provided in the Supporting information. Figure 7.1 shows a schematic of the workflow used to create the immunosensor to trap and measure hIAPP. We use 3 nm thick films of thermally evaporated gold on $CaF_2$ as the substrates for the immunochemistry.[9] There are many antibodies specific to hIAPP. We use the anti-amylin polyclonal antibody (Thermo Fisher Scientific, PA1-37075), which is derived from Rabbit anti-IgG and raised against the N-terminal sequence of synthetic hIAPP. The antibody is incubated in the presence of $CS_2$ in phosphate buffered saline (PBS) for 24 hours to chemically link the amine side chains of the lysine residues to the gold surface,29 as shown in Figure 7.1(a-b). The $CS_2$ reacts with the amine groups, and the thiol links the antibodies to the gold before being rinsed three times with PBS. To prevent non-specific binding of the amylin, the antibody functionalized substrate is soaked in 1% casein in deuterated buffer for 1 hour (Figure 7.1(c)), before again being rinsed three times. Following this procedure, 2D IR spectra are collected in a pump-probe geometry using a mid-IR pulse shaper as described in the Supporting Information. The intensity of 2D IR signals confirmed that the antibody tethering reaction was complete in <12 hours. We also found that PBS buffer as the solvent for antibody tethering gave stronger 2D IR signals than ethanol, used previously.[239] 2D IR spectroscopy also confirmed that the casein saturated all available binding sites, deduced by repeating this step (between Figure 7.1(b) and (c)) in the sample preparation multiple times. Signals only increased in 2D IR measurements after the first wash indicating that the available binding sites are occupied.

The above procedure creates an antibody coated plasmonic surface with minimal amounts of non-specific binding. Because the antibody and casein blocking agents are much larger proteins than the hIAPP antigen, the background signal is expected to be 10-100 larger than the signal from hIAPP from the estimate of the molecular weight provided by the manufacturer. To remove this background, we use a flow cell. First, a background spectrum

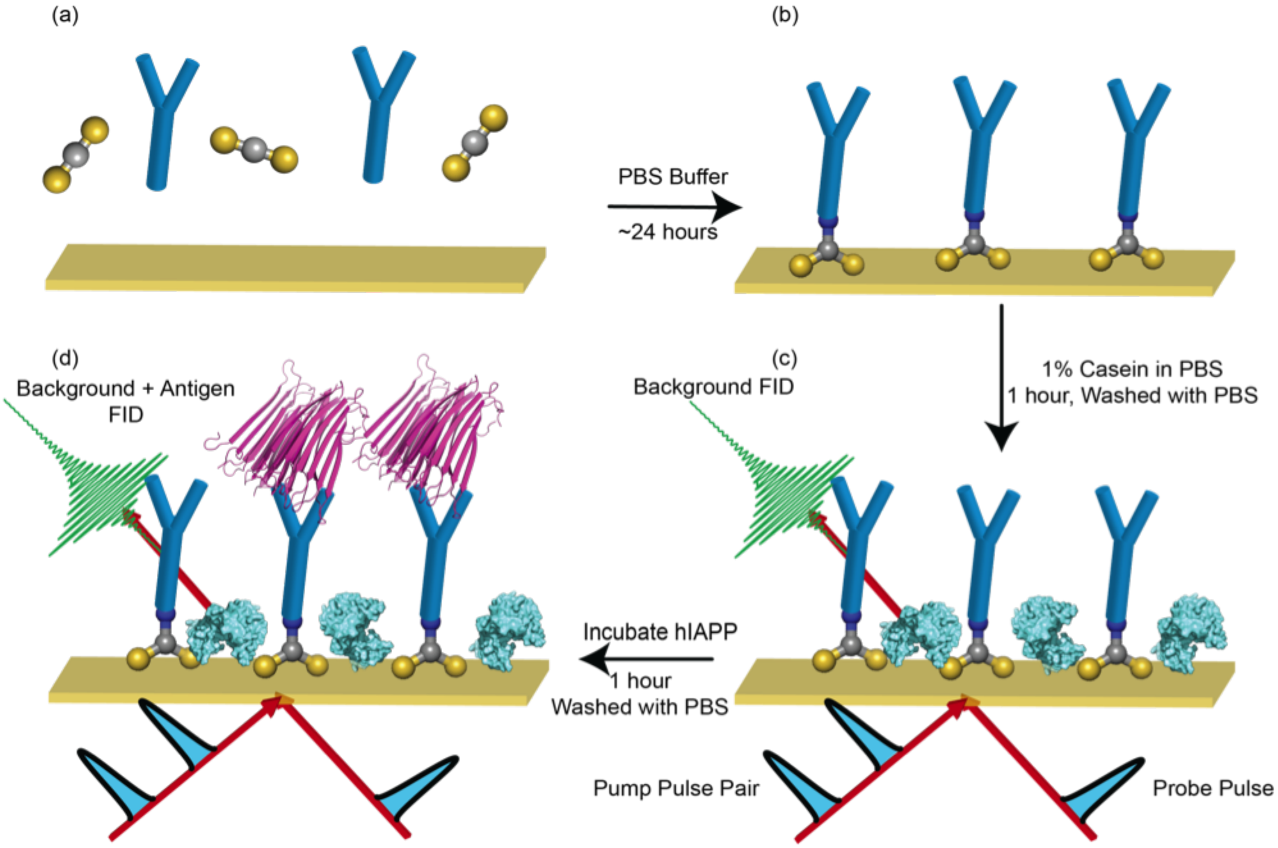

Figure 7.1: (a) Diagram of the antibodies on the gold surface with trapped amylin. (b) Design of the flow cell used to introduce the analyte on to the gold-coated substrate.

is collected and then the analyte is added and a second spectrum is collected, as shown in Figure 7.1(d). As has been established in the FTIR community, extremely small changes in ΔOD can be measured using a flow cell. A flow cell is particularly important for 2D IR measurements, because the 2D IR signals depend on the overlap of the laser pulses in the sample and other variables that alter the signal magnitude. Thus, a flow cell minimizes systematic subtraction errors. The pump-probe signal strengths measured of the antibody and casein background is 1-3 ΔmOD, with the measured change in ΔOD (ΔΔOD) created by the antigen peptide on the order of 10-100 $\Delta\Delta\mu$OD.

With the above procedure, we first tested the immunosensor against an aggregated sample of hIAPP, which we have previously reported on numerous occasions.[25,103,237,240] We aggregated 1 mM of hIAPP, synthesized according to previously published methods,[120,241] in buffer overnight to create amyloid fibrils. Amyloid fibrils are extremely stable species and so under these conditions very small amounts of monomers and oligomers would be expected. The aggregated sample was flowed over the antibody substrate and allowed to bind for 1 hour before copious rinsing with deuterated PBS buffer. Figure 7.2 compares the 2D spectra of the sensor before (a) and after (b) addition and rinsing of the amylin. The peak of the antibody and casein is centered at around 1645 $\text{cm}^{-1}$. There is a small excited state absorption background from the 3 nm gold;[51] this additional background signal is smaller than the amylin signal, and not noticeable in these figures. Upon addition of the hIAPP, the spectrum broadens to lower frequencies. Subtracting (a) from (b), reveals the difference 2D IR spectrum in Figure 7.2(d), which is the spectrum of the hIAPP fibrils bound to the antibody with the antibodies, casein and the excited state absorption background eliminated. The difference spectrum is dominated by a peak at 1629 $\text{cm}^{-1}$ with a minor peak at 1650 $\text{cm}^{-1}$. These experiments establish that the background from the antibody can be reliably subtracted to give the spectrum of the bound antigen.

In Figure 7.2(e), the 2D IR spectrum is shown for the bulk solution sample of hIAPP

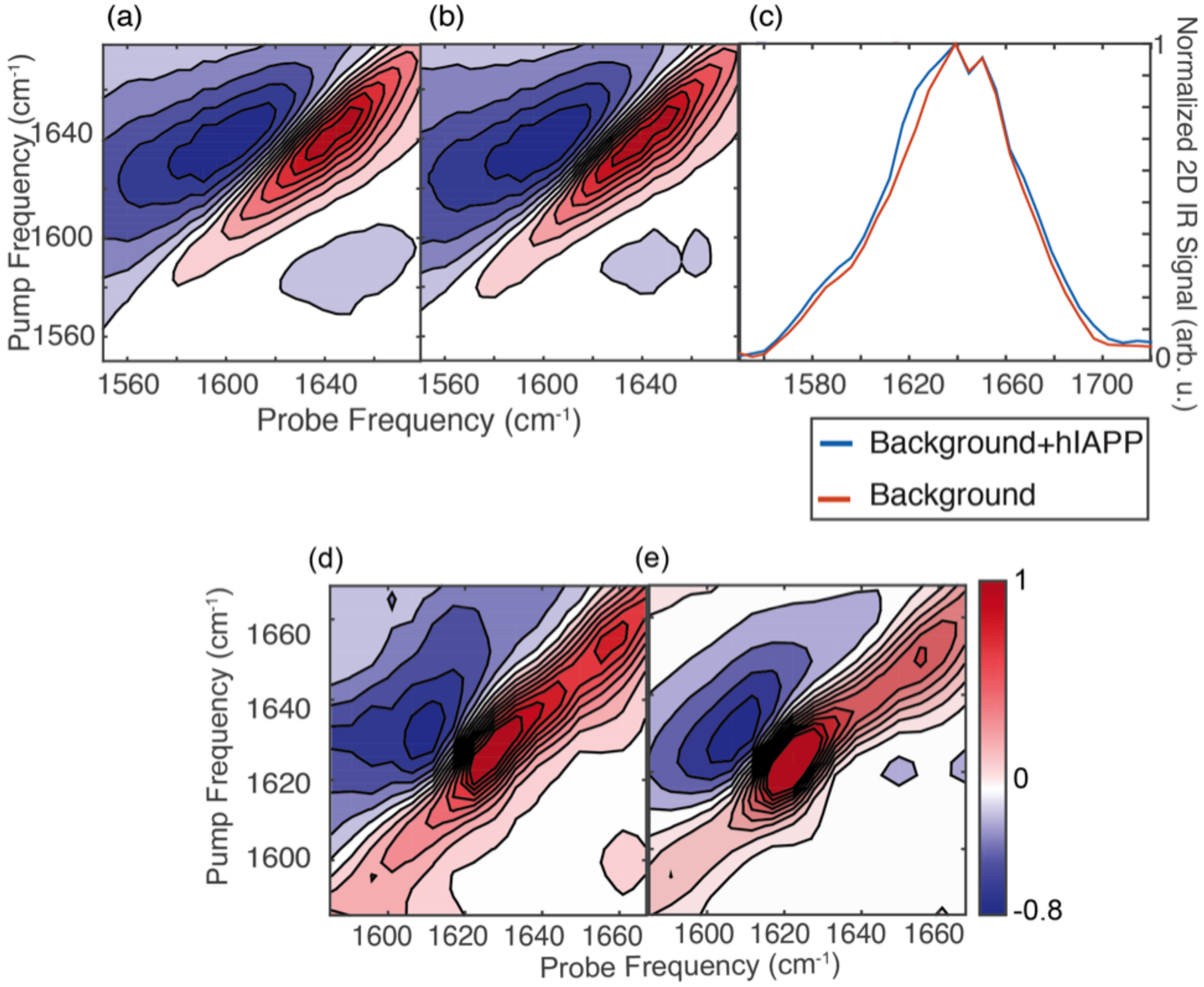

Figure 7.2: (a) 2D IR spectrum of the antibodies and casein on the gold surface. (b) 2D IR spectrum of the same sensor, but after addition and rinsing of the isotope labeled amylin solution. (c) Normalized diagonal slices of the 2D spectra shown in (a) and (b). (d) 2D IR difference spectrum generated by subtracting (a) from (b). (e) Solution 2D IR spectrum of the same amyloid fibrils that bound to the antibody in (d).

fibrils measured above, but immediately prior to passing through the flow cell. Figure 7.2(d-e) compares the 2D IR spectra of the hIAPP in the bulk and the subtracted 2D spectrum of the bound peptides. We observe that the bulk and surface spectra have very similar line shapes, with a 4 $\text{cm}^{-1}$ difference in the peak frequency; The solution spectrum is dominated by a peak at 1625 $\text{cm}^{-1}$ while the bound peptide exhibits a peak at 1629 $\text{cm}^{-1}$. It is possible that the frequency difference is a result of the structure being deformed upon binding to the antibody. However, previous experiments using similar immuno-sensors have suggested that the binding does not significantly alter the secondary structure and antibodies used for x-ray crystallography are presumed not to alter the structure. Instead, it is more likely that the antibody binds to a subset of hIAPP structures. The amide I frequency of amylin depends on the aggregation conditions, which alter the amyloid fibril structure. For example, the amide I frequency ranges by 1614-1624 $\text{cm}^{-1}$ depending on the conditions under which the fibrils are formed, with higher concentrations typically resulting in a lower frequency, reflecting more ordered $\beta$-sheet structure.[163] Amylin also has different structural polymorphs that exhibit different frequencies at the Valine-17 position.[242,243] Consequently, there is a natural degree of heterogeneity in structure that correlates to the amide I frequency. Consequently, the frequency difference between the bulk- and antibody-bound aggregates likely indicates that the antibody preferentially binds to a subset of aggregate structures.[163] The isotope labeled frequencies presented below support this hypothesis.

Isotope labels are often used to obtain residue-specific structural information with FTIR and 2D IR spectroscopy.[244–247] With experiments like these in mind, we measured hIAPP synthesized with a $^{13}\text{C}^{18}\text{O}$ isotope labeled in the backbone carbonyl of the G24 residue. This label effectively decouples the single amino acid residue from the rest of the amide bonds and shifts the local mode frequency about 65 $\text{cm}^{-1}$. Isotope labels are often used in 2D IR spectroscopy as a probe of structure and local environment.[248] We again ensured that the isotope labeled peptide was in a fibrillar structure by aggregating the hIAPP overnight, again at 1 mM concentration. hIAPP typically aggregates in less than 6 hours. Figure 7.3 compares the 2D IR spectra of aggregated hIAPP in solution (a) and the difference spectrum when bound to antibody (b). Interestingly, the spectra are not identical. The solution feature shows a distinct peak at 1585 cm$^{-1}$, consistent with our previously published results in the fibril state.[103] Upon binding, we observe two peaks, one at about 1585 cm$^{-1}$ and another at 1578 cm$^{-1}$. Thus, we conclude that the antibodies are binding two conformations of hIAPP, one of which is the majority species in solution. The 1578 cm$^{-1}$ peak indicates that the G24 isotope labels are more strongly coupled compared to the final fibril obtained in solution, in which G24 residues in a disordered loop.[8] These observations are inconsistent with the antibody altering the conformation of a single structure, because one would still not expect two different isotope labeled frequencies. Instead, we conclude that these antibodies are binding at least two different structures and enriching a subpopulation of one polymorphic structure. Additional labels could be used for a more thorough structural investigation. antibodies are generated using a polypeptide that matched the N-terminal sequence of hIAPP. Additional polymorphs might be observed using other antibodies if the polymorphs are different in other regions outside of the G24 residue.

We next added hIAPP to the antibody sensor prior to aggregation, before fibrils have formed. The peptide was dissolved in PBS buffer at a concentration of 33 $\mu$M and immediately introduced to the antibody sensor. Figure 7.4 shows the spectrum obtained after subtraction. We observe an inhomogenously broadened peak at 1646 cm$^{-1}$ with a small shoulder at about 1660 cm$^{-1}$. Without antibodies, 33 $\mu$M is too low of a concentration to obtain a spectrum of hIAPP in the bulk, but the antibody bound spectrum looks nearly identical to our group's measurements on the early-aggregation timescales of hIAPP in bulk solution at a 1 mM concentration.[240] Thus, we conclude that the antibody binds structure of the disordered state bound to the antibody is similar to that in solution, and that the oligomeric structure studied at 1 mM concentrations with standard transmission 2D IR spec-

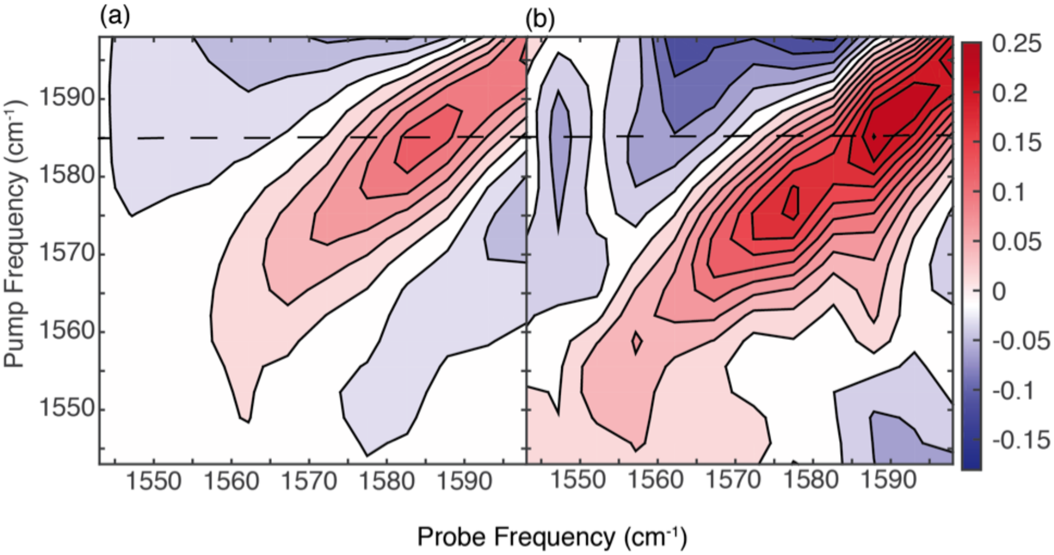

Figure 7.3: Difference spectrum of the G24 labeled hIAPP in the isotope labeled region of the amide-I spectrum. The spectrum is normalized to the most intense diagonal feature.

troscopy is equivalent to the oligomeric structures that exist at 33 $\mu$M. These experiments validate the use of high concentration studies for studying oligomer structure.[238]

We previously published data proposing an aggregation mechanism in which all fibrillar polymorphs originate from the same oligomer structure.[243] The data presented here support that hypothesis, because we see no polymorphs when the antibodies are incubated with hIAPP during the lag time, prior to fibril formation when only oligomers are present. Polymorphs are observed when the antibodies are exposed to fibrils, implying that polymorphs arise after formation of the oligomers, consistent with our previous publication.[243] Additional studies with other antibodies might be useful to further test that hypothesis.

We also performed several control experiments. To confirm that the Amylin Polyclonal Antibodies are specific to hIAPP as advertised by the manufacturer, we added a concentrated solution of hen egg white lysozyme (HEWL, 1 mg/ml) and observed no change in the background signal (Supporting information, Figure 7.5). Additionally, we added a concentrated solution of hIAPP (2 mM) with only casein added and no antibody. We observed no non-specific binding of hIAPP to the casein or bare gold substrate in the difference 2D spec-

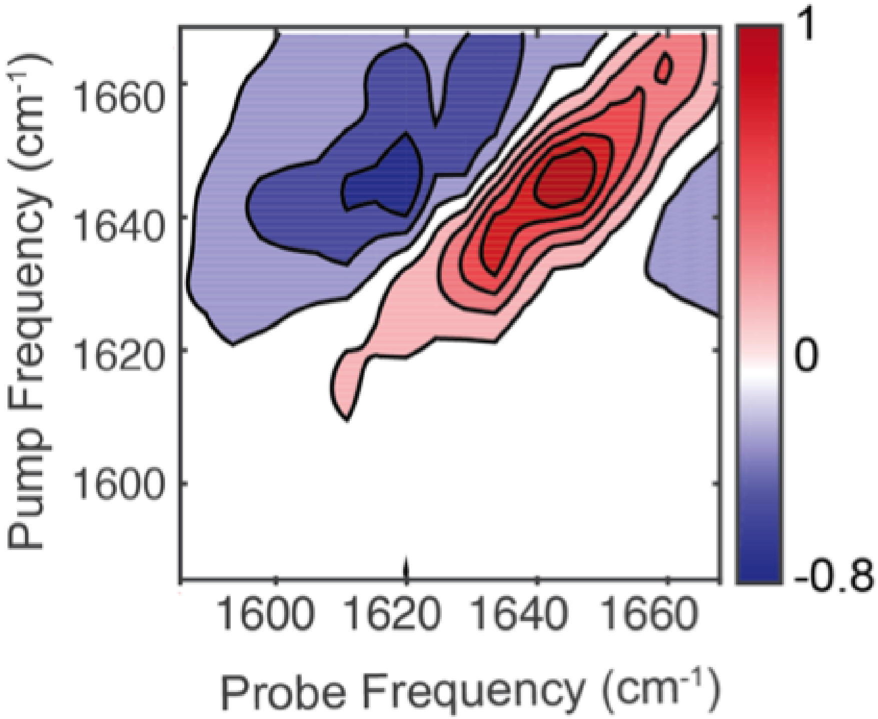

Figure 7.4: 2D IR difference spectrum of monomeric hIAPP bound to the immunosensor.

trum (Supporting Information, Figure 7.6). Thus, the spectra above are indeed generated by hIAPP.

In conclusion, we have presented a 2D IR immuno-biosensor to extract and investigate the structure of hIAPP. We show that 2D IR spectrometers have sufficient signal-to-noise to subtract off the antibody background and can trap hIAPP in both its aggregated and oligomeric structures. The signal-to-noise also enables data collection on singly isotope labels polypeptides for residue-specific structural information. For a G24 labeled hIAPP, we observe two isotope labeled peaks, indicating that the antibodies are binding two different fibrillar polymorphs. In contrast, antibodies soaked in hIAPP prior to aggregation produced spectra of oligomers that resembled the bulk solution, supporting a mechanism in which the fibrillar polymorphs arise after a common oligomer structure.[243] There exist many antibodies specific for hIAPP that could be used to further investigate the distribution of polymorphs.

Antibodies also exist for many other amyloid-forming proteins to which this technique can be extended and might be correlated with the progression of the disease.[228] The plasmonic enhancement that enables monolayer sensitivity for immobilized structures at the surface allows for a flow cell to be used for proteins and opens up many new avenues of exciting research using 2D IR spectroscopy as a probe of structure. We anticipate that this will enable researchers to use these immuno-sensors to enable the study of protein structures extracted from blood serum and tissues: a routine procedure in biology.

## 7.3 Supporting Information

### 7.3.1 2D IR Measurements

The pulse-shaping based 2D IR spectrometer has been described in detail previously,1 with a few minor modifications. A Ti:Sapphire regenerative amplifier (Libra, Coherent) generates 50 fs pulses centered at 800 nm. The average power is about 3.5 W with about 3.5 mJ per pulse. This is used to pump a commercial optical parametric amplifier (OPA, Topas, Light Conversion) to generate a combined 850 mW of signal and idler pulses. A home-build difference frequency generation (DFG) apparatus based on AgGaS2 is used to generate mid-IR light centered at about 6050 nm with a pulse energy of about 15 $\mu$J. The FWHM of the mid-IR spectrum is typically around 250 cm$^{-1}$ and the pulse duration about 100 fs measured with a home-built FROG set up. The mid-IR light is split in to separate pump and probe lines with a 90/10 wedged CaF$_2$ beam splitter. The pump light is directed in to a home-build mid-IR 4f pulser shaper that utilizes a Ge acousto optic modulator (AOM). The shaper allows for amplitude and phase modulation in the frequency domain on a shot-to-shot basis. The pump pulse is shaped in order to generate a pump pulse pair with computer-controlled time delays and relative phases. The delays are scanned on a shot-to-shot basis out to 3.1 ps. We perform measurements in the rotating frame by changing the phase of the moving pulse as a function of the pump pulse time delay to allow unambiguous undersampling of the experimental interferograms. The measurements reported are collected with a rotating frame of 1500 $cm^{-1}$ and 40 fs time steps. The pump frequency axis is corrected with the rotating frame frequency during data processing. This significantly reduces the amount of time needed to collect a single 2D spectrum.

The pump and probe are spatially overlapped at the sample with gold parabolic mirrors. The relative timing between the pump and probe pulses is controlled with a motorized translation stage. For the experiments reported in this paper, the waiting time is set to maximize the transient absorption signal, which corresponds to a waiting time of about 150 fs for the pulse durations used here. The signal is self-heterodyned with the probe pulse and dispersed on a 32x1 MCT array detector.3 The spectra in the main text were averaged for about 1 hour.

### 7.3.2 Preparation of Gold Substrates

3 nm thick-gold films were deposited on CaF2 substrates by thermal evaporation of gold pellets purchased from Kurt Lesker (99.999% purity). The base pressure prior to deposition was 4e-7 torr. A deposition rate of 0.1 Angstrom/s was maintained and the thickness was monitored using a quartz crystal microbalance. The rotational speed of the stage was 60 rpm.

### 7.3.3 Synthesis of hIAPP

Both the isotope and native hIAPP was synthesized with FMOC solid-phase peptide synthesis using an automated microwave assisted peptide synthesizer (Liberty Blue, CEM) according to previous reports.[120] The isotope-labeled amino acids were synthesized from $^{13}C$ C1-labeled FMOC protected amino acids (Cambridge Isotope Laboratories). The $^{18}O$ was exchanged using 18O water. In contrast to previous methods, we used 1,4 dioxanes containing 4 M HCl for anhydrous acidification. Synthesized peptides were cleaved from the resin and side-chain protecting groups removed using an acidic cleavage cocktail comprised of trifluoroaceticacid, thioanisole, 1,2-ethanedithiol, and anisole in a 90:5:4:1 ratio by volume, respectively, at 37°C for 30 minutes in a microwave-assisted cleavage system (Accent, CEM). The synthesized peptide was incubated in a 1:1 ratio of dimethylsulfoxide (DMSO) and 20% acidic acid for 12 hours to ensure proper formation of the disulfide bond. Peptides were purified using reverse-phase HPLC using a C18 preparative column (XSelect, CSH, Waters). Two rounds of purification were employed to guaranteed purity and the masses of the peptides were confirmed with MALDI-TOF-MS.

### 7.3.4 Functionalizing the Gold Surface with Anti-Amylin Antibodies

All chemistry to link the antibodies to the surface was completed in a purchased flow cell. The anti-amylin antibodies were used as received without further purification. A 300 $\mu$l solution of antibodies in PBS buffer was used for each experiment. 285 $\mu$l of PBS buffer was mixed with 10 $\mu$l of the antibody stock solution (1 mg/ml) and 5 $\mu$l of CS2. Approximately 100 $\mu$l of the mixture was then introduced through the flow cell to completely cover the substrate surface. Antibody solution was used within 24 hours of preparation.

### 7.3.5 Control Experiments with Hen Egg White Lysozyme

To test the specificity of the purchased anti-amylin antibodies, we completed the experiments reported in the main text, but instead of using the hIAPP, we used Hen Egg White Lysozyme (HEWL). This experiment tests the ability of the antibodies to specifically extract hIAPP from a complex solution. We purchased the HEWL from Sigma Aldrich and used without further purification. The sensor was prepared as stated in the preceding section, and then a 5 mM solution of HEWL was incubated on the antibody-functionalized sensor for about

2 hours. The solution was then rinsed with PBS buffer and spectrum collected. Figure 7.5 shows the difference spectrum obtained after soaking the antibodies. We observe to 2D IR signal from the HEWL, indicating that the antibody sensor is specific to hIAPP. We note that the anti-amylin will not likely distinguish between amylin of different species because of similarities in the N-terminal sequence.

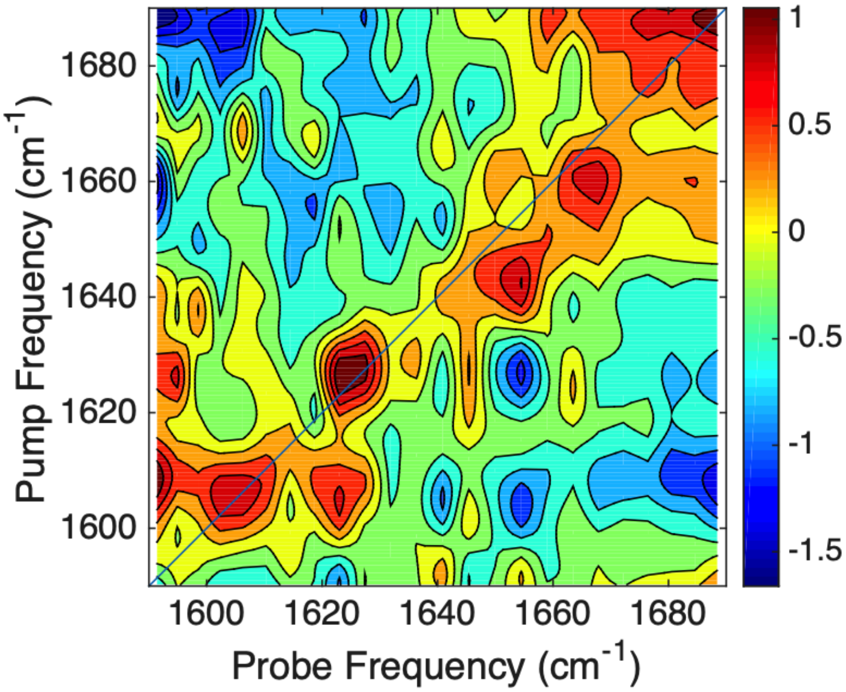

Figure 7.5: Difference spectrum of the added HEWL. No signal is observed.

### 7.3.6 Control Experiments to Determine Binding of hIAPP to Casein

To confirm that the hIAPP cannot bind to the casein or residual free binding sites on the gold, we processed the antibody sensor as in the main text, but instead of introducing the anti-amylin, we introduced casein to be chemically linked to the gold surface. Although the exact concentration of the antibody in buffer is not known and cannot be determined, we approximated the same conditions by assuming the antibody has the same molecular weight as rabbit IgG. The sensor was processed with the casein to block free binding sites identically to the main text. hIAPP was added at 5 mM concentration to maximize the likelihood of binding. Figure 7.6 shows the residual 2D IR difference spectrum. We observe no signal and thus conclude that the hIAPP does not bind to the gold or casein.

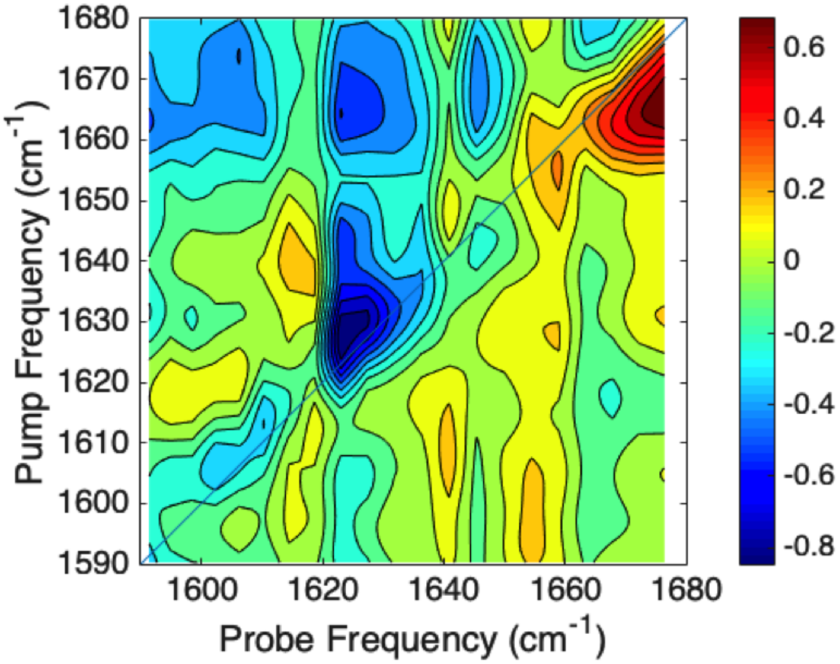

Figure 7.6: Difference spectrum of the added hIAPP to a sensor without the anti-amylin. No discernible signal is present.

# Chapter 8

# High Repetition Rate 2D IR Spectroscopy with a Yb:KGW Amplifier

Contents

## 8.1 Introduction

Two-dimensional infrared spectroscopy is a nonlinear, third-order technique used to study molecular structure and dynamics. Researchers in diverse fields such as biophysics, materials science, and chemical physics are continuing to find useful applications of 2D IR spectroscopy in their respective fields.

One factor limiting the wide spread application of 2D IR is time necessary to collect spectra and the relatively high concentrations needed for good signal-to-noise. Additionally, new applications of 2D IR microscopy will almost certainly require increased speeds in data acquisition. Titanium sapphire regenerative amplifiers, the most common source of high energy mid-IR pulses, are limited to a few kilohertz. Such a repetition rate limits the minimum change in optical density (ΔOD) one can measure. This effectively limits the minimum sample concentration and limits the technique to oscillators with relatively high transition dipole strengths. Ytterbium doped amplifiers are one potential route for extending 2D IR spectroscopy to repetition rates of hundreds of kilohertz.

In this article, we present the design of a home-built optical parametric amplifier that is pumped by a Yb:KGW amplifier at 50-200 kHz. Difference frequency generation (DFG) of the ouput signal and idler generate mid-IR pulses in the 5-6 $\mu$m range, although 5-10 $\mu$m is possible. The 2-4 $\mu$m range can also be accessed with the idler of the OPA directly. We also demonstrate the acquisition of 2D IR spectra at 50 kHz and compare the signal-to-noise of comparable systems on a traditional Ti:Sapph apparatus. Our results indicate that high-repetition rate 2D spectroscopy leads to improved signal-to-noise even at the cost of lower pulse energy and therefore, smaller signals. Additionally, the home-built OPA coupled with the relatively low cost Yb:KGW amplifier offers an economical approach for more researchers to explore the field.

## 8.2 Methods

### 8.2.1 OPA Design

Our design of the optical parametric amplifier is based on the paper by Mucke et al.[249] Figure 8.1 shows a detailed schematic of the OPA. A Pharos (Light Conversion, 50-200 kHz, 20 W, max pulse energy 400 $\mu$J, 290 fs) is used to pump the OPA. To prevent optical damage, we only pump with about 13 W by internally attenuating the 20 W output. A small portion of the fundamental, ∼0.2 W, is used to generate white light in a 10 mm YAG crystal, which is used to seed the first stage. The White light pulse is stretched in an SF11 stertcher. The majority of the fundamental is sent through a Type II BBO crystal to generate 3 W of 515 nm. The 515 nm and white light continuum are mixed in a Type-II $\beta$-barium borate (BBO) crystal. To generate mid-IR pulses at 5 $\mu$, 737 nm light is amplified to also generate 20 mW of idler at 1.7 $\mu$. The idler in the first stage is used to seed the second stage which consists of a Type-II potassium titanyl phosphate (KTP). The remaining 1030 nm is mixed with the seed to generate 2 W of signal and idler at, 1.7 and 2.6 $\mu$m, respectively. These pulses are then separated with a dichroic mirror and recombined to be focused in to a Gallium selenide crystal (GaSe). With the powers reported above, we routinely generate 55-60 mW of mid-IR, which corresponds to about 1.2 $\mu$J per pulse. A low-pass filter is used to separate the signal and idler from the mid-IR.

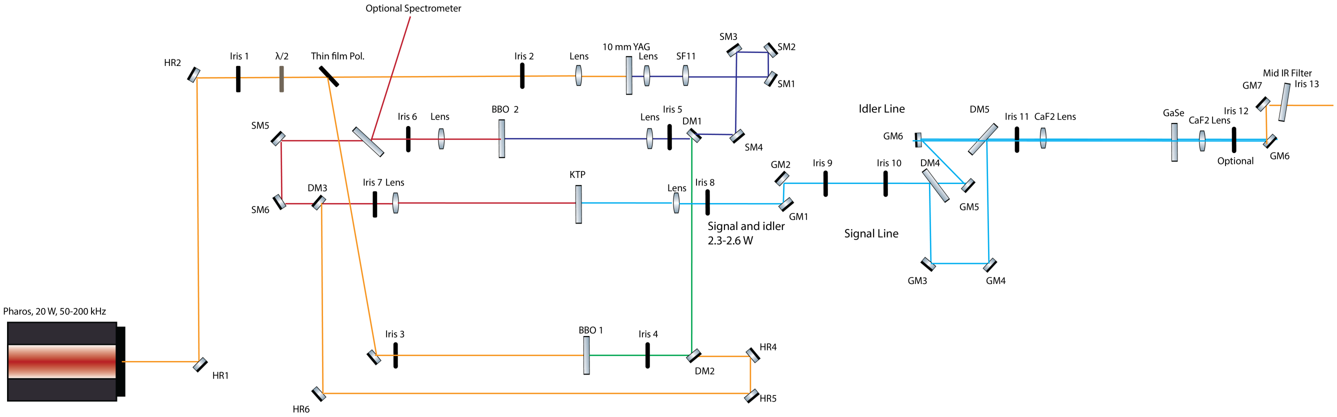

Figure 8.1: Schematic and beam diagram for the 100 kHz mid-IR OPA. HR: 1030 High Reflector, $\lambda/2$: Half Wave plate, SM:Silver mirror, DM: Dichroic mirror, GM: Gold Mirror

.

### 8.2.2 2D IR Spectroscopy

Our approach to doing 2D IR spectroscopy has been described in detail previously. In brief, we split the mid-IR pulse in to pump and probe pulses with a $CaF_2$ beam splitter. To generate the two pump pulses, we use a $4f$ Germanium pulse shaper to modulate pulses in the frequency domain. This generates a pair of pulses with computer-controlled time-delays and relative phases. The data presented in this chapter is collected at 50 kHz as we are limited by the read out rate of our MCT mid-IR detector.

## 8.3 Results

### 8.3.1 Pulse Bandwidth

Figure 8.2 shows a representative spectrum of the mid-infrared light centered at 2080 cm$^{-1}$. We observe that we generate about 115 cm$^{-1}$ of bandwidth at 4.8 $\mu$m. More bandwidth could be obtained by optimizing crystal thicknesses and adding in slight angles between seed and pump pulses.

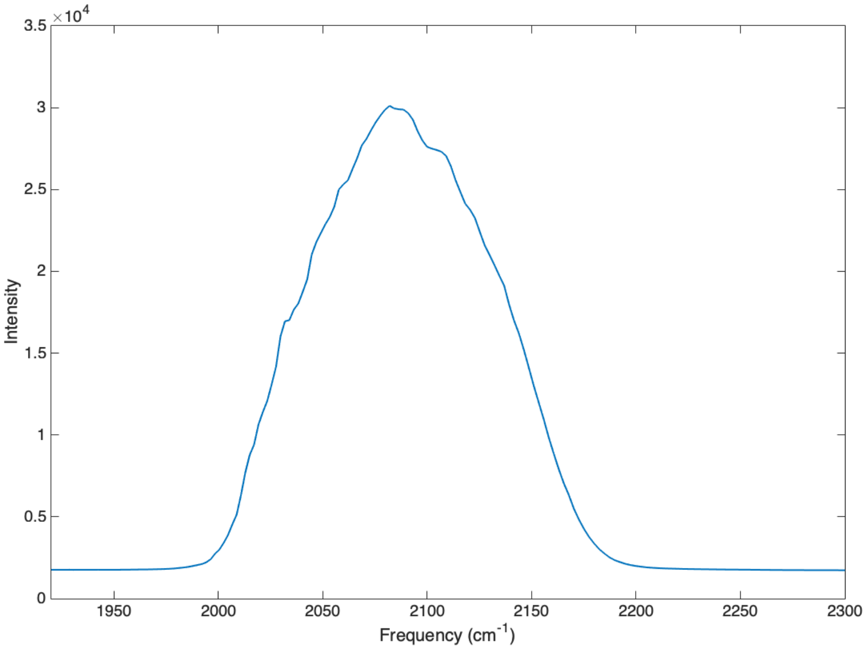

Figure 8.2: Measured Spectrum of the mid-IR pulse generated from the OPA in Figure 8.1

.

### 8.3.2 Pulse Characterization

To characterize the pulse duration, we use an Indium Gallium Arsenide (InGaAs) detector with a band gap of 2.6 $\mu$m. When illuminating with 5 $\mu$m light, a current will only be measured when there is a two-photon interaction. This makes it a convenient detector for measuring the pulse's autocorrelation. We use the frequency calibrated pulse shaper to scan between ± 2 ps in 4 fs steps. Figure 8.3 shows a representative autocorrelation after dispersion compensation in the shaper. From inspection, we can observe that our pulse is ∼250 fs at full width half maximum. This is consistent with mid-IR pulse durations with Yb:KGW sources.[250]

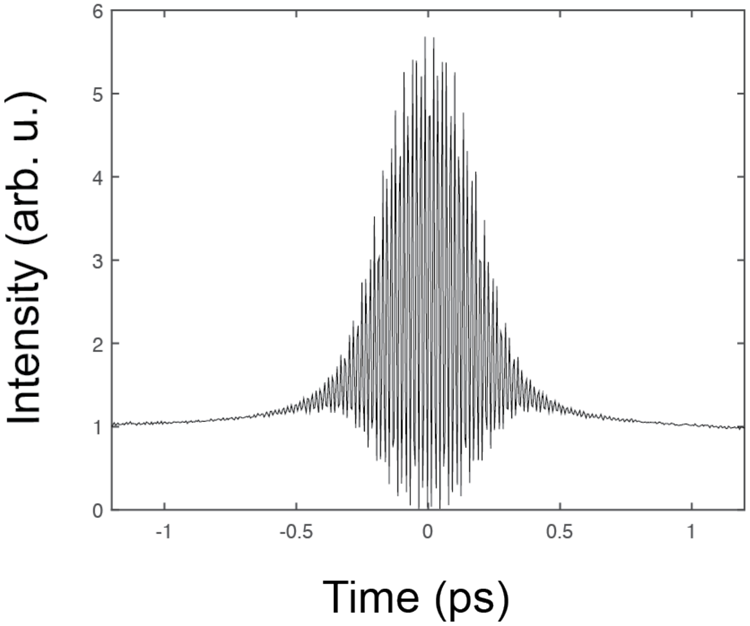

Figure 8.3: Measured Autocorrelation of the mid-IR pulse. The extracted duration is about 250 fs.

.

### 8.3.3 2D IR Measurements

To begin with, we study the 2D IR spectra of some transition metal carbonyl molecules. Specifically, we use pentachlororhenium carbonyl (ReCO). We set the concentration of ReCO in chloroform to so that the optical density (OD) is ∼ 0.9. The measured transient absorption signal for this sample, with 250 nJ of shaped mid-IR pump light, was about 40 ΔmOD. With a strong signal, the time needed to average is extremely low. Indeed, if we obtain high signal-to-noise 2D spectra in a single laser shot per coherence time. Figure 8.5 shows a single shot per coherence time 2D IR spectrum for the same sample as in Figure 8.4. In contrast to our past measurements of similar samples, it is clear that meaningful chemical information can be extracted from this spectrum that was collected in 8 ms.

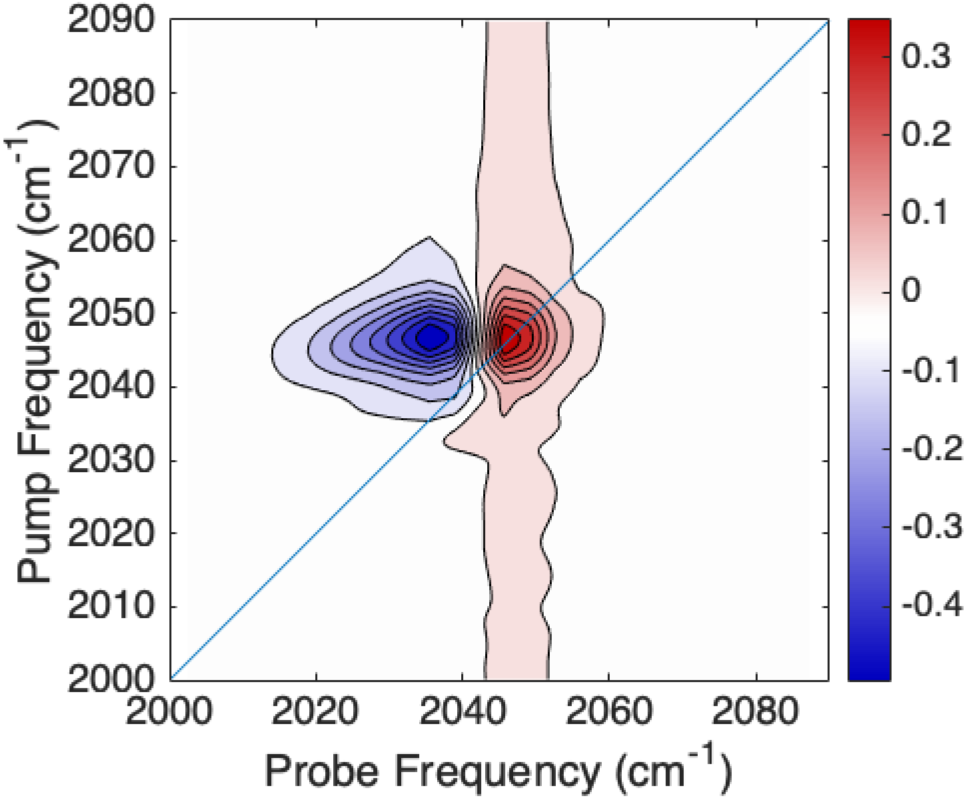

Figure 8.4: 2D IR spectrum of ReCO averaged for 1 minute.

.

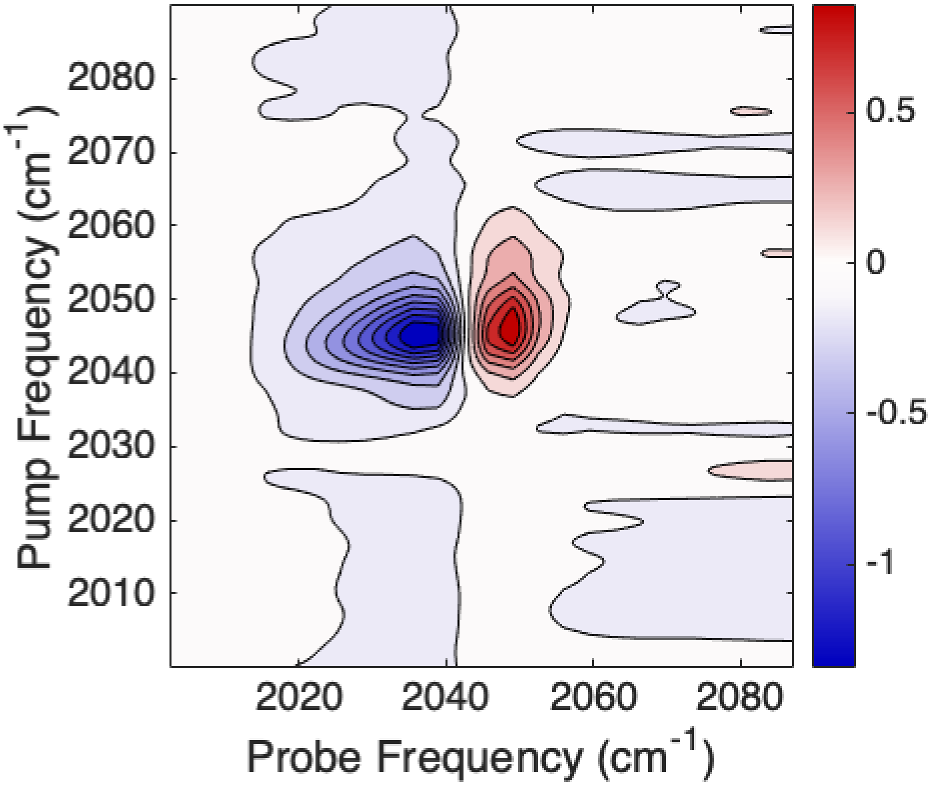

Figure 8.5: Single shot 2D IR spectrum of ReCO collected with the Yb:KGW amplifier. The spectrum is collected in approximately 8 ms.The signal-to-noise is approximately 130.

.

# Appendix A

# Publications

[12] Farrell, K.; **Ostrander, J.S.**; Jones, A.C; Zanni, M.T. ”Design and Implementation of a 100 kHz 2D IR Spectrometer” *In Preparation*

[11] **Ostrander, J.S.**; Lomont, J.P.; Rich, K.L.; Feingold, B.R.; Petti, M.K; Birdsall, E.R.; Zanni, M.T. ”Monolayer Sensitivity Enables a 2D IR Immuno-biosensor for Studying Protein Structures: Application to Amyloid Polymorphs” *Submitted*

[10] Alperstein, A.M.; **Ostrander, J.S.**; Zhang, T.O.; Zanni, M.T. ”Amyloid found in human cataracts with two-dimensional infrared spectroscopy” *Proc. Natl. Academy of Sciences. 16*, (14) 6602-6607 (2019)

[9] Petti, M.K.; **Ostrander, J.S.**; Saraswart, V.; Birdsall, E; Rich, K.L.; Lomont, J.P.; Arnold, M.S.; Zanni, M.T. ”Enhancing the signal strength of surface sensitive 2D IR spectroscopy” *J. Chem. Phys.*, *150*, 024707 (2019)

[8] Saraswat, V.; Jacopbergger, R.; **Ostrander, J.S.**; Hummell, C.; Way, A.; Zanni, M.T.; Arnold, M.S. ”Water Permeation Through Size-Controlled Graphene Oxide Laminates” *ACS Nano*, *122*, 7855-7865. (2018)

[7] Lomont, J.P.; Rich, K.L.; Maj, M., Ho, J.J., **Ostrander, J.S.**; Zanni, M.T. ”2D IR Spectroscopy Can Distinguish Stable A$\beta$ Fibers from Less Stable $\beta$-Sheet Rich Oligomers” *J. Phys. Chem. B*, *122*, 144-153. (2018)

[6] Lomont, J.P.; **Ostrander, J.S.**; Ho, J.J.; Petti, M.K.; Zanni, M.T. ”Not All $\beta$-sheets Are the Same: Amyloid Infrared Spectra, Transition Dipole Strengths, and Couplings Investigated with 2D IR Spectroscopy” *J. Phys. Chem. B*, *121*(38), 8935-8945. (2017)

[5] **Ostrander, J.S.**; Knepper, R.; Tappan, A.S.; Kay, J.J. Zanni, M.T.; Farrow, D.A. ”Energy Transfer Between Coherently Delocalized States in the Explosive Pentathyritol Tetranitrate (PETN) Revealed with 2D IR Spectroscopy” *J. Phys. Chem. B*, *121*(6), 1352-1361. (2017)

[4] Ghosh, A..; **Ostrander, J.S.**; Zanni, M. T. “Watching Proteins Wiggle: Mapping Structures with Two-dimensional Infrared Spectroscopy.” *Chemical Reviews* **2017**, *117*(16), 10726-10759.

[3] **Ostrander, J.S.**; Serrano, A.L..; Ghosh, A..; Zanni, M. T. “Spatially Resolved 2D IR Spectroscopy via Wide-Field Microscopy” *ACS Photonics* **2016**, *3*(7), 1315-1323.

[2] Ghosh, A..; Serrano, A.L..; Oudenhoven, T.A.; **Ostrander, J.S**.; Eklund, E.C.; Blair, A.F.; Zanni, M. T. “Experimental Implementations of 2D IR Spectroscopy through a Horizontal Shaper Design and a Focal Plane Array Detector” *Optics Letters* **2016**, *41*(3), 524.

[1] Serrano, A.L..; Ghosh, A..; **Ostrander, J.S.**; Zanni, M. T. “Wide-field FTIR Microscopy with mid-IR Pulse Shaping.” *Optics Express* **2015**, *23*(14), 17815-17827.

# Bibliography

[1] Ghosh, A.; Ostrander, J. S.; Zanni, M. T. *Chemical Reviews* **2017**, *117*(16), 10726–10759.

[2] Fersht, A. *Structure and Mechanism in Protein Science: A Guide to Enzyme Catalysis and Protein Folding;* W.H. Freeman, 1st ed., 1998.

[3] Ginsberg, N. S.; Cheng, Y.-C.; Fleming, G. R. *Accounts of Chemical Research* **2009**, *42*(9), 1352–1363.

[4] Manor, J.; Mukherjee, P.; Lin, Y.-S.; Leonov, H.; Skinner, J. L.; Zanni, M. T.; Arkin, I. T. feb **2009**, *17*(2), 247–254.

[5] Hamm, P.; Zanni, M. T. *Concepts and Methods of 2D Infrared Spectroscopy;* Cambridge University Press: New York, 1 ed., 2011.

[6] Cho, M. *Two-Dimensional Optical Spectroscopy;* CRC Press: Boca Raton, FL, 1st ed., 2009.

[7] Baiz, C. R.; Kubarych, K. J.; Geva, E. *Journal of Physical Chemistry B* **2011**, *115*(18), 5322–5339.

[8] Lomont, J. P.; Ostrander, J. S.; Ho, J. J.; Petti, M. K.; Zanni, M. T. *Journal of Physical Chemistry B* **2017**, *121*(38), 8935–8945.

[9] Petti, M. K.; Ostrander, J. S.; Saraswat, V.; Birdsall, E. R.; Rich, K. L.; Lomont, J. P.; Arnold, M. S.; Zanni, M. T. *The Journal of Chemical Physics* **2019**, *150*(2), 024707.

[10] Ostrander, J. S.; Knepper, R.; Tappan, A. S.; Kay, J. J.; Zanni, M. T.; Farrow, D. A. *Journal of Physical Chemistry B* **2017**, *121*(6), 1352–1361.

[11] Schatz, G. C.; Ratner, M. A. *Quantum Mechanics in Chemistry;* Dover: Mineloa, NY, 2002.

[12] Grechko, M.; Zanni, M. T. *The Journal of Chemical Physics* **2012**, *137*(18), 184202.

[13] Lee, C.; Cho, M. *Journal of Physical Chemistry B* **2004**, *108*(52), 20397–20407.

[14] Torii, H.; Tasumi, M. *The Journal of Physical Chemistry* **1990**, *94*(1), 227–231.

[15] Barth, A. *Biochimica et Biophysica Acta (BBA) - Bioenergetics* **2007**, *1767*(9), 1073–1101.

[16] Jansen, T. L. C.; Dijkstra, A. G.; Watson, T. M.; Hirst, J. D.; Knoester, J. *Journal of Chemical Physics* **2006**, *125*(4), 1–9.

[17] Mukamel, S. *Annual Review of Physical Chemistry* **2000**, *51*, 691–729.

[18] Mukamel, S.; Abramavicius, D. *Chemical Reviews* **2004**, *104*(4), 2073–2098.

[19] Jansen, T. L. C.; Knoester, J. *Journal of Chemical Physics* **2006**, *124*(4), 044502.

[20] Moran, A.; Mukamel, S. *Proceedings of the National Academy of Sciences* **2004**, *101*(2), 506–510.

[21] Zhuang, W.; Abramavicius, D.; Mukamel, S. *Proceedings of the National Academy of Sciences of the United States of America* **2005**, *102*(21), 7443–8.

[22] Hamm, P.; Woutersen, S. *Bulletin of the Chemical Society of Japan* **2002**, *75*(5), 985–988.

[23] Krimm, S.; Bandekar, J. In *Advances in Protein Chemistry*, Vol. 38; 1986; pages 181–364.

[24] Mukherjee, P.; Kass, I.; Arkin, I. T.; Zanni, M. T. *Proceedings of the National Academy of Sciences* **2006**, *103*(10), 3528–3533.

[25] Ling, Y. L.; Strasfeld, D. B.; Shim, S.-h.; Raleigh, D. P.; Zanni, M. T. *The Journal of Physical Chemistry B* **2009**, *113*(8), 2498–2505.

[26] Demirdöven, N.; Cheatum, C. M.; Chung, H. S.; Khalil, M.; Knoester, J.; Tokmakoff, A. *Journal of the American Chemical Society* **2004**, *126*(25), 7981–7990.

[27] Asplund, M. C.; Zanni, M. T.; Hochstrasser, R. M. *Proceedings of the National Academy of Sciences* **2000**, *97*(15), 8219–8224.

[28] Skoff, D. R.; Laaser, J. E.; Mukherjee, S. S.; Middleton, C. T.; Zanni, M. T. *Chemical Physics* **2013**, *422*, 8–15.

[29] Karthick Kumar, S. K.; Tamimi, a.; Fayer, M. D. *The Journal of Chemical Physics* **2012**, *137*(18), 184201.

[30] Roberts, S. T.; Loparo, J. J.; Tokmakoff, A. *The Journal of Chemical Physics* **2006**, *125*(8), 084502.

[31] Huang, J. Y.; Shen, Y. R. *Physical Review A* **1994**, *49*(5), 3973–3981.

[32] Mukamel, S. *Principles of Nonlinear Optical Spectroscopy;* Oxford University Press: New York, 1st ed. ed., 1995.

[33] Du, Q.; Superfine, R.; Freysz, E.; Shen, Y. R. *Physical Review Letters* **1993**, *70*(15), 2313–2316.

[34] Dutta, C.; Benderskii, A. V. *Journal of Physical Chemistry Letters* **2017**, *8*(4), 801–804.

[35] Nguyen, K. T.; King, J. T.; Chen, Z. *Journal of Physical Chemistry B* **2010**, *114*(25), 8291–8300.

[36] Wang, J.; Even, M. A.; Chen, X.; Schmaier, A. H.; Waite, J. H.; Chen, Z. *Journal of the American Chemical Society* **2003**, *125*(33), 9914–9915.

[37] Chen, Z.; Shen, Y. R.; Somorjai, G. A. *Annual Review of Physical Chemistry* **2002**, *53*(1), 437–465.

[38] Kraack, J. P.; Hamm, P. *Chemical Reviews* **2017**, *117*(16), 10623–10664.

[39] Xiong, W.; Laaser, J. E.; Mehlenbacher, R. D.; Zanni, M. T. *Proceedings of the National Academy of Sciences* **2011**, *108*(52), 20902–20907.

[40] Ho, J.-J.; Ghosh, A.; Zhang, T. O.; Zanni, M. T. *The Journal of Physical Chemistry A* **2018**, *122*(5), 1270–1282.

[41] Rosenfeld, D. E.; Gengeliczki, Z.; Smith, B. J.; Stack, T. D. P.; Fayer, M. D. *Science* **2011**, *334*(6056), 634–639.

[42] Yan, C.; Thomaz, J. E.; Wang, Y.-L.; Nishida, J.; Yuan, R.; Breen, J. P.; Fayer, M. D. *Journal of the American Chemical Society* **2017**, *139*(46), 16518–16527.

[43] Willets, K. A.; Van Duyne, R. P. *Annual Review of Physical Chemistry* **2007**, *58*(1), 267–297.

[44] Stiles, P. L.; Dieringer, J. A.; Shah, N. C.; Van Duyne, R. P. *Annual Review of Analytical Chemistry* **2008**, *1*(1), 601–626.

[45] Neubrech, F.; Huck, C.; Weber, K.; Pucci, A.; Giessen, H. *Chemical Reviews* **2017**, *117*(7), 5110–5145.

[46] Selig, O.; Siffels, R.; Rezus, Y. *Physical Review Letters* **2015**, *114*(23), 233004.

[47] Gandman, A.; Mackin, R.; Cohn, B.; Rubtsov, I. V.; Chuntonov, L. *The Journal of Physical Chemistry Letters* **2017**, *8*(14), 3341–3346.

[48] Rezus, Y. L. A.; Selig, O. *Optics Express* **2016**, *24*(11), 12202.

[49] Donaldson, P. M.; Hamm, P. *Angewandte Chemie International Edition* **2013**, *52*(2), 634–638.

[50] Kraack, J. P.; Lotti, D.; Hamm, P. *The Journal of Chemical Physics* **2015**, *142*(21), 212413.

[51] Lotti, D.; Hamm, P.; Kraack, J. P. *Journal of Physical Chemistry C* **2016**, *120*(5), 2883–2892.

[52] Kraack, J. P.; Sévery, L.; Tilley, S. D.; Hamm, P. *The Journal of Physical Chemistry Letters* **2018**, *9*(1), 49–56.

[53] Nishida, J.; Yan, C.; Fayer, M. D. *The Journal of Chemical Physics* **2017**, *146*(9), 094201.

[54] Laaser, J. E.; Zanni, M. T. *The Journal of Physical Chemistry A* **2013**, *117*(29), 5875–5890.

[55] Hochstrasser, R. M. *Chemical Physics* **2001**, *266*(2-3), 273–284.

[56] Goodman, J. W. *Introduction to Fourier Optics;* 2nd ed., 1996.

[57] Helbing, J.; Hamm, P. *Journal of the Optical Society of America B* **2011**, *28*(1), 171.

[58] Réhault, J.; Maiuri, M.; Brida, D.; Manzoni, C.; Helbing, J.; Cerullo, G. In *Springer Proceedings in Physics*, Vol. 162; 2015; pages 462–465.

[59] Middleton, C. T.; Buchanan, L. E.; Dunkelberger, E. B.; Zanni, M. T. *The Journal of Physical Chemistry Letters* **2011**, *2*(18), 2357–2361.

[60] Shim, S. H.; Strasfeld, D. B.; Zanni, M. T. *Optics Express* **2006**, *14*(26), 13120–13130.

[61] Lewis, E. N.; Treado, P. J.; Reeder, R. C.; Story, G. M.; Dowrey, A. E.; Marcott, C.; Levin, I. W. *Analytical Chemistry* **1995**, *67*(19), 3377–3381.

[62] Snively, C. M.; Katzenberger, S.; Oskarsdottir, G.; Lauterbach, J. *Optics Letters* **1999**, *24*(24), 1841.

[63] Yeh, K.; Kenkel, S.; Liu, J.-N.; Bhargava, R. *Analytical Chemistry* **2015**, *87*(1), 485–493.

[64] Hughes, C.; Henderson, A.; Kansiz, M.; Dorling, K. M.; Jimenez-Hernandez, M.; Brown, M. D.; Clarke, N. W.; Gardner, P. *Analyst* **2015**, *140*(7), 2080–2085.

[65] Bhargava, R. *Applied Spectroscopy* **2012**, *66*(10), 1091–1120.

[66] Jamin, N.; Dumas, P.; Moncuit, J.; Fridman, W.-H.; Teillaud, J.-L.; Carr, G. L.; Williams, G. P. *Proceedings of the National Academy of Sciences* **1998**, *95*(9), 4837–4840.

[67] Baker, M. J.; Trevisan, J.; Bassan, P.; Bhargava, R.; Butler, H. J.; Dorling, K. M.; Fielden, P. R.; Fogarty, S. W.; Fullwood, N. J.; Heys, K. A.; Hughes, C.; Lasch, P.; Martin-Hirsch, P. L.; Obinaju, B.; Sockalingum, G. D.; Sulé-Suso, J.; Strong, R. J.; Walsh, M. J.; Wood, B. R.; Gardner, P.; Martin, F. L. *Nature Protocols* **2014**, *9*(8), 1771–1791.

[68] Kaindl, R. A.; Wurm, M.; Reimann, K.; Hamm, P.; Weiner, A. M.; Woerner, M. *Journal of the Optical Society of America B* **2000**, *17*(12), 2086.

[69] Witte, T.; Zeidler, D.; Proch, D.; Kompa, K. L.; Motzkus, M. *Optics Letters* **2002**, *27*(2), 131.

[70] Shim, S.-H.; Strasfeld, D. B.; Fulmer, E. C.; Zanni, M. T. *Optics Letters* **2006**, *31*(6), 838.

[71] Dudovich, N.; Oron, D.; Silberberg, Y. *Nature* **2002**, *418*(6897), 512–514.

[72] Ogilvie, J. P.; Beaurepaire, E.; Alexandrou, A.; Joffre, M. *Optics Letters* **2006**, *31*(4), 480–482.

[73] Baiz, C. R.; Schach, D.; Tokmakoff, A. *Optics Express* **2014**, *22*(15), 18724.

[74] Lowenthal, S.; Joyeux, D. *Journal of the Optical Society of America* **1971**, *61*(7), 847.

[75] Manning, C. J.; Griffiths, P. R. *Applied Spectroscopy* **1997**, *51*(8), 1092–1101.

[76] King, J. T.; Baiz, C. R.; Kubarych, K. J. *Journal of Physical Chemistry A* **2010**, *114*(39), 10590–10604.

[77] Kim, K.; Park, Y. *Optics Letters* **2012**, *37*(19), 4161.

[78] Kole, M. R.; Reddy, R. K.; Schulmerich, M. V.; Gelber, M. K.; Bhargava, R. *Analytical Chemistry* **2012**, *84*(23), 10366–10372.

[79] Redding, B.; Cerjan, A.; Huang, X.; Lee, M. L.; Stone, A. D.; Choma, M. A.; Cao, H. *Proceedings of the National Academy of Sciences* **2015**, *112*(5), 1304–1309.

[80] Dixon, L.; Cheong, F. C.; Grier, D. G. *Optics Express* **2011**, *19*(17), 16410.

[81] Stelzer, E. H. K. *Journal of Microscopy* **1998**, *189*(1), 15–24.

[82] Born, M.; Wolf, E. *Principles of Optics;* Cambridge University Press, 7th ed., 1999.

[83] Nasse, M. J.; Walsh, M. J.; Mattson, E. C.; Reininger, R.; Kajdacsy-Balla, A.; Macias, V.; Bhargava, R.; Hirschmugl, C. J. *Nature Methods* **2011**, *8*(5), 413–416.

[84] Carr, G. L. *Review of Scientific Instruments* **2001**, *72*(3), 1613.

[85] Beale, A. M.; Jacques, S. D. M.; Weckhuysen, B. M. *Chemical Society Reviews* **2010**, *39*(12), 4656.

[86] Griffiths, P.; De Haseth, J. *Fourier Transform Infrared Spectrometry;* 2nd ed. ed., 2007.

[87] Kise, D. P.; Magana, D.; Reddish, M. J.; Dyer, R. B. *Lab Chip* **2014**, *14*(3), 584–591.

[88] Petersen, P. B.; Tokmakoff, A. *Optics Letters* **2010**, *35*(12), 1962–1964.

[89] Thomson, M. D.; Blank, V.; Roskos, H. G. *Optics Express* **2010**, *18*(22), 23173.

[90] Yu, Y.; Zhang, B.; Gai, X.; Zhai, C.; Qi, S.; Guo, W.; Yang, Z.; Wang, R.; Choi, D.-Y.; Madden, S.; Luther-Davies, B. *Optics Letters* **2015**, *40*(6), 1081.

[91] Chan, K. L. A.; Kazarian, S. G. *Analytical Chemistry* **2013**, *85*(2), 1029–1036.

[92] Bassan, P.; Byrne, H. J.; Bonnier, F.; Lee, J.; Dumas, P.; Gardner, P. *The Analyst* **2009**, *134*(8), 1586.

[93] Reddy, R. K.; Walsh, M. J.; Schulmerich, M. V.; Carney, P. S.; Bhargava, R. *Applied Spectroscopy* **2013**, *67*(1), 93–105.

[94] Ostrander, J. S.; Serrano, A. L.; Ghosh, A.; Zanni, M. T. *ACS Photonics* **2016**, *3*(7), 1315–1323.

[95] Denk, W.; Strickler, J. H.; Webb, W. W. *Science* **1990**, *248*(4951), 73–76.

[96] Campagnola, P. J.; Loew, L. M. *Nature Biotechnology* **2003**, *21*(11), 1356–1360.

[97] Li, B.; Claytor, K. E.; Yuan, H.; Vo-Dinh, T.; Warren, W. S.; Fischer, M. C. *Optics Letters* **2012**, *37*(13), 2763–5.

[98] Wong, C. Y.; Cotts, B. L.; Wu, H.; Ginsberg, N. S. *Nature Communications* **2015**, *6*, 5946.

[99] Liu, N.; Kumbham, M.; Pita, I.; Guo, Y.; Bianchini, P.; Diaspro, A.; Tofail, S. A. M.; Peremans, A.; Silien, C. *ACS Photonics* **2016**, *3*(3), 478–485.

[100] Volkmer, A.; Cheng, J. X.; Xie, X. S. *Physical Review Letters* **2001**, *87*(2), 2–5.

[101] Fuller, F. D.; Ogilvie, J. P. *Annual Review of Physical Chemistry* **2015**, *66*(1), 667–690.

[102] Jones, K. C.; Peng, C. S.; Tokmakoff, A. *Proceedings of the National Academy of Sciences* **2013**, *110*(8), 2828–2833.

[103] Buchanan, L. E.; Dunkelberger, E. B.; Tran, H. Q.; Cheng, P.-N.; Chiu, C.-C.; Cao, P.; Raleigh, D. P.; de Pablo, J. J.; Nowick, J. S.; Zanni, M. T. *Proceedings of the National Academy of Sciences* **2013**, *110*(48), 19285–19290.

[104] Moran, S. D.; Woys, A. M.; Buchanan, L. E.; Bixby, E.; Decatur, S. M.; Zanni, M. T. *Proceedings of the National Academy of Sciences* **2012**, *109*(9), 3329–3334.

[105] Asbury, J. B.; Steinel, T.; Stromberg, C.; Gaffney, K. J.; Piletic, I. R.; Goun, A.; Fayer, M. D. *Physical Review Letters* **2003**, *91*(23), 237402.

[106] Roberts, S. T.; Mandal, A.; Tokmakoff, A. *The Journal of Physical Chemistry B* **2014**, *118*(28), 8062–8069.

[107] Stirnemann, G.; Laage, D. *The Journal of Physical Chemistry Letters* **2010**, *1*(10), 1511–1516.

[108] Kiefer, L. M.; Kubarych, K. J. *The Journal of Physical Chemistry A* **2015**, *119*(6), 959–965.

[109] Bredenbeck, J.; Helbing, J.; Hamm, P. *Journal of the American Chemical Society* **2004**, *126*(4), 990–991.

[110] Jones, B. H.; Huber, C. J.; Spector, I. C.; Tabet, A. M.; Butler, R. L.; Hang, Y.; Massari, A. M. *The Journal of Chemical Physics* **2015**, *142*(21), 212441.

[111] Ghosh, A.; Hochstrasser, R. M. *Chemical Physics* **2011**, *390*(1), 1–13.

[112] Lin, Z.; Rubtsov, I. V. *Proceedings of the National Academy of Sciences* **2012**, *109*(5), 1413–1418.

[113] Anna, J. M.; Kubarych, K. J. *Journal of Chemical Physics* **2010**, *133*, 174506.

[114] Zanni, M. T.; Ge, N.-H.; Kim, Y. S.; Hochstrasser, R. M. sep **2001**, *98*(20), 11265–11270.

[115] Fournier, F.; Guo, R.; Gardner, E. M.; Donaldson, P. M.; Loeffeld, C.; Gould, I. R.; Willison, K. R.; Klug, D. R. *Accounts of Chemical Research* **2009**, *42*(9), 1322–31.

[116] Yew, E. Y. S.; Sheppard, C. J. R.; So, P. T. C. *Optics Express* **2013**, *21*(10), 12951–12963.

[117] Toytman, I.; Simanovskii, D.; Palanker, D. *Optics Express* **2009**, *17*(9), 7339–7347.

[118] Tekavec, P. F.; Lott, G. A.; Marcus, A. H. *The Journal of Chemical Physics* **2007**, *127*(21), 214307.

[119] Karki, K. J.; Widom, J. R.; Seibt, J.; Moody, I.; Lonergan, M. C.; Pullerits, T.; Marcus, A. H. *Nature Communications* **2014**, *5*(1), 5869.

[120] Middleton, C. T.; Woys, A. M.; Mukherjee, S. S.; Zanni, M. T. *Methods* **2010**, *52*(1), 12–22.

[121] Serrano, A. L.; Ghosh, A.; Ostrander, J. S.; Zanni, M. T. *Optics Express* **2015**, *23*(14), 17815–17827.

[122] De, A. K.; Monahan, D.; Dawlaty, J. M.; Fleming, G. R. *The Journal of Chemical Physics* **2014**, *140*(19), 194201.

[123] Tian, P.; Keusters, D.; Suzaki, Y.; Warren, W. S. *Science* **2003**, *300*(5625), 1553–1555.

[124] Afiz, M.; Clark, R.; D'Urso, N. *Dalton Transactions* **1972**, *33*(1258), 1258–1263.

[125] Martin, M. C.; Dabat-Blondeau, C.; Unger, M.; Sedlmair, J.; Parkinson, D. Y.; Bechtel, H. A.; Illman, B.; Castro, J. M.; Keiluweit, M.; Buschke, D.; Ogle, B.; Nasse, M. J.; Hirschmugl, C. J. *Nature Methods* **2013**, *10*(9), 861–864.

[126] Gull, S.; Skilling, J. *IEE Proceedings F Communications, Radar and Signal Processing* **1984**, *131*(6), 646.

[127] Woys, A. M.; Lin, Y.-S.; Reddy, A. S.; Xiong, W.; de Pablo, J. J.; Skinner, J. L.; Zanni, M. T. *Journal of the American Chemical Society* **2010**, *132*(8), 2832–2838.

[128] Dunbar, J. A.; Osborne, D. G.; Anna, J. M.; Kubarych, K. J. *The Journal of Physical Chemistry Letters* **2013**, *4*(15), 2489–2492.

[129] Spencer, A. P.; Spokoyny, B.; Ray, S.; Sarvari, F.; Harel, E. *Nature Communications* **2016**, *7*(1), 10434.

[130] Baiz, C. R.; Nee, M. J.; McCanne, R.; Kubarych, K. J. *Optics Letters* **2008**, *33*(21), 2533–2535.

[131] Ghosh, A.; Serrano, A. L.; Oudenhoven, T. A.; Ostrander, J. S.; Eklund, E. C.; Blair, A. F.; Zanni, M. T. feb **2016**, *41*(3), 524.

[132] Cooper, P. *Explosives Engineering;* Wiley-VCH, 1st ed., 1996.

[133] Manner, V. W.; Tappan, B. C.; Scott, B. L.; Preston, D. N.; Brown, G. W. *Crystal Growth and Design* **2014**, *14*(11), 6154–6160.

[134] Zhurova, E. A.; Stash, A. I.; Tsirelson, V. G.; Zhurov, V. V.; Bartashevich, E. V.; Potemkin, V. A.; Pinkerton, A. A. *Journal of the American Chemical Society* **2006**, *128*(45), 14728–14734.

[135] Wu, C. J.; Fried, L. E. *The Journal of Physical Chemistry A* **2000**, *104*(27), 6447–6452.

[136] Kuklja, M. M.; Rashkeev, S. N.; Zerilli, F. J. *Applied Physics Letters* **2006**, *89*(7), 2004–2007.

[137] Ma, Y.; Zhang, A.; Xue, X.; Jiang, D.; Zhu, Y.; Zhang, C. *Crystal Growth and Design* **2014**, *14*(11), 6101–6114.

[138] Shan, T. R.; Wixom, R. R.; Mattsson, A. E.; Thompson, A. P. *Journal of Physical Chemistry B* **2013**, *117*(3), 928–936.

[139] Tokmakoff, A.; Fayer, M. D.; Dlott, D. D. *The Journal of Physical Chemistry* **1993**, *97*(9), 1901–1913.

[140] Hong, X.; Chen, S.; Dlott, D. D. *J. Phys. Chem.* **1995**, *99*, 9102–9109.

[141] Aubuchon, C.; Rector, K.; Holmes, W.; Fayer, M. *Chemical Physics Letters* **1999**, *299*(1), 84–90.

[142] Khalil, M.; Demirdöven, N.; Tokmakoff, A. *The Journal of Physical Chemistry A* **2003**, *107*(27), 5258–5279.

[143] Rubtsova, N. I.; Nyby, C. M.; Zhang, H.; Zhang, B.; Zhou, X.; Jayawickramarajah, J.; Burin, A. L.; Rubtsov, I. V. *The Journal of Chemical Physics* **2015**, *142*(21), 212412.

[144] Ge, N. H.; Zanni, M. T.; Hochstrasser, R. M. *Journal of Physical Chemistry A* **2002**, *106*(6), 962–972.

[145] Pein, B. C.; Sun, Y.; Dlott, D. D. *Journal of Physical Chemistry A* **2013**, *117*(29), 6066–6072.

[146] Iwaki, L. K.; Dlott, D. D. *Journal of Physical Chemistry A* **2000**, *104*(40), 9101–9112.

[147] King, J. T.; Anna, J. M.; Kubarych, K. J. *Physical Chemistry Chemical Physics* **2011**, *13*(13), 5579.

[148] Kuroda, D. G.; Hochstrasser, R. M. *The Journal of Chemical Physics* **2011**, *135*(20), 204502.

[149] Vorobyev, D. Y.; Kuo, C. H.; Kuroda, D. G.; Scott, J. N.; Vanderkooi, J. M.; Hochstrasser, R. M. *Journal of Physical Chemistry B* **2010**, *114*(8), 2944–2953.

[150] Vorobyev, D. Y.; Kuo, C. H.; Chen, J. X.; Kuroda, D. G.; Nathan Scott, J.; Vanderkooi, J. M.; Hochstrasser, R. M. *Journal of Physical Chemistry B* **2009**, *113*(46), 15382–15391.

[151] Kurochkin, D. V.; Naraharisetty, S. R. G.; Rubtsov, I. V. *Proceedings of the National Academy of Sciences* **2007**, *104*(36), 14209–14214.

[152] Yue, Y.; Qasim, L. N.; Kurnosov, A. A.; Rubtsova, N. I.; Mackin, R. T.; Zhang, H.; Zhang, B.; Zhou, X.; Jayawickramarajah, J.; Burin, A. L.; Rubtsov, I. V. *Journal of Physical Chemistry B* **2015**, *119*(21), 6448–6456.

[153] Chen, H.; Wen, X.; Guo, X.; Zheng, J. *Physical Chemistry Chemical Physics* **2014**, *16*(27), 13995.

[154] Chen, H.; Zhang, Q.; Guo, X.; Wen, X.; Li, J.; Zhuang, W.; Zheng, J. *Journal of Physical Chemistry A* **2015**, *119*(4), 669–680.

[155] Dlott, D. D. *Annual Reviews of Physical Chemistry* **1999**, *50*(1), 251–78.

[156] Dlott, D. D. *Materials Science and Technology* **2006**, *22*(4), 463–473.

[157] Frisch, M.; Trucks, G.; Schlegel, H.; Scuseria, G.; Robb, M.; Cheeseman, J.; Scalmani, G.; Barone, V.; Mennucci, B.; Petersson, G.; Nakatsuji, H.; Caricato, M.; Li, X.; Hratchian, H.; Izmaylov, A. F.; Bloino, J.; Zheng, G.; Sonnenberg, J.; Hada, M.; Ehara, M.; Toyota, K.; Fukuda, R.; Hasegawa, J.; Ishida, M.; Nakajima, T.; Honda, Y.; Kitao, O.; Nakai, H.; Vreven, T.; Montogomery, J.A., J.; Peralta, J.; Ogliaro, F.; Bearpark, M.; Heyd, J.; Brothers, E.; Kudin, K.; Staroverov, V.; Kobayashi, R.; Normand, J.; Raghavachari, K.; Rendell, A.; Burant, J.; Iyengar, S.; Tomasi, J.; Cossi, M.; Rega, N.; Millam, J.; Klene, M.; Knox, J.; Cross, J.; Bakken, V.; Adamo, C.; Jaramillo, J.; Gomperts, R.; Stratmann, R.; Yazyev, O.; Austin, A.; Cammi, R.; Pomelli, C.; Ochterski, J.; Martin, R.; Morokuma, K.; Zakrzewski, V.; Voth, G. A.; Salvador, P.; Dannenberg, J.; Dapprich, S.; Daniels, A.; Farkas, O.; Foresman, J.; Ortiz, J.; Cioslowski, J.; Fox, D. *Gaussian 09, Revision D.01;* 2009.

[158] Cheam, T. C.; Krimm, S. *Chem. Phys. Lett.* **1984**, *107*(6), 613–616.

[159] Knepper, R.; Tappan, A. S.; Wixom, R. R.; Rodriguez, M. A. *Journal of Materials Research* **2011**, *26*(13), 1605–1613.

[160] Anna, J. M.; Baiz, C. R.; Ross, M. R.; McCanne, R.; Kubarych, K. J. *International Reviews in Physical Chemistry* **2012**, *31*(3), 367–419.

[161] Jonas, D. M.; Lang, M. J.; Nagasawa, Y.; Joo, T.; Fleming, G. R. *Journal of Physical Chemistry* **1996**, *100*(30), 12660–12673.

[162] Fournier, J. A.; Carpenter, W.; De Marco, L.; Tokmakoff, A. *Journal of the American Chemical Society* **2016**, *138*(30), 9634–9645.

[163] Dunkelberger, E. B.; Grechko, M.; Zanni, M. T. *Journal of Physical Chemistry B* **2015**, *119*(44), 14065–14075.

[164] Zheng, J.; Kwak, K.; Asbury, J.; Chen, X.; Piletic, I. R.; Fayer, M. D. *Science* **2005**, *309*(5739), 1338–1343.

[165] Ramasesha, K.; Roberts, S. T.; Nicodemus, R. A.; Mandal, A.; Tokmakoff, A. *The Journal of Chemical Physics* **2011**, *135*(5), 054509.

[166] Gruzdkov, Y. A.; Gupta, Y. M. *Journal of Physical Chemistry A* **2001**, *105*(25), 6197–6202.

[167] Ye.; Koshi, M. *The Journal of Physical Chemistry B* **2006**, *110*(37), 18515–18520.

[168] Giammanco, C. H.; Kramer, P. L.; Yamada, S. A.; Nishida, J.; Tamimi, A.; Fayer, M. D. *The Journal of Chemical Physics* **2016**, *144*(10), 0–19.

[169] Kramer, P. L.; Nishida, J.; Fayer, M. D. *The Journal of Chemical Physics* **2015**, *143*(12), 124505.

[170] Bakulin, A. A.; Selig, O.; Bakker, H. J.; Rezus, Y. L.; Müller, C.; Glaser, T.; Lovrincic, R.; Sun, Z.; Chen, Z.; Walsh, A.; Frost, J. M.; Jansen, T. L. C. *The Journal of Physical Chemistry Letters* **2015**, *6*(18), 3663–3669.

[171] Bian, H.; Zhao, W.; Zheng, J. *The Journal of Chemical Physics* **2009**, *131*(12), 124501.

[172] Mehlenbacher, R. D.; Wu, M.-y.; Grechko, M.; Laaser, J. E.; Arnold, M. S.; Zanni, M. T. *Nano Letters* **2013**, *13*(4), 1495–1501.

[173] Painter, P.; Coleman, M.; Koenig, J. *The Theory of Vibrational Spectroscopy and its Application to Polymeric Materials;* John Wiley: New York, 1982.

[174] Scholes, G. D.; Smyth, C. *The Journal of Chemical Physics* **2014**, *140*(11), 110901.

[175] Hamm, P.; Lim, M.; Hochstrasser, R. M. *The Journal of Physical Chemistry B* **1998**, *102*(31), 6123–6138.

[176] Ungnade, H. E.; Roberts, E. M.; Kissinger, L. W. *The Journal of Physical Chemistry* **1964**, *68*(11), 3225–3228.

[177] Deschamps, J. R.; Parrish, D. A. *Propellants, Explosives, Pyrotechnics* **2015**, *40*(4), 506–513.

[178] Shimamura, K.; Misawa, M.; Ohmura, S.; Shimojo, F.; Kalia, R. K.; Nakano, A.; Vashishta, P. *Applied Physics Letters* **2016**, *108*(7), 071901.

[179] Shimamura, K.; Misawa, M.; Li, Y.; Kalia, R. K.; Nakano, A.; Shimojo, F.; Vashishta, P. *Applied Physics Letters* **2015**, *107*(23), 231903.

[180] Stingel, A. M.; Calabrese, C.; Petersen, P. B. *The Journal of Physical Chemistry B* **2013**, *117*(49), 15714–15719.

[181] Rubtsov, I. V.; Wang, J.; Hochstrasser, R. M. *Proceedings of the National Academy of Sciences of the United States of America* **2003**, *100*(10), 5601–5606.

[182] Ho, J. J.; Skoff, D. R.; Ghosh, A.; Zanni, M. T. *Journal of Physical Chemistry B* **2015**, *119*(33), 10586–10596.

[183] Ghosh, A.; Ho, J.-J.; Serrano, A. L.; Skoff, D. R.; Zhang, T.; Zanni, M. T. *Faraday Discuss.* **2015**, *177*, 493–505.

[184] Bredenbeck, J.; Ghosh, A.; Smits, M.; Bonn, M. *Journal of the American Chemical Society* **2008**, *130*(7), 2152–2153.

[185] Hoffmann, F. *Surface Science Reports* **1983**, *3*(2-3), 107.

[186] Golden, W. *Journal of Catalysis* **1981**, *71*(2), 395–404.

[187] Martin, I.; Goormaghtigh, E.; Ruysschaert, J.-M. *Biochimica et Biophysica Acta (BBA) - Biomembranes* **2003**, *1614*(1), 97–103.

[188] Buffeteau, T.; Desbat, B.; Turlet, J. M. *Applied Spectroscopy* **1991**, *45*(3), 380–389.

[189] Fahrenfort, J. *Spectrochimica Acta* **1961**, *17*(7), 698–709.

[190] McQuillan, A. J. *Advanced Materials* **2001**, *13*(12-13), 1034–1038.

[191] Wang, H.; Yan, E. C.; Borguet, E.; Eisenthal, K. B. *Chemical Physics Letters* **1996**, *259*(1-2), 15–20.

[192] Fu, L.; Liu, J.; Yan, E. C. Y. *Journal of the American Chemical Society* **2011**, *133*(21), 8094–8097.

[193] Geiger, F. M. *Annual Review of Physical Chemistry* **2009**, *60*(1), 61–83.

[194] Stiopkin, I. V.; Weeraman, C.; Pieniazek, P. A.; Shalhout, F. Y.; Skinner, J. L.; Benderskii, A. V. *Nature* **2011**, *474*(7350), 192–195.

[195] Wang, Z.; Carter, J. A.; Lagutchev, A.; Koh, Y. K.; Seong, N.-H.; Cahill, D. G.; Dlott, D. D. *Science* **2007**, *317*(5839), 787–790.

[196] Bredenbeck, J.; Ghosh, A.; Nienhuys, H.-k.; Bonn, M. *Accounts of Chemical Research* **2009**, *42*(9), 1332–1342.

[197] Nihonyanagi, S.; Yamaguchi, S.; Tahara, T. *Chemical Reviews* **2017**, *117*(16), 10665–10693.

[198] Petti, M. K.; Lomont, J. P.; Maj, M.; Zanni, M. T. *The Journal of Physical Chemistry B* **2018**, *122*(6), 1771–1780.

[199] Kraack, J. P.; Kaech, A.; Hamm, P. *Journal of Physical Chemistry C* **2016**, *120*(6), 3350–3359.

[200] Kraack, J. P.; Hamm, P. *Physical Chemistry Chemical Physics* **2016**, *18*(24), 16088–16093.

[201] Mackin, R. T.; Cohn, B.; Gandman, A.; Leger, J. D.; Chuntonov, L.; Rubtsov, I. V. *The Journal of Physical Chemistry C* **2018**, *122*(20), 11015–11023.

[202] Réhault, J.; Helbing, J. *Optics Express* **2012**, *20*(19), 21665.

[203] Johnson, T. R.; Mann, B. E.; Teasdale, I. P.; Adams, H.; Foresti, R.; Green, C. J.; Motterlini, R. *Dalton Transactions* **2007**, (15), 1500.

[204] King, J. T.; Arthur, E. J.; Brooks, C. L.; Kubarych, K. J. *The Journal of Physical Chemistry B* **2012**, *116*(19), 5604–5611.

[205] Fulmer, E. C.; Ding, F.; Mukherjee, P.; Zanni, M. T. *Physical Review Letters* **2005**, *94*(6), 067402.

[206] Laaser, J. E.; Christianson, J. R.; Oudenhoven, T. A.; Joo, Y.; Gopalan, P.; Schmidt, J. R.; Zanni, M. T. *Journal of Physical Chemistry C* **2014**, *118*(11), 5854–5861.

[207] Oudenhoven, T. A.; Joo, Y.; Laaser, J. E.; Gopalan, P.; Zanni, M. T. *The Journal of Chemical Physics* **2015**, *142*(21), 212449.

[208] Sawai, M. V.; Waring, A. J.; Kearney, W. R.; McCray, P. B.; Forsyth, W. R.; Lehrer, R. I.; Tack, B. F. *Protein Engineering, Design and Selection* **2002**, *15*(3), 225–232.

[209] Ding, B.; Laaser, J. E.; Liu, Y.; Wang, P.; Zanni, M. T.; Chen, Z. *The Journal of Physical Chemistry B* **2013**, *117*(47), 14625–14634.

[210] Yamaguchi, S.; Huster, D.; Waring, A.; Lehrer, R. I.; Kearney, W.; Tack, B. F.; Hong, M. *Biophysical Journal* **2001**, *81*(4), 2203–2214.

[211] Nowinski, A. K.; Sun, F.; White, A. D.; Keefe, A. J.; Jiang, S. *Journal of the American Chemical Society* **2012**, *134*(13), 6000–6005.

[212] Kitagawa, K.; Morita, T.; Kimura, S. *The Journal of Physical Chemistry B* **2004**, *108*(39), 15090–15095.

[213] Jansen, T. L. C. *The Journal of Physical Chemistry B* **2014**, *118*(28), 8162–8169.

[214] Roach, P.; Farrar, D.; Perry, C. C. *Journal of the American Chemical Society* **2005**, *127*(22), 8168–8173.

[215] Cho, B.; Tiwari, V.; Jonas, D. M. *Analytical Chemistry* **2013**, *85*(11), 5514–5521.

[216] Osawa, M.; Ataka, K.-i. *Surface Science* **1992**, *262*(3), L118–L122.

[217] Nishikawa, Y.; Nagasawa, T.; Fujiwara, K.; Osawa, M. *Vibrational Spectroscopy* **1993**, *6*(1), 43–53.

[218] Osawa, M.; Ataka, K.-I.; Yoshii, K.; Nishikawa, Y. *Applied Spectroscopy* **1993**, *47*(9), 1497–1502.

[219] Chuntonov, L.; Kumar, R.; Kuroda, D. G. *Phys. Chem. Chem. Phys.* **2014**, *16*(26), 13172–13181.

[220] Englander, S. W.; Mayne, L. *Annual Review of Biophysics and Biomolecular Structure* **1992**, *21*(1), 243–265.

[221] Liu, Y.; Liu, Y.; Mernaugh, R. L.; Zeng, X. *Biosensors and Bioelectronics* **2009**, *24*(9), 2853–2857.

[222] Cui, X.; Liu, M.; Li, B. *Analyst* **2012**, *137*(14), 3293–3299.

[223] Piro, B.; Reisberg, S. *Sensors* **2017**, *17*(4), 794.

[224] Griffin, L.; Lawson, A. *Clinical & Experimental Immunology* **2011**, *165*(3), 285–291.

[225] Kayed, R.; Leapman, R. D.; Guo, Z.; Yau, W.-M.; Mattson, M. P.; Tycko, R. *Science* **2003**, *300*(5618), 486–489.

[226] Ma, B.; Zhao, J.; Nussinov, R. *Biochimica et Biophysica Acta* **2016**, *1860*(11), 2672–2681.

[227] Tycko, R. *Neuron* **2015**, *86*(3), 632–645.

[228] Nabers, A.; Perna, L.; Lange, J.; Mons, U.; Schartner, J.; Güldenhaupt, J.; Saum, K.; Janelidze, S.; Holleczek, B.; Rujescu, D.; Hansson, O.; Gerwert, K.; Brenner, H. *EMBO Molecular Medicine* **2018**, *10*(5), e8763.

[229] Nabers, A.; Ollesch, J.; Schartner, J.; Kötting, C.; Genius, J.; Haußmann, U.; Klafki, H.; Wiltfang, J.; Gerwert, K. *Journal of Biophotonics* **2016**, *9*(3), 224–234.

[230] Nabers, A.; Ollesch, J.; Schartner, J.; Kötting, C.; Genius, J.; Hafermann, H.; Klafki, H.; Gerwert, K.; Wiltfang, J. *Analytical Chemistry* **2016**, *88*(5), 2755–2762.

[231] Baiz, C. R.; Tokmakoff, A. *Biophysical Journal* **2014**, *106*(2), 459a–459a.

[232] Cooper, G. J. S.; Leighton, B.; Dimitriadis, G. D.; Parry-Billings, M.; Kowalchuk, J. M.; Howland, K.; Rothbard, J. B.; Willis, A. C.; Reid, K. B. M. *Proceedings of the National Academy of Sciences of the United States of America* **1988**, *85*(October), 7763–7766.

[233] Wiltzius, J. J.; Sievers, S. A.; Sawaya, M. R.; Eisenberg, D. *Protein Science* **2009**, *18*(7), 1521–1530.

[234] Luca, S.; Yau, W.-M.; Leapman, R.; Tycko, R. *Biochemistry* **2007**, *46*(47), 13505–13522.

[235] Abedini, A.; Cao, P.; Plesner, A.; Zhang, J.; He, M.; Derk, J.; Patil, S. A.; Rosario, R.; Lonier, J.; Song, F.; Koh, H.; Li, H.; Raleigh, D. P.; Schmidt, A. M. *Journal of Clinical Investigation* **2018**, *128*(2), 682–698.

[236] Raleigh, D.; Zhang, X.; Hastoy, B.; Clark, A. *Journal of Molecular Endocrinology* **2017**, *59*(3), R121–R140.

[237] Maj, M.; Lomont, J. P.; Rich, K. L.; Alperstein, A. M.; Zanni, M. T. *Chemical Science* **2018**, *9*(2), 463–474.

[238] Serrano, A. L.; Lomont, J. P.; Tu, L. H.; Raleigh, D. P.; Zanni, M. T. *Journal of the American Chemical Society* **2017**, *139*(46), 16748–16758.

[239] Almeida, I.; Cascalheira, A. C.; Viana, A. S. *Electrochimica Acta* **2010**, *55*(28), 8686–8695.

[240] Strasfeld, D. B.; Ling, Y. L.; Shim, S.-H.; Zanni, M. T. *Journal of the American Chemical Society* **2008**, *130*(21), 6698–6699.

[241] Marek, P.; Woys, A. M.; Sutton, K.; Zanni, M. T.; Raleigh, D. P. *Organic Letters* **2010**, *12*(21), 4848–4851.

[242] Tycko, R. *Protein Science* **2014**, *23*(11), 1528–1539.

[243] Buchanan, L. E.; Maj, M.; Dunkelberger, E. B.; Cheng, P. N.; Nowick, J. S.; Zanni, M. T. *Biochemistry* **2018**, *57*(46), 6470–6478.

[244] Mukherjee, S.; Chowdhury, P.; DeGrado, W. F.; Gai, F. *Langmuir* **2007**, *23*(22), 11174–11179.

[245] Torres, J.; Kukol, A.; Goodman, J. M.; Arkin, I. T. *Biopolymers* **2001**, *59*(6), 396–401.

[246] Flanagan, J. C.; Baiz, C. R. *Biophysical Journal* **2019**, *116*(3), 317a.

[247] Scheerer, D.; Chi, H.; McElheny, D.; Keiderling, T. A.; Hauser, K. *The Journal of Physical Chemistry B* **2018**, *122*(46), 10445–10454.

[248] Kim, Y. S.; Liu, L.; Axelsen, P. H.; Hochstrasser, R. M. *Proceedings of the National Academy of Sciences* **2008**, *105*(22), 7720–7725.

[249] Mucke, O.; Aliauskas, S.; Verhoef, A.; Puglys, A.; Baltuska, A.; Smilgeviius, V.; Pocius, J.; Gininas, L.; Danielius, R.; Forget, N. In *Advances in Solid State Lasers Development and Applications;* InTech, 2010.

[250] Donaldson, P.; Greetham, G.; Shaw, D.; Parker, A.; Towrie, M. *The Journal of Physical Chemistry A* **2018**, *122*(3), 780–787.